Department of Chemistry

Exploring electroactive porous metalorganics – on-surface synthesis and applications

Andre Mähringer

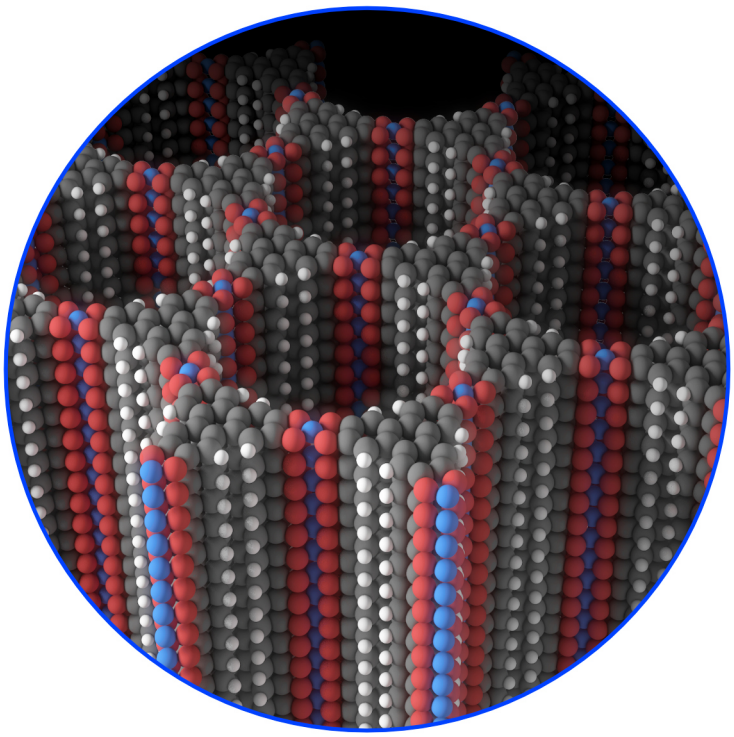

Physical Chemistry

Dissertation zur Erlangung des Doktorgrades
der Fakultät für Chemie und Pharmazie
der Ludwig-Maximilians-Universität München

Exploring electroactive porous metalorganics – on-surface synthesis and applications

Andre Richard Mähringer

aus

Duisburg, Deutschland

2021

Erklärung

Diese Dissertation wurde im Sinne von § 7 der Promotionsordnung vom 28. November 2011 von Herrn Prof. Dr. Thomas Bein betreut.

Eidesstattliche Versicherung

Diese Dissertation wurde eigenständig und ohne unerlaubte Hilfe erarbeitet.

München, den 28. Januar 2021

.....

M. Sc. Andre Richard Mähringer

Dissertation eingereicht am	05.02.2021
1. Gutachter:	Prof. Dr. Thomas Bein
2. Gutachter:	Prof. Dr. Achim Hartschuh
Mündliche Prüfung am	18.03.2021

Acknowledgement

An erster Stelle möchte ich all Jenen meinen größten Dank aussprechen die mir bei der Fertigstellung dieser Dissertation geholfen haben. Auch wenn ich nicht alle Unterstützer namentlich nennen kann, möchte ich allen danken die bei der Erstellung dieser Arbeit beteiligt waren. Hier möchte ich ausdrücklich meinen zahlreichen Co-Autoren danken, mit denen ich im Laufe der Jahre erfolgreich zusammen arbeiten durfte.

Mein besonderer Dank gilt Dana Medina als meine zentrale Ansprechpartnerin und wissenschaftliche Mentorin. Den größten Beitrag zum Zustandekommen dieser Arbeit hat ohne Zweifel sie vollbracht. Vielen Dank an dieser Stelle auch an die großzügige wissenschaftliche Freiheit, die mir während meiner Promotion von ihr gewährt wurde. Ohne diese Freiheit wäre wohl nie die Kreativität für die vielen Projekte entstanden, die wir schließlich gemeinsam in Manuskriptform gegossen haben. Gerade weil die Zusammenarbeit stets fordernd und das Niveau hoch war, kann ich mich glücklich schätzen eine solch großartige Mentorin gehabt zu haben.

Mein bester Dank geht auch an meinen Doktorvater Prof. Thomas Bein für die kontinuierliche Unterstützung im Verlauf meiner Forschungstätigkeit. Hier seien besonders die vielen fruchtbaren Diskussionen in unseren group und sub-group meetings erwähnt, welche mich stets für neue Projekte motiviert haben. Dankbar bin ich für seine finanzielle Unterstützung im Rahmen von NIM, CeNS, e-conversion und Soltech, die mir die Teilnahme an vielen unvergesslichen Konferenzen und Workshops ermöglicht haben. Daher freut es mich umso mehr, dass ich gemeinsam mit ihm in zahlreichen hochrangigen Fachjournalen publizieren durfte.

Schlussendlich gilt mein besonderer Dank meinen liebevollen Eltern, Heike und Achim Mähringer. Ohne ihre konstante finanzielle und seelische Unterstützung sowie ihre Ratschläge und Weisheit wäre diese Arbeit niemals zustande gekommen. Auch in den schwierigsten Stunden waren sie immer für mich da und ich wäre nicht hier ohne ihre wunderbare Zuwendung. Ich danke euch.

Abstract

This thesis deals with the on-surface synthesis and novel design of framework materials for the use in energy-conversion and -storage applications. The focus is on porous coordination polymers, specifically, metal-organic frameworks (MOFs). MOFs are regarded as an emerging class of materials owing an interesting spectrum of properties such as porosity, chemical versatility and nanocrystallinity. In recent years, the fundamental property of electrical conductivity was added to this portfolio, rendering MOFs promising candidates for their implementation in solid-electrodes, semiconductors, transistors, chemical sensors, supercapacitors or solar cells.

Before integrating MOFs in such highly desired applications, and moreover, to enable the study of their electrochemical and photophysical properties, stands the challenging task to prepare this class of materials in an ordered and well-defined fashion on surfaces. To shed light on this issue, this thesis presents a method for producing thin films of 2D frameworks featuring thicknesses at the nanometerscale with high precision and homogeneity. The first three chapters of this thesis illustrate the synthesis of oriented and crystalline MOF films beginning with 2D materials suitable as electrode materials in charge storage applications, over superhydrophilic and -oleophobic surfaces for anti-fog coatings, and closing with nanoarchitectures for oil-water separation. The results of these studies led to the filing of an international patent application. The last two chapters focus on the design and synthesis of novel electroactive MOFs to systematically expand the research field of these promising materials.

In the introduction section, the background of electroactive MOFs is provided. Here, the first discovered electrically conducting metalorganics are introduced and compared to recently reported 3D derivatives. Next, state-of-the-art techniques for the fabrication of MOF thin films are discussed as well as their advantages and disadvantages regarding the obtained film morphology. In this context, the focus will be on 2D MOF materials. At this point the scientific background for the film growth method of choice in this thesis is provided: the vapor-assisted conversion method (VAC).

In chapter 3 the preparation of two-dimensional triphenylene-based MOFs on different surfaces is discussed. Films grown on quartz substrates allowed for a detailed photophysical characterization by means of UV-VIS, photoluminescence, and transient absorption spectroscopy. The latter revealed the existence of excited states on a nanosecond time scale, sufficiently long to extract the formed photoinduced charge carriers from the MOF based films. This was achieved by fabricating a basic photovoltaic device with an ITO/MOF/Al architecture, thus establishing triphenylene-based MOFs as photoactive materials. Our results point to the intriguing capabilities

of these conducting triphenylene-based materials and the use as possible photoabsorbers enabled through VAC thin film synthesis.

Chapter 4 describes the synthesis of highly oriented and nanostructured MOF films on gold and quartz surfaces. These nanostructured MOF films feature extreme wetting phenomena, specifically superhydrophilic and underwater superoleophobic properties showing water and underwater oil-contact angles of 0° and up to 174°, respectively. The self-cleaning capability of nanostructured and needle-like films was illustrated by measuring time-dependent oil droplet rolling-off a tilted surface. The deposition of the nanostructured film on a large glass substrate allowed for the realization of an efficient, transparent anti-fog coating, enabling a clear vision through the substrates even at extreme temperature gaps of up to 120°C. This work illustrates the strong link between MOF film morphology and obtained surface properties by controlling the film growth process.

We transferred the previously acquired knowledge of how to create extreme surface wetting properties to the growth of Co-CAT-1 nano-architectures on gold-coated woven stainless steel meshes with 50 µm apertures allowing for gravity-driven, highly efficient oil-water separation. Chapter 5 describes the use of this MOF-based membrane for achieving high oil-water separation efficiencies for a number of oily liquids, including the notorious pollutant, crude oil. The results discussed here point towards the intriguing impact of suitable nanoscale surface architectures as means of encoding on-surface extreme wetting properties, yielding energy-efficient water-selective large-aperture membranes.

In the next two chapters the focus switches from the film synthesis to the design of novel MOFs. In chapter 6 we expanded the robust MOF-74 topology by installing an anthracene motif into the framework backbone. Here *4,4'*-(anthracene-9,10-diyl)*bis*(2-hydroxybenzoic acid) was employed as photophysical active building block and merged with five different divalent metal ions resulting in a series of highly crystalline MOFs, coined ANMOF-74(M). Compared to the original MOF-74 materials we observed a conductivity enhancement of up to six orders of magnitude. The observations made in this chapter highlight the importance of building block design and the careful choice of the embedded MOF topology for receiving materials with desired properties such as photoluminescence and electrical conductivity.

In the last chapter 7 we demonstrate the synthesis of a novel cubic MOF comprising hexahydroxytriphenylene units and Fe^{III} ions. In contrast to previously reported examples of hexahydroxytriphenylene combined with 3D transition metals, the 3D connected framework obtained here shows electrical conductivity, large surface area and high crystallinity. This chapter expands the paradigm of intrinsically electroactive 3D MOFs, and thus, serves as solid

basis for the development of novel highly porous, ordered frameworks with enhanced electrical conductivity.

A summary of the knowledge gained in this thesis as well as a perspective on the field of electroactive frameworks and thin film synthesis is enclosed.

Contents

1. Introduction **1**

1.1. Metal-organic frameworks - principles of reticular chemistry 1

1.2. Electrically conducting MOFs - a new player enters the stage 4

1.2.1. Charge-transport in MOFs 5

1.3. Electroactive MOFs based on triphenylene moieties 6

1.3.1. Teaching an "old" molecule new tricks - layered MOFs based on catechols 6

1.3.2. Expanding the family of layered and eletroactive MOFs 8

1.3.3. Switching topology - from 2D to 3D catechol frameworks 12

1.4. MOF-74 topology - a versatile platform 16

1.5. Thin film growth - opening new horizons 17

1.5.1. Oriented MOF film growth - general concerns 18

1.5.2. State-of-the-art - thin film growth of 2D MOF 19

1.5.3. A new way - vapor-assisted conversion 24

2. Analytical methods **27**

2.1. X-ray powder diffraction 27

2.1.1. Theory - diffraction of X-rays 27

2.1.2. Methods of X-ray diffraction 28

2.1.3. Phase analysis - Rietveld and Pawley refinement 30

2.2. Grazing incidence wide-angle X-ray scattering 31

2.2.1. Experimental set-up 32

2.2.2. Scattering geometry 33

2.3. Electron microscopy 35

2.3.1. Scanning electron microscopy 36

2.3.2. Energy-dispersive X-ray spectroscopy 37

2.3.3. Transmission electron microscopy 38

2.4. IR spectroscopy 38

2.5. Spectrophotometry 39

2.5.1. UV/VIS/NIR spectroscopy 39

2.5.2. Photoluminescence measurements 40

2.5.3. Transient absorption spectroscopy 41

2.6. Nuclear magnetic resonance spectroscopy 42

2.7. X-ray photoelectron spectroscopy 43

2.8. Atomic force microscopy 44

2.9. ^{57}Fe-Mößbauer spectroscopy . . . 45
2.10. Electron paramagnetic resonance spectroscopy . . . 48
2.11. Physisorption analysis . . . 49
2.12. Thermogravimetric analysis . . . 51
2.13. Electrical conductivity measurements . . . 51
2.13.1. Four-point probe resistance measurement . . . 51
2.13.2. Two-point probe resistance measurement . . . 53
2.14. Contact-angle measurements . . . 53
2.14.1. Theory - surface wetting models . . . 54
2.14.2. Experimental methods . . . 55
2.15. ICP spectroscopy . . . 56
2.16. Cyclic voltammetry . . . 57

3. Oriented thin films of electroactive triphenylene catecholate-based two-dimensional metal-organic frameworks 61
3.1. Introduction . . . 62
3.2. Results and discussion . . . 65
3.3. Conclusion . . . 72
3.4. Experimental methods . . . 73
3.4.1. Substrate preparation . . . 73
3.4.2. Synthesis of M-CAT-1 thin films through VAC . . . 73
3.4.3. Synthesis of Ni-, Co-, and Cu-CAT-1 films on gold surfaces . . . 74
3.4.4. Synthesis of Ni-CAT-1 films on quartz and ITO substrates . . . 74
3.4.5. Synthesis of Co-CAT-1 films on quartz substrates . . . 74
3.5. Appendix . . . 77
3.5.1. Characterization . . . 77
3.5.2. Experimental . . . 78
3.5.3. Bulk synthesis . . . 79
3.5.4. Film formation *via* vapor-assisted conversion (VAC) . . . 80
3.5.5. Synthesis of Ni-, Co- and Cu-CAT-1 films on gold surfaces . . . 81
3.5.6. Synthesis of Ni-CAT-1 films on ITO substrates . . . 81
3.5.7. Synthesis of Ni-1 CAT-1 films on glass substrates . . . 81
3.5.8. Synthesis of Co-CAT-1 films on glass substrates . . . 82
3.5.9. Solar Cell device fabrication . . . 82
3.5.10. Characterization of the M-CAT-1 bulk material . . . 83
3.5.11. Characterization of M-CAT-1 thin films . . . 87

3.5.12. Additional analysis 101

4. Nanostructured and oriented metal-organic framework films enabling extreme surface wetting properties 107

4.1. Introduction 108
4.2. Results and discussion 110
4.3. Conclusion 119
4.4. Appendix 121
4.4.1. Characterization 121
4.4.2. Experimental 122
4.4.3. Characterization of the M-CAT-1 bulk material 125
4.4.4. Reference contact angle measurements 128
4.4.5. Characterization of M-CAT-1 thin films 130
4.4.6. Anti-fog coating experiments 134
4.4.7. Wetting models 135
4.4.8. Stability tests 136

5. Energy efficient, ultrahigh flux separation of oily pollutants from water with superhydrophilic nanoscale metal-organic framework architectures 139

5.1. Introduction 140
5.2. Results and discussion 142
5.3. Conclusion 150
5.4. Appendix 153
5.4.1. Materials and methods 153
5.4.2. Vapor-assisted conversion 154
5.4.3. Analysis of SSM, Au@SSM and MOF@Au@SSM meshes 155
5.4.4. Characterization of surface wetting properties 158
5.4.5. Characterization of oil-water separation 160
5.4.6. Stability tests of the MOF@Au@SSM 169
5.4.7. Electrostatic hydration stabilization calculation 172

6. A highly crystalline anthracene-based MOF-74 series featuring electrical conductivity and luminescence 175

6.1. Introduction 176
6.2. Results and discussion 177
6.3. Conclusions 184

6.4. Appendix . . . 186
6.4.1. Characterization methods . . . 186
6.4.2. Experimental . . . 188
6.4.3. Characterization . . . 192

7. An electrically conducting three-dimensional iron-catecholate porous framework 207
7.1. Introduction . . . 208
7.2. Results and discussion . . . 211
7.3. Conclusion . . . 218
7.4. Appendix . . . 221
7.4.1. Characterization . . . 221
7.4.2. Experimental . . . 224
7.4.3. Additional information . . . 225
7.4.4. Zero-Field ^{57}Fe-Mössbauer, EPR-spectroscopy & VT SQUID magnetization data . . . 229
7.4.5. Structure solution . . . 232
7.4.6. Charge-carrier pathway simulations . . . 234

8. Summary and outlook 237

A. Miscellaneous 240
A.1. Electrical conductivity in a helical and highly crystalline ethyne-anthracene based MOF-74 . . . 241
A.2. Single-crystals of rare-earth metal catecholate based frameworks featuring defined emission profiles and electrical conductivity . . . 243
A.3. Taking stock of stacking . . . 245
A.4. List of publications . . . 251
A.5. Patents . . . 252
A.6. Conferences . . . 252
A.7. Workshops and seminars . . . 253

1. Introduction

Parts of the introduction are based on the following publication:

Dana. D. Medina, Andre Mähringer and Thomas Bein, *Isr. J. Chem.* **2018**, *58*, 1089-1101.

Department of Chemistry, Ludwig-Maximilians-Universität (LMU), Butenandtstr. 11 (E), 81377 Munich, Germany.

Dedicated to Omar Yaghi at the occasion of winning the 2018 Wolf Prize in Chemistry.

DOI: 10.1002/ijch.201800110.

1.1. Metal-organic frameworks - principles of reticular chemistry

The science of metal-organic frameworks (MOFs), hybrid materials consisting of organic ligands and metal-containing nodes, constitutes one of the most dynamic developments in solid state chemistry in recent years.[1] MOFs feature intriguing properties such as permanent porosity, well-defined cavities, ultra-high surface areas and long-range order.[2] These properties combined with the ability of encoding chemical functionalities and structural features through the rational design of the organic ligands allow for the synthesis of MOFs for a specific task such as gas storage,[3] catalysis,[4] optoelectronics,[5] energy conversion or storage.[6]

Purely inorganic porous materials such as zeolites can be seen as the intellectual predecessor of MOFs and are well-established in industrial applications due to their superior performance as robust absorber materials, selective ion exchangers in detergents or catalysts for petroleum refining.[7] Although zeolites exhibit high chemical and thermal stabilities,[8] this class of materials features mainly microporosity. Furthermore, the limited capability to incorporate different metal ions as well as lightweight elements in the backbone of the framework had shown a lack in design flexibility and chemical diversity for conventional zeolites.[9] A possible solution to this issue is the concept of reticular chemistry pioneered by Yaghi and coworkers assembling pre-designed rigid building blocks into ordered scaffolds, which are held together by strong bonds.[10] The use of organic compounds with pre-designed geometry and chemical functionalities allows for the synthesis of highly ordered networks with pre-determined structure.

MOFs are the first class of crystalline and porous materials obtained by the principle of reticular chemistry.[11] First reports on these intriguing materials by Yaghi and Kitagawa attracted massive scientific attention mainly due to their permanent porosity, ultrahigh surface areas, well-defined framework structures and tunable functionalities.[12] In general MOFs are composed of metal ions or metal clusters (SBU-secondary building units) coordinated by multifunctional, rigid organic linker molecules. Both building blocks are connected by coordinating bonds forming a 2D or 3D

network with defined cavities.[13] An example of the MOF construction principle is illustrated in Figure 1.1 by using a linear linker molecule and central SBU featuring cubic geometry.

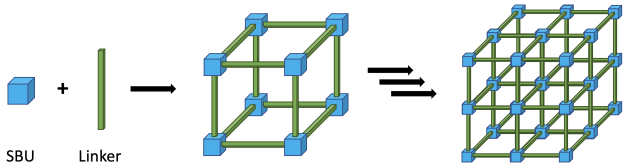

Figure 1.1 – Schematic building principle of metal-organic frameworks constructed of a tetragonal metal containing building block (SBU) and a linear linker forming a MOF topology with cubic symmetry.

Yaghi and coworkers prepared the first metal-organic analogues to zeolites in 1999. The obtained nanocrystalline material was coined MOF-5 ($Zn_4O[(O_2C)-C_6H_4-(CO_2)]_3$). This archetype of MOF structure exhibits a cubic symmetry composed of $[Zn_4O]^{6+}$ clusters (SBUs), which are octahedrally coordinated by six 1,4-dibenzendicarboxylate (BDC) molecules, leading to a cubic unit cell with zincoxo-clusters (SBUs) at the corners and linear linkers at the edges.[14] Based on the MOF-5 structure, Yaghi and coworkers established for the first time the concept of reticular chemistry by incorporating twelve different linear linkers, by varying length and functionality of the molecular backbone, without changing the underlying cubic network topology, resulting in sixteen isoreticular MOFs (IRMOF series).[15] This series is displayed in Figure 1.2.

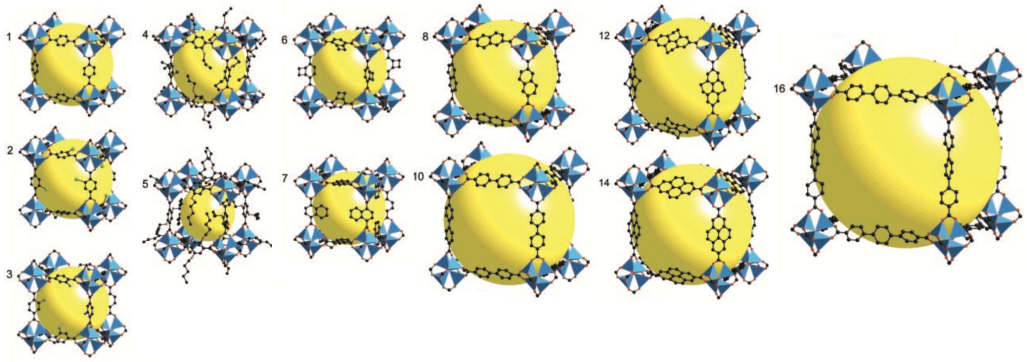

Figure 1.2 – Single-crystal structures of IRMOF-n (n=1-16, based on the archetype structure of MOF-5). The double-interpenetrated IRMOF-m series (M = 9, 11, 13, and 15) are not displayed.[15]

Reticular chemistry takes advantage of the fact that the topology of the targeted framework does not vary as long as the building blocks feature the same chemical functionalities and symmetry to form the respective node. The concept enable the use of organic building blocks with increasing lengths, but same geometry, for the design of MOFs familiar in topology but with enlarged pore apertures. This powerful concept was adapted for a wide diversity of linkers to give different isoreticular MOF series. For example, some of the most prominent MOF series are based on the

principle of reticular chemistry - MOF-74, MOF-5, MIL-88B, and UiO-66. However, it should be noted that interpenetration of the frameworks can occur, *e.g.,* for MOF-5, the IRMOF-m (m = 9, 11, 13, 15) shows a doubly-interpenetrated structure. Often MOFs undergo these changes at a certain linker size, where the structural dimensions cannot be anymore physically expanded and the network would collapse.

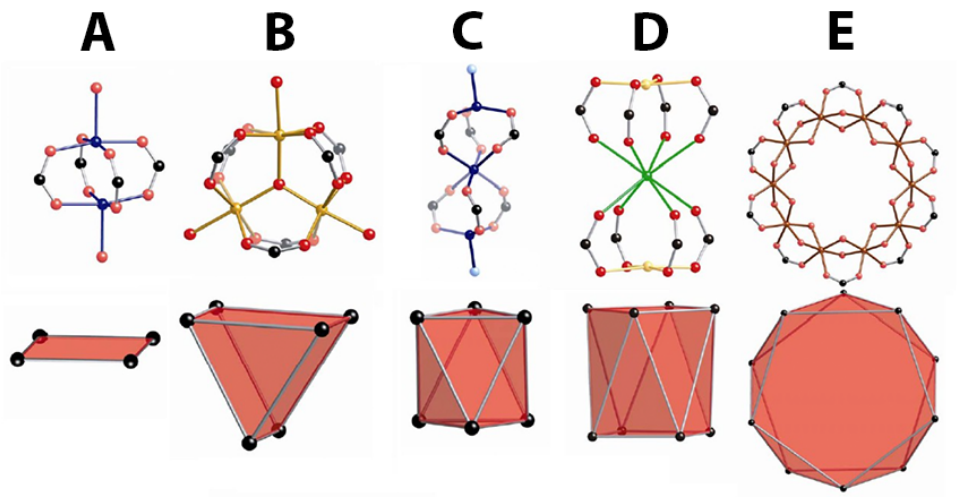

Figure 1.3 – Schematic illustration of different SBUs with their distinctive connectivity. Upper row presenting the coordination bonding in the SBU, lower row depicting ideal polyhedra geometry. **A)** Paddle-wheel-SBU of Cu(II)OAc with the connectivity of four, depicted as a square. **B)** Connectivity of six forming a trigonal prism. SBUs exhibiting this connection are typically built up from Fe^{3+} or Cr^{3+} (MIL series). **C)** Connectivity of six shaping a trigonal anti-prism, for example $[Co_2(Piv)_6(NEt_3)_2]$. **D)** SBUs with the connectivity of eight are comprised of two paddle-wheel units bridged by a Sr or Pb atom, for example $[Au_2Sr(Ac)_8]$. **E)** A cooncetivity of ten leads to the formation of edge sharing octahedra forming pentagonal anti-prism, *e.g.,* example $[V_{10}(Ac)_{10}(MeOH)_{20}]$.[17]

Nowadays, the concept of reticular chemistry is well-established in the synthesis of porous frameworks, since it allows for an easy modification of the linker molecule with various hydrophobic, hydrophilic or even ionic side functionalities without changing the fundamental topology of the MOF.[16] On the other hand, modification of the SBU is more difficult, due to the pre-determined connectivity and geometry of the MOF structure by the central SBU motif, as shown in Fig. 1.3, which means that changing the SBU often leads to a change in the underlying MOF topology itself.

Adding the option of altering the connectivity in the organic linker as well (see Figure 1.4), *e.g.,* by chemical elongation or modification, the diversity of structures that can be designed is almost endless. By carefully choosing a respective MOF synthesis, key properties, such as the specific

surface area, pore shape, symmetry, and chemical composition of the targeted framework can be predesigned.

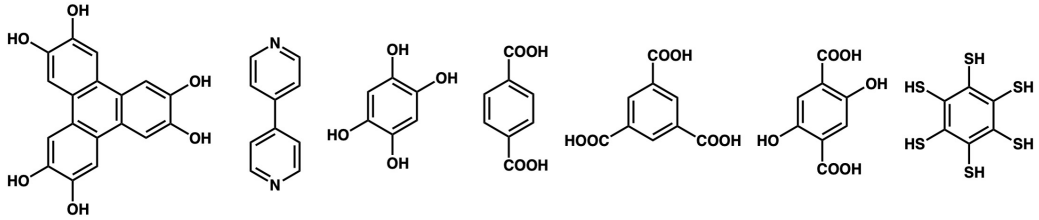

Figure 1.4 – An assembly of various MOF linkers. The illustrated organic building blocks exhibit different connectivities, lengths and molecular dimensions.

1.2. Electrically conducting MOFs - a new player enters the stage

Generally, MOFs were considered to be electrical insulators exhibiting only low electrical conductivities reaching values lower than $10^{-10}\,\mathrm{S\,cm^{-1}}$,[18] limiting their application in nanoelectronics such as super-capacitors,[19] fuel cells,[20] Li-ion batteries,[21] solar cells or field-effect transistors.[22] Hence, most studies and applications of MOFs focused on specific host-guest interactions such as molecular separations,[23] catalysis[24] and molecular recognition.[25] The main challenge in designing electrically conducting MOFs can be found in the way how these materials are constructed: In most cases the network is built up from hard metal ions or clusters which are coordinated by redox-inactive functional groups, predominantly carboxylates or aldehydes, through hard nitrogen or oxygen atoms.[26] Due to the coordination bonding between the functional group of the linker molecule and the inorganic metal clusters, no low-energy pathways for charge transport are commonly available.[21] Only recently, with the development of advanced design strategies and synthesis protocols such as including redox active molecular building blocks and incorporating a combination of transition metals in the frameworks, MOFs are creating increasing interest as an emerging class of electrically conducting materials. Combining the fundamental property of electrical conductivity with the inherent porosity of MOF materials would allow for the construction of multifunctional devices enabling a number of promising merits:[27]

- The crystalline nature (unit cell, exact position of atoms, symmetry) of electroactive MOFs allows for a deeper understanding of their structure-property relationship:
  - Theoretical and experimental studies of charge-carrier pathways based on the crystal structure can be conducted
  - The difference in electrical properties depending on the different crystal direction can be monitored

  - MOFs can be immobilized with different crystal orientation on a substrate to study their electrochemical properties

- Reticular chemistry allow for the simple predesign of MOF topology
- Altering the electrochemical properties by chemical post-modification of the molecular backbone, *e.g.,* metal- or linker exchange, doping
- Defined cavities and large surface areas allow for the infiltration of pores enabling host-guest interactions, *e.g.,* charge-transfer
- Mixed valency of metal ions can be introduced to alter the electronic properties of the framework.

1.2.1. Charge-transport in MOFs

Despite the obstacles, there are a few design principles allowing for the synthesis of electroactive MOFs. This section sheds light on the charge-transport mechanism and the structural conditions which need be to fulfilled.

Depending on the mode of MOF assembly, different charge carrier transport pathways are conceivable within the framework domains. One possible transport domain is a continuous highly-ordered electrically conductive inorganic channel held together and defined by the organic ligands.[28] Another possible transport domain is the molecular stack, where the metal nodes position appropriate (e.g., photoactive or redox active) organic ligands in a specific spatial manner that allows for charge carrier percolation along the well-ordered molecular columns.[29] A synchronized interaction between metal-based channels and molecular ligands is another interesting possible mode of charge carrier dynamics in MOFs. This requires adequate band alignment and electronic level offsets between the metal nodes and the organic ligands that consequently can result in an internal charge transfer. Charge carrier transport in both domains requires sufficient orbital overlap between the metal nodes and the organic phases that may allow for a delocalization of π-electrons throughout the MOF.[30] In order to overcome these issues in the rational design of highly conducting MOF materials, suitable metals with sufficient orbital overlap can be used to enhance delocalization of charge carriers in the system. Ideal candidates such as redox-active Cu(II) or Fe(II) might be suitable for the integration as metal centers in electroactive MOFs.[21] In combination with redox-active functional groups, e.g.,-OH, -NH_2 or -SH, promising materials may be expected featuring high electrical conductivity values as well as interesting properties in terms of energy storage or catalysis.[27] Here, the critical point in the design of such electrically conducting MOFs is the integration of suitable organic linkers forming the exact required composition. Furthermore, the intrinsic (often permanent) porosity

and well-defined cavities in MOFs can serve as an ordered template for positioning electroactive guest molecules, resulting in a continuous conducting phase.[31,32] In addition, filling the pores of a conducting MOF with a complimentary electrically conducting phase can create another pathway for the realization of highly-ordered hybrid conducting materials.[32,33] According to these possible structural design strategies and charge migration pathways that can be principally realized in MOFs, an increasing number of structures and studies dedicated to the electroactive nature of MOFs have been reported.[18,34]

1.3. Electroactive MOFs based on triphenylene moieties

1.3.1. Teaching an "old" molecule new tricks - layered MOFs based on catechols

In this chapter we take look on the most important class of compounds in this thesis - catechol and its derivatives. This class of materials are known for decades in organic-coordination chemistry but witnessed an unexpected revival in recent years as building blocks for crafting highly conducting MOFs. Frameworks based on catechols found broad applications as chemiresistive sensors, transistors, mixed-metal alloys, supercapacitors, electrode materials and solar cells. In the following we will introduce this class of materials.

The compound catechol, in literature also known as *pyrocatechol*, 1,2-dihydroxybenzene or benzene-1,2-diol, represents the *ortho* isomer of the three isomeric benzenediols with the chemical formula $C_6H_4(OH)_2$ (see. Figure 1.5). The most important derivatives include benzenehexathiol (BHT), the tricatechol 2,3,6,7,10,11-hexahydroxytriphenylene (HHTP), amino-modified 2,3,6,7,10,11-hexaaminotriphenylene hexahydrochloride (HATP · 6 HCl) and the thiol-functionalized 2,3,6,7,10,11-hexathioltriphenylene (HTT) analogue.

In recent years, catechol and its derivatives have turned out as suitable candidates for the fabrication of electrically conductive MOFs.[27,35] A tremendous amount of reports concerning catechol and relatives were published in recent years. The foundation for this rally was set by Yaghi *et al.* in 2012 presenting two-dimensional (2D) porous extended frameworks composed of the conjugated tricatecholate, 2,3,6,7,10,11-hexahydroxytriphenylene ($H_{12}C_{18}O_6$), and Ni(II), Co(II) and Cu(II) ions, respectively.[35] This new class of porous crystalline materials was termed metal-catecholates (M-CAT-1). In these frameworks, catecholate-containing organic building blocks, i. e., the redox-active 2,3,6,7,10,11-hexahydroxytriphenylene (HHTP) moieties are connected through planar metal coordination links to form honeycomb structures. These extended 2D-coordination polymers aggregate, assisted by dispersive forces, to form highly-ordered structures. The M-CAT-1 series consists of three frameworks containing different metals, namely the Ni-, Co-, Cu-CAT-1. These MOFs are synthesized under hydrothermal conditions (e.g., in water at

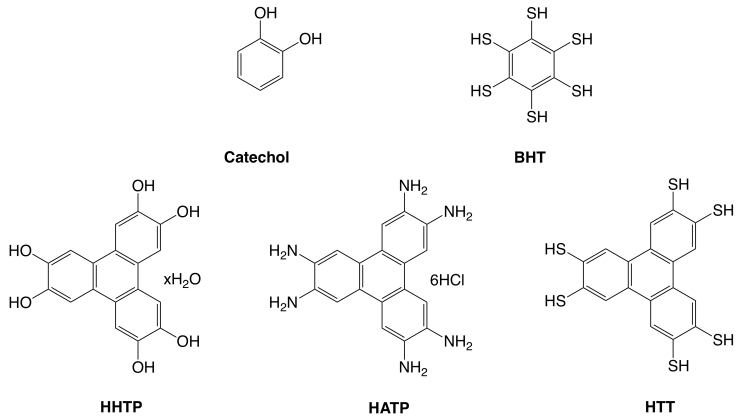

Figure 1.5 – Chemical structure of catechol, benzenehexathiol (BHT), 2,3,6,7,10,11-hexahydroxytriphenylene (HHTP), 2,3,6,7,10,11-hexaaminotriphenylene hexahydrochloride (HATP · 6HCl) and 2,3,6,7,10,11-hexathioltriphenylene (HTT).

85°C for 24 h) from a reactive precursor solution of HHTP with the respective metal acetate, and are obtained as insoluble dark-colored powders. The M-CATs are crystalline and feature an elongated crystallite morphology with a hexagonal cross-section. In Yaghi's report,[35] permanent microporosity was determined for the Ni- and Co-CAT-1, with a pore size of 1.2 nm and BET surface areas of $425\,m^2\,g^{-1}$ and $490\,m^2\,g^{-1}$, respectively. An eclipsed 2D layer packing was suggested as an adequate model for the Ni- and Co-CATs resulting in hexagonal open porous structures. Single crystal analysis performed on Co-CAT-1 crystals revealed the mode of layer stacking for this framework. Indeed, Co-CAT-1 exhibits a honeycomb-like structure and thereby forms a 1D ordered channel system (Figure 1.6).

A closer view at the crystal structure reveals that Co-CAT-1 consists of two distinct alternatively stacked layers. In the first layer, the HHTP molecules are connected through octahedrally coordinated metal sites to form an extended honeycomb-like sheet. In contrast, the successive layer consists of discrete HHTP-metal-water complex units that are not interconnected. These two adjacent layers are packed through dispersive forces, where the HHTP molecules in the layers are rotated by 60° with respect to each other and the continuous layer is slightly corrugated. Considering this type of crystal packing, charge carrier percolation in porous M- CATs is likely to occur through both types of HHTP molecular arrangements, along the *c*-axis and in the plane of the 2D extended sheets. Electrical conductivity measured under vacuum for Cu-CAT-1 single crystals contacted through four gold electrodes revealed electrical conductivity values of about $2\times10^{-1}\,S\,cm^{-1}$.

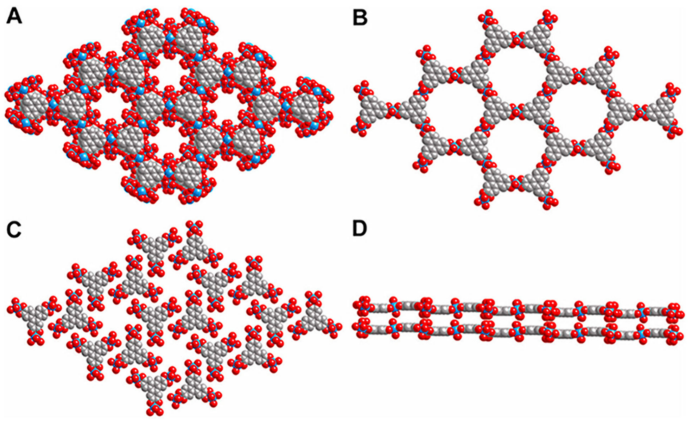

Figure 1.6 – Scheme of the single-crystal structure of Co-CAT-1. A) View along the c-axis. B) Extended honeycomb layer of Co-CAT-1. C) Layer formed *via* trinuclear complexes $Co_3(HHTP)(H_2O)_{12}$. D) Extended corrugated layers. View along the [110]-direction. Adapted with permission from [35]

1.3.2. Expanding the family of layered and eletroactive MOFs

Using a modified redox-active HHTP ligand and nickel ions, an additional member of the 2D MOF family based on the electron-rich *o*-diiminobenzosemiquinonate $Ni(isq)_2$ linkage was reported by Dinca and co-workers.[36] In that report, the reaction of 2,3,6,7,10,11-hexaaminotriphenylene hexahydrochloride (HATP·6HCl) with ammoniacal $NiCl_2$ solution under ambient conditions led to the precipitation of a 2D MOF structure, the $Ni_3(HITP)_2$ (HITP = hexaiminotriphenylene). This MOF exhibits a long-range order, and a slipped-parallel layer stacking model was suggested for its 2D layer packing (Figure 1.7). In later reports,[37] nitrogen sorption data were given for the $Ni_3(HITP)_2$ structure illustrating microporosity and a pore size of 1.5 nm with the highest BET surface area of $630\,m^2\,g^{-1}$. Crystalline films of $Ni_3(HITP)_2$ could be obtained by placing quartz substrates into the solvothermal reaction vessel. Optical absorption measured on a film revealed broad band absorption across the visible region reaching into the near IR. Two-point probe and van-der-Pauw measurements at room temperature revealed an estimated bulk (pressed pellet) and film electrical conductivity of $2\,S\,cm^{-1}$ and $40\,S\,cm^{-1}$, respectively. The authors attributed these remarkable results mainly to the presence of the $Ni(isq)_2$ motif in the structure, facilitating the charge transport in the network by offering in- plane conjugation paths through the metal center and extended delocalization of the p-electrons. Taking advantage of the electrical conductivity of $Ni_3(HITP)_2$, Dinca and co-workers recently illustrated the utility of $Ni_3(HITP)_2$ in a variety of electrochemical and sensing applications such as chemiresistive sensors, electrochemical double layer capacitors and electrocatalysts, as discussed in the following.

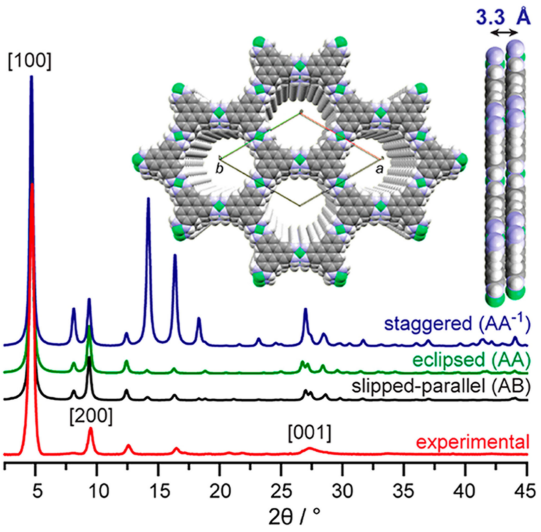

Figure 1.7 – Recorded experimental and simulated PXRD patterns of $Ni_3(HITP)_2$ (staggered, eclipsed and slipped-parallel MOF layers). Space filling drawings of the slipped parallel structure of the layers depicted as inset with a sheet distance of 3.3 Å .[36]

The electrocatalytic performance of $Ni_3(HITP)_2$ deposited on a conducting electrode immersed in alkaline medium in an electrochemical cell was demonstrated with an ORR.[37] In that work, the catalytic activity of $Ni_3(HITP)_2$ was studied with regards to its well-defined metal site, namely the square planar Ni-N_4 site which, in principle, can serve as an active site for oxygen reduction similar to existing technologies based on metal electrocatalysts containing M-N_4 units. Using a glassy carbon/$Ni_3(HITP)_2$ electrode in the electrochemical oxygen reduction resulted in a performance comparable to the most active, non-platinum containing electrocatalysts while maintaining the apparent stability of the MOF film during the electrochemical cycling. In a subsequent study, monitoring the oxygen and proton concentration during the reaction and studying vital reaction parameters such as pH dependent catalytic performance, the oxidation state of the Ni element during the ORR, and establishing a reaction law for the process allowed the authors to propose a mechanism suggesting that the oxidized triphenylene ligand acts as the catalytic center in the reaction.[38]

The attractive combination of permanent porosity, defined cavities, high BET surface area, chemical and thermal stability and high electrical conductivity of $Ni_3(HITP)_2$ triggered a study exploring the performance of $Ni_3(HITP)_2$ as a sole electrochemical double layer capacitor electrode.[39] The authors aimed at the utility of $Ni_3(HITP)_2$ as a sole electrode due to relatively mild conditions under which the MOF is synthesized and the well-defined pore system. The

pore diameter of $Ni_3(HITP)_2$ is adequately large to accommodate electrolyte guest agents such as tetraethylammonium tetra-fluoroborate ($TEABF_4$), typically employed in such electrochemical double layer capacitor devices, and thus allows for swift electrolyte movement upon electrochemical cycling. In addition, the electrical conductivity of $Ni_3(HITP)_2$ is sufficiently high to avoid the incorporation of carbon-based conductive additives to enhance the electrode performance. The working potential window for the $Ni_3(HITP)_2$ powder (hand-pressed onto a Pt-mesh electrode) was determined to be about 1 V in a three-electrode electrochemical cell (anodic scan between 0.02-0.5 V and cathodic scan between 0.02-0.6 V), where the pelletized MOF powder exhibits a purely capacitive response. After determining the $Ni_3(HITP)_2$ capacitance response region, its capacitance performance as a sole electrode was studied in a two-electrode symmetrical super-capacitor cell. Prior to the measurements the sole electrode was prepared by pressing $Ni_3(HITP)_2$ powder (pressure of 100 kg-force cm^{-2}) into a solid continuous pellet consisting of $Ni_3(HITP)_2$ particles and featuring interstitial voids in the rage of 1 mm. The gravimetric capacitance obtained at low discharge rates normalized to the surface area yielded a value of 18 mF cm^{-2}, which was higher than other carbon-based materials with the exception of holey carbon.

Xu and co-workers reported on the construction of a microporous field-effect transistor device based on $Ni_3(HITP)_2$ membranes.[40] In that work, membranes of about 100 nm thickness and average roughness of 1.5 nm were produced on a silicon wafer by an air-liquid deposition method. By heating the $Ni_3(HITP)_2$ precursor solution to 60°C, solid particles appeared at the water-air interface, and these particles aggregated to form a continuous uniform layer. The authors related the thickness of such a membrane to the reaction time, where longer reaction times yielded thicker blue-colored membranes, with maximal thickness of 100 nm achieved after 3 min. The membrane surface topography was studied by atomic force microscopy (AFM), revealing an ultra-smooth surface with average surface roughness of about 1 nm, suitable for device fabrication. Subsequently, the $Ni_3(HITP)_2$ membrane was transferred to a silicon/SiO_2 wafer by a stamping process. The deposition of top gold electrodes enabled further characterization of these membranes in the form of a field effect transistor (FET) device. The drain-source I-V characterization revealed that the charge carrier concentration in the $Ni_3(HITP)_2$ membrane could be modulated by the applied gate-source voltage. Furthermore, the $Ni_3(HITP)_2$ FET device showed a p-type transistor behavior showing that the $Ni_3(HITP)_2$ membrane features holes as majority charge carriers. The average calculated hole-mobility for the membranes was 38.8 $cm^2\,V^{-1}\,s^{-1}$. These values are significantly higher than those of most organic semiconducting materials and in the range of inorganic oxide semiconductors. Because of the non- oriented nature of the MOF crystals in the membrane, the authors suggested that the active charge carrier transport pathways are both in the plane and along the stacked MOF layers.

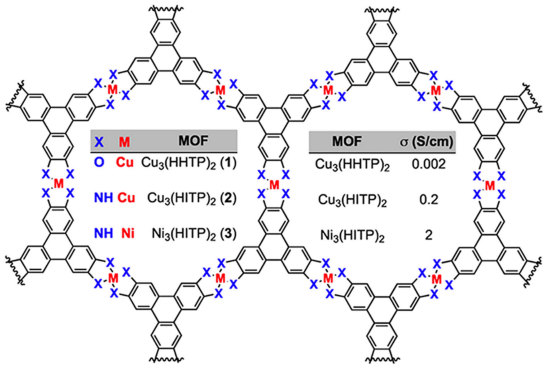

Figure 1.8 – Chemical structures of the hexaamino based 2D MOFs and their reported electrical conductivities with different metal centers (two-point probe/pellet).[42]

Dinca and co-workers extended the group of electrically conducting 2D HITP-based MOFs with the synthesis of the $Cu_3(HITP)_2$ framework (isostructural to $Ni_3(HITP)_2$) (Figure 1.8).[41,42] Electrical conductivity measured for $Cu_3(HITP)_2$ pressed pellets yielded conductivity values of up to $0.2\,S\,cm^{-1}$ (two-point probe), which is a lower value compared to the performance of $Ni_3(HITP)_2$. $Cu_3(HITP)_2$ films were produced by a simple approach of drop casting a $Cu_3(HITP)_2$ powder suspended in acetone onto conductive glass substrates. Using this synthesis approach, a $Cu_3(HITP)_2$ film was produced on a glass substrate modified with patterned interdigitated gold electrodes. This device was then encapsulated in a flow chamber connected to nitrogen and ammonia gas-inlets. A constant voltage of 100 mV was applied between the two electrodes and the current was monitored while a gas flow of nitrogen and ammonia mixtures was introduced into the chamber. These experiments revealed a reversible current response of the cast $Cu_3(HITP)_2$ powder towards diluted ammonia vapor, capable of detecting sub-ppm levels. Interestingly, in contrast to the electrical response detected with $Cu_3(HITP)_2$, devices fabricated based on $Ni_3(HITP)_2$ showed no significant electrical response upon exposure to ammonia vapor. In subsequent work, a comparative study including $Cu_3(HITP)_2$, $Ni_3(HITP)_2$ and Cu-CAT-1 structural analogs was performed regarding their chemiresistive sensor response towards a large variety of volatile organic compounds.[42]

With a view on extending the triphenylene-based 2D MOF family, a dithiolene link can be used for constructing an electron-rich framework. A derivative of such a MOF, namely a single-layer coordination polymer consisting of hexathioltriphenylene and Ni atoms was reported by Feng and co-workers.[43] The single layer immobilized onto a conducting electrode was introduced as an efficient platform for electro- catalytic water splitting and hydrogen evolution. Later, a mixed linker approach was employed to synthesize 2D MOFs where hexathioltriphenylene and

hexaminotriphenylene were connected *via* cobalt or nickel ions.[44] These MOFs, however, exhibited moderate crystallinity compared with related structures. The authors sought to immobilize reactive molecular metal dithiolene-diamine complexes, i.e., containing the MS_x Ny_y (x/y = 2/2, 0/4, 4/0) motifs using the 2D MOF scaffold. Such metal complexes embedded in carbon-based supports are considered as promising alternatives for the high-cost Pt catalysts used in electrocatalytic water splitting and hydrogen evolution reaction (HER) applications. The authors assumed that the well-defined hexagonal layer layout favors a preferred arrangement of the catalytic active sites as well as a sufficient exposure of the active sites due to the porosity of the framework. Furthermore, integration of the complexes into a solid state-material was expected to result in their increased stability and possibly reactivity in aqueous media. Therefore, Feng and co-workers studied the performance of molecular MS_x Ny_y (x/y = 2/2, 0/4, 4/0) complexes in the form of single-layer coordination nano-sheets prepared by an interfacial Langmuir Blodgett (LB) method, MOF bulk powders and MOF/graphene composites for water splitting and the HER. In that study, the authors found that the catalytic activity for H_2 generation of the 2D MOFs of different metal-complexes followed a reactivity order of $MS_2N_2 > MN_4 > MS_4$.

1.3.3. Switching topology - from 2D to 3D catechol frameworks

Up to this point we have discussed the synthesis and physical properties of layered MOF structures that feature in-plane conjugation and graphite-like molecular stacks. These frameworks combine appreciable crystallinity, porosity and high electrical conductivity, which is in some cases comparable to dense conducting materials. As mentioned above, further expanding the family of 2D MOF materials requires meeting the strict conditions of ligand symmetry and appropriate functionality for forming a layered structure. In contrast, three-dimensional MOFs (3D MOFs) offer an enormous structural diversity through the combination of numerous types of bonding, building blocks and topologies. For example, appropriate secondary building units (SBUs) can serve as ordered inorganic pathways that are able, in principle, to conduct charges. Certain MOF topologies enable charge percolation paths in the semiconducting redox-active organic domains mainly through charge hopping between successive layers.[45] In addition, typically 3D MOFs are highly porous, which at first glance might look disadvantageous for charge percolation due to low crystal density, however, the open porous structure can give access to unique arrangements of ordered inter-penetrated and intercalated guest molecules.[46] Hence, 3D MOFs offer large structural variations and opportunities for design that can be relevant for tuning and optimizing charge carrier mobility. In recent years, a number of 3D MOFs were reported to be electrically active, typically featuring moderate electrical conductivity. Therefore, inducing high charge carrier mobility in 3D structures is still a great challenge. In the following, we will discuss some

of the recently reported structures and synthesis approaches intended to boost charge transport in 3D MOFs. We focus here on 3D catechol frameworks.

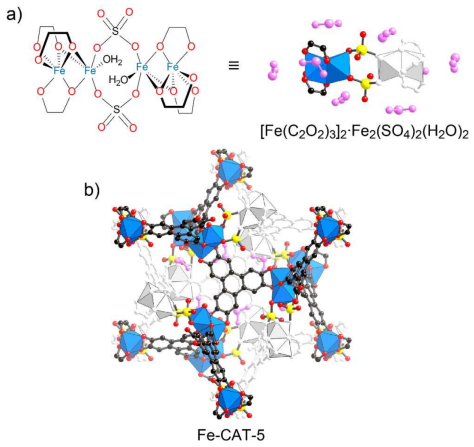

Figure 1.9 – a) Displays the bridging $Fe_2(SO_4)_2(H_2O)_2$ cluster, which connects the two Fe-CAT-5 networks with *srs* topology forming b) an overall two-fold interpenetrated framework.[47]

Yaghi and coworkers reported in 2015 a series of 3D catecholate-based frameworks coined M-CAT-5 (M = Fe, V, Ti).[47] All prepared MOFs from this series show a cubic symmetry with the *srs* topology. Fe- and Ti-CAT-5 are two-fold interpenetrated *srs* networks while the V-CAT-5 framework is non-interpenetrated. The authors elaborated that the cubic framework features an anionic backbone with DMA guest molecules located in the cavities acting as counter-ions enabling efficient proton conductivity pathways. To support this assumption, Fe-CAT-5 was measured to exhibit a proton conductivity (impedance measurements on pellets) of 5.0×10^{-2} S cm^{-1} at 98% relative humidity at room temperature. The report notes that this ultra-high proton conductivity arises from the incorporation of sulfate ions in the negatively charged framework backbone bridging the two interpenetrating networks in the structure (Figure 1.9). This structural feature is not present in Ti-CAT-5, therefore, only a proton conductivity of 8.2×10^{-4} S cm^{-1} at 98% relative humidity was measured. Crystals suitable for single-crystal X-ray diffraction (SCXRD) could be obtained by dissolving iron(II) sulfate and the HHTP building block with tetrabutylammonium nitrate in a solvent mixture of DMF/water/methanol (10/1/1; v:v). The solvothermal reaction was carried out in Teflon liners placed inside a stainless-steel autoclave at 180 °C for 48 h. After the synthesis, truncated octahedrally shaped crystallites with black appearance could be collected. For Ti- and V-CAT-5 no single-crystals could be isolated but the measured PXRD patterns were Rietveld refined against the Fe-CAT-5 structure. According to the SCXRD analysis, Fe-CAT-5 crystallizes in the space group *Pa-3* (No. 205) featuring a lattice constant of a = 17.75 Å. Nitrogen sorption isotherms at 77 K revealed BET surface areas

of about 450 and 725 $m^2\ g^{-1}$ for the Ti- and the V derivative. For the Fe-CAT-5 compound no nitrogen uptake could be measured.

Parallel to the work of Yaghi, Long and coworkers reported in 2015 the first example of a 3D catechol framework composed of iron(III) and semiquinoid linkers.[48] The net sum formula of the compound was stated as $(NBU_4)_2Fe^{III}{}_2(dhbq)_3$ ($dhbq^{2-/3-}$ = 2,5-dioxidobenzoquinone/1,2-dioxido-4,5-semiquinone). The material was obtained by dissolving iron(II) sulfate, 2,5-dihydroxybenzoquinone and tetrabutylammonium bromide in dd-water at pH 3.0 (by adding conc. HCl) in a glass vial. The reaction vessel was degassed, flame-sealed and placed in a preheated oven at 120 °C for 24 h. After the reaction, cubic crystals with black appearance were collected under nitrogen atmosphere. The structure was examined by SCXRD and is depicted in Figure 1.10. $(NBU_4)_2Fe^{III}{}_2(dhbq)_3$ crystallizes in the cubic space group *I43d* comprised of two interpenetrated (10,3)-a nets with tetrabutylammoinium counter ions filling the pores in the structure. Activation of the sample at 150°C under vacuum confirmed the lack of microporosity. ^{57}Mößbauer spectroscopy revealed the presence of an iron(III) high spin species leading to the conclusion that the organic semiquinoid ligands encounter reduction during the synthesis and the iron(II) is oxidized to iron (III). According to the authors, this charge-transfer provides explanation for the deep black appearance of the isolated crystallites. Moreover, two-point probe measurements on pressed pellets gave electrical conductivity values of 0.16 S cm^{-1}, which sets the record up-to-date for catechol based frameworks.

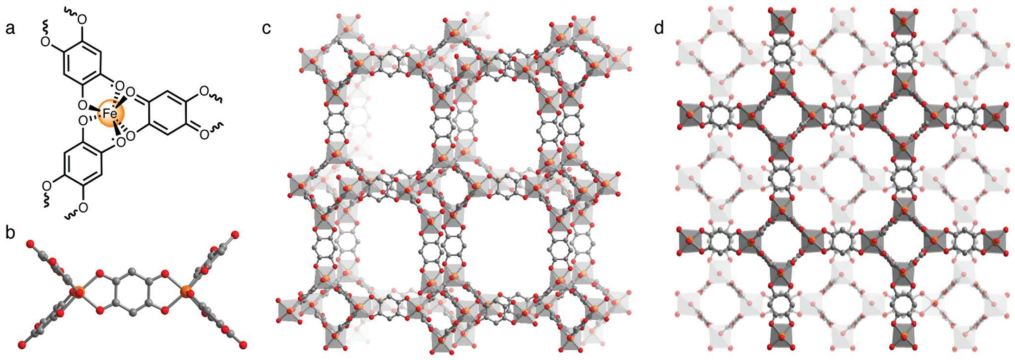

Figure 1.10 – a) Octahedral coordination of iron(III) by three semiquinoid linkers of which two are radical ions ($dhbq^{3-}$) and one paramagnetic ($dhbq^{2-}$). b) Depiction of semiquinoid linker bridging between two iron centers. c) One of the two interpenetrating nets (10,3)-a nets. d) Two nets combined yield the 3D structure of $(NBU_4)_2Fe^{III}{}_2(dhbq)_3$.[48]

In analogy to the M-CAT-1 series, Dinca and coworkers introduced a family of 3D catecholate-based MOFs composed of Ln(III) (Ln = La, Nd, Ho, Yb) ions and the HHTP building block.[49] Employing a solvothermal synthesis of lanthanide(III) nitrate with HHTP in a mixture of water and *N,N'*-dimethylimidazolidinone (DMI) in the presence of sodium acetate and under the

exclusion of oxygen at 80 °C for 16 h afforded green-blue mircrocrystalline powders. The obtained microcrystalline powder is composed of rod-like crystallites with hexagonal cross-section being 1-200 µm in length. The structure was obtained from Rietveld refinement of powder X-ray diffraction data. It was found that the whole rare-earth metal series (LnHHTP; Ln= La, Nd, Ho, Yb) is isostructural. Similar to the structure of M-CAT-1, LnHHTP frameworks are composed of hexagonal and honeycomb-like 2D layers with a crystallographic pore diameter of 1.94 nm. In contrast to its 2D analog, Ln(III) ions are located between the sheets, bridging two adjacent layers, leading to the formation of a 3D network. Nitrogen sorption confirmed the microporosity, with BET surface areas of about 200-510 $m^2\ g^{-1}$. The authors suggest that an adjustment of the layer stacking distance is possible by choosing lanthanide metals differing in their ionic radii. Ions with smaller ionic radii would enable a more densely packed structure allowing a more efficient charge transport along the metal-oxo chains perpendicular to the sheets in the structure. The authors denote electrical conductivity values from 0.9×10^{-4} S cm^{-1} for LaHHTP up to 0.05 S cm^{-1} for HoHHTP. These values confirm that rare-earth catechol based frameworks are among the most conducting 3D MOFs reported in literature so far.

Very recently, the same lab team presented the synthesis of a cubic and non-interpenetrated metal-organic framework based on catecholate building blocks and rare-earth metal ions.[50] By combining lanthanoid (III) nitrate (Ln = Eu, Y, La) with HHTP in a mixture of water and *N,N'*-dimethylimidazolidinone (DMI) at 120 °C, they obtained octahedral crystallites with yellow appearance suitable for single-crystal X-ray diffraction analysis. The whole series crystallizes in the cubic space group F*d3m*. The SBU can be described as hexanuclear nitrate-catecholate cluster in which the lanthanide ions are positioned in a chair-like geometry surrounded by nitrate ions. Each SBU is coordinated by six triphenylene linkers forming a network with *spn* topology building tetrahedral cages similar to the faujasite zeolite structure type (see Figure 1.11).

Interestingly, the yellow colored crystallites undergo oxidation over time (disregarding the storage atmosphere, *e.g.,* air or argon) turning into a deep black color. The authors attributed this behavior to oxidation of the catechol units forming semiquinones. Moreover, this series of isotropic MOFs showed electrical conductivities of 10^{-4}-10^{-5} S cm^{-1}. The values were retrieved from two-point probe measurements on pressed pellets. It should be noted that the presented materials are non-interpenetrated and exhibit BET surface areas of up to 780 $m^2\ g^{-1}$. The from the authors presented combination of porosity and electrical conductivity within one material is remarkable since not many examples for these MOFs are known in literature.

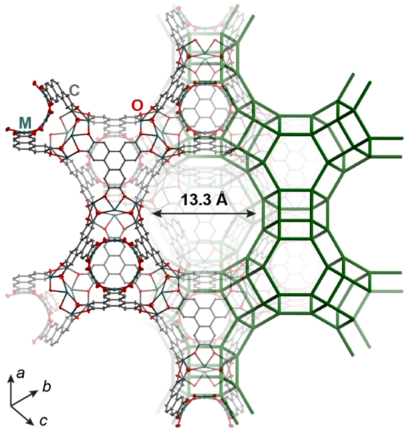

Figure 1.11 – Depiction of the single-crystal structure of LnHHTP MOFs (Ln = Eu, Y, La). The view is along the [111] direction. Green overlays resemble the faujasite structure, which is similar to the proposed structure of LnHHTP.[50]

1.4. MOF-74 topology - a versatile platform

Another promising platform for altering the structural, photophysical and electronic properties in porous frameworks is the MOF-74 topology.[51] The structure of MOF-74 (Zn), M_2(DHBDC) (M = Mg, Mn, Fe, Zn, Co, Ni; DHBDC = 2,5-dihydroxybenzene-1,4-dicarboxylate) is visualized in Figure 1.12.[51] **A** displays the view along the hexagonally shaped pore. The framework is built up from one-dimensional infinite metal-oxide SBUs, $(\text{-M-O-})_\infty$, (shown in **B** as blue colored octahedra), which are bridged in the *ab*-plane *via* the DHBDC linkers. MOF-74 is a chemically and thermally robust structure rendering it as a versatile framework for chemical post-modification or altering the integrated organic building block without changing the underlying network topology. For example, Yaghi *et al.* reported the first IRMOF-74 series in 2012 by systematic expansion from its original link of one phenyl to eleven phenyl rings, respectively.[52] All the members of the IRMOF-74 series exhibit non-interpenetrated structures and robust frameworks featuring pore apertures ranging from 14 to 98 Å.

Normally, the family of MOF-74 is regarded as chemical insulators since they are composed of redox-inactive chemical functionalities such as carboxyl and hydroxyl groups, and "hard" metal ions (Zn, Mg, Ni, Co). The first prominent demonstration rendering this class of MOFs material suitable for applications in the field semiconductors was shown by Dinca and coworkers.[53] in 2013. In that report, the authors exchanged the electron-poor -O- at the *ortho*-position by the electron-rich -S- atom aiming to reduce the energy-mismatch between the sulfur-based ligand and the metal-ion. By the reaction of a manganese (II) precursor and 2,5-disulfhydrylbenzene-1,4-dicarboxylic acid (H_4DSBDC), the novel MOF-74 compound Mn_2(DSBDC) was obtained. The

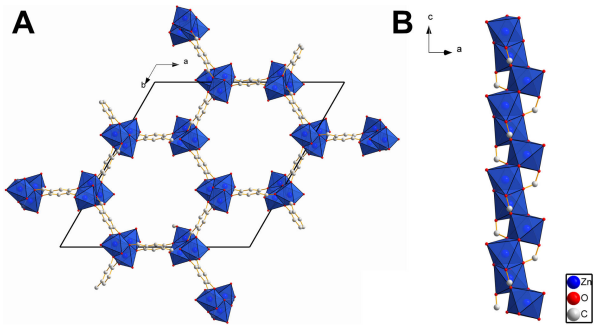

Figure 1.12 – Crystal structure of MOF-74(Zn).[51] **A)** View along the crystallographic [001] direction visualizing the hexagonal 1D channels formed by inorganic 1D metal-oxo clusters (SBU) linked *via* the benzene ring substitutions of the 2,5-dihydroxybenzene-1,4-dicarboxylate. **B)** 1D (-M-O-)$_\infty$ chains curled in a helical fashion. Zn-O octahedra are colored in blue. Water and DMF guest molecules are omitted for clarity. Oxygen, zinc and carbon atoms are illustrated in red, blue and grey, respectively.

material was isolated showing a porosity with BET surface areas of 978 m^2 g^{-1}. Flash-photolysis time-resolved microwave conductivity measurements and time-of-flight analysis revealed intrinsic charge-carrier mobilities (sum of hole and electron mobility) of up to 0.01 cm^2 V^{-1} s^{-1}, which is in the realm of mobilities measured for organic semiconductors. The authors attributed this high mobility to the electronic participation of sulfur in the charge-carrier pathway along the 1D (-Mn-S-)$_\infty$ chains. In contrast, the corresponding electrical conductivity values of pelletized Mn_2(DSBDC) and Mn_2(DOBDC) were found to be 10^{-12} S cm^{-1} and 10^{-13} S cm^{-1}, respectively. These results are referred to the low charge-density in this materials. This issue was overcome in 2015 by the same group illustrating the synthesis of Fe_2(DSBDC) and Fe_2(DOBDC).[54] Here, the iron(II) donates charge carriers giving a boost of one million-fold in electrical conductivity for both materials (10^{-6} S cm^{-1} and 10^{-7} S cm^{-1}, respectively). The authors concluded that iron(II) plays a critical role in the design of electroactive and porous materials.

1.5. Thin film growth - opening new horizons

The fabrication of thin, porous MOF films defines a critical point in the emerging field of MOFs,[55] since it provides an entry to applications such as electroluminescence,[56] QCM-based sensors and optoelectronics.[57] Therefore, large area homogeneous films with precise thickness and crystal orientation are needed.

Another important aspect in thin film synthesis is the surface morphology. While smooth and homogenous films are, *e.g.,* more favorable for integration in devices comprising layered architectures, rough and nanostructured films can be used to create surfaces with extreme wetting properties. Nanostructured films find broad application in technologies, *e.g.,* oil-water separation,

self-cleaning surfaces, molecular sieving or nanofiltration. The wetting properties of those films are encoded by their surface morphology, *i.e.* roughness, rather than their chemical composition. Surface roughness is therefore an important parameter to be controlled in the MOF film synthesis.

The following chapter section focuses on the state-of-the-art methods regarding preparation of oriented MOF thin films, representing a key step for the implementation MOF thin films in functional devices.[55]

1.5.1. Oriented MOF film growth - general concerns

The field of MOF thin film growth is well-established with a remarkable number of reports. Therefore, we focus in this section on the methods used for obtaining oriented MOF thin films and introduce some prominent strategies. Orientation of crystals plays a crucial role in MOF thin films, since MOFs are crystalline materials showing, in some cases, crystallographic anisotropy. Owing to anisotropy, fundamental properties such as charge-carrier pathways and migration depend strongly on the particular crystallographic direction of the framework. This becomes even more important in porous materials, where crystal orientation may impact the pore accessibility. Next to the crystal orientation, also the thickness resemble an important parameter to be addressed. Here, there is a need for preparing MOFs thin films in the nanometerscale since wide range of spectroscopic methods require low optical density to gain insights into photophysical processes of these materials.

The first and most common technique is the film growth of oriented MOF films under solvothermal conditions.[58] Fischer *et al.* employed this method to obtain microcrystalline phase-pure $[Cu_3(btc)_2]$ (btc = 1,3,5-benzenetricarboxylic acid; $[Cu_3(btc)_2]$ = HKUST-1) and $[Zn_2(bdc)_2(dabco)]$ (bdc = 1,4-benzenedicarboxylate; dabco = 1,8-diazabicyclooctane) on alumina and silicon surfaces modified with self-assembled organic monolayers (SAMs).[58] However, the growth of both materials was found to be remarkably surface selective, depending strongly on the interface such as silicon, alumina, sapphire or SAM-modified surfaces. Here, $[Cu_3(btc)_2]$ showed oriented growth on both *c*-plane sapphire and COOH-terminated SAMs on SiO_2/Si (100) wafers.

Another approach for the synthesis of oriented MOF films was introduced by Bein *et al.* First, an aged mother solution of HKUST-1 was synthesized *via* a solvothermal route and, second, carboxylate-terminated SAM-functionalized substrates were placed up-side down in the reaction vessel.[59] By changing the functionalization of the terminating group, *e.g.,* hydroxyl, methyl or carboxyl, different crystallite orientations in the MOF film were observed.

A route termed layer-by-layer approach was displayed by Woell and coworkers, in which the MOF film is grown at room temperature on SAM functionalized substrates by repeating immersion

cycles.[60] Therefore, the substrate is first dipped into a solution of the metal precursor and subsequently into a solution of organic ligand and rinsed in between the cycles with pure solvent.

In 2010, Bein *et al.* reported a synthesis of oriented MOF films by a gel-route procedure.[61] In this method, the metal precursor is stored in a polymer gel layer placed on a substrate. Subsequently, a linker solution was deposited on top of the gel layer, leading to an oriented film growth at the gel-substrate interface.

In 2010, Kitagawa *et al.* fabricated preferentially oriented MOF thin films on a solid surface (NAFS-1), consisting of metalloporphyrin building units by coupling the layer-by-layer growth technique with the Langmuir-Blodgett method.[62] Hereby, a monolayer of MOF is formed at the interface between the metal and linker precursor solution and the substrate under force. After a subsequent washing step a second layer can be formed.

A method similar to the layer-by-layer approach was described by Woell *et al.* in 2010 producing monolithic, oriented, crystalline and highly porous coatings on solid substrates *via* a spray-assisted layer-by-layer method.[63] Instead of modified substrates in a precursor solution as in the case of the conventional layer-by-layer method, the precursors are sequentially spray-coated onto the surface. With the help of this technique micrometer thick films of several MOF types on modified Au substrates, including HKUST-I and layer-pillar MOFs, were prepared.

These illustrate the main aspects and challenges in the MOF thin film growth characteristics. First of all, the growth of MOF thin films can be extremely surface selective. Depending on the MOF structure, the metal incorporated and the surface chosen as nucleation site, the growth behavior can vary significantly. Often the surface needs to be pre-modified in a way that preferred nucleation sites are provided. Surface-functionalization can be carried out by using self-assembled monolayers (SAMs), silanes, thin layers of solid precursor or plasma-cleaning. However, it would be preferable to prepare films without organic modifications of the substrate since they might influence the latter electrical and photophysical analysis by acting as electrical isolating barriers. Unfortunately, many MOF structures require a substrate pre-modification, by *e.g.,* SAMs, for growing them as thin films, which is one of the main reasons why the preparation of pure MOF films on surfaces is such a detrimental challenge. Furthermore, no general approach is existing for the transfer of film growth methods from one MOF structure to another making the establishment of synthesis protocols extremely difficult.

1.5.2. State-of-the-art - thin film growth of 2D MOF

In the last section we discussed general approaches which are suitable to prepare oriented thin MOF films. In this section we will shift the focus towards different routes to prepare crystalline

MOF films of 2D analogues. For the sake of simplicity the emphasis will be on catechol and derivative materials. The different approaches are categorized and for each respective method a short example is illustrated.

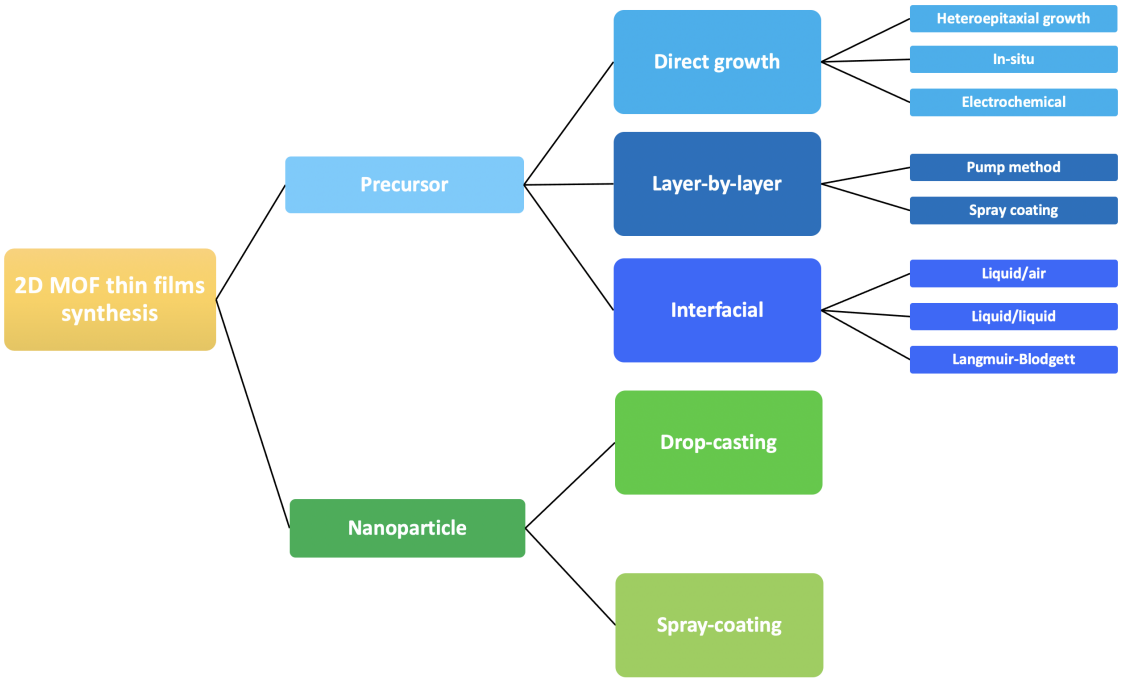

Figure 1.13 – Overview and categorization of various methodologies for preparing 2D MOF films with catechol and derivative motifs.

Figure 1.13 illustrates the assembly of methodologies for preparing 2D MOFs films. The two major routes are both bottom-up approaches: either the MOF is grown directly onto the substrate from the synthesis of the respective **precursors**, or the film is fabricated by the deposition of pre-synthesized **nanoparticles**. The latter can be divided into two approaches. First, the nanoparticles can be simply deposited by **drop-casting** a suspension onto the desired substrate followed by a subsequent drying step. Second, the nanoparticles are deposited *via* **spray-coating** on the surface. In contrast, the precursor route can be split up into three different sub-branches: First, **direct-growth** of the MOF from the solvothermal reaction of molecular precursors, secondly, in a sequential **layer-by-layer** approach, and third, from **interfacial** synthesis at the contact between two phases. These methods are further categorized into final sub-levels. The interfacial synthesis can be located at the **liquid/air,** or the **liquid/liquid** interface or conducted with the **Langmuir-Blodgett** technique. For the layer-by-layer technique films can be fabricated using the **pump method** or the precursors can be alternately deposited by

spray-coating. At last, the direct growth can be experimentally carried out as **heteroepitaxial growth, in-situ** or **electrochemical.**

For every method mentioned a short example will be given and the related advantages and disadvantages will be discussed.

Campbell *et al.* prepared films of Cu_3(hexaaminotriphenylene)$_2$ from the pre-synthesis of nanoparticles and dispersing them in acetone.[64] The dispersion was then **drop-casted** onto ITO substrates followed by a drying step. Obtained films exhibit decent crystallinity, however, the texture is rough and non-homogenous observing thicknesses in the micrometer range. Nevertheless, the authors report the synthesis of mechanically robust films which could be used for detecting ammonia vapor. This technique allow for the fast and simple fabrication procedure as well as the capability to transfer the method to other MOF topologies. However, the quality of the obtained films is not suitable for device fabrication.

Another interesting film synthesis approach was shown by B. Hoppe *et al.* using **spray-coating**.[65] In a first step, the authors manipulated the shape of Cu-CAT-1 nanoparticles by the addition of modulators into the reactive reaction mixture to give instead of rod-like crystallites, nanoplatelets were obtained. Here, the modulators inhibited the growth of the MOF crystals along the c-axis. The authors attributed the change in crystal habit to the presence of ammonia modulator in the precursor solution. Subsequently, a stable aqueous suspension of Cu-CAT-1 nanoplatelets in water was prepared. Owing to the a 2D shape of the nanoplatelets, the authors could spray-coat large areal surfaces (DIN A4 size) yielding crystalline and preferentially oriented films. An advantage of spray-coating is the option to deposit the material of choice on every surface, hence, the authors coated various substrates including flexible substrates made of polycarbonate foil. It should be noted that this elegant route requires the pre-synthesis of nanoparticles in a defined shape (important aspect for the latter obtained crystallite orientation) and the preparation of stable suspensions, which is not possible for every respective MOF. Moreover, the spray-coated films feature thicknesses in the micrometer scale leading to non-transparent substrates. Furthermore, the obtained film topography is of rather rough nature, making it difficult to integrate into nanoelectronic devices where nanometer scale layer thicknesses and homogenous surfaces are required.

The **in-situ** approach was carried out by Sheberla *et al.*. In this approach, Ni_3(hexaamino triphenylene)$_2$ films were directly synthesized under solvothermal conditions on the surface.[36] Hereby, the substrate to be covered is placed upside down in the reactive precursor solution. The growth of the films occurs on the desired surface while on the upper surface only MOF powder is precipitating. Films obtained exhibit thicknesses at the nanometer scale and show a smooth and homogenous appearance. However, the films consist of densely packed randomly oriented

crystallites. It should be noted that this method suffers from very poor yields since a major fraction of the precursor will form MOF nanoparticles precipitating on the bottom of the reaction vessel or on the upper side of the substrate. Since the films exhibit thickness of several hundred nanometers they are optically transparent allowing for using photophysical studies. In another study, Smith *et al.* used a similar approach but instead of quartz substrates they conducted a templated growth of Ni-CAT and Co-CAT-1 nanoparticles by offering a preferred nucleation site, here, graphitic electrodes patterned onto a polymeric support.[66] They obtained randomly distributed MOF crystallites on the electrodes showing no homogenous surface. Using this film method strategy MOF based gas sensors were grown exclusively the graphitic electrodes, without observing a nucleation on the polymeric support.

Heteropepitaxial growth was conducted by Q. Ma *et al.*. This route is based on the partial conversion of a metal substrate acting as a metal source for the organic linker in solution.[67] In a step-wise fabrication, a metal mesh composed of Cu was converted to $Cu(OH)_2$ nanowires by immersing the mesh into a solution containing sodium hydroxide and ammonium persulfate. Subsequently, this reactive substrate was immersed in a solution containing HHTP linkers leading to the heteroepitaxial growth of MOF (Cu-CAT-1)-based hierarchical nanostructures (MHS). The Cu-CAT-1 is growing from the nanowires in all spatial directions forming a brush-like hetero-structure. The synthesis route introduced by Q. Ma *et al.* is restricted to Cu comprising MOF systems, since it relies on the conversion of Cu to the reactive $Cu(OH)_2$ as precursor. On the other hand, the synthesis leads to the formation of highly textured and nanostructured films which can be highly desirable for certain applications, *e.g.,* surfaces with extreme wetting properties.

M. l. Gonzales-Juarez *et al.* presented in 2020 another approach of preparing Cu-CAT-1 films by a one-step **electrochemical** deposition process.[68] On SiO_2 substrates covered with a thin layer of gold, a copper film was deposited by electrodeposition. This substrate was placed in a precursor bath containing HHTP linker solution. By applying a voltage, the copper film was subjected to an anodic dissolution forming with HHTP in a one-step reaction the respective Cu-CAT-1 film on the surface. For additional electrical characterization, the obtained films were transferred by peeling-off using a PMMA film. The final films obtained are highly textured and nanostructured. In SEM analysis, agglomerates of 5 µm are visible composed of the typical needle-like Cu-CAT-1 crystallites.

M. S. Yao *et al.* used a **layer-by-layer** approach for preparing films of Cu-CAT-1 for chemiresistive gas sensors.[69] By using a spray system, alternate deposition of precursors and solvents was carried out. This allowed for precise control over thickness and surface roughness, since the thickness correlates linear with the roughness. Cu-CAT-1 films obtained were at the scale of

20-100 nm, showing decent crystallinity and a preferential orientation. A similar method was used by X. Song *et al.*.[70] The authors employed a liquid-phase epitaxy (layer-by-layer growth) to grow Cu-CAT-1 on silane functionalized substrates. A cycled dip-coating procedure was employed comprised of different baths containing 1) HHTP 2) ethanol 3) $Cu(OAC)_2$ and 4) ethanol. By cycling the prefunctionlized substrate in the different baths the formation of a crystalline and preferentially oriented Cu-CAT-1 film could be observed. Also with this method precise control over the film thickness is possible and homogenous and compact films at the nanometerscale were prepared. However, a drawback of this liquid layer-by-layer approach is the need for pre-functionalization of the substrate to create nucleation sites for the film growth.

G. Wu *et al.* prepared films of Ni_3(hexaaminotriphenylene)$_2$ by an interfacial reaction **liquid/air** synthesis.[71] Here, a precursor solution was placed in an open beaker and heated up to 60 °C. At the liquid/air interface a 100 µm thick film was formed. A drawback of the method is the need for film transfer onto solid substrates to enable further characterization and processing. It should be highlighted that the authors prepared with this technique compact, homogeneous, crystalline, but non-oriented films. The control over the film thickness is here still a challenge.

To overcome the issue of controlling the film thickness, V. R. Gimenez *et al.* prepared crystalline and oriented films of Cu-CAT-1 by a combination of sequential steps.[72] 1) Synthesis of the film at the liquid/air interface, 2) mechanical compression of the film until 3) sufficient pressure for a continuous film is reached and 4) transfer with the **Langmuir-Blodgett** method. The films were transferred to SAM-functionalized substrates. Using this sequential method, ultra-thin and homogeneous films of Cu-CAT-1 were obtained with preferential orientation. Moreover, the compression of the film at the interface allows for a fine-tuning of the thickness, which was not possible before.

Lastly, the interfacial synthesis can also occur at the **liquid/liquid** interface. In this context, Kambe *et al.* reported the synthesis of nickel bis(dithiolene) nanosheets.[73] The nickel precursor was dissolved in the aqueous solution and the linker in dichloromethane. The formed film at the liquid/liquid interface was transferred on a HOPG substrate for further analysis. However, the resulting nanosheets lacked in large area homogeneity and crystallinity. It should be noted that this reaction pathway is more favorable for highly reactive precursors which can only hardly processed into thin films using the *prior* discussed methods.

Although, great advances were made in the field of 2D MOF films fabrication, homogeneity, large coverage or applicability are still important challenges to address. In 2017, the review *Simplicity as a Route to Impact in Materials Research* was published in *Advanced Materials* by Cademartiri *et al.* highlighting the importance of simple solutions for academic, technological, or scientific challenges, defined in the article as inexpensive, reliable, predictable, highly performing,

"stackable" and "hackable".[74] Related to the field of oriented MOF film growth, a universally usable technique, being simple and efficient, is definitely desired.

1.5.3. A new way - vapor-assisted conversion

In this section we will introduce the predominant method for producing high-quality thin films used throughout this thesis - vapor-assisted conversion (VAC).

VAC was first introduced for preparing high-quality thin films of reticular framework materials in the group of Prof. Bein by Medina and coworkers in 2015.[75] In this work, the deposition of different covalent-organic frameworks (COFs) on various substrates was studied. The procedure was developed for the boronate ester COFs namely BDT-COF (BDT = benzodithiophene), COF-5 and pyrene-COF films on gold, silicon, glass and fluorine doped tin oxide (FTO) at room temperature. In a typical synthesis, the organic precursors were dissolved in a polar solvent mixture forming the precursor solution. Subsequently, 150-200 µL of the precursor solution was drop-casted on a clean substrate, which was then placed in a desiccator and stored for up to 72 h at room temperature, obtaining films with a good coverage consisting of randomly distributed COF crystallites. Due to the critical role of the vapor composition used in the synthesis, the approach was termed *vapor-assisted conversion* (VAC).

Very recently, Virmani and coworkers described the synthesis of oriented and crystalline MOF films by adopting the vapor-assisted conversion approach.[76] The method was applied to the well-known zirconium based UiO-66, UiO-66(NH_2), UiO-67, and UiO-68(NH_2) as well as the porous interpenetrated Zr-organic framework, PPPP-PIZOF-1. Using the VAC approach, continuous MOF films oriented along the [111] crystal axis were prepared on bare gold substrates, gold surfaces modified with thiol SAMs and on silicon substrates. For the synthesis, a modified procedure of the vapor-assisted conversion from Medina *et al.* was used. The respective substrates were placed on a substrate holder platform in an autoclave containing a solvent mixture. Subsequently, a defined amount of precursor solution was drop-cast as thin layer on top of the substrate and the autoclave was sealed and immediately transferred to a preheated oven at elevated temperature. After the heating process a continuous film was obtained. Systematic studies were performed highlighting the concentration of modulator, droplet volume, reaction time and temperature as key synthesis parameters for the fabrication of oriented and crystalline framework films. The possibility to synthesize the whole UiO-series as films on different substrates underlines the chemical robustness of the VAC process.

The vapor-assisted conversion approach features several important advantages compared to the previously discussed routes for preparing thin films of porous materials: (i) the VAC method is simple and can be carried out in every lab. (ii) It is cheap, because no high-tech and cost

intensive equipment is required and (iii) efficient, due to the fact that only the right amounts of precursors in the droplet are utilized and no excessive use of linker as in solvothermal approaches is necessary. Most importantly (iv), the method is "hackable" and can be easily modified, tuned and customized to the related issue and challenge of the chemist.

Ultimately, vapor-assisted conversion provides a versatile platform allowing the control of a wide range of easily accessible parameters, which renders it as the predestined method of choice for the preparation of MOF thin films in this thesis.

References

[1] a) T. R. Cook, Y.-R. Zheng, P. J. Stang, *Chem. Rev.* **2013,** *113,* 734, b) H. Furukawa, K. E. Cordova, M. O'Keeffe, O. M. Yaghi, *Science* **2013,** 341, 1230444, c) J. Jiang, Y. Zhao, O. M. Yaghi, *J. Am. Chem. Soc.* **2016,** *138,* 3255, d) G. Ferey, *Chem. Soc. Rev.* **2008,** *37,* 191.

[2] a) M. P. Suh, H. J. Park, T. K. Prasad, D.-W. Lim, *Chem. Rev.* **2012,** *112,* 782, b) H. Wu, Q. Gong, D. H. Olson, J. Li, *Chem. Rev.* **2012,** *112,* 836, c) K. Sumida, D. L. Rogow, J. A. Mason, T. M. McDonald, E. D. Bloch, Z. R. Herm, T.-H. Bae, J. R. Long, *Chem. Rev.* **2012,** *112,* 724.

[3] Ye, J., Johnson, J. K. *ACS Catal.* **2015,** 5, 2921-2928.

[4] I. Fechete, J. C. Vedrine, **Molecules,** 20, 5638.

[5] H. Chang, H. Wu, *Adv. Funct. Mater.* **2013,** 23, 1984-1997.

[6] N. M. Dorval Courchesne, M. T. Klug, K. J. Huang, M. C. Weidman, V. J. Cantu, P. Y. Chen, S. E. Kooi, D. S. Yun, W. A. Tisdale, N. X. Fang, A. M. Belcher, P. T. Hammond *J. Phys. Chem. C* **2015,** 119, 13987-14000.

[7] a) M. Simo, S. Sivashanmugam, C. J. Brown, V. Hlavacek, *Ind. Eng. Chem. Res.* **2009,** 48, 9247-9260. b) V. J. J. Inglezakis, *Colloid Interface Sci.* **2005,** 281, 68-79. c) P. E. Eberly, *Ind. Eng. Chem. Prod. Res. Dev.* **1971,** 10, 433-437.

[8] X. C. Huang, Y. Y. Lin, J. P. Zhang, X. M. Chen, *Angew. Chem. Int. Ed.* **2006,** 45, 1557-1559.

[9] D. Y. Hong, Y. K. Hwang, C. Serre, G. Ferey, J. S. Chang, *Adv. Funct. Mater.* **2009,** 19, 1537-1552.

[10] O. M. Yaghi, M. O'Keeffe, N. W. Ockwig, H. K. Chae, M Eddaoudi, J. Kim, *Nature* **2003,** 423, 705-714.

[11] X. Feng, X. Ding, D. Jiang, *Chem. Soc. Rev.* **2012,** 41, 6010-6022.

[12] a) L. J. Murray, M. Dinca, J. R. Long, *Chem. Soc. Rev.* **2009,** 38, 1294-1314. b) H. C. Zhou, S. Kitagawa, *Chem. Soc. Rev.* **2014,** 43, 5415-5418. c) J. E. Clements, J. R, Price, S. M. Neville, C. J. Kepert, *Angew. Chem. Int. Ed.* **2014,** 53, 10164-10168. d) X. Zhou, W. Huang, J. Shi, Z. Zhao, Q. Xia, Y. Li, H. Wang, Z. Li, *J. Mater. Chem. A* **2014,** 2, 4722-4730.

[13] a) A. Vlad, M. Cazacu, M. F. Zaltariov, A. Bargan, S. Shova, C. Turta, *J. Mol. Struct.* **2014,** 1060, 94-101. b) R. Haldar, S. Bonakala, P. Kanoo, S. Balasubramanian, T. K. Maji, *CrystEngComm* **2014,** 16, 4877-4885.

[14] H. Li, M. Eddaoudi, M. O'Keeffe, O. M. Yaghi, *Nature* **1999,** 402, 276-279.

[15] M. Eddaoudi, J. Kim, N. Rosi, D. Vodak, J. Wachter, M. O'Keeffe, O. M. Yaghi, *Science* **2002,** 295, 469-472.

[16] a) M. Eddaoudi, D. B. Moler, H. Li, B. Chen, T. M. Reineke, M. O'Keeffe, O. M. Yaghi, *Acc. Chem. Res.* **2001,** 34, 319-330. b) C. Serre, C. Mellot-Draznieks, S. Surble, N. Audebrand, Y. Filinchuk, G. Ferey, *Science* **2007,** 315, 1828-1831.

[17] D. J. Tranchemontagne, J. L. Mendoza-Cortes, M. O'Keeffe, O. M. Yaghi, *Chem. Soc. Rev.* **2009,** 38, 1257-1283.

[18] L. Sun, M. G. Campbell, M. Dinca, *Angew. Chem. Int. Ed.* **2016,** 55, 3566-3579.

[19] P. Simon, Y. Gogotsi, *Nat Mater* **2008,** 7, 845-854.

[20] N. Brandon, D. Brett, *Philos. Trans. R. Soc. A* **2006,** 364, 147-159.

[21] D. M. D'Alessandro, J. R. R. Kanga, J. S. Caddy, *Aust. J. Chem.* **2011,** 64, 718-722.

[22] G. Wu, J. Huang, Y. Zang, J. He, G. Xu, *J. Am. Chem. Soc.* **2017,** 139, 1360-1363.

[23] J.-R. Li, J. Sculley, H.-C. Zhou, *Chem. Rev.* **2012,** *112,* 869.

[24] L. Zhu, X.-Q. Liu, H.-L. Jiang, L.-B. Sun, *Chem. Rev.* **2017,** *117,* 8129.

[25] L. E. Kreno, K. Leong, O. K. Farha, M. Allendorf, van Duyne, J. T. Hupp, *Chem. Rev.* **2012,** *112,* 1105.

[26] M. A. Nasalevich, M. van der Veen, F. Kapteijn, J. Gascon, *CrystEngComm* **2014,** 16, 4919-4926.

[27] A. D. Burrows, **2017** *The Chemistry of Metal-Organic Frameworks. Synthesis, Characterization, and Applications,* 2 Volumes. Edited by Stefan Kaskel.

[28] L. Sun, T. Miyakai, S. Seki, M. Dinca, *J. Am. Chem. Soc.* **2013,** *135,* 8185.

[29] a) S. S. Park, E. R. Hontz, L. Sun, C. H. Hendon, A. Walsh, T. van Voorhis, M. Dinca, *J. Am. Chem. Soc.* **2015,** *137,* 1774, b) C. F. Leong, B. Chan, T. B. Faust, D. M. D'Alessandro, *Chem. Sci.* **2014,** *5,* 4724.

[30] a) S. R. Ahrenholtz, C. C. Epley, A. J. Morris, *J. Am. Chem. Soc.* **2014,** *136,* 2464, b) L. Sun, C. H. Hendon, M. A. Minier, A. Walsh, M. Dinca, *J. Am. Chem. Soc.* **2015,** *137,* 6164.

[31] a) M. D. Allendorf, M. E. Foster, F. Leonard, V. Stavila, P. L. Feng, F. P. Doty, K. Leong, E. Y. Ma, S. R. Johnston, A. A. Talin, *J. Phys. Chem. Lett.* **2015,** *6,* 1182, b) D.M. D'Alessandro, *Chem. Commun.* **2016,** *52,* 8957, c) S. Goswami, D. Ray, K.-I. Otake, C.-W. Kung, S. J. Garibay, T. Islamoglu, A. Atilgan, Y. Cui, C. J. Cramer, O. K. Farha, *Chem. Sci.* **2018,** *9,* 4477, d) J. Liu, T. Wächter, A. Irmler, P. G. Weidler, H. Gliemann, F. Pauly, V. Mugnaini, M. Zharnikov, C. Wöll, *ACS Appl. Mater. Interfaces* **2015,** *7,* 9824.

[32] A. A. Talin, A. Centrone, A. C. Ford, M. E. Foster, V. Stavila, P. Haney, R. A. Kinney, V. Szalai, F. El Gabaly, H. P. Yoon, *Science* **2014,** *343,* 66.

[33] a) B. Le Ouay, M. Boudot, T. Kitao, T. Yanagida, S. Kitagawa, T. Uemura, *J. Am. Chem. Soc.* **2016,** *138,* 10088, b) I. Hod, W. Bury, D. M. Gardner, P. Deria, V. Roznyatovskiy, M. R. Wasielewski, O. K. Farha, J. T. Hupp, *J. Phys. Chem. Lett.* **2015,** *6,* 586.

[34] C. F. Leong, P. M. Usov, D. M. D'Alessandro, *MRS Bull.* **2016,** *41,* 858.
[35] M. Hmadeh, Z. Lu, Z. Liu, F. Gandara, H. Furukawa, S. Wan, V. Augustyn, R. Chang, L. Liao, F. Zhou, *Chem. Mater.* **2012,** *24,* 3511.
[36] D. Sheberla, L. Sun, M. A. Blood-Forsythe, S. Er, C. R. Wade, C. K. Brozek, A. Aspuru-Guzik, M. Dinca, *J. Am. Chem. Soc.* **2014,** *136,* 8859.
[37] E. M. Miner, T. Fukushima, D. Sheberla, L. Sun, Y. Surendranath, M. Dinca, *Nat. Commun.* **2016,** *7,* 10942.
[38] E. M. Miner, S. Gul, N. D. Ricke, E. Pastor, J. Yano, V. K. Yachandra, T. van Voorhis, M. Dinca, *ACS Catal.* **2017,** *7,* 7726.
[39] D. Sheberla, J. C. Bachman, J. S. Elias, C.-J. Sun, Y. Shao-Horn, M. Dinca, *Nat. Mater.* **2017,** *16,* 220.
[40] G. Wu, J. Huang, Y. Zang, J. He, G. Xu, *J. Am. Chem. Soc.* **2017,** *139,* 1360.
[41] M. G. Campbell, D. Sheberla, S. F. Liu, T. M. Swager, M. Dinca, *Angew. Chem. Int. Ed.* **2015,** *54,* 4349.
[42] M. G. Campbell, S. F. Liu, T. M. Swager, M. Dinca, *J. Am. Chem. Soc.* **2015,** *137,* 13780.
[43] R. Dong, M. Pfeffermann, H. Liang, Z. Zheng, X. Zhu, J. Zhang, X. Feng, *Angew. Chem. Int. Ed.* **2015,** *54,* 12058.
[44] R. Dong, Z. Zheng, D. C. Tranca, J. Zhang, N. Chandrasekhar, S. Liu, X. Zhuang, G. Seifert, X. Feng, *Chem. Eur. J.* **2017,** *23,* 2255.
[45] a) S. R. Ahrenholtz, C. C. Epley, A. J. Morris, *J. Am. Chem. Soc.* **2014,** *136,* 2464, b) I. Hod, M. D. Sampson, P. Deria, C. P. Kubiak, O. K. Farha, J. T. Hupp, *ACS Catal.* **2015,** *5,* 6302, c) D. M. D'Alessandro, *Chem. Commun.* **2016,** *52,* 8957, d) N. Kornienko, Y. Zhao, C. S. Kley, C. Zhu, D. Kim, S. Lin, C. J. Chang, O. M. Yaghi, P. Yang, *J. Am. Chem. Soc.* **2015,** *137,* 14129, e) C. R. Wade, M. Li, M. Dinca, *Angew. Chem. Int. Ed.* **2013,** *52,* 13377, f) L. Sun, C. H. Hendon, M. A. Minier, A. Walsh, M. Dinca, *J. Am. Chem. Soc.* **2015,** *137,* 6164, g) C. Hua, P. W. Doheny, B. Ding, B. Chan, M. Yu, C. J. Kepert, D. M. D'Alessandro, *J. Am. Chem. Soc.* **2018,** *140,* 6622.
[46] Z. Guo, D. K. Panda, M. A. Gordillo, A. Khatun, H. Wu, W. Zhou, S. Saha, *ACS Appl. Mater. Interfaces* **2017,** *9,* 32413.
[47] T. T. Nhung, H. F. Nguyen, F. Gandara, C. A. Trickett, H. M. Jeong, K. E. Cordova, O. M. Yaghi *J. Am. Chem. Soc.* **2015,** 137, 15394-15397.
[48] E. L. Darago, M. L. Aubrey, C. J. Yu, M. I. Gonzalez, J. R. Long *J. Am. Chem. Soc.* **2015,** 137, 15703-15711.
[49] G. Skorupskii, B. A. Trump, T. W. Kasel, *et al. Nat. Chem.* **2020** 12, 131-136.
[50] G. Skorupskii, M. Dinca *J. Am. Chem. Soc.* **2020,** 142, 6920-6924.
[51] N. L. Rosi, J. Kim, M. Eddaoudi, B. Chen, M. O'Keeffe, O. M. Yaghi, *J. Am. Chem. Soc.* **2005,** 127, 1504-1518.
[52] H. Deng, S. Grunder, K. E. Cordova, C. Valente, H. Furukawa, M. Hmadeh, F. Gandara, A. C. Whalley, Z. Liu, S. Asahina, H. Kazumori, M. O'Keeffe, O. Terasaki, J. F. Stoddart, O. M. Yaghi, *Science* **2012,** 336, 1018-1023.
[53] L. Sun, T. Miyakai, S. Seki, M. Dinca. *J. Am. Chem. Soc.* **2013,** 135, 8185-8188.
[54] L. Sun, C. H. Hednon, M. A. Minier, A. Walsh, M. Dinca *J. Am. Chem. Soc.* **2015,** 137, 6164-6167.
[55] O. Shekhah, J. Liu, R. A. Fischer, C. Wöll, *Chem. Soc. Rev.* **2011,** 40, 1081-1106.
[56] Y. Takashima, V. M. Martinez, S. Furukawa, M. Kondo, S. Shimomura, H. Uehara, M. Nakahama, K. Sugimoto, S. Kitagawa, *Nat. Commun.* **2011,** 2, 168-170.
[57] E. Biemmi, N. S., A. Darga, Bein, T. *Microporous Mesoporous Mater.* **2008,** 114, 380-386.
[58] D. Zacher, A. Baunemann, S. Hermes, R. A. Fischer, *J. Mater. Chem.* **2007,** 17, 2785-2792.
[59] E. Biemmi, C. Scherb, T. Bein, *J. Am. Chem. Soc.* **2007,** 129, 8054-8055.
[60] Shekhah, O. Wang, H. Kowarik, S. Schreiber, F. Paulus, M. Tolan, M., Sternemann, C. Evers, F. Zacher, D. Fischer, R. A. Wöll, C. *J. Am. Chem. Soc.* **2007,** 129, 15118-15119.
[61] A. Schoedel, C. Scherb, T. Bein, *Angew. Chem. Int. Ed.* **2010,** 49, 7225-7228.
[62] R. Makiura, S. Motoyama, Y. Umemura, H. Yamanaka, O. Sakata, H. Kitagawa, *Nat Mater* **2010,** 9, 565-571.
[63] H. K. Arslan, O.Shekhah, J. Wohlgemuth, M. Franzreb, R. A. Fischer, C. Wöll, *Adv. Funct. Mater.* **2011,** 21, 4228-4231.
[64] M. G. Campbell, D. Sheberla, S. F. Liu, T. M. Swager, M. Dinca, *Angew. Chem. Int. Ed.* **2015**, 54, 4349-4352.
[65] B. Hoppe, K. D. J. Hindricks, D. P. Warwas, H. A. Schulze, A. Mohmeyer, T. J. Pinkvos, S. Zailskas, M. R. Krey, C. Belke, S. König, M. Fröba, R. J. Haug, P. Behrens, *CrystEngComm* **2018,** 20, 6458-6471.
[66] M. K. Smith, K. E. Jensen, P. A. Pivak, K. A. Miricia *Chem. Mater.* **2016**, 15, 5264-5268.
[67] Q. Ma, P. Yin, M. Zhao, Z. Luo, Y. Huang, Q. He, Y. Yu, Z. Liu, Z. Hu, B. Chen, H. Zhang, *Adv. Mater.* **2019,** 31, 1808249.
[68] M. l. Gonzales-Juarez, E. Flores, M. Martin-Gonzalez, I. Nandhakumar, D. Bradshaw, *J. Mater. Chem. A* **2020,** 8, 13197-13206.
[69] M. S. Yao, X. J. Lv, Z. H. Fu, W. H. Li, W .H. Deng, G. D. Wu, G. Xu, *Angew. Chem. Int. Ed.* **2017,** 56, 16510.
[70] X. Song, X. Wang, Y. Li, C. Zheng, B. Zhang, C.-a. Di, F. Li, C. Jin, W. Mi, L. Chen, W. Hu, *Angew. Chem. Int. Ed.* **2020,** 59, 1118.
[71] G. Wu, J. Huang, Y. Zang, J. He, G. Xu, G. Xu, *J. Am. Chem. Soc.* **2017,** 139, 1360-1363.
[72] V. Rubio-Gimenez, M. Galbiati, J. Catells-Gil, N. Almora- Barrios, J. Navarro-Sanchez, G. Escorcia-Ariza, M. Mattera, T. Arnold, J. Rawle, S. Tatay, *Adv. Mater.* **2018,** *30,* 1704291.
[73] T. Kambe, R. Sakamoto, K. Hoshiko, K. Takada, M. Miyachi, J.- H. Ryu, S. Sasaki, J. Kim, K. Nakazato, M. Takata, *J. Am. Chem. Soc.* **2013,** *135,* 2462.
[74] X. Tian, K. R. Lind, B. Yuan, S. Shaw, O. Siemianowski, L. Cademartiri, *Adv. Mater.* **2017,** 1604681-1604685.
[75] D. D. Medina, J. M. Rotter, Y. Hu, M. Dogru, V. Werner, F. Auras, J. T. Markiewicz, P. Knochel, T. Bein, *J. Am. Chem. Soc.* **2015,** 137, 1016-1019.
[76] E. Virmani, J. M. Rotter, A. Mähringer, T. Zons, A. Godt, T. Bein, S. Wuttke, D. Medina, *J. Am. Chem. Soc.* **2018,** 140, 4812-4819.

2. Analytical methods

2.1. X-ray powder diffraction

X-ray powder diffraction is routinely used as a destruction-free analysis of solid crystalline materials and intermediates. The information obtained from this technique gives direct insights into the crystal structure of the examined material. Diffraction methods have therefore a great impact in various research fields *e.g.,* organic and inorganic chemistry, material science or medicine. This great importance is also reflected in the evolution of X-ray research during the course of history. The first Nobel prize in physics in 1901 was awarded to Wilhelm Conrad Röntgen for the discovery of X-rays.[1,2] A few years later, 1914, Max von Laue was rewarded with the Nobel prize in physics concerning the discovery of X-ray interferences at crystalline materials.[1,3] Based on this work, W.H. Bragg and W. L. Bragg performed several X-ray diffraction experiments on different crystalline compounds such as diamond and zincblende, being able to determine the crystal structure of those materials for the first time.[4,5] This achievement was honored with the Nobel prize in 1915. The following accumulation of Nobel prizes in this context from 1917-1936 set the ground for the fundamental research in X-ray physics.[1] Nowadays, X-ray diffraction is used in all kinds of research areas from medicine to solid-state physics.

2.1.1. Theory - diffraction of X-rays

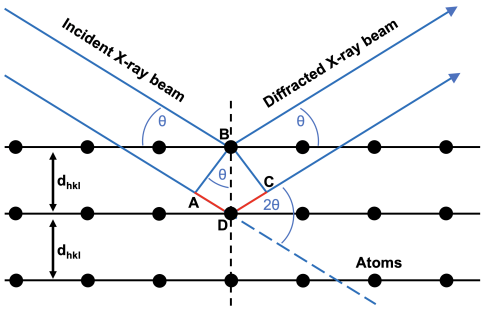

Figure 2.1 – Reflection of incident X-ray beams at the crystallographic planes (*hkl*) with the distance d_{hkl}. The X-ray beam is diffracted under the angle θ and the constructive interference is recorded by a detector.

In principle, the wavelength of the incident X-ray is the same dimension as the interatomic distances, which is typically at the order of several Angstroms (Å; 10^{-10} m). By fulfilling this condition, the X-ray beam is diffracted at distinctive angles to the crystal planes leading to constructive and destructive interference. The intensity maxima produced by constructive

inference are collected by a detector (see Figure 2.1). This relation is described by the Bragg equation (see eq. 2.1).

$$n\lambda = 2d \sin\theta \tag{2.1}$$

The principle behind diffraction can be explained in a nutshell: if two incident beams are reflected on adjacent lattice planes with distance d_{hkl}, the second beam takes a longer path of $\overline{ADC}$. If the difference in path length equals an integer multiple of λ, positive interference is observed. This can only occur if the incident beam is reflected at distinctive angles θ at the lattice plane d_{hkl}. The created pattern of constructive interface is transformed into a plot of intensity versus the diffraction angle $2\,\theta$ (diffraction pattern). This pattern can either be used as a "fingerprint" of the analyzed sample and compared to similar diffraction patterns from crystal databases like ICDD-JCPDS for qualitative phase identification or subjected to more advanced analysis methods.

2.1.2. Methods of X-ray diffraction

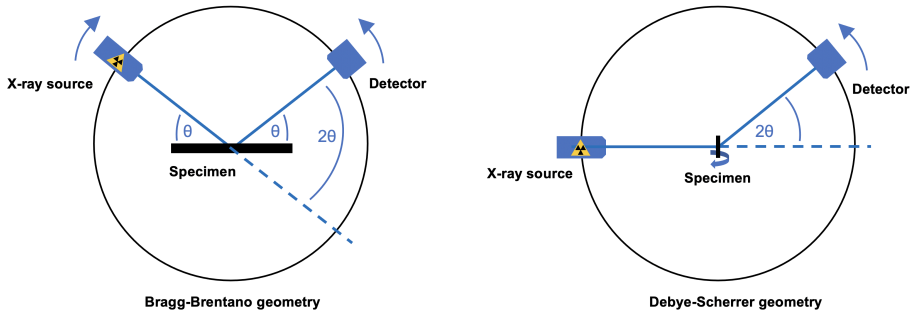

Figure 2.2 – Different diffraction geometries for PXRD analysis. (Left) Bragg-Brentano and (right) the Debye-Scherrer geometry.

The X-ray beam in modern diffraction instruments is still produced like the one from the first "Urröntgenröhre" invented by J. E. Lilienfeld in 1911.[6] In an evacuated vacuum tube, a cathode creates electrons by the thermionic effect,[7] which are subsequently accelerated by a tube voltage (normally 40-50 kV) onto an anode. The anode material is typically composed of copper, molybdenum or silver. The electrons approaching the anode produce in the first place a broad continuum of *Bremsstrahlung* (98-99%).[1] due to the deceleration. The residual electrons lead to ionization of the anode material which results in a characteristic intensive emission. This emission results from the ejection of electrons from the K-shell and the refill from the L-shells.[8] In the refilling process, energy in the form of a well-defined radiative emission is released. The

most intensive transition is the $K\alpha_1$ line, which is commonly used for the diffraction process. The *Bremsstrahlung* is cut away from this characteristic line by X-ray mirrors or filters. Depending on the probed material either Cu-$K\alpha_1$ (1.93991 Å), or Mo-$K\alpha_1$ (0.713543 Å) is employed.[9] The use of Mo-$K\alpha_1$ is useful if the probed sample contains elements such as iron or cobalt, featering an absorption edge close to Cu-$K\alpha_1$ energy. Here, a broad continuum of fluorescence from the sample is observed and the use of a shorter wavelength such as Mo-$K\alpha_1$ is recommended.

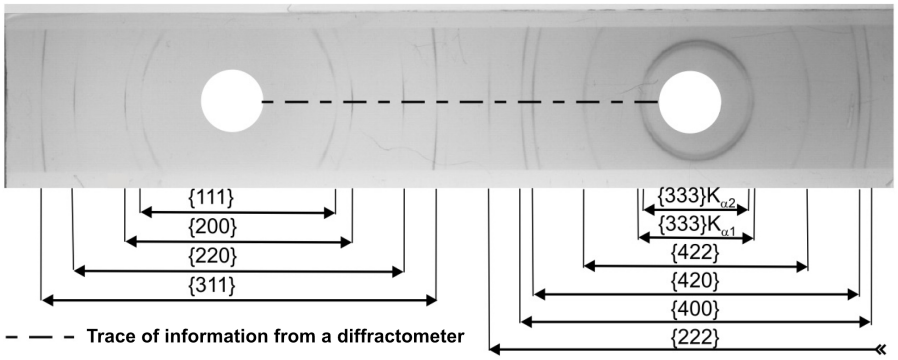

Figure 2.3 – Debye-Scherrer shot of a preferentially oriented sample (gold).[1] The trace of information from a diffractometer is depicted as dotted line. The shot depicts the preferential crystallite orientation as black arc shaped reflections on the film.

The most widely spread diffraction techniques are the Bragg-Brentano and the Debye-Scherrer method (see Figure 2.2).[1] In Bragg Brentano, the sample is placed tangentially to the centre of the diffraction circle, while the X-ray source and the detector are situated at the edges of a focusing circle.[10] The focusing conditions are fulfilled when the X-ray source, the flat sample and the detector are simultaneously situated at the same time on the focusing circle. Crystallographic planes (*hkl*) parallel to the surface sample will give a reflection *hkl* if θ is equal to the Bragg diffraction angle θ *hkl*. In contrast, the Debye-Scherrer geometry uses an X-ray line source which is stationary and parallel to the specimen.[11] The crystalline sample is filled in a capillary and rotated around its axis to achieve diffraction for all lattice planes. The detector is moving on a focusing circle recording the diffracted intensity. A major difference between the two techniques can be found in the limited ability to rotate the sample in the Bragg-Brentano geometry. In Debye-Scherrer, the rotation brings more planes of a polycrystalline sample in diffraction (see Figure 2.3). This drawback can lead to misleading information in the Bragg-Brentano geometry if the sample contains crystallites with preferential orientation or it is highly textured.[1] These features are reflected in the accumulation of diffraction rings forming arcs or points. The appearance of these diffraction rings can be probed in the Debye-Scherrer geometry. An advantage of the Bragg-Brentano method is the ability to analyze thin film samples, since Deybe-Scherrer requiers transmission mode which is often not possible when using non-transparent samples. Furthermore,

Bragg-Brentano enables the use of different X-rays measurements such as grazing incidence XRD, in which the interaction volume of the sample with the incident X-ray (*e.g.,* in the case of films at the nanometer-scale) can be increased leading to higher diffraction intensities.

2.1.3. Phase analysis - Rietveld and Pawley refinement

Diffraction patterns encode a variety of information.[12] While the peak positions reveal the unit cell parameters, the peak intensity gives the position of the atomic parameters, whereas peak shapes yield information about defects, crystallinity and disorder. The full width at half maximum (FWHM) contains information concerning the domain size of particles. The latter is known as the Scherrer equation:[13]

$$L = \frac{K \cdot \lambda}{\Delta(2\theta) \cdot \cos\theta} \tag{2.2}$$

L = size of the ordered (crystalline) domains ; K = shape factor (0.9); λ = X-ray wavelength; θ = angle; $\Delta(2\theta)$ = FWHM of the reflection.

Furthermore, PXRD patterns can be subjected to a set of fitting techniques. These techniques give information about parameters containing structural information. Most commonly used for data obtained from powder samples are the Rietveld and Pawley refinement. In a Pawley refinement, the diffraction profile is fitted by only the following parameters: $I_{(hkl)}$ Intensity of the peaks, $A\,B\,C$ (unit cell parameters), instrumental error and $U\,V\,W$ (peak width parameters). Here, the peak intensities are refined as fit variables.[14] The Pawley fit, in contrast to the Rietveld refinement, does not require an underlying crystal structure. In the Rietveld analysis, a crystal structure is necessary since the positional parameters of all the atoms in the unit cell are refined.[15] Furthermore, the Rietveld analysis can also give information about phase quantification, occupation sites or isotropic and anisotropic parameters making it a very powerful technique. The fundamental principle is that all data points i of a PXRD pattern with intensity y_{io} are described by an analytical function (calc. intensity y_{ic}). The functions are optimized in the refinement process by the method of least squares:

$$S_y = \sum w_i |y_{io} - y_{ic}|^2 \;\rightarrow \text{ Optimize to minimum} \tag{2.3}$$

As scaling factor w_i the reciprocal relation of data point i is used:

$$w_i = \frac{1}{y_{io}} \tag{2.4}$$

The theoretical calculation of the datapoint i is done by the following equation:

$$y_{ic} = S \sum_K H_K \cdot L_K \cdot P_K \cdot A \cdot S_r \cdot E_X \cdot |F_K|^2 \cdot \Phi(2\theta_i - 2\theta_K) + y_{ib} \tag{2.5}$$

S = scaling factor ; L_K = Lorentz- and polarization factor; P_K = texture factor; A = absorption factor; E_X = extinction factor; $2\theta_K$ = calc. position of Bragg interference; $2\theta_i$ = angle at data point i; y_{ib} = background intensity at data point i; K = h,k,l of Bragg reflection; H_K = plane scaling factor; S_r = roughness factor; Φ = profile function; F_K = structure factor.

To evaluate the quality and process of the Rietveld refinement, the reduction of S_y, different figures of merit can quantify the fit. Most important are the profile residual R_p (without background correction) and the weighted profile residual R_{wp} (including background correction) and the goodness of fit (GOF):

$$R_p = \frac{\sum_i |y_{io} - y_{ic}|}{\sum_i |y_{io} - y_{ib}|} \tag{2.6}$$

$$R_w p = \sqrt{\frac{\sum_i w_i (y_{io} - y_{ic})^2}{\sum_i w_i (y_{io} - y_{ib})^2}} \tag{2.7}$$

$$GOF = \frac{R_{wp}}{R_E} = \sqrt{\frac{\sum_k w_i (y_{io} - y_{ic})^2}{(N - P)}} \tag{2.8}$$

with R_E:

$$R_E = \sqrt{\frac{(N - P)}{\sum_i w_i (y_{io})^2}} \tag{2.9}$$

N = number of data points; P = number of refined parameters.

2.2. Grazing incidence wide-angle X-ray scattering

Grazing incidence wide-angle X-ray scattering (GIWAXS) is a versatile and frequently used technique in the field of micro- and nano-structured thin films and particles.[16] It was first discovered by Levine and coworkers in 1989 for the study of gold nanoparticles on silicon (001) surfaces.[17] Nowadays, it has become a widely employed technique in various research fields such as materials science or medicine.[16,18] In contrast to powder X-ray diffraction, the incident X-ray beam is scattered at grazing incidence in reflection mode leading to strong scattering signals collected on an area detector. GIWAXS measurements therefore allow to access a wide range of

information about the analyzed film such as symmetry, spacing, order, grain size and orientation of crystallites.[16]

2.2.1. Experimental set-up

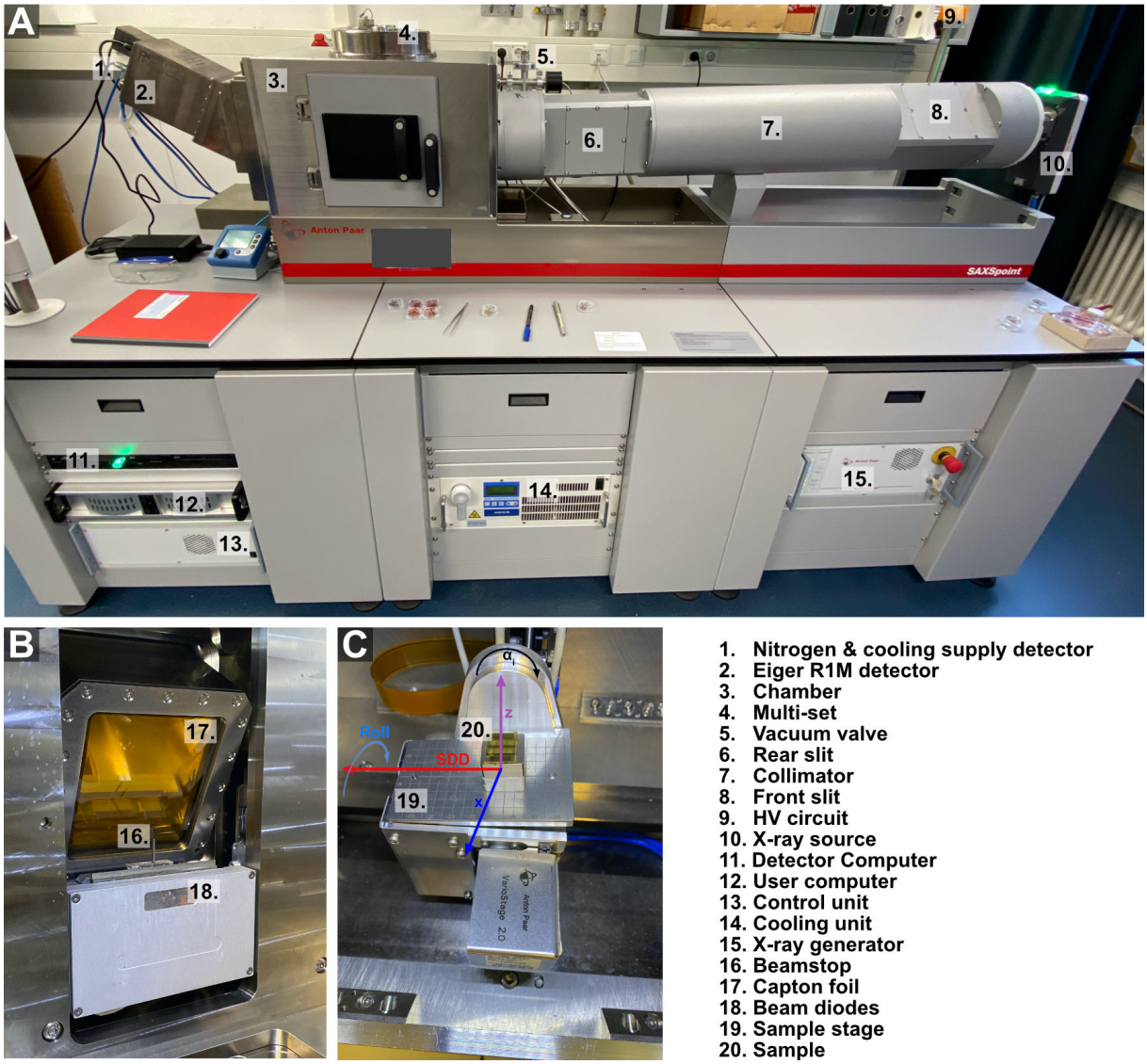

Figure 2.4 – Principal set-up of a GIWAXS instrument. **A** Overview on a SAXSPoint 2.0 instrument from A. Paar with point collimation. **B** Arrangement of the CCD detector, beamstop and beam diodes in the vacuum chamber. **C** Sample stage with sketch of the different alignment parameters (height (z-direction), sample-detector distance (SDD; y-direction), x-position, roll (tilt angle in the xz-plane) and the incidence angle α_i).

The principal set-up of a GIWAXS instrument is shown in Figure 2.4. An important aspect in SAXS experiments is the divergence of the X-ray radiation from the source and the scattered beam. If this divergence is greater than the scattering angle (typically 0.1 °), it is difficult to distinguish the scattered signal from the incident primary beam. This issue is solved in modern SAXS experiments by introducing an enhanced collimation system. By using a combination of multilayers, slits and mirrors the X-ray divergence from the source can be kept very small. For the analysis of textured samples, the point collimation is preferred, while for scanning large area samples a line focus is employed. After passing the collimation system, the focused X-ray beam is illuminating the sample under the grazing incidence angle, which is dependent on the sample-detector distance (SDD) and the substrate refractive index. This relation is given by the following formula:

$$\alpha_i = \tan^{-1}\left(\frac{\Delta px \cdot 0.075\,mm}{\text{sample-detector-distance}}\right)/2 \tag{2.10}$$

Δpx = difference of the pixel position of the primary beam to the specular beam; 0.075 = Pixel size (Eiger series).

To maximize the scattering signal, the sample plane is aligned to the incoming beam by adjusting the x-position, height, roll and α_i-angle *via* the sample stage. The experimental set allows for investigation of different 2θ regimes. A small SSD enables the operator to measure wide-angle X-ray scattering (WAXS mode), while an ultra-long SDD resolves very small scattering angles (SAXS mode).

The primary beam is covered by the beamstop to prevent overshadowing of the relatively weak scattering signal of the sample. It can either be made from transparent Ni-alloy allowing simultaneous measurement of the primary beam and the scattered signal or can be crafted from non-transparent W-alloy. The latter completely blocks the primary beam so that no contribution of the beamstop to the probed scattering signal is detected. The scattered signal is collected by an area CCD detector giving a 2D diffraction pattern of the sample.

2.2.2. Scattering geometry

The principle of the GIWAXS scattering geometry is displayed in Fig. 2.5. A monochromatic X-ray beam with the wavevector K_i and the wavenumber $k_0 = (2\pi)/(\lambda)$ is penetrating the sample surface under the incident angle α_i and is scattered under the exit angle α_f. The angles are typically in the range of 0.1°.[19] Due to energy conservation, the beam is scattered along k_f and the scattering wavevector $\mathbf{q}$ is defined by:

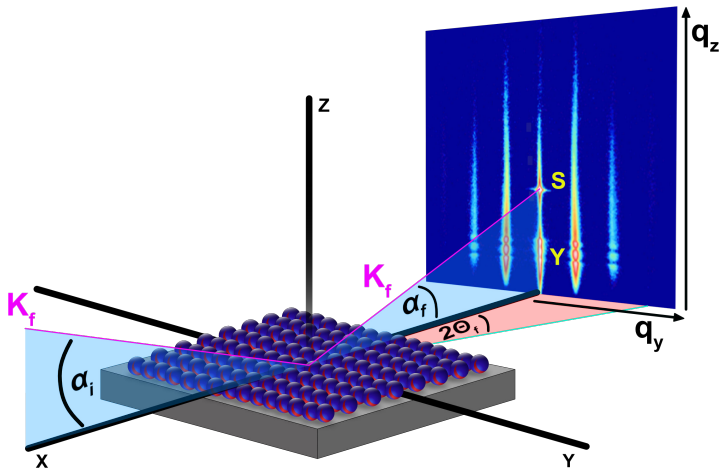

Figure 2.5 – Illustration of the GIWAXS scattering principle. The sample is placed along the spatial coordinates with the following designation: x is the direction along the surface parallel, y the direction perpendicular to it and the z-axis is aligned orthogonally to the surface plane. The angle of the incident monochromatic X-ray beam with the wavevector K_f is denoted with α_i, and the exit angle α_f. After illuminating the sample, the X-rays are scattered along K_f in the direction (α_f, $2\Theta_f$). The color code (jet) indicates the differences in the scattering intensity on the two-dimensional detector. Characteristic features are the specular reflection (denoted S) and the Yoneda reflection (denoted Y). q_x and q_y are the scattering wavevectors for the spatial directions.[16]

$$\mathbf{q} = (q_x, q_y, q_z) \tag{2.11}$$

The components are described by eq. 2.12:

$$q_{x,y,z} = \begin{bmatrix} \cos(\alpha_f)\cos(2\Theta_f) - \cos(\alpha_i) \\ \cos(\alpha_f)\sin(2\Theta_f) \\ \sin(\alpha_f) + \sin(\alpha_i) \end{bmatrix} \tag{2.12}$$

If the wave vector components are $q_x = q_y = 0$ and $q_z \neq 0$, specular scattering appears, while at $q_x, q_y \neq 0$ off-specular-scattering probes the in-plane structure of the sample. In experimental practice, the direct beam and the specularly reflected beam are suppressed by several orders of magnitude by a beam stop to avoid saturation of the detector allowing for separating the diffuse scattering from the specular reflectivity.[20] One typical feature of diffuse scattering is the Yoneda reflection, which arises when the incident or exit angle equals the critical angle $\alpha_{i,f} = \alpha_c$ (see Figure 2.5 denoted as Y).[21] Hereby, the intensity is drastically increased because the standing wave field of the incident and the reflected waves reaches its maximum. However, the specular

reflection is based on the scattering geometry in reflection mode and arises at $2\alpha_f$ with respect to the sample horizon when α_i equals α_f.

The obtained 2D data can be analyzed by simple qualitative evaluation, linecut extraction, peak indexing, modeling or fitting. Most important for this work is the qualitative interpretation of the measured 2D diffraction data, which provides crucial structural insights into the investigated films. For example, diffuse scattering indicates disorder or roughness of the surface (see Figure 2.6), while halo rings reveal randomly distributed crystallites on the sample surface. Reflection in the shape of arches indicates the presence of a preferentially oriented film. An array of defined reflections displays a completely oriented film, *e.g.,* similar to a single crystal. Intensity distributions along the rings provide information about the orientation of the crystallites.[16,19]

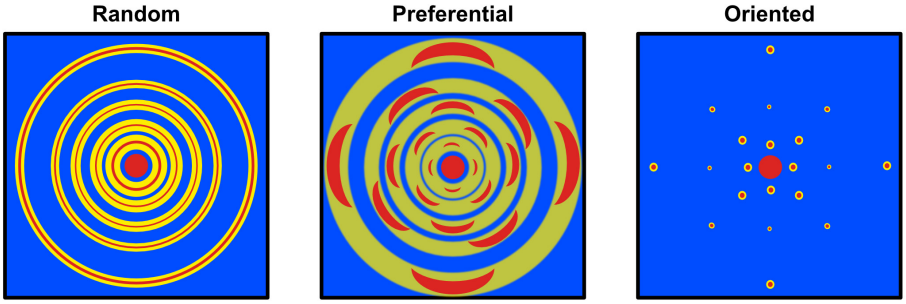

Figure 2.6 – Examples of 2D scattering patterns. From left to right: non-oriented (*e.g.,* polycrystalline powder), preferentially oriented (*e.g.,* fibers, nanostructured films) and oriented samples (*e.g.,* single crystals).[18]

Linecuts are useful analytical tools to extract 1D plots from 2D data. For this purpose, 1D radial average, radial (in-plane, out-of-plane) or straight (along q_z) linecuts can be applied to the measured data resulting in a plot of intensity against q_y. The q-values can be transformed to conventional 2Θ using the following equation:

$$2\Theta = 2\sin^{-1}\left(\frac{|q|\lambda}{4\pi}\right) \tag{2.13}$$

2.3. Electron microscopy

The first electron microscope was invented by Ruska and coworkers in 1932 by imaging small stainless-steel meshes illustrating the capability of this new technique.[22] Later on Ruska developed at Siemens the first commercial electron microscope.[23] He was rewarded with the Nobel prize in physics in 1986 for his pioneering work in this field. Today, electron microscopy finds application in nearly every research area from nanoscience to biology.[24] Electron microscopy is a technique that allows one to investigate specimens with much higher resolution than normal optical light

microscopes and is therefore suitable for analyzing material properties at the nanometer scale. The electron microscope uses electrons with wavelengths at the scale of a few picometers (1 pm = 10^{-12} m), more than 1000 times shorter than the wavelength in the visible spectrum (400-700 nm) to image even very small structures at the nanoscale.[24]

2.3.1. Scanning electron microscopy

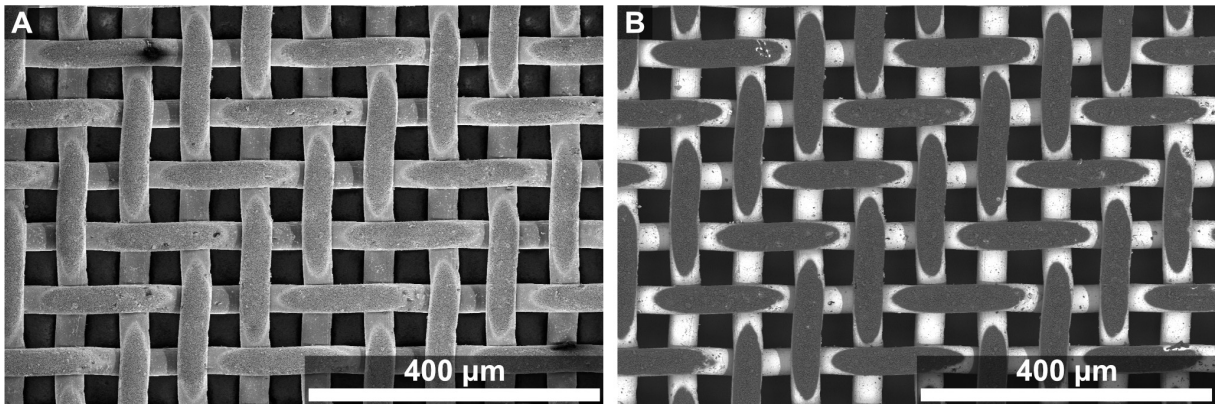

Figure 2.7 – Examples of **A** SE and **B** BSE imaging. The displayed images show MOF-patterns grown onto a gold-coated stainless-steel grid.

Scanning electron microscopy (SEM) is a type of electron microscopy that screens the sample with a high-energy electron beam to create a variety of signals revealing information about the surface morphology, topography and material composition. The primary electrons are emitted by a field emission gun or another electron source, and are subsequently accelerated to an energy of 0.2-30 keV and focused by electromagnetic lenses to a spot of 0.4-5 nm onto the sample surface.[25] Furthermore, the beam is deflected by electromagnetic lenses, which allows for scanning of a surface in the x- and y-direction. After penetrating the specimen, signals with different intensity are created due to the degree of interaction of the electron beam with the sample surface and are collected by a detector. These intensities are detected and translated into grey scale values, resulting in a grey scale image of the sample surface. The most important signal types are secondary electrons produced by interaction of the incident electron beam with the electrons of the scanned atoms. The high energy of the primary electrons ejects electrons from the sample by inelastic scattering interactions. Here, only secondary electrons near the surface can escape from the sample. From edges and corners of the sample more electrons are ejected due to the larger exposed surface area, while in cavities and valleys less electrons are ejected. This difference in topography is then monitored by the detector and transferred to different grey scale intensities forming the impression of a 3D topography image. Another type of detectable signals

are backscattered electrons (BSE) which are produced by an elastic scattering process. The primary beam electrons are scattered by heavy elements in the specimen. After the scattering process, these back-scattered electrons have less energy compared to the primary electrons and can therefore by separated and detected. The backscattering coefficient increases with the atomic number of the investigated element. Heavier elements scatter more electrons than light-weight elements, thus more backscattered electrons are detected and the heavy elements appear brighter in the SEM greyscale image as the surrounding. Hereby, backscattered electrons are used to establish the material contrast in a grey scale image in order to distinguish materials with different backscattering coefficients from each other.[24] An example is given in Figure 2.7 by an MOF-pattern grown onto a gold-coated stainless-steel grid. In the left image, only secondary electrons are detected, thus the material contrast between the MOF and the gold is hardly visible. The imaging of BSE allows for distinguishing between the heavy element from the gold-coating (bright shining spots - strong signal) and the MOF (dark spots - low signal) being mainly composed of light-weight carbon, hydrogen and oxygen atoms.

2.3.2. Energy-dispersive X-ray spectroscopy

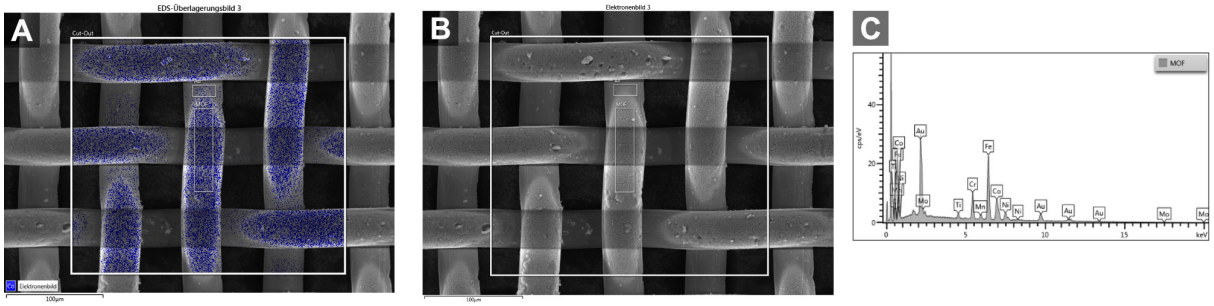

Figure 2.8 – Examples of EDX mapping and spectroscopy. **A** EDX-mapping of cobalt ions on the grid. **B** Underlying SEM image used for EDX mapping. **C** Overall EDX spectrum of the sample.

Energy-dispersive X-ray spectroscopy (EDX) is used an analytical technique to investigate the elemental composition of a specimen. When the electron beam penetrates the sample surface, it can be subject to inelastic scattering by inner K-shell electrons. These inner- electrons can be ejected from the atom leaving an electron vacancy. After the scattering process, an electron from the higher shells can undergo a downward transition to refill the vacancy resulting in a release of X-ray photons with specific energy. The energy of these characteristic X-ray photons correlates with the atomic number Z of the atom involved in the scattering process and quantum numbers of the respective transitions. Therefore, the detected X-rays can be attributed to specific elements giving insights regarding the sample composition. In modern SEM instruments, the

recorded EDX spectra can be implemented in the SEM images as an overlay giving information about the elemental as well as spatial composition of the sample. Figure 2.8 shows the position of cobalt ions in the MOF structure being visible as blue signal in the SEM image. In Figure 2.8**C** the EDX spectrum for the examined spot is displayed showing the overall elemental sample composition as plot of intensity vs energy. Every characteristic energy can be attributed to the respective elemental electron transition allowing the identification of the element.

2.3.3. Transmission electron microscopy

In transmission electron microscopy (TEM), an electron beam generated by an electron gun is focused by electromagnetic lenses on a thin specimen placed on an amorphous carbon grid or another suitable support. The specimen is penetrated by electrons being either deflected or undeflected depending on the scattering process during the sample interaction. To achieve the transmission of electrons through the sample, ultra-thin specimens (<50 nm) and high acceleration voltages (100 keV-1 MeV) are required.[25] The imaging mode can be changed by altering the aperture size. If the undeflected (direct) electron beam is depicted, focused and magnified on an imaging device, typically a fluorescence screen or a CCD camera, the image is coined *bright-field image*. This image is generated from weakening of the primary electron beam and determined by the thickness/mass contrast (thicker regions of the specimen will appear darker), atomic number/Z-contrast (areas with higher Z will appear darker) and the diffraction contrast (Bragg diffraction in the sample will reduce intensity of the primary electrons).[26]

2.4. IR spectroscopy

Infrared(IR)-radiation was first discovered in 1800 by the musician and astronomer Herschel measuring the temperature of the sun spectrum after passing a prism. He recognized an increasing temperature beyond the red light at the end of the visible spectrum concluding the existence of an invisible form of light - infrared radiation.[27] 105 years later, the first absorption spectra based on IR radiation could be measured by Coblentz.[28] Later, Lord Rayleigh was the first to link the measured IR spectrum to the Fourier-transform theory.[29] Today, IR spectroscopy is a destruction-free technique that uses energies in the infrared region of the electromagnetic spectrum to study different vibration modes of molecules and materials. These modes provide qualitative and quantitive information about functional groups in a given structure.

Besides the investigation of specific groups of a molecule, the electromagnetic "fingerprint", which is unique for each molecular structure, can be obtained and compared to similar IR spectra in databases such as SDBS for direct identification of the molecule.[30] IR spectroscopy uses the fact

that molecules (with a change in dipole moment during vibrations) absorb specific frequencies according to their characteristic structure. These absorptions match the resonance frequencies of the molecule, which result in different vibrations. The basic principle of this technique is typically the measurement of an interferogramm by a Michelson interferometer, which is converted by Fourier transformation into a typical IR spectrum (transmittance versus wavenumber).

2.5. Spectrophotometry

2.5.1. UV/VIS/NIR spectroscopy

UV/VIS/NIR-spectroscopy is a powerful method to quantitatively investigate samples with optical absorption properties in the ultraviolet, visible or in the near-infrared spectral range. A breakthrough in this field was achieved by Beckmann in 1941 presenting the first spectrometer.[31] This revolution was the driving force for several high impact inventions during world war II including the synthesis of penicillin, measurement of Vitamin A concentrations in supply rations and the development of synthetic rubber.[32] Today, UV-VIS-NIR spectroscopy is an universal tool in nearly every lab to measure the transitions from the electronic ground state to excited states in materials. Here, the absorbance of the sample is measured versus the incoming wavelength. These spectra can be used to gain versatile insights about the examined material: measurement of molecular concentration (Lambert-Beer-law), electronic structures (*e.g.,* band gap), color, sample thicknesses in solids, extinction coefficient or the index of refraction.

One application of UV/VIS/NIR-spectroscopy is to estimate the band gap energy of different semiconducting materials. In order to excite an electron from the highest occupied molecular orbital (HOMO) to the lowest unoccupied molecular orbital (LUMO) a photon with discrete energy is required to match the energy gap between the orbitals, according to the following formula:

$$E = \frac{hc}{\lambda} \tag{2.14}$$

E = Energy of the band gap; h = planck constant; λ = wavelength; c = speed of light.

The band gap can be calculated by taking the strongest cut-off in the recorded spectral data, where the absorbance value is minimum and inserting the $\lambda_{cut-offwavelength}$ in Eq. 2.14. The most common method for extracting band gap energies is the *Tauc* plot.[33] This determination of the optical band gap is based on *Tauc's* equation:[34]

$$\alpha(E)h\nu = A(h\nu - E_g^{direct})^{1/2} \tag{2.15}$$

E_g^{direct} = band gap energy for allowed direct transition; E = photon energy; h = planck constant; λ = wavelength; ν =frequency; A= constant; α = absorption coefficient.

Straight line segments in the $TAUC$ plot denote the onset of the absorption and indicate the presence of band gaps for direct allowed transitions. These linear regions are extrapolated to $(\alpha(E)h\nu)^2 = 0$ whereby the energy of the optical band gap can be directly obtained.

2.5.2. Photoluminescence measurements

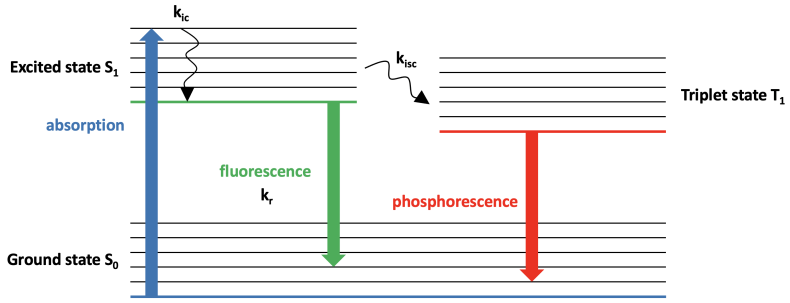

Figure 2.9 – Jablonski diagram visualizing the different processes of absorption, fluorescence and phosphorescence. k_{isc}, k_{ic} and k_r denoting the rates of intersystem crossing, internal conversion and radiative emission events, respectively.[35]

The term luminescence (latin "lumen" = light) was first introduced in 1888 by Wiedemann. It was defined as "all those phenomena of light which are not solely conditioned by the rise in temperature".[36] Luminescence comprises the two major events of light emission, fluorescence (life times of pico to nanoseconds) and phosphorescence (microseconds to seconds). Both processes are related to energy transitions between electronic states in a material, which can be directly probed with steady-state fluorescence spectroscopy. Hereby, an electron in the ground state S_0 is excited by either a pulsed or a continuous wave (CW) laser promoting the electron to an energetically higher state S_1. The transitions that can occur subsequently are described by a Jablonski diagram named after the polish physicist Aleksander Jablonski (Figure 2.9).[37] The following down-conversions are typically possible: fluorescence, phosphorescence, internal conversion (IC), intersystem crossing (ISC) or vibrational relaxation. Most systems exhibit non-radiative decay in the form of vibrational relaxation where the energy is converted into vibrational or phonon energy. Intersystem crossing allows for a formally spin-forbidden transition. The luminescence is called phosphorescence. Typically this state exhibits long life times. Furthermore, the excited electron can also emit a photon being down-converted to the ground state.

To measure the lifetime of excited states which are in the realm of about 1-100 ns, time-correlated single photon counting (TCSPC) is used.[38] First, repetitive fluorescence is induced by a pumped laser source. Second, the time delay between excitation and emission is measured by ultra-fast electronics. Using light attenuating and count rate statistics for the detector and precisely timed laser pulses, single photon events can be detected. These single photon events are sorted into a histogram featuring a range of time "bins". Typically, the count rate drops exponentially while the time proceeds (see eq. 2.16).

$$I = I_0 e^{-t/\tau} \tag{2.16}$$

The fluorescence lifetime τ can be divided into the radiative (k_r) and the non-radiative (k_{nr}) part according to eq. 2.17. Using bi- or multi-exponential functions the lifetime of the different species can be calculated as well as their contribution to the sum of all decay dynamics.

$$\tau = \frac{1}{k_{nr} + k_r} \tag{2.17}$$

2.5.3. Transient absorption spectroscopy

Steady-state fluorescence spectroscopy measures only the excited radiative states in a species. In order to detect a multitude of processes involving electronic states, ultrafast transient absorption spectroscopy (TAS) as pump-probe technique is employed. In principle, TAS is used to measure the change of absorption upon excitation. The experimental set-up is displayed in Figure 2.10. In a nutshell, one synchronous laser set-up creates simultaneously a pump pulse with a specific energy and wavelength (*e.g.,* blue light) and a white light probe pulse. The probe pulse is sent over a delay system and a chopper with a specific frequency to promote photoexcited states in the transparent sample. These excited states are detected by the white light probe. Owing to ultrafast electronics and timing only every second white light probe has been previously pumped. The detector measures the absorption spectra and subtracts the absorption of the ground state from the absorption spectra of the excited state giving ΔA. In TAS, the pump pulse can be in the range of femtoseconds allowing for the detection of fast decay dynamics.[39]

The main spectral features observed in TAS are photo-induced absorption (PIA), stimulated emission (SE) and ground-state bleach (GSB). Figure 2.11 illustrates the different features in TA spectroscopy. For PIA, the probe light is completely transmitted without absorption prior to the pump pulse. After the pump pulse, the absorption spectra shows an increase in intensity. The mathematical subtraction of both leads to an increase in the absorption of light, hence, a positive spectral feature. This is interpreted as the absorption of light originating from excited

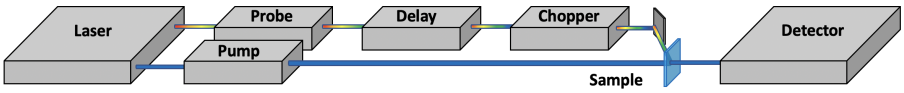

Figure 2.10 – Schematic set-up for a transient absorption spectroscopy measurement. The laser source generates pump and probe pulses. The probe pulses are delayed and sent *via* chopper onto the transparent sample. The white light probe is spatially overlapping with the pump pulse on the sample. The detector records the change in absorption.

states. However, PIA can arise from a combination of signals from several species, *e.g.*, singlets or triplets. To distinguish between the signals, one can exploit the different kinetics of PIA for example by pumping with different intensities. SE is similar to the steady-state PL spectrum. Without an initial pump, the absorbance spectrum remains unchanged. After the pump pulse, excited states can be probed showing radiative emission. Hence, less photons are absorbed and the recorded spectral feature is negative. The probed emission is normally attributed to singlet states S_1. The last feature remaining is the GSB. Without an initial pump, the recorded spectrum resembles the steady-state absorption spectrum. By promoting electrons from the ground states to the excited state, the S_0 is depopulated and absorbs less light than without the pump. The mathematical subtraction of the spectra gives an overall negative feature. Since the GSB can originate from different transitions, it contains information from singlets, triplets or charges. The interpretation of GSB spectral features is therefore not straightforward.[39]

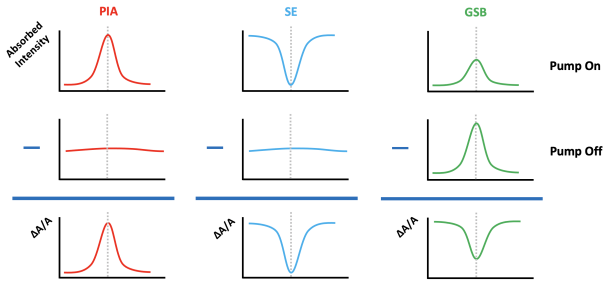

Figure 2.11 – Explanation and illustration of the different spectral features in TA spectroscopy. From left to right: photo-induced absorption (PIA), stimulated emission (SE) and ground-state bleach (GSB).

2.6. Nuclear magnetic resonance spectroscopy

Nuclear magnetic resonance (NMR) is a commonly used standard technique to elucidate the chemical structure of organic compounds. Nuclear-magnetic resonance signals were first discovered by the two independent research groups Bloch and Purcell in 1946 of which both were rewarded the Nobel prize later in 1952. In a nutshell, by applying an external magnetic field, nuclei

exhibiting a spin of $I = 1/2$ such as ^{1}H and ^{13}C show a splitting of their energy levels based on the Zeeman effect $(2I + 1)$. The energy of the Zeeman levels is described by Eq. 2.18:

$$E = -m\gamma\hbar B_0 \tag{2.18}$$

E = Zeeman energy level; γ = gyromagnetic constant; $\hbar$ = reduced Planck constant; B_o = external magnetic field; m = magnetic quantum number

Electromagnetic radiation in the radio frequency range promotes transitions between the Zeeman energy levels by fulfilling the resonance condition:

$$v_1 = \frac{\gamma}{2\pi}\left(1 - \sigma\right) B_o \tag{2.19}$$

v_1 = resonance frequency; σ = deshielding constant.

Eq. 2.19 displays the proportional relation between the measured resonance frequency and the deshielding constant of the respective nuclei, which provides direct information about the electronic and chemical environment in the elucidated structure. [40]

2.7. X-ray photoelectron spectroscopy

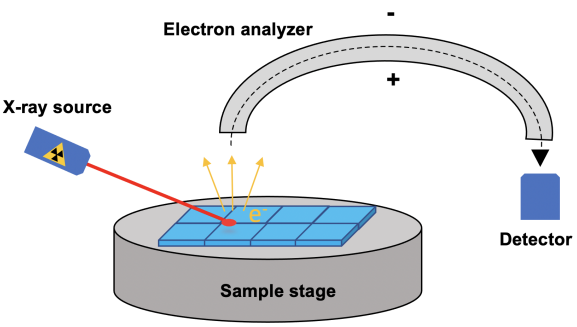

Figure 2.12 – Illustration of the working principle of XPS. Electrons are ejected from the atomic shell of the probed sample by irradiation with X-rays. The released electrons are sorted in an electron analyzer by their kinetic energy and subsequently collected by a detector.

X-ray photoelectron spectroscopy utilizes the release of photoelectrons into vacuum from a sample by the radiation of X-rays from an Al $K_{\alpha 1}$ or Mg $K_{\alpha 1}$ source. The incident X-ray beam upon illumination of the sample surface creates elastically scattered electrons. The electrons are sorted by an electron analyzer and the kinetic energy is measured. From the kinetic energy, the binding energy (BE) of the electron can be calculated giving information about the chemical composition

as well as the chemical environment of the sample. XPS is a very surface sensitive technique since the penetration depth is only 0.5-2 nm. Therefore, and to prevent the energy loss of electrons by scattering, XPS is carried out under ultra-high vacuum (UHV) of about 10^{-9}-10^{-8} Pa.[41] The schematic experimental set-up is depicted in Figure 2.12

XPS is based on the following equation derived by Rutherford in 1914:

$$E_k = h\nu - E_b \tag{2.20}$$

E_k = kinetic energy of the electron; $h\nu$ = energy of the X-ray; E_b = binding energy of the electron.

Pioneering work in this field was performed by Siegbahn and coworkers in 1967, introducing also the term electron spectroscopy for chemical analysis (ESCA).[42] From XPS chemical information can be obtained by measuring the BE values of the recorded electron spectrum. These values can be compared to series of spectra summarized in several publications, *e.g.,* Moulders *et al.*[43] Since the BE of the electrons is probed, XPS allows for studying the electronic core levels of atoms including s, p and d levels with their splitting by spin-orbit coupling. Moreover, the valence state of the respective atoms can be examined due to the fact that a decrease in valence charge (*e.g.,* oxidation) leads to higher BE values and the increase (*e.g.,* reduction) to lower BE values. This can be described by the following formula:[41]

$$\Delta E = k\Delta q + \Delta V \tag{2.21}$$

ΔE = change in BE of a core level; k = factor; Δq = difference in valence charge; ΔV = change in the effective potential.

2.8. Atomic force microscopy

The atomic force microscope (AFM) was first presented by Gerber and coworkers in 1985.[44] AFM provides a 3D topographic image of the sample surface on the nanoscale with a lateral resolution of 0.1-10 nm, by measuring distinct forces, mainly Van-der-Waals and Coulomb forces, between a very sharp tip supported at the end of a flexible cantilever and the sample surface.[45] Depending on the recorded forces and topography, the cantilever undergoes a deflection, which is detected by a laser beam and reflected from the back of the cantilever onto a position sensitive quadrant photodiode detector (see Figure 2.13). In principle, the detector measures the bending of the cantilever in *z*-direction while the tip is screened over the sample in *xy*-direction to generate a pseudo-color image in which each pixel represents an *xy*-position on the sample, and the color displays the recorded signal.[46]

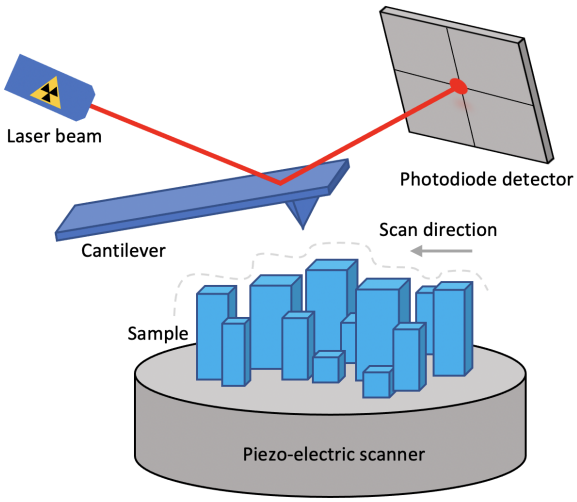

Figure 2.13 – Illustration of the AFM working principle. An incident laser beam is reflected from the back of a cantilever onto a position sensitive quadrant photodiode detector, while the tip is screening the sample in *xy*-position. The sample is placed on a piezo-electric scanner to maintain the adjusted tip-surface distance depending on the imaging mode.[47]

AFM can be used in three different imaging modes depending on the different types of interaction between the sample and surface. In *contact mode,* the tip is in direct contact with the surface measuring the repulsive forces by maintaining a constant bending of the cantilever resulting in a topographic image of the surface. Similar to the *contact mode*, in *tapping mode,* the cantilever oscillates at its resonance frequency and touches slightly on the surface. By adjusting a constant oscillation amplitude, a fixed-tip-sample interaction is maintained and an image of the surface is obtained. In contrast, the *non-contact mode* measures the attractive Van-der-Waals forces by oscillating above the sample with no contact to the surface. The amplitude is maintained constant and the surface topography can be measured.[45]

2.9. ^{57}Fe-Mößbauer spectroscopy

In his PhD thesis the German physicist Rudolf L. Mößbauer discovered in 1958 the resonance phenomena of atomic nuclei.[48,49] For this breakthrough he was rewarded three years later with the Nobel prize. To honor his discovery, the resonance phenomena of nuclei are named Mößbauer effect. The physical basis is the resonant and recoil-free emission and absorption of γ-radiation, which is the underlying principle of the so called ^{57}Fe-Mößbauer spectroscopy.

If an excited nucleus emits a γ-photon, a recoil effect is observed due to momentum conservation.[50,51] The emitted photon energy $E_0 = E_a - E_g$ (E_a = energy in the excited state; E_g =energy

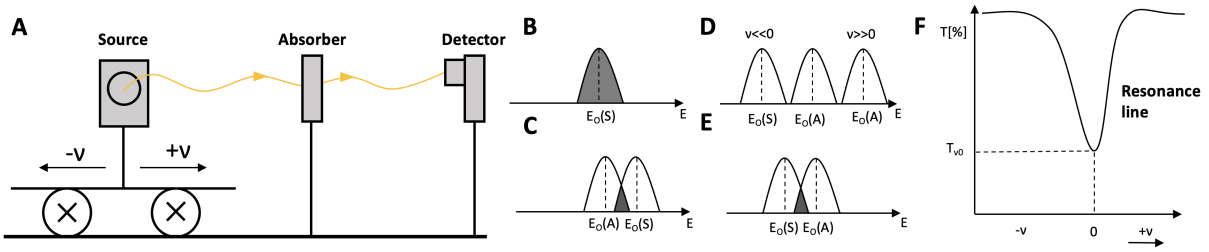

Figure 2.14 – **A** Experimental set-up of a Mößbauer experiment. $E_0(S)$ and $E_0(A)$ transition energy of the emitter and the absorber nuclei, respectively. **B-E** Overlap of the recoil-free absorption and emission at different relative velocities. **B** $v = 0$, **C** $v > 0$, **D** $v < 0$, **E** $v << 0$; $v >> 0$, respectively. **F** Typical Mößbauer plot of relative velocity against relative transmission.[50,51]

in the ground state) is consequently reduced by the amount of the recoil energy $E_y = E_0 - E_R$ (E_R = recoil energy). This difference in energy is also required to excite another nucleus (resonance), therefore, the emission band of the emitter atom and the absorbance band of the absorber atom do not match anymore. Thus, no Mößbauer effect is observed in liquid phases. To achieve recoil-free resonance, one can embed the absorber and the emitter into a solid matrix under reduced temperature to transform the recoil energy into inner energy (phonon vibration) or translational energy. Mößbauer quantified the effect by the following equation:

$$\frac{E_0^2}{2mc^2} = k \cdot \Theta \tag{2.22}$$

E_0 = energy difference between ground an excited state; Θ = Debye temperature; k = Boltzmann-constant.

The experimental set-up of Mößbauer spectroscopy is depicted in Figure 2.14A. The γ-radiation is created in-situ by a ^{57}Co source undergoing K-reduction to an excited ^{57}Fe nuclei. These Mößbauer nuclei relax to the ground state emitting γ-photons. These photons excite the probed atoms in an absorber (typically the same as in the emitter, ^{57}Fe), which also emit photons of the same energy collected by a detector. In a typical experiment, the source is moved relative to the source with a velocity $\pm v$ against the absorber. Using the Doppler effect, the photons, depending on the frequency, exhibit higher or lower energy by addition or subtraction of the momentum. Therefore, one can probe systematically a velocity range (Figure 2.14B, C, D, E) to find the resonance lines of the probed nuclei. The Mößbauer spectrum is plotted as relative velocity on the x-axis versus the relative transmission on the y-axis.

From a Mößbauer spectrum different information can be retrieved, *e.g.,* isomeric shift (δ [mm/sec]; oxidation state), quadrupolar splitting (ΔE_Q [mm/sec]; molecular symmetry) and the magnetic splitting (ΔE_M [mm/sec]; magnetic properties). As an example, the isomeric shift is discussed due to its information concerning the Fe^{II}/Fe^{III} valency in solid matter.[50,51] The energy between

the ground and the excited state of the emitter nuclei is described by E_0. However, since the nucleus is not exactly localized on a point spot but rather as a 3D expansion in space, electrons can within a certain probability be "in" in the nucleus, which is expressed by:

$$r = 0,\ |\psi(0)|^2 \tag{2.23}$$

Therefore, the transition energy of the nucleus E_0 is slightly changed to E_S. Two factors contribute to E_S: the electron density at the nuclei and the space expansion of the nuclei at the ground and the excited state. This can be described by:

$$\Delta E(S) = E_S - E_0 = const \cdot |\psi(0)|_S^2 \cdot (R_a^2 - R_g^2) \tag{2.24}$$

$(R_a^2 - R_g^2)$ = difference between ground an excited state (nuclei factor).

For the absorber nuclei, the following equation is valid:

$$\Delta E(A) = E_A - E_0 = const \cdot |\psi(0)|_A^2 \cdot (R_a^2 - R_g^2) \tag{2.25}$$

If the chemical environment is different between emitter and absorber, this can be measured relatively, giving the equation:

$$\delta = \Delta E(A) - \Delta E(S) = E_A - E_S \tag{2.26}$$

leading to:

$$\delta = const \cdot (|\psi(0)|_A^2 - |\psi(0)|_S^2) \cdot (R_a^2 - R_g^2) \tag{2.27}$$

$const = 2/5\pi Ze^2$ with Z (proton number) and e (element charge).

Consequently, δ offers a sensitive probe for the oxidation state since a change in the electron shell also effects the electron density of the nuclei. Iron^{II} owns the electron configuration [Ar]3d^6 where the 4s electrons are given away to the bonding partner. If this iron ion undergoes further oxidation, 3d electrons removed, hence, 3s electrons are moving closer to the nucleus. The nucleus factor $(R_a^2 - R_g^2)$ features for ^{57}Fe a negative sign, consequently, an increasing electron density at the nucleus leads to a negative isomeric shift. Therefore, Fe^{VI} ions are at the far negative end of the scale while Fe^{II} compounds show more positive isomeric shift (Figure 2.15). By this shift the oxidation state of iron ions can effectively be probed.

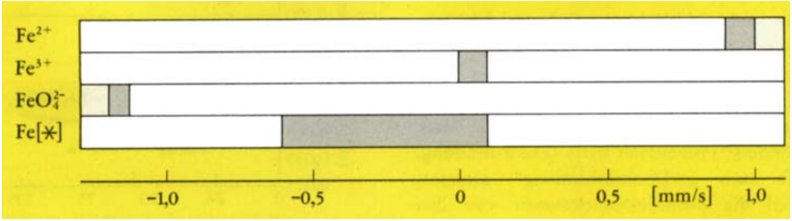

Figure 2.15 – Isomeric shift as function of the oxidation state of different ^{57}Fe compounds.[52]

2.10. Electron paramagnetic resonance spectroscopy

Electron-spin resonance (EPR) spectroscopy is a method for detecting unpaired electrons in a probed sample providing insights into the magnetic structure of the material.[53] The effect was first discovered by Zavoisky *et al.* in 1945.[54] Similar to NMR spectroscopy, every electron owns a spin moment $s = 1/2$ with the magnetic components $m_s = \pm 1/2$. Therefore, in the presence of an external magnetic field B_0, the electron spin can either be parallel or anti-parallel aligned to the field. The specific energy between the splitting is based on the Zeman effect:

$$E = m_s g_e \mu_B B_0 \tag{2.28}$$

m_s = magnetic component; g_e = Lande factor; μ_B = Bohr magneton; B_0 = external magnetic field.

Therefore, the energy between the levels is described by:

$$\Delta E = g_e \mu_B B_0 \tag{2.29}$$

In a continuous-wave (CW) EPR experiment, the unpaired electrons of the probed sample can be excited to the higher energetic states by absorbing a photon matching the energy transition ΔE. The atom is typically irradiated by a fixed microwave frequency (X-Band = 10 GHz). Thus, the equation becomes:

$$h\nu = g_e \mu_B B_0 \tag{2.30}$$

Then, the magnetic field is systematically scanned, *e.g.,* from 100-800 mT. The obtained absorbance spectrum is normally displayed as the first derivative. The spectral interpretation of EPR data is not straightforward, an extended simulation is required to gain insights into the spin-dynamics.

2.11. Physisorption analysis

Surface area as well as sorption and desorption behavior of porous solids can be described by the BET (Brunauer-Emmett-Teller) equation 2.31:

$$\frac{n^a}{n_m^a} = \frac{C \cdot p/p_0}{(1 - p/p_0) \cdot [1 + (C - 1)p/p_0]} \tag{2.31}$$

n^a = amount adsorbed per gram adsorbent; n_m^a = monolayer capacity; C = BET constant; p/p^0 = relative pressure.

The BET equation was introduced in 1938 by Brunauer, Emmett and Teller to give access to the monolayer capacity and the surface area of porous materials.[55] The BET equation is used in the linear form in order to obtain the parameters C and n_m^a (monolayer capacity).

$$\frac{p}{n^a \cdot (p - p_0)} = \frac{C - 1}{n_m^a \cdot C}\frac{p}{p_0} + \frac{1}{n_m^a \cdot C} \tag{2.32}$$

According to the linear BET equation 2.32, C and the monolayer capacity can be obtained by plotting $\frac{p}{n^a \cdot (p - p_0)}$ against $\frac{p}{p_0}$. Here, the constant C indicates the magnitude of the adsorbent-adsorbate interaction energy giving information about the shape of the isotherm in the BET range. When C is about ∼80 (see Figure 2.16), the "knee" of the isotherm is well-defined and the point B, which indicates the completion of the first monolayer and start of the multilayer adsorption, can be identified. If C is lower than ∼50, the "knee" of the isotherm is hardly visible and point B cannot be isolated concluding that the value n_m^a might not be reasonable. A high C (∼150) is related to the filling of narrow pore cavities or high-energy surface sites. Furthermore, the BET-equation in the linear form requires a range of linearity (0.05 <p/p_0> 0.3). In the region near the complete monolayer adsorption (point B) the theory and the gas adsorption experiment agree well. Only in this case the true value of n_m can be calculated.[56]

In general, the BET-theory is based on certain assumptions:[57]

- Multilayer adsorption
- The first layer is based on the *Langmuir adsorption* (monolayer adsorption)
  - The surface is energetically uniform
  - No interactions between the adsorbed species occur
- Second and further layers: condensation of gas into liquid phase

Due to the fact that the BET-theory is based on the above mentioned assumptions, the theory also has its limitations:[57]

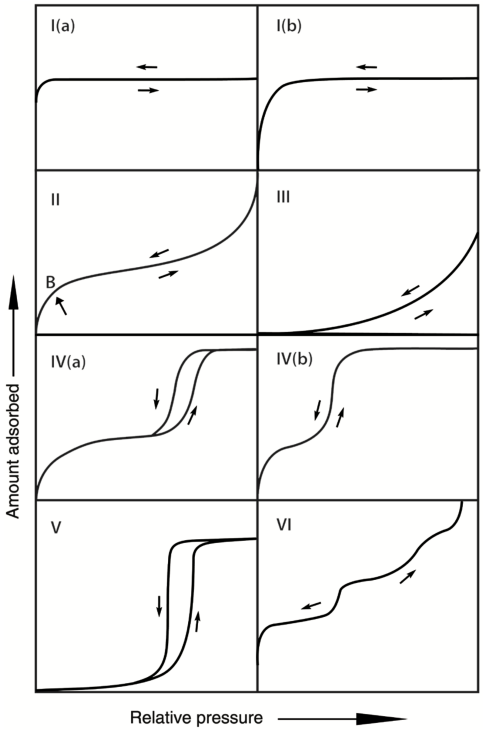

Figure 2.16 – Classification of the isotherms according to IUPAC.[56]

- The BET-theory ignores that the surface of the structure is not homogenous and also lateral adsorbate-adsorbate interactions can occur
  - High energy sites will be occupied at lower relative pressures, which is the reason for the nonlinearity of BET-plots at $p\,p_0^{-1} < 0.05$
- Polarization forces lead to a higher heat of adsorption in the second layer than in the third and so forth
  - which is the reason for the nonlinearity of the BET-equation at $p\,p_0^{-1} > 0.3$
  - It is difficult to distinguish between mono-multilayer adsorption and a micropore-filling mechanism
  - The measurement of the surface area does not reflect the *real* surface, but a *characteristic* BET surface area

The following isotherms are distinguished according to IUPAC:[58]

- *Type I* isotherms are also denoted as *Langmuir isotherms*. They are characteristic for microporous solids, where the adsorption (*micropore filling*) saturates after pore filling is complete. *Type I(a)* isotherms are found for microporous materials exhibiting mainly

narrow micropores ($\sim < 1\,\text{nm}$), while *I(b)* is given by microporous materials with a broader pore size distribution including wider micropores or narrow mesopores ($\sim < 2.5\,\text{nm}$)

- *Type II* isotherms are obtained by nonporous or macroporous adsorbents. They display unrestricted monolayer-multilayer adsorption.
- *Type III* isotherms are given by nonporous or macroporous materials with weak interactions between the adsorbent and the adsorbate.
- *Type IV* isotherms are given by mesoporous materials and show the feature of *capillary condensation*. In the case of *type IV(a)* isotherms, capillary condensation is accompanied by hysteresis. *IV(b)* isotherms are given by mesoporous materials having mesopores of smaller width leading to completely reversible adsorption and desorption.
- *Type V* isotherms correspond to rather weak adsorptive-adsorbent interactions of the mesoporous solids.
- *Type VI* isotherms exhibit a stepwise multilayer adsorption on a uniform non-porous surface. The step-height indicates the monolayer capacity for each layer.

As discussed above, the obtained isotherms were classified into six groups (I-VI) according to their porosity and sorption behavior as well as the interaction between the adsorbent and the adsorptive (see Figure 2.16).[56]

2.12. Thermogravimetric analysis

Thermogravimetric analysis (TGA) is a technique in which the mass of a substance is monitored as a function of temperature or time as the sample specimen is subjected to a temperature program in a controlled atmosphere.[59] The shape of the measured TGA trace allows the analysis of the temperature-dependent mass changes, such as the outgassing of water or solvents and condensation or decomposition of the investigated material. In a TGA measurement, the sample is placed in a pan that is combined with a precision balance. The pan is situated in a furnace and is heated with a linear heating rate under the desired atmosphere (*e.g.,* N_2), for example up to 900°C, while the balance detects the mass loss over time.

2.13. Electrical conductivity measurements

2.13.1. Four-point probe resistance measurement

The van der Pauw technique is a widely and commonly used method developed by Leo J. van der Pauw in 1958 to access properties of 2D materials: the resistivity, doping type, sheet carrier

density of the majority carrier as well as the mobility of the majority carrier.[60,61] The sample has to fulfill five requirements to utilize this technique:

- uniform sample thickness
- no isolating holes
- homogenous surface coverage
- the contact nodes have to be positioned on the edges of the sample
- area of contact of any individual contact should be at least an order of magnitude smaller than the area of the entire sample

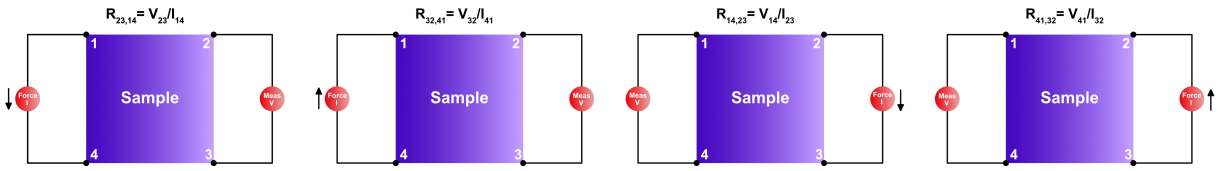

Figure 2.17 – Illustration of the Van der Pauw method. Four probes are connected to the edges of the sample in equal distance. By applying a current between two neighboring nodes the voltage drops across the opposite nodes. The image displays the measurement of $R_{vertical}$.

Figure 2.17 depicts the principle of the van der Pauw method. The set-up employs four nodes acting as ohmic contacts connected to the boundaries of an arbitrary flat sample. To perform a measurement, a current is applied across one sample edge (see Figure 2.17, for instance I_{14}) and the corresponding voltage across the opposite edge is measured (V_{23}). By using the ohmic law the resistance can be calculated.

$$R_{23,14} = \frac{V_{23}}{I_{14}} \tag{2.33}$$

A more precise measurement can be obtained by applying the reversed polarity method by repeating the resistance measurements after switching polarities of both the current source and the voltage meter. Hereby, eight measurements are conducted to obtain the averaged $R_{vertical}$ and $R_{horizontal}$ (Figure 2.17 illustrates the measurements for obtaining $R_{vertical}$). The advantage of this particular method is that any offset voltages, *e.g.,* thermoelectric potentials due to the *Seebeck effect* as well as resistance issues arising from contacting the sample, will be cancelled out.

$R_{vertical}$ and $R_{horizontal}$ are given by the following equations:

$$R_{vertical} = \frac{R_{12,34} + R_{21,43} + R_{34,12} + R_{43,21}}{4} \tag{2.34}$$

$$R_{horizontal} = \frac{R_{23,41} + R_{32,14} + R_{41,23} + R_{14,32}}{4} \tag{2.35}$$

The sheet resistance R_S can be expressed as:

$$R_S = \rho \cdot d \tag{2.36}$$

ρ = specific resistance; d = film thickness

and can be calculated by the van der Pauw equation:

$$e^{-\pi R_{vertical}/R_S} + e^{-\pi R_{horizontal}/R_S} = 1 \tag{2.37}$$

Since the Van der Pauw equation can only be solved numerically, Eq. 2.37 is transformed to:

$$\rho = \frac{\pi d}{\ln(2)} \frac{R_{horizontal} + R_{vertical}}{2} f\left(\frac{R_{horizontal}}{R_{vertical}}\right) \tag{2.38}$$

$f\left(\frac{R_{horizontal}}{R_{vertical}}\right)$ = van der Pauw factor

Finally, Eq. 2.38 can be rearranged to yield the electrical conductivity of the sample:

$$\sigma = \frac{\ln(2)}{\pi d} \frac{2}{(R_{horizontal} + R_{vertical})\, f\left(\frac{R_{horizontal}}{R_{vertical}}\right)} \tag{2.39}$$

2.13.2. Two-point probe resistance measurement

$$\sigma = \frac{I}{V} \times \frac{L}{W \cdot T} \tag{2.40}$$

L = probe distance; I = current range; V = voltage range; W = width of the contact; T = sample thickness.

Alternatively to the van der Pauw method, $I - V$ curves can be obtained by two-point probe methods and the resistance can be calculated by eq. 2.40.[62] In contrast to four-probe methods, the sum of resistances of the material and the probe contacts is measured. Hence, two-point probe measurements often suffer from contacting issues.

2.14. Contact-angle measurements

The process of wetting, the interaction of water with a surface, is one of the most important phenomena in everyday life. From the self-cleaning mechanism of plants (Lotus effect) over the

Namib desert beetle collecting water from humidity-rich air to technological advances in titanium implants, printing processes or antimicrobial properties of coatings.[63–66] In order to tailor the materials surface characteristics one needs to study first the fundamental property of surface wetting. This is done by performing contact-angle measurements.

2.14.1. Theory - surface wetting models

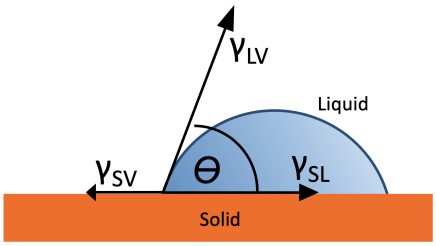

Figure 2.18 – Illustration of the Young contact angle. A droplet is wetting an ideal solid surface in equilibrium (Young state). The Young contact angle Θ is measured between the solid-liquid γ_{SL}, solid-vapor γ_{SV} and the liquid-vapor interfacial surface tension γ_{LV}.

Wetting is described by the contact angle, which is defined as the angle between the liquid-vapor interface and the solid-liquid at the three-phase contact point (see Figure 2.18). The contact is normally measured from the liquid-air interface. The first description of the contact angle was given in 1805 by the Young equation:[67]

$$\cos\Theta = \frac{\gamma_{SV} - \gamma_{SL}}{\gamma_{LV}} \tag{2.41}$$

Θ = Young contact angle; γ_{SV} = solid-vapor interfacial tension; γ_{SL} = solid-liquid interfacial tension; γ_{LV} = surface tension of the liquid.

The Young equation treats the surface as ideal solid surface being chemically homogenous and non-reactive. According to the Young equation, surfaces with high surface energy exhibit low contact angles, while surfaces with low surface energy show high contact angles. Solid surfaces with water contact angles under 90° are classified as hydrophilic, above 90° as hydrophobic. Moving to the realm of extreme wetting properties, surfaces exhibiting contact angles under 10° or above 150° are denoted as superhydrophlic or superhydrophobic, respectively.[69] Surface properties are either based on the chemical composition of the material or related to its surface texture. Wenzel set in 1936 the contact angle in relation to the fine structuring of its surface:

$$\cos\Theta_W = r \cdot \cos\Theta \tag{2.42}$$

Θ_W = Wenzel contact angle - apparent contact angle; r = roughness ratio - ratio of true to apparent surface area; Θ = Young contact angle.

According to the Wenzel equation the contact angle increases if the roughness of the surface is increased. A more detailed view on heterogenous surfaces is given by the Cassie-Baxter model:[68]

$$\cos\Theta_{CB} = r_F \cdot f \cdot \cos(\Theta_\Gamma) + f - 1 \tag{2.43}$$

$\Theta_C B$ = Cassie-Baxter contact angle - apparent contact angle; r_F = roughness ratio of the wetted surface area; f = fraction of the solid wetted.

A visualization of the different contact angles is given in Figure 2.19

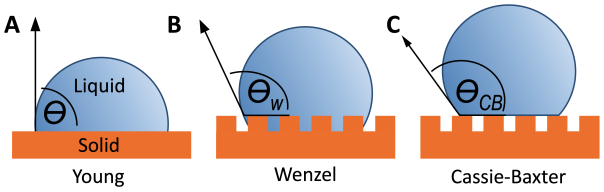

Figure 2.19 – Schematic depiction of different surface wetting models for non- and textured solid surfaces. From left to right: Young, Wenzel and Cassie-Baxter.

2.14.2. Experimental methods

Contact angles are measured by using a goniometer set-up as shown in Figure 2.20. A droplet of liquid is placed by a syringe onto an adjustable sample stage. The droplet is illuminated from the back by a light source while a camera is capturing images of the droplet positioning process. By subjecting the images to an analysis software, different fitting procedures are applied to extract the contact angle of the droplet curvature. This method is denoted as sessile drop technique. Taking a high-speed camera, the wetting dynamics of the wetting process can be studied. However, the results from this "static" contact angle can sometimes be misleading since the droplet might not be in the global energy minimum and therefore in the stable state corresponding to the Young state.[70] To get more accurate data, an alternative would be the measurement of the advancing and the receding contact angle (ACA and RCA), which resemble the highest and the lowest contact angle in the hysteresis range, as function of the droplet volume. Unfortunately, this technique is usually not integrated in commercial goniometers.

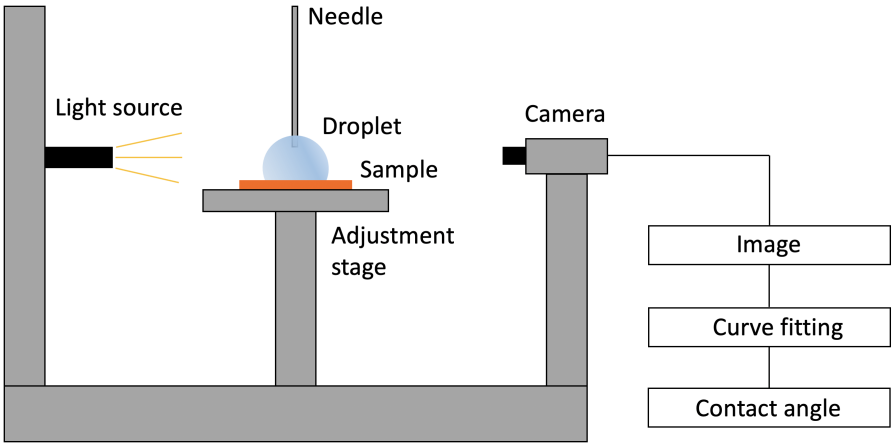

Figure 2.20 – Illustration of a goniometer set-up for contact angle measurements. The set-up is composed of a light source, a needle containing the liquid, sample stage, camera and the computer for data evaluation.

The profile and the curvature of the droplet are determined by different fitting procedures. The best-established procedure is the Young-Laplace method, also referred to as axisymmetric drop-shape analysis (ADSA).[71] The method is based on the Young-Laplace equation and is the only fitting procedure on a physical basis:

$$\Delta p = \gamma \left(\frac{1}{R_1} - \frac{1}{R_2} \right) \tag{2.44}$$

Δp = Laplace pressure; γ =surface tension; R_1 R_2 = principal radii of curvature.

Here, a rotational axis normal to the solid surface is set and therefore, the solid-liquid-air interface can be treated as circular. The surface tension is taken as a free adjustable parameter in the fitting procedure. However, since the Young-Laplace method is based on axisymmetric drop shapes, it will produce difficulties for non-axisymmetric curvatures as they can appear in very hydrophilic or hydrophobic surfaces.

2.15. ICP spectroscopy

Inductively coupled plasma atomic emission spectroscopy is an efficient method for the qualitative and quantitative analysis of chemical elements. Here, the sample is dissolved in a liquid and injected *via* a nebulizer into a plasma flame. The plasma is produced by the interaction of radio frequency of 27 or 41 MHz with argon flushing over a copper induction coil within a quartz tube. Thus, a stable plasma with temperatures of about 10,000 K is created.[72] This plasma is used to excite atoms in order to produce emission of characteristic radiation. After ionization a

spectrometer analyzes the characteristic emission from the respective elements. The measured intensities can be referenced to previously measured standards, thus, the concentration of the probed elements can be determined.[73]

2.16. Cyclic voltammetry

Cyclic voltammetry is a measurement technique to study electrochemical processes in and at electrodes. The method uses a standard three-electrode set-up comprising a working (probed material), a counter and a reference electrode placed in an electrochemical cell. The cell contains an electrolyte solution and the electrodes are connected to a potentiostat with computer interface for the data evaluation. With this experimental set-up various electrochemical experiments can be conducted. Typically, the potential is varied in a defined range and the resulting current is recorded. By changing different parameters such as the scan speed, scan direction or step-size the oxidation as well as reduction processes in the electrochemical cell can be studied. CV measurements can be employed to retrieve a wide range of information, *e.g.,* capacitance, cycle stability, photocurrent or reversibility of redox processes. However, for organic semiconducting materials, the determination of the HOMO energy level is of special interest, since the LUMO level can be easily accessed by simply adding the optical band gap obtained from UV-VIS absorption measurements to the electrochemically estimated HOMO level. Knowledge about the HOMO and LUMO levels enable the integration of organic semiconductors into several devices where defined energy alignment is required, *e.g.,* solar cells, transistors or hole-only devices.

Cycling voltammetry of organic semiconductors estimates the HOMO level by measuring the first oxidation process in the scan. The energy which is required to extract electrons from this electronic state is E_{ox}. Ferrocene is used to reference the oxidation signal (ferrocene E_{ox} = -4.4 eV). Therefore, the HOMO level can be calculated using the following equation:[74,75]

$$E(HOMO) = -e[E_{ox}^{onset} + 4.4] \tag{2.45}$$

References

[1] Spiess, L., Teichert, G., Schwarzer, R., Behnken, H., Genzel, C. **2019.** *Moderne Röntgenbeugung: Röntgendiffraktometrie für Materialwissenschaftler, Physiker und Chemiker.* Springer-Verlag. Volume series: 3., ISBN: 3834882321.

[2] Röntgen W. C. *Sitzungsberichte der Würzburger Physik.-medic. Gesellschaft. Würzburg,* **1896,**1, 1-9.

[3] Friedrich, W., Knipping, P., Laue, M. *Ann. Phys.* **1913,** 346, 971-988.

[4] Bragg, W., Bragg, W. *Nature* **1913,** 91, 557.

[5] Bragg, W., Bragg, W. *Proc. R. Soc. Lond. A* **1913,** 88, 428-438.

[6] Lilienfeld, J. E., Verfahren zur Erzeugung von Röntgenstrahlen beliebig einstellbaren Härtegrades unabhängig vom Vakkum. Application date: 10.10.1911. DE. Application number: DE 256 534.

[7] Dushman, S. *Phys. Rev.* **1923,** 21, 623.

[8] Siegbahn, M. *Nature* **1916,** 96, 676.

[9] Deslattes, R. D., Kessler, E. G. Jr., IndelicatoP., de Billy, L., Lindroth, E., Anton, J., Coursey J.S., Schwab, D.J., Chang, C., Sukumar, R., Olsen, K., and Dragoset, R.A., X-ray Transition Energies (version 1.2). **2005** *National Institute of Standards and Technology, Gaithersburg.*
[10] Brentano, J., *Proc. Phys. Soc. London* **1924,** 37, 184.
[11] Debye, P., Scherrer, P. *Nachr. Ges. Wiss. Göttingen* **1916,** 1-26.
[12] Pecharsky, V., Zavalij, P.. **2008.** Fundamentals of Powder Diffraction and Structural Characterization of Materials. Springer Science & Business Media. Volume series: 2., ISBN: 0387095780.
[13] Scherrer, P. *Nachr. Ges. Wiss. Göttingen* **1918,** 1-3.
[14] Pawley, G. S., *J. Appl. Cryst.* **1981,** 14, 357-361.
[15] Rietveld, H. M., *J. Appl. Cryst.* **1969,** 2, 65-71.
[16] Ezquerra, T., Garcia-Gutierrez, M. Nogales, A. Gomez, M. **2009.** *Applications of Synchrotron Light to Scattering and Diffraction in Materials and Life Sciences.* Springer-Verlag: Heidelberg, Volume series: 1.,. ISBN: 978-3-540-95967-0.
[17] Levine, J., Cohen J., Chung, Y., Georgopoulos, P. *J. Appl. Cryst.* **1989,** 22, 528-532.
[18] Smilgies, D. **2017** *GISAXS - grazing-incidence small-angle scattering. The SAXS Guide.* Graz: Anton Paar, Volume series: 4.
[19] Müller-Buschbaum, P. *Anal. Bioanal. Chem.* **2003,** 376, 3-10.
[20] Stamm, M. **2008.** *Polymer Surfaces and Interfaces: Characterization, Modification and Applications.* Springer Berlin Heidelberg: Berlin, Heidelberg, Volume series: 1., ISBN: 978-3-540-73864-0.
[21] Yoneda, Y. *Phys. Rev.* **1963,** 131, 2010-2013.
[22] Ruska, E. *Zeitschrift für Physik* **1932,** 78, 318-339.
[23] Siemens & Halske Aktiengesellschaft, Berlin und München. *Elektronenmikroskop.* Inventor: Ruska, E., Schuchmann, H. Application date: 18.01.1939. DE. Application number: S 0007474.
[24] Michler, G. H. **2019** *Kompakte Einführung in die Elektronenmikroskopie: Techniken, Stand, Anwendungen, Perspektiven.* Springer Spektrum. Volume series: 1., ISBN: 978-3-658-26687-5.
[25] Bandyopadhyay, A., Bose, S. **2013** *Characterization of Biomaterials*; Elsevier Science: Amsterdam, Volume series: 1., ISBN: 9781493301379.
[26] Egerton, R. F. **2005** *Physical principles of electron microscopy. An introduction to TEM, SEM and AEM.* Springer Verlag. Volume series: 1., ISBN: 0-387-25800-0.
[27] Rowan-Robinson, M. **2013 Night Vision: Exploring the Infrared Universe.** Cambridge University Press. Volume series: 1.„ ISBN: 9781139176019.
[28] Coblentz, William W. **1905** *Investigations of Infra-Red Spectra.* Washington, D.C., Carnegie institution of Washington. Volume series: 1.
[29] Lord Rayleigh, O. M. *Phil. Mag.* **1912,** 24, 864.
[30] Naumer, H. Heller, W. **2005** *Untersuchungsmethoden in der Chemie.* Wiley, Volume series: 3., ISBN: 3527308636.
[31] Beckmann, A. O. "Announcing an Important New Beckman Development THE BECKMAN Spectrophotometer". **1941**. News Edition of the American Chemical Society. American Chemical Society.
[32] Thackray, Arnold; Myers, Jr., Minor **2000**. *Arnold O. Beckman: one hundred years of excellence. Philadelphia, Pa.: Chemical Heritage Foundation.* Volume series: 1., ISBN 978-0-941901-23-9.
[33] Tauc, J., Grigorovici, R., Vancu, *A. Mater. Res. Bull.* **1968,** 3, 37-46.
[34] Tumuluri, A., Lakshun Naidu, K., James Raju, K. *Int. J. ChemTech. Res.* **2014,** 6, 3353.
[35] *A practical guide to time-resolved luminescence lifetime determination using dedicated Time-Correlated Single-Photon Counting systems*, HORIBA Jobin Yvon IBH Ltd, Glasgow, Scotland, UK.
[36] Valeur, B. **2001** *New Trends in Fluorescence Spectroscopy: Applications to Chemical and Life Sciences.* Springer Verlag, Series Volume: 1., ISBN: 978-3-642-56853-4.
[37] Jablonski, A. *Nature* **1933** 131, 839-840.
[38] Wahl, W. *Time-Correlated Single Photon Counting, Technical Note.* PicoQuant GmbH, Rudower Chaussee 29, 12489 Berlin, Germany, info@picoquant.com.
[39] Berera, R., van Grondelle, R., Kennis, J.T.M. *Photosynth Res* **2009,** 101, 105-118.
[40] Friebolin, H. **2013** Ein- und zweidimensionale NMR-Spektroskopie: Eine Einführung; Wiley: Weinheim, Volume series: 5., ISBN: 9783527334926.
[41] Oswald S. **2013** *Encyclopedia of Analytical Chemistry* John Wiley & Sons, Ltd. ISBN: 9780470027318.
[42] Siegbahn K., Nordling C., Fahlmann A., Nordberg R., Hamrin K., Hedman J., Johansson G., Bergmark T., Karlsson S.- E. , Lindgren I., Lindberg B., *Nova Acta Regiae Soc. Sci. Upsaliensis* **1967,** 4, 20.
[43] Moulder J. F., Stickle W. F., Sobol P. E., Bomben K. D., **1995** *Handbook of X-ray Photoelectron Spectroscopy.* Physical Electronics Inc., Eden Prairie, MN, ISBN: 9780962702624.
[44] Binnig, G., Quate, C. F., Gerber, Ch.*Phys. Rev. Lett.* **1986,** 56, 930.
[45] Colton, R. **1998** *Procedures in Scanning Probe Microscopies*; Wiley: New Jersey, Volume series: 1., ISBN: 9780471959120.
[46] Binnig, G., Quate, C. F., Gerber, C. *Phys. Rev. Lett.* **1986,** 56, 930-933.
[47] Maver, U., Maver, T.; Persin, Z.; Mozetic, M.; Vesel, A.; Gaberscek, M.; Stana-Kleinschek, K. **2013** *Polymer Science* IntechOpen. Volume series: 1., ISBN: 978-953-51-0941-9.
[48] Gütlich, P. **1970,** *Physikalische Methoden in der Chemie: Mößbauer-Spektroskopie I.* Chemie in unserer Zeit, 4, 133-144.
[49] Gütlich, P. **1971,** *Physikalische Methoden in der Chemie: Mö ßbauer-Spektroskopie II.* Chemie in unserer Zeit, 5, 131-141.
[50] Mößbauer, R. L. *Z. Physik* **1958,** 151, 124.
[51] Mößbauer, R. L. *Naturwissenschaften* **1958,** 45, 538.
[52] Fluck, E., Kerler, W., Neuwirth, W. *Angew. Chem.* **1963,** 75, 461, 461-472.
[53] Roessler, M. M., Salvadori E. *Chem. Soc. Rev.* **2018,** 47, 2534.
[54] Zavoisky E. *Spin-magnetic resonance in paramagnetics.* **1945** 9, 211-245.
[55] Brunauer, S. P., Emmett, H., Teller, E. *J. Am. Chem. Soc.* **1938,** 60, 309-319.
[56] Sing, K. S. W., Everett, D. H., Haul, R. A. W., Moscou, L., Pierotti, R. A., Rouquerol, J., Siemieniewska, T. **2008** *Reporting Physisorption Data for Gas/Solid Systems* In Handbook of Heterogeneous Catalysis. Wiley-VCH Verlag GmbH & Co. KGaA. ISBN: 9783527312412
[57] Lecture notes of A. Trunschke, Surface area and pore size determination, Fritz-Haber-Institut der Max-Planck-Gesellschaft 2007.
[58] Matthias, T., Katsumi, K., V., N. A., P., O. J., Francisco, R.-R., Jean, R., W., S. K. S. *Pure Appl. Chem.* **2015,** 87, 1051.
[59] PerkinElmer, *Thermogravimetric Analysis (TGA) - A Beginner's Guide*; Waltham, MA, 2010.

[60] van der Pauw, L. *J. Philips Tech. Rev.* **1958,** 20, 220-224.
[61] van der Pauw, L. *J. Philips Res. Repts.* **1958,** 13, 1-9.
[62] Sun, L., Campbell, M. G., Dinca, M., *Angew. Chem. Int. Ed.* **2016,** 55, 3566.
[63] Barthlott, W., Neinhuis, C. *Planta* **1997,** 202, 1-8.
[64] Parker, A. R. & Lawrence, C. R. *Nature* **2001** 414, 33-34.
[65] Zhao, G. *J. Biomed. Mater. Res. Part A* **2005,** 74, 49-58.
[66] Tian, D., Song, Y., Jiang, L. *Chem. Soc. Rev.* **2013** 42, 5184-5209.
[67] Young, T. *Philos. Trans. R. Soc. Lond.* **1805,** 95, 65-87.
[68] Cassie, A. B. D., Baxter, S. *Trans. Faraday Soc.* **1944,** 40, 546-551.
[69] Drelich, J., Chibowski E., Desheng, Meng D., Terpilowski, K. *Soft Matter* **2011,** 7, 9804-9828.
[70] Huhtamäki, T., Tian X., Korhonen, J.T. *et al. Nat Protoc* **2018,** 13, 1521-1538.
[71] Hoorfar, M. Neumann, A. W. *Adv. Colloid Interface Sci.* **2006,** 121, 25-49.
[72] Uden, P. C. **1992** *Element-Specific Chromatographic Detection by Atomic Emission Spectroscopy*, ACS Symposium Series, American Chemical Society: Washington, DC.
[73] Skoog, D. A., Leary, J. J. **1996** *Instrumentelle Analytik.* Springer, Berlin, ISBN 3-540-60450-2.
[74] Leonat, L., Sbarcea, G., Branzoi, I. C. *Sci. Bull.* **2013,** 75, 3.
[75] Bredas, J. L., Silbey, R., Boudreux, D. S., Chance, R. R., *J. Am. Chem. Soc.* **1983,**105, 6555.

3. Oriented thin films of electroactive triphenylene catecholate-based two-dimensional metal-organic frameworks

This chapter is based on the following publication:

Andre Mähringer[†,§], Andreas C. Jakowetz[†,§], Julian M. Rotter[†,§], Bernhard J. Bohn[‡,§], Jacek K. Stolarczyk[‡,§], Jochen Feldmann[‡,§], Thomas Bein[*,†,§], and Dana D. Medina[*,†,§], ACS Nano **2019**, *13*, 6711-6719.

[†]Department of Chemistry, Ludwig-Maximilians-Universität (LMU), Butenandtstr. 11 (E), 81377 Munich, Germany.

[‡]Chair for Photonics and Optoelectronics, Nano-Institute Munich, Department of Physics, Ludwig-Maximilians-Universität (LMU), Königinstr. 10, 80539 Munich, Germany.

[§]Nanosystems Initiative Munich (NIM) and Center for NanoScience (CeNS), Schellingstr. 4, 80799 Munich, Germany.

*Corresponding Author

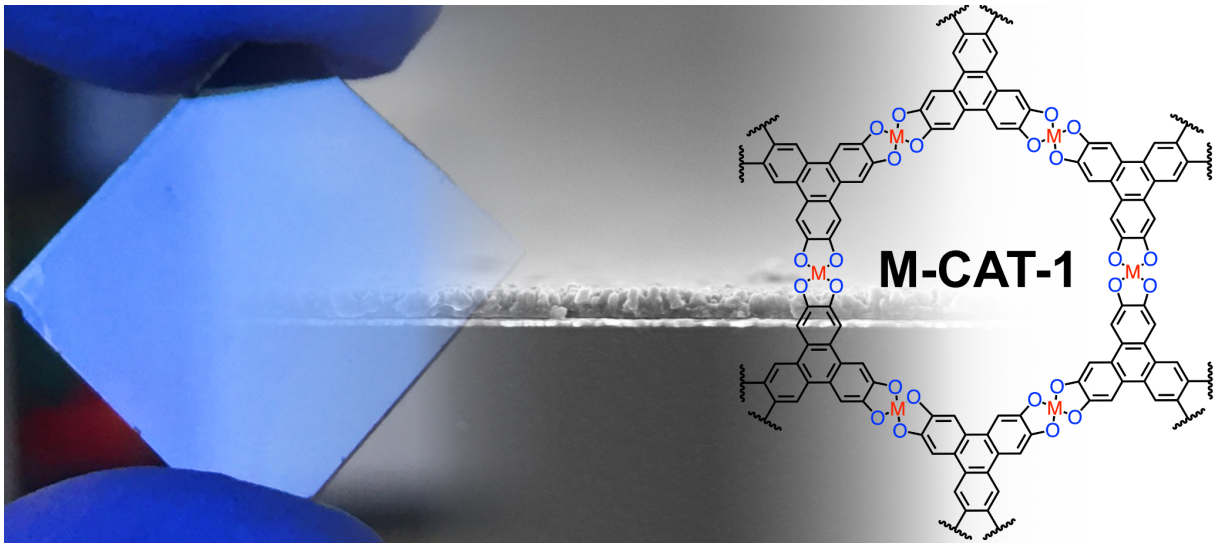

DOI: 10.1021/acsnano.9b01137.

Abstract

Two-dimensional triphenylene-based metal-organic frameworks (TP-MOFs) attract significant scientific interest due to their long-range order combined with significant electrical conductivity. The deposition of these structures as oriented films is expected to promote their incorporation into diverse optoelectronic devices. However, to date, a controlled deposition strategy applicable for the different members of this MOF family has not been reported yet. Herein, we present the synthesis of highly oriented thin films of TP-MOFs by vapor-assisted conversion (VAC). We targeted the M-CAT-1 series comprising hexahydroxytriphenylene organic ligands and metal-ions such as Ni^{2+}, Co^{2+}, and Cu^{2+}. These planar organic building blocks are connected in-plane to the metal-ions through a square planar node forming extended sheets which undergo self-organization into defined stacks. Highly oriented thin Ni- and Co-CAT-1 films grown on gold substrates feature a high surface coverage with a uniform film topography and thickness ranging from 180 to 200 nm. The inclusion of acid modulators in the synthesis enabled the growth of films with a preferred orientation on quartz and on conductive substrates such as indium-doped tin oxide (ITO). The van der Pauw measurements performed across the M-CAT-1 films revealed high electrical conductivity values of up to $10^{-3}\,S\,cm^{-1}$ for both the Ni- and Co-CAT-1 films. Films grown on quartz allowed for a detailed photophysical characterization by means of UV-vis, photoluminescence, and transient absorption spectroscopy. The latter revealed the existence of excited states on a nanosecond time scale, sufficiently long to demonstrate a photoinduced charge generation and extraction in Ni-CAT-1 films. This was achieved by fabricating a basic photovoltaic device with an ITO/Ni-CAT-1/Al architecture, thus establishing this MOF as a photoactive material. Our results point to the intriguing capabilities of these conductive M-CAT-1 materials and an additional scope of applications as photoabsorbers enabled through VAC thin-film synthesis.

3.1. Introduction

Metal-organic frameworks (MOFs) are a prominent class of porous materials well-known for their ultrahigh surface area and crystalline nature.[1–4] In recent years, the intrinsic property of electrical conductivity was added to this portfolio of properties, hence expanding the scope of possible applications for these well-defined structures.[5–7] An emerging type of electroactive MOF is based on the formation of extended molecular sheets with defined voids by employing planar ligands of distinct symmetries, which are interconnected in-plane by metal ions.[8–15] These extended sheets are packed in a graphite-like manner *via* dispersive forces yielding well-defined microporous channels oriented perpendicular to the sheets. This class of materials can be

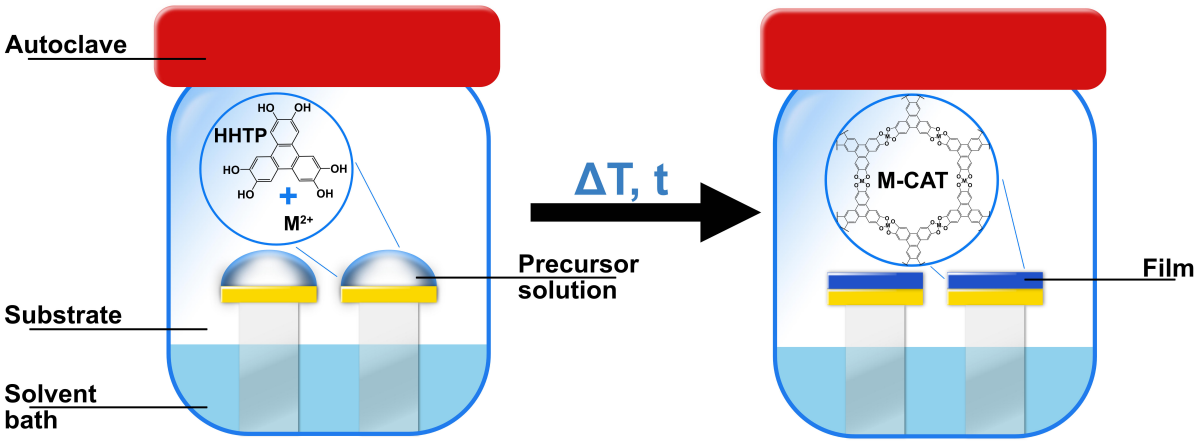

Figure 3.1 – Scheme of the VAC setup, in which the substrates are placed on top of the glass spacers above the solvent bath in a reaction vessel. A liquid layer containing the organic linker (HHTP), inorganic precursor (M^{2+} = Ni^{2+}, Co^{2+}, or Cu^{2+}), and further additives such as modulators is deposited onto the substrate. The tightly sealed vessel is then placed in a preheated oven for the adjusted time. During the reaction, the liquid precursor layer is converted into a thin solid film covering the whole surface.

referred to as a two-dimensional (2D) MOF featuring a layered structure.[16–20] One prominent group of such MOFs consists of the triphenylene motif, which can be chemically modified either with hydroxyl-, amino-, or thiol ligating groups. MOFs based on the conjugated tricatecholate 2,3,6,7,10,11-hexahydroxytriphenylene (HHTP) and the square-planar coordinated metal-ions Ni(II), Co(II), and Cu(II) are referred to as metal-catecholates (M-CAT-1; M = Ni^{2+}, Co^{2+}, and Cu^{2+}).[19] The M-CAT-1 exhibits intriguing physical properties such as high electrical conductivity (10^{-1} S cm^{-1} for a Cu-CAT-1 single-crystal) or charge storage capacities, which make these MOFs interesting candidates for energy conversion, chemical sensing, or storage applications.[19,21–25] Typically, these MOFs precipitate from a reactive precursor solution as insoluble polycrystalline bulk materials, hence limiting their post-synthesis handling options with regards to surface deposition.

The use of 2D TP-MOFs as coatings or in thin-film-based technologies requires their controlled immobilization on the desired surfaces. For example, in light-harvesting applications a specific film thickness is required to ensure optimized light absorption. Furthermore, control over crystal morphology, size, and orientation in the film would enable fine-tuning with regard to the desired optoelectronic properties. To date, the development of deposition methods enabling the synthesis of layered structured TP-MOF thin films featuring high crystallinity still present great challenges. As a result, the excited-state dynamics in thin oriented 2D TP-MOF films are still largely unknown.

A particular case is Cu-CAT-1, which was synthesized as a 10 nm ultrathin film by solution processing,[26] wherein interfacial processing steps such as liquid-liquid (LL) and layer-by-layer (LbL) techniques were combined. Upon transfer onto quartz substrates decorated with interdigitated gold electrodes functionalized with self-assembled monolayers, the film conductivity was determined to be in the range of $10^{-4}\,\mathrm{S\,cm^{-1}}$, a value 3 orders of magnitude smaller than the conductivity measured for a single crystal.[26] Such a difference in conductivity can be attributed to the transition from a single crystal to a polycrystalline thin film where loss mechanisms such as charge carrier percolation across grain boundaries can affect the device behavior.[27–31,33] This observed loss of conductivity underscores the need for growing highly oriented films where the crystals are oriented such that the effective charge carrier trajectories are aligned between electrodes, thereby enabling conductivity more similar to that of single crystals. Accordingly, developing an on-surface synthesis strategy adequate for oriented thin films of the electroactive TP-MOFs resulting in high crystallinity, homogeneous surface coverage, good adherence to the substrate, and high electrical conductivity remains a challenging goal.

Recently, we have introduced the synthesis of porous and crystalline framework films through vapor-assisted conversion (VAC).[32,34] VAC for MOFs has been inspired by the well established steam-assisted and dry-gel conversions applied for the synthesis of bulk materials and films of crystalline frameworks such as zeolites.[35–40] In principle, VAC utilizes precursors in a cast-layer solution which react to form a continuous film on a surface, by exposure to a vapor in a closed vessel and usually at elevated temperature (Figure 3.1). VAC is a versatile synthesis approach allowing for the variation of the synthesis parameters with regard to solvents, temperature, surfaces, and even modulators. As a result, VAC can be applied to different systems by identifying optimized synthesis conditions for the desired material, for example, *via* high-throughput screening. In the case of zirconium-based MOFs, we established the direct deposition onto different surfaces through VAC. Under the conditions employed in that study, the MOF films showed large surface coverage, accessible pores, and the additional advantage of preferred crystal orientation with respect to the surface.[32]

Here, we report the one-reactor, in situ synthesis of well- oriented thin films of the M-CAT-1 series grown on gold and oxide surfaces using VAC. The obtained films were examined regarding their crystallinity, crystal orientation, and electrical conductivity and were compared with highly crystalline powder pellets of these materials. Photophysical properties of thin Ni- and Co-CAT-1 films grown on quartz substrates were examined by means of optical absorption and photoluminescence (PL). Transient absorption measurements revealed the presence of reasonably long-lived photoexcited charges in the oriented Ni-CAT-1 films. Finally, we integrated the Ni-CAT-1 into a basic solar device illustrating that charges can be extracted from the MOF active layer and that Ni-CAT-1 is a photoactive material.

3.2. Results and discussion

Syntheses of M-CAT-1 Bulk Material. For the purpose of growing thin films, we developed VAC thin-film synthesis protocols suitable for the M-CAT-1 series on different substrates. To meet the required conditions for the thin-film growth, namely sufficient surface wetting enabling on-surface crystallization, we modified the reported M-CAT-1 bulk synthesis conditions with respect to the solvents utilized and the concentration of the precursors. We first synthesized M-CAT-1 bulk powders under the modified reaction conditions, confirming the formation of highly crystalline and porous frameworks. Briefly, the M-CATs were synthesized under solvothermal conditions from a stoichiometric precursor solution comprising HHTP, the respective metal acetate dissolved in a solvent mixture (1:1 v/v) of water and 1- propanol (operating as a solvent and modulator). Adding the precursors into the solvent mixture resulted in an instantaneous color change of the solution from clear to dark blue. After 18 h reaction time at elevated temperatures, a dark powder was isolated from the reaction mixture. Powder X-ray diffraction (PXRD) analysis of the obtained powders verified the formation of a highly crystalline M-CAT-1 (see Figure 3.8). In agreement with literature reports,[19] nitrogen sorption measurements for Ni-, Cu-, and Co-CAT-1 revealed type I(a) isotherms, enabling the extraction of a pore size of about 1.1 nm and surface areas of 430, 306, and 465 $m^2\ g^{-1}$ for Ni-, Cu-, and Co-CAT-1, respectively (Figures 3.11 and 3.12). Scanning electron micrographs (SEM) showed the typical needle-like morphology and hexagonally shaped crystallites of this class of MOFs (Figure 3.8). Notably, under the employed conditions, we observed an increase of the crystal length ranging from 1-2 µm for the Ni-CAT-1 to 3-4 µm for the Co-CAT-1 and up to 10 µm for the Cu-CAT-1. Furthermore, transmission electron microscopy (TEM) analysis of the Ni-CAT-1 showed the characteristic honeycomb structure in projections along the crystal *c*-axis (Figure 3.10). Crystalline pellets fabricated from the respective M-CAT-1 bulk material showed electrical conductivities of 6.8×10^{-3}, 3.2×10^{-2}, and 2.7×10^{-2} S cm^{-1} for Ni-, Co-, and Cu-CAT-1, respectively, values only slightly lower than the conductivity reported for a Cu-CAT-1 single-crystal (Figure 3.13; Table1). This confirms the formation of high-quality M-CAT-1 bulk materials and efficient charge percolation across the crystalline domains.

Highly Oriented Thin M-CAT-1 Films on Gold Surfaces. Next, we synthesized M-CAT-1 thin films under reaction conditions similar to those obtained for the bulk materials. As a starting point, we conducted the VAC thin-film synthesis on bare gold surfaces. Here, the respective metal acetate and HHTP precursors were dissolved at a stoichiometric ratio in a water/1-propanol (1:1 v/v) mixture providing the precursor solution (for details see SI). A droplet (40 µL) of the as-prepared precursor solution was spread onto a gold substrate (1.0 cm × 1.2 cm) placed on an elevated platform in the reaction vessel containing a solvent reservoir (water and 1- propanol, 1:1

v/v) as the vapor source (see Figure 3.1). Then the vessel was sealed and placed in a preheated oven at 85°C. After 3 h at this temperature, the vessel was allowed to cool down to room temperature. The substrates were then removed from the reaction vessel and rinsed extensively with acetone, revealing a blue iridescent film on top of the gold surface (insets in Figure 3.2a-c).

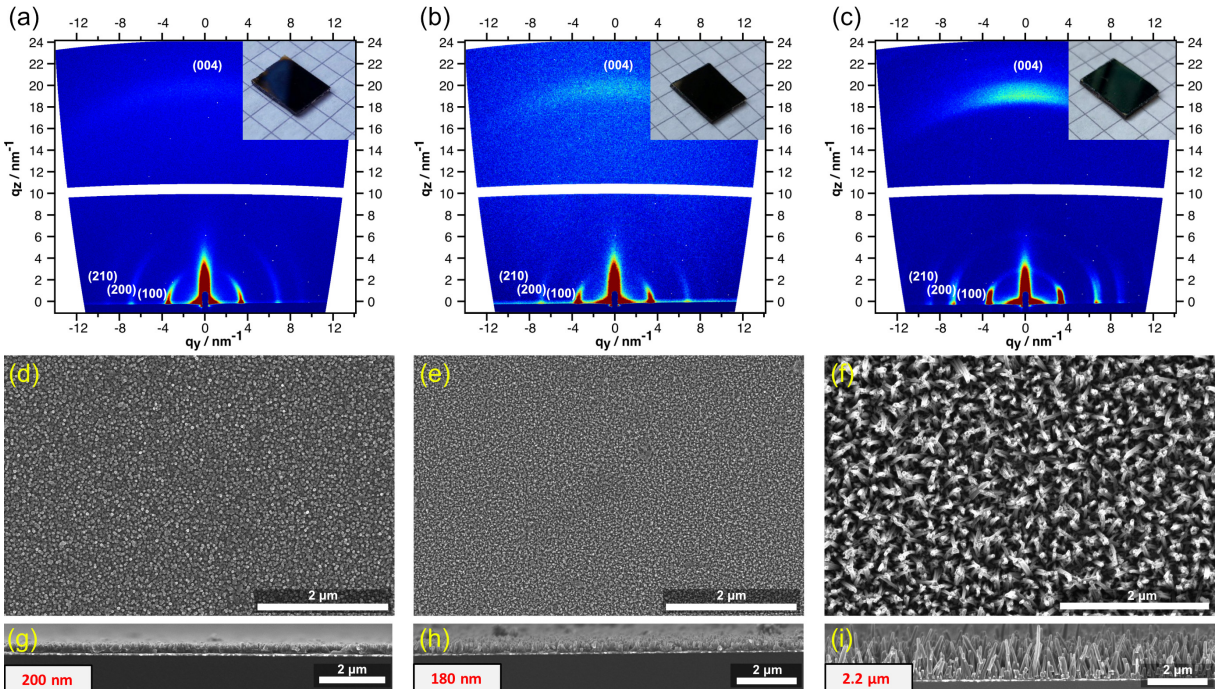

Figure 3.2 – (a-c) 2D GIWAXS patterns of Ni, Co, and Cu-CAT-1 films, respectively, revealing a high degree of orientation and crystallinity (the Miller indexes according to the set of planes are in white). The corresponding macroscopic photographs of the respective films grown on 1.0 cm × 1.2 cm gold substrates are shown as insets. (d-f) Top-view SEM micrographs of Ni-, Co-, and Cu-CAT-1 films, respectively. (g-i) Cross-section SEM images of Ni-, Co-, and Cu-CAT-1 showing the uniform film thickness indicated by the red numbers at the respective bottom left.

The successful growth of M-CAT-1 deposits through VAC was investigated by means of 2D grazing-incidence wide-angle X-ray scattering (2D GIWAXS) and SEM analysis (Figure 3.2). The GIWAXS patterns indicate the formation of the M-CAT-1 structure, and the observed reflections were indexed according to the corresponding reported M-CAT-1 PXRD patterns. Distinct reflections at $q_y = 3.9\,nm^{-1}$ (100), $q_y = 7.1\,nm^{-1}$ (200), and $q_y = 9.2\,nm^{-1}$ (210) near $q_z = 0\,nm^{-1}$, referred to as out-of-plane reflections, show that a preferential orientation of the crystallites is present, with the crystal *c*-axis corresponding to the (001) reflection aligned orthogonally to the surface. The (004) reflection corresponds to an interlayer distance of 3.3 Å and is observed as a diffuse arc at around $q_z = 19\,nm^{-1}$, also pointing toward a crystal orientation with the *c*-axis normal to the substrate surface.[41,42] Furthermore, the diffraction patterns of

the M-CAT-1 deposits feature a high crystallinity indicated by the pronounced (100) reflection intensity (Figure 3.2a-c). Top-view SEM micrographs of the Ni- and the Co-CAT-1 samples (Figure 3.2d, e) reveal long-range surface coverage with MOF crystallites over the whole substrate, thereby forming a continuous film. Furthermore, the films are crack-free over a large area, with no undesired impurities visible on top of the surface. Cross-section SEM analysis (Figure 3.2g, h) reveals uniform Ni- and Co-CAT-1 films with thicknesses of about 200 nm. Notably, under the VAC conditions employed here, the typical pillar-like crystallite morphology of the M-CAT-1 series is preserved in these thin films. These needle-like crystallites are oriented orthogonally to the surface and are densely packed, forming a continuous film. In contrast to these observations, the Cu-CAT-1 films feature individual, preferentially oriented crystals of about 2 µm length on the surface, resulting in less densely packed and thicker films (Figure 3.2f, i). To improve the Cu-CAT-1 film packing density and obtain substantially thinner films, further film synthesis screening was performed. The synthesis of Cu-CAT-1 films under the same conditions but with copper nitrate trihydrate as a metal precursor yielded a thin, highly faceted and oriented film consisting of Cu-CAT-1 rods of about 220 nm × 40 nm aligned perpendicularly to the surface.

Transmission electron microscopy (TEM) analysis of Ni-, Co-, and Cu-CAT-1 materials removed from the gold surface reveals highly crystalline solids in all of the examined samples (Figure 3.3a, c, e). Projections along the crystal *c*-axis show crystalline domains of about 50-60 nm in diameter and a hexagonal honeycomb-like structure for all frameworks. Furthermore, the absence of amorphous solids in the samples was confirmed by examination at lower magnifications and over a large number of crystals (Figure 3.14, 3.15), indicating high on-surface reaction yields obtained under the VAC conditions. In the case of Cu-CAT-1, TEM analysis shows that the material removed from the films consists of elongated crystallites with faceted hexagonal cross sections, in accordance with the bulk morphology observed by SEM analysis (Figure 3.16 and 3.8e, f). With a view on ultimately integrating such films into devices, the surface roughness is of key importance for obtaining high-quality interfaces between successive functional layers. To assess the surface roughness of the M- CAT-1 films, atomic force microscopy (AFM) surface scans were carried out in tapping mode, examining film areas of 5 µm × 5 µm (Figure 3.3b, d, f). The Ni- and Co-CAT-1 films feature a granulated surface texture consisting of the near vertically aligned well-packed crystallites (Figure 3.3b, d). This type of texture is observed throughout the examined film areas with no additional impurities on top of the films. For the Cu-CAT-1 films, the AFM scans reveal larger crystallites with a surface topography more rugged than that of the Ni- and Co-CAT-1 films. These observations correspond to a calculated RMS surface roughness of 8, 20, and 93 nm for the Ni-, Co-, and Cu- CAT-1 oriented films, respectively.

Oriented Thin M-CAT-1 Films on Conductive Metal-Oxide Surfaces. To date, the fabrication of triphenylene-based 2D MOF devices has mainly relied on the transfer of the

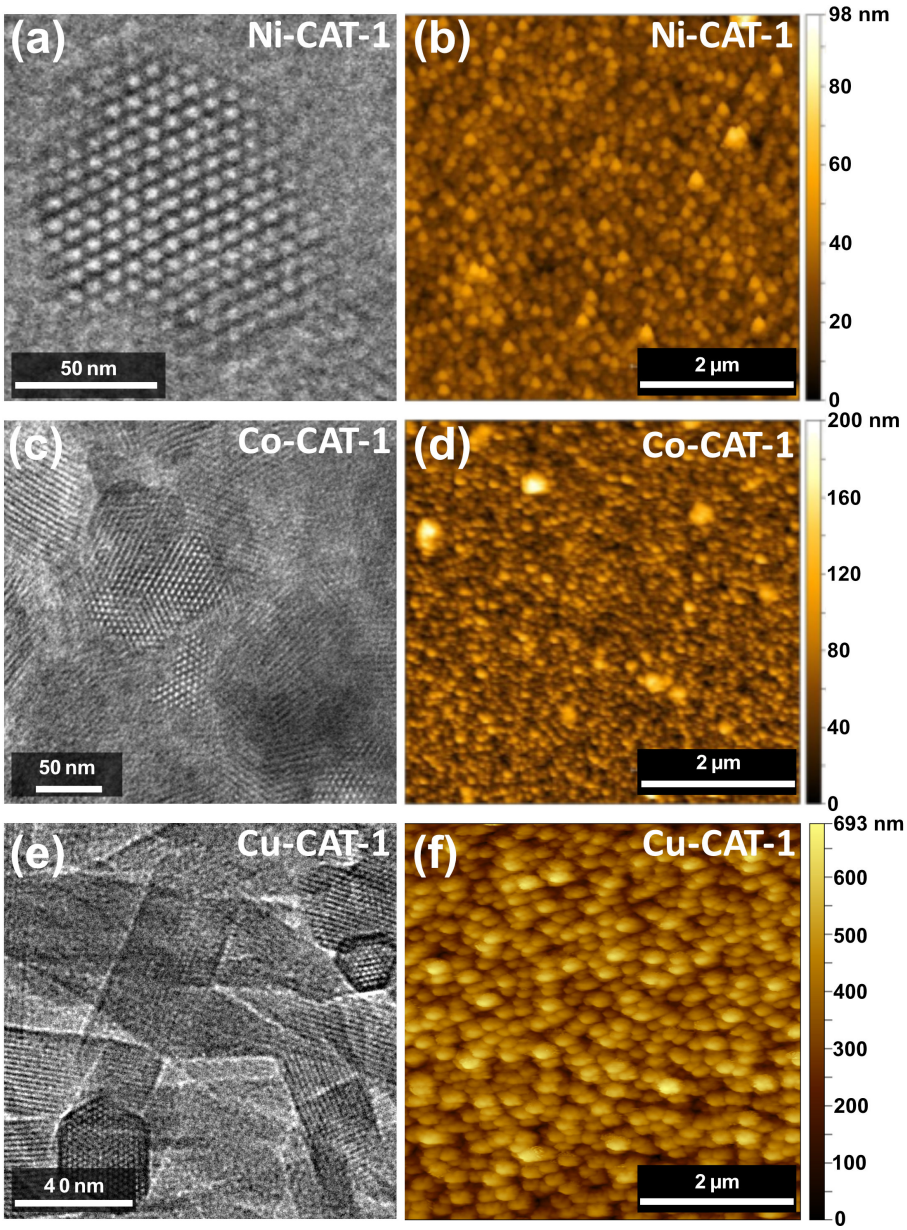

Figure 3.3 – (a), (c), and (e) TEM images of Ni-CAT-1, Co-CAT-1, and Cu-CAT-1 removed from films originally grown on gold substrates, respectively. (b), (d), and (f) AFM scans of a 5 µm × 5 µm area of the respective films with a color bar displaying the film heights.

respective MOF films from reactive interfaces onto a conductive substrate by stamping or on employing LbL techniques.[15,26,43,44]

In contrast, the VAC approach implemented here allows for the direct growth of 2D MOFs with preferential orientation on conductive surfaces. Interestingly, replacing the gold substrate

with a glass-supported indium-doped tin oxide (ITO) and employing the same VAC synthesis conditions as described above resulted in the formation of MOF crystals within the liquid layer that precipitated as randomly distributed crystallites on the ITO surface (Figure 3.36). This illustrates the pivotal role of favorable interactions between the growing crystals and the surface for obtaining a thin film under VAC conditions. To suppress the homogeneous MOF nucleation in the liquid layer and induce a heterogeneous nucleation on the ITO surface, an additional acetic or salicylic acid modulator was included into the initial precursor solution of the Ni- and Co-CAT-1, respectively. Employing an acid modulator had an evident effect, resulting in a clear precursor solution that was stable for several days at room temperature. A color change to dark blue on an ITO substrate became visible only after about 3 h reaction time at 85°C in the VAC setup. The ITO substrates recovered from the VAC reactor were thoroughly washed with acetone and dried under dynamic vacuum revealing a dark blue and iridescent film covering the whole ITO surface (Figure 3.39). Notably, this procedure is suitable for the synthesis Ni- and Co-CAT-1 thin films, while the growth of a high-quality Cu-CAT-1 film could not be realized. Under the VAC synthesis conditions examined here, we observed large crystal Cu-CAT-1 agglomerates on the substrate surface (Figure 3.37).

Similar to the films grown on gold, GIWAXS analysis of the obtained thin films (Ni- and Co-CAT-1) on ITO substrates showed the formation of crystalline MOFs with the crystal *c*-axes preferentially vertically oriented on the surface (Figure 3.28 and 3.31). SEM top-view micrographs of the Ni-CAT-1 films display a long-range surface coverage of the substrate with faceted and hexagonal nanopillars aligned perpendicularly to the ITO surface forming a dense film (Figure 3.28 as inset). For the Co-CAT-1 films, a high surface coverage was also obtained, however with evident voids of about 100 nm between the MOF crystals (Figure 3.31). SEM cross-section analysis revealed film thicknesses of about 300 nm and 1 µm for Ni- and Co-CAT-1, respectively.

Electrical Conductivity in Oriented Thin Films of M- CAT-1. To enable the electrical and photophysical characterization of the MOF thin films, they were also grown on quartz and glass substrates following the acid modulator approach, and we were able to synthesize thin films of Ni- and Co-CAT-1 with preferred orientation on these transparent substrates (Figures 3.29 and 3.30). These films show a pillar-like structure with similarities to the morphology observed for Cu-CAT-1 on a gold substrate (Figure 3.2). This allowed us to carry out van der Pauw measurements (contact distance 5 mm) on Ni- and Co-CAT-1 thin films, revealing conductivity values of 1.1×10^{-3} S cm^{-1} and 3.3×10^{-3} S cm^{-1}, respectively (for more details see Table S2). Notably, the values obtained for the Ni-CAT-1 are within the same order of magnitude as those measured for the compressed pellet sample, and the values obtained for the Co-CAT-1 are only slightly lower, indicating the formation of highly crystalline M-CAT-1 films, sufficient surface coverage, and charge percolation across the oriented crystal columns. Furthermore,

in the pellet, a continuous conduction path is achieved by applying significant pressure on a presynthesized large amount of sample to ensure good crystallite contact. In the films presented here, comparably good conduction paths and crystal contact are obtained at once by the direct on-surface deposition utilizing specific, low amounts of precursors.

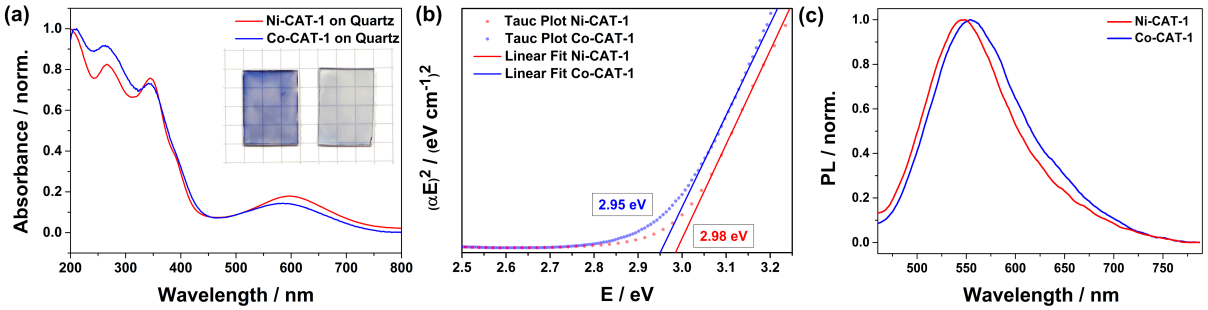

Figure 3.4 – (a) Normalized transmission absorption spectra of a Ni- (red) and Co-CAT-1 (blue) thin film on quartz substrates. Macroscopic photographs are depicted as insets (left: Ni-CAT-1, right: Co-CAT-1). (b) Tauc plots of the Ni- and Co-CAT-1 UV-vis absorbance spectra calculated for a direct band transition model. (c) Normalized PL (λ_{exc} = 378 nm) spectra for Ni- (red) and Co-CAT-1 (blue) thin films.

Investigations on the Charge Carrier Dynamics via Ultrafast Transient Absorption Spectroscopy. UV-vis absorption spectra of Ni- and Co-CAT-1 grown on quartz substrates (Figure 3.4a) reveal that the M-CAT-1 films strongly absorb in the UV and the blue region of the visible spectrum with an absorption onset at around 420 nm. Assuming a direct and allowed band gap transition, the band gaps were estimated *via* Tauc plots to be 2.98 and 2.95 eV for the Ni- and Co-CAT- 1 materials, respectively (Figure 3.4b). In addition, a pronounced broad absorption band is present for both materials at around 610 nm and attributed to the oxidized linker component, HHTP. This is in good agreement with the UV-vis spectra measured for representative MOF fragments and precursors (Figure 3.40) and also with the reported UV-vis spectra measured on ultrathin 10 nm Cu-CAT-1 films.[26] Both materials exhibit a weak and broad PL with maxima at around 550 and 570 nm for Ni- and Co-CAT-1, respectively (Figure 3.4c).

To assess the carrier lifetimes in the M-CAT-1, we performed time-resolved spectroscopic studies of the Ni- CAT-1. Time-correlated single photon counting (TCSPC) measurements (Figure 3.43) show that the PL is very short-lived and that the signal is not resolvable within the instrument response of around 80 ps. Given that the PL signal is proportional to the product of the electron and hole populations, this implies either ultrafast recombination or charge separation. Therefore, we performed transient absorption measurements with ultrashort 100 fs pulses which offer higher temporal resolution and with the signal dependent on the sum of contributions of the electrons and holes can probe the presence of photoexcited charge carriers. To this end, the Ni-CAT-1 sample was excited with pump pulses at 400 nm, and the differential absorption spectra were

probed by broad band pulses with a tunable time delay to the pump of up to 3 ns (Figure 3.5a). The very broad peak of negative ΔOD centered on 610 nm can be attributed to the bleaching of the absorption of the oxidized linker, observed in the steady-state spectra (cf. Figure 3.4a). The band edge bleach of Ni-CAT-1 is not clearly discernible in Figure 3.5a since the overall signal in this wavelength region below 450 nm is dominated by a strong photoinduced absorption signal.

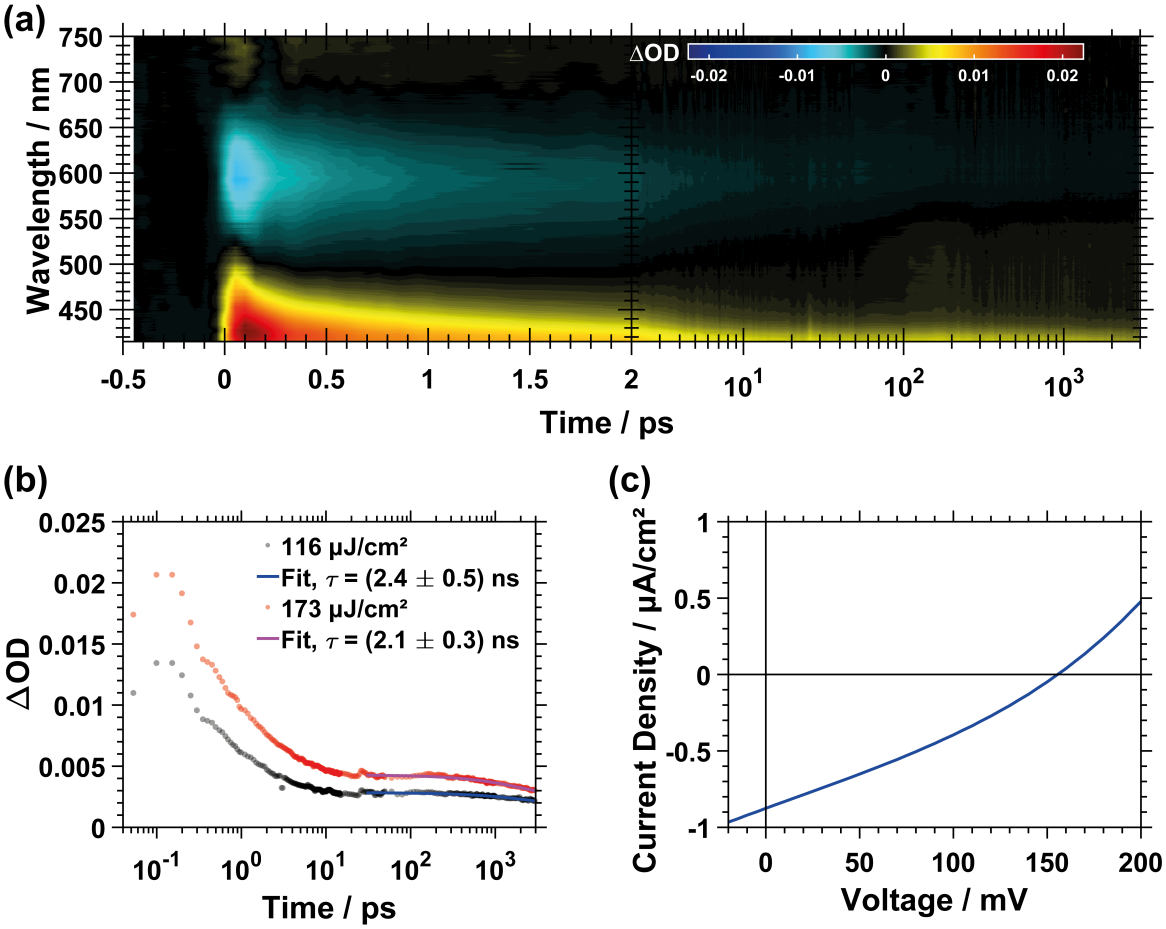

Figure 3.5 – (a) Transient absorption data of Ni-CAT-1, excited at 400 nm with an excitation density of 173 µJ cm^{-2} per pulse. Red areas indicate an increased absorption, while blue regions represent a reduced optical density, as shown by the color bar. (b) Kinetic traces of the Ni-CAT-1 photoinduced absorption feature, integrated between 415 and 450 nm for fluences of 116 µJ cm^{-2} (gray) and 173 µJ cm^{-2} (red). (c) Current-voltage measurement of an ITO/Ni-CAT-1/Al solar cell device, measured under 100 mW cm^{-2} AM 1.5G illumination.

However, an additional experiment with pump excitation at 350 nm (Figure 3.45) indicates that they follow similar dynamics. This allows us to focus the analysis on the kinetic traces of the photoinduced absorption, averaged between 415 and 450 nm and plotted in Figure 3.5b. Although there is an initial fast decay during the first picosecond corresponding likely to the

charge separation, nearly 15% of the initial signal still remains after 3 ns. The decay dynamics (see Figure 3.5b) are independent of the excitation density, hence excluding Auger recombination effects. The longer time traces (time delays above 30 ps) have been fitted with an exponential function, estimating lifetimes to be longer than 2 ns. Crucially, this shows the presence of photoexcited states after at least 3 ns, which might be sufficient for light-harvesting in a thin-film based device.

Extraction of Charge Carriers in Ni-CAT-1 Thin Films. To explore whether photoinduced electron-hole pairs can be obtained, separated, and extracted in M-CAT-1 materials, we integrated the Ni-CAT-1 film into a basic solid-state solar cell device with an ITO/Ni-CAT-1/Al architecture (see Figure 3.7). For this purpose, we contacted a 200 nm oriented Ni- CAT-1 film grown on an ITO-coated glass substrate with an aluminum electrode. This device architecture exhibits a suitable energy band alignment for directed charge transfer (Figure 3.44). The highest occupied molecular orbital (HOMO) level of the Ni-CAT-1 was extracted from differential pulsed voltammetry measurements to be −5.9 eV performed on an oriented thin Ni- CAT-1 film grown on a gold substrate, immersed in a 0.1 M dichloromethane solution with NBu_4PF_6 serving as the electrolyte. The lowest unoccupied molecular orbital (LUMO) was calculated to be −2.9 eV by adding the band gap obtained from the Tauc plot to the HOMO level.

The prepared devices showed diode characteristics and the corresponding current-voltage (J-V) curve under AM 1.5G illumination is plotted in Figure 3.5c. The short-circuit current ($J_{sc} = 8.76 \times 10^{-4}$ mA cm^{-2}) and open-circuit voltage ($V_{oc} = 156$ mV) are, along with the fill factor (FF) of around 30%, strongly limited through the device architecture lacking charge selective layers. However, this experiment demonstrates that photogenerated charge carriers can be extracted from the material and that this 2D MOF can be used as a photoactive layer in solid-state photovoltaic devices. Furthermore, this set of experiments illustrates that the Ni-CAT-1 molecular stacks are able to serve as a directional conduction path for the photogenerated charge carriers in the oriented thin film.

3.3. Conclusion

Here, we developed a synthetic strategy for controlled on- surface growth of highly oriented thin films of the electroactive M-CAT-1 series through VAC. By controlling the reaction parameters, we were able to synthesize these MOF materials on a variety of substrates, ranging from bare gold to transparent electrodes and glasses. This allowed for the detailed electrical and optical characterization of the Ni- and Co-CAT derivatives. While the films exhibit significant electrical conductivity of up to 10^{-3} S cm^{-1} , transient absorption spectroscopy revealed the presence of long-lived excited states over several nanoseconds. Ultimately, by growing thin films

on ITO substrates, we successfully integrated Ni- CAT-1 as an active layer in a MOF-based solid-state photovoltaic device. We anticipate that other more electron-rich 2D MOF systems, for example, hexaaminotriphenylene or related materials combining the favorable property of electrical conductivity and significant optical absorbance into the NIR region, can be grown as thin films through the VAC technique thus paving the way for using these MOFs as functional active layers in light-harvesting devices.

3.4. Experimental methods

3.4.1. Substrate preparation

The preparation of the gold-substrates is based on the procedure described by *et al.*[45] Seven microscope glass slides (*Menzel*, 76 mm × 26 mm) in a support made of Teflon were cleaned by ultrasonic treatment in acetone, followed by four sequential washing steps with 2-propanol, a 1:100 mixture of *Hellmanex III* and water, water, and finally again with 2-propanol (*Chromasolv*). Oxygen plasma cleaning (*Diener electronic*, Plasma Surface Technology) for 30 min was conducted, followed by the mounting of the glass slides in a vacuum deposition unit installed in a glovebox (*MBraun Labmaster Pro SP* equipped with an *Inficon SQC-310C Deposition controller*). 10 nm of titanium as an adhesion layer and 40 nm of gold were thermally deposited under high vacuum onto the microscope glass slides. The substrates for the experiments were prepared by cutting commercially available microscope slides (*Menzel*, 76 mm × 26 mm), gold coated glass slides, and indium-doped tin oxide (ITO, TEC7, *Pilkingtion*) into pieces of 1.2 × 1.0 cm, while quartz substrates were cut into dimensions of 2.0 × 1.5 cm. Afterward, ITO, microscope slides (glass), and quartz substrates were cleaned with a detergent (*Hellmanex III*, 2 vol%), rinsed with water, followed by ethanol, and dried in nitrogen flow *prior* to use.

3.4.2. Synthesis of M-CAT-1 thin films through VAC

For the film formation using VAC, a glass autoclave (*Schott Duran*, borosilicate 3.3, ISO4796, 100 mL) with a PBT cap equipped with a Teflon seal was used. The bottom part of the autoclave was filled with 14 Raschig rings (10 mm × 10 mm, soda-lime glass) to obtain an elevated flat platform for the substrate. A mixture of water and 1-propanol was filled into the autoclave. Afterward, a substrate (1.2 cm × 1 cm) was placed on top of the Raschig-rings and fully coated with a drop of a freshly prepared MOF precursor solution. The autoclave was closed and transferred into a preheated oven where it was kept for the specified time. Afterward, the autoclave was removed from the oven and cooled down for 10 min before the substrate was rinsed with dry acetone.

3.4.3. Synthesis of Ni-, Co-, and Cu-CAT-1 films on gold surfaces

The HHTP precursor (2.69×10^{-3} mmol; 0.875 mg) and the metal precursors nickel acetate (5.0×10^{-3} mmol; 1.25 mg), cobalt acetate (5.0×10^{-3} mmol; 1.25 mg), or copper trifluoroacetylacetonate (5.0×10^{-3} mmol; 1.25 mg) were mixed in a defined ratio (1:2) and dissolved in a solvent mixture of water and 1-propanol (1.5 mL : 1.5 mL) by sonication for 20 s at maximum power. The obtained precursor solution was filtered through a syringe filter to remove any remaining particles. Subsequently, 40 µL of the solution (HHTP: 0.899 mmol L^{-1}; MOAc: 1.674 mmol L^{-1}) was deposited onto a clean 1.2×1.0 cm gold substrate. Four of these set-ups were placed onto glass spacers in an autoclave loaded with a solvent mixture of water and 1-propanol (2.5 mL : 2.5 mL). The autoclave was sealed immediately and placed into a preheated oven at 85°C for 3.5 h. The experimental setup of the VAC is shown in Figure 3.6. Afterwards, the autoclave was removed from the oven and cooled down for 10 min before the substrate was rinsed with dry acetone.

3.4.4. Synthesis of Ni-CAT-1 films on quartz and ITO substrates

The HHTP precursor (5.4×10^{-3} mmol; 1.75 mg) and the nickel acetate (10.0×10^{-3} mmol; 2.5 mg) were mixed in a defined ratio (1:2) and dissolved in a solvent mixture of water and 1-propanol (1 mL : 1 mL) with the addition of acetic acid (50 µL). 40 µL of the respective precursor solution (HHTP: 5.35 mmol L^{-1}; NiAc: 10.7 mmol L^{-1}; HOAc: 1.745 mol L^{-1}) was deposited onto a clean 1.2×1.0 cm ITO substrate. Four of these set-ups were placed onto glass spacers in an autoclave loaded with a solvent mixture of water and 1- propanol (2.5 mL : 2.5 mL). The autoclave was sealed immediately and placed into a preheated oven at 85°C for 18 h. Afterward, the autoclave was removed from the oven and cooled down for 10 min before the substrates were rinsed with dry acetone.

3.4.5. Synthesis of Co-CAT-1 films on quartz substrates

The HHTP precursor (5.4×10^{-3} mmol; 1.75 mg) and the cobalt acetate (11.0×10^{-3} mmol; 3 mg) were mixed in a defined ratio (1 : 2.5 n : n) and dissolved in a solvent mixture of water, 1-propanol (1 mL : 1 mL) with addition of 50 µL of a salicylic acid (0.89 mmol; 125 mg) containing solution in a water, 1-propanol mixture (1 mL : 1 mL). 40 µL of the respective precursor solution (HHTP: 5.35 mmol L^{-1}; CoAc: 12.85 mmol L^{-1}; salicylic acid: 11.23 mmol L^{-1}) was deposited onto a clean 1.2×1.0 cm glass substrate. Four of these set-ups were placed onto glass spacers in an autoclave loaded with a solvent mixture of water and 1-propanol (2.5 mL : 2.5 mL). The autoclave was sealed immediately and placed into a preheated oven at 85°C for 18 h. Afterward, the

autoclave was removed from the oven and cooled down for 10 min before the substrates were rinsed with dry acetone.

References

[1] Furukawa, H.; Cordova, K. E.; O'Keeffe, M.; Yaghi, O. M. The Chemistry and Applications of Metal-Organic Frameworks. *Science* **2013**, 341, 1230444.

[2] Ferey, G.Hybrid Porous Solids: Past, Present, Future. *Chem. Soc. Rev.* **2008**, 37, 191-214.

[3] Jiang, J.; Zhao, Y.; Yaghi, O. M. Covalent Chemistry Beyond Molecules. *J. Am. Chem. Soc.* **2016**, 138, 3255-3265.

[4] Cook, T. R.; Zheng, Y.-R.; Stang, P. J. Metal-Organic Frameworks and Self-Assembled Supramolecular Coordination Complexes: Comparing and Contrasting the Design, Synthesis, and Functionality of Metal-Organic Materials. *Chem. Rev.* **2013**, 113, 734-777.

[5] Takaishi, S.; Hosoda, M.; Kajiwara, T.; Miyasaka, H.; Yamashita, M.; Nakanishi, Y.; Kitagawa, Y.; Yamaguchi, K.; Kobayashi, A.; Kitagawa, H. Electroconductive Porous Coordination Polymer $Cu[Cu(pdt)_2]$ Composed of Donor and Acceptor Building Units. *Inorg. Chem.* **2009**, 48, 9048-9050.

[6] Stavila, V.; Talin, A. A.; Allendorf, M. D. MOF-Based Electronic and Opto-Electronic Devices. *Chem. Soc. Rev.* **2014**, 43, 5994-6010.

[7] Kobayashi, Y.; Jacobs, B.; Allendorf, M. D.; Long, J. R. Conductivity, Doping, and Redox Chemistry of a Microporous Dithiolene-Based Metal-Organic Framework. *Chem. Mater.* **2010**, 22, 4120-4122.

[8] Nagatomi, H.; Yanai, N.; Yamada, T.; Shiraishi, K.; Kimizuka, N. Synthesis and Electric Properties of a Two-Dimensional Metal-Organic Framework Based on Phthalocyanine. *Chem.-Eur. J.* **2018**, 24, 1806-1810.

[9] Dou, J.-H.; Sun, L.; Ge, Y.; Li, W.; Hendon, C. H.; Li, J.; Gul, S.; Yano, J.; Stach, E. A.; Dinca. M. Signature of Metallic Behavior in the Metal-Organic Frameworks M_3(hexaiminobenzene)$_2$ (M = Ni, Cu). *J. Am. Chem. Soc.* **2017**, 139, 13608-13611.

[10] Feng, D.; Lei, T.; Lukatskaya, M. R.; Park, J.; Huang, Z.; Lee, M.; Shaw, L.; Chen, S.; Yakovenko, A. A.; Kulkarni, A.; Xiao, J.; Fredrickson, K.; Tok, J. B.; Zou, X.; Cui, Y.; Bao, Z. Robust and Conductive Two-Dimensional Metal-Organic Frameworks With Exceptionally High Volumetric and Areal Capacitance. *Nat. Energy.* **2018**, 3, 30-36.

[11] Pal, T.; Kambe, T.; Kusamoto, T.; Foo, M. L.; Matsuoka, R.; Sakamoto, R.; Nishihara, H. Interfacial Synthesis of Electrically Conducting Palladium Bis(dithiolene) Complex Nanosheet. *Chem-PlusChem* **2015**, 80, 1255-1258.

[12] Huang, X.; Sheng, P.; Tu, Z.; Zhang, F.; Wang, J.; Geng, H.; Zou, Y.; Di, C.-A.; Yi, Y.; Sun, Y.; Xu, W.; Zhu, D. A Two- Dimensional pie-d Conjugated Coordination Polymer With Extremely High Electrical Conductivity and Ambipolar Transport Behaviour. *Nat. Commun.* **2015**, 6, 7408.

[13] Kambe, T.; Sakamoto, R.; Hoshiko, K.; Takada, K.; Miyachi, M.; Ryu, J.-H.; Sasaki, S.; Kim, J.; Nakazato, K.; Takata, M.; Nishihara, H. pie-Conjugated Nickel Bis(dithiolene) Complex Nano- sheet. *J. Am. Chem. Soc.* **2013**, 135, 2462-2465.

[14] Jin, Z.; Yan, J.; Huang, X.; Xu, W.; Yang, S.; Zhu, D.; Wang, J. Solution-Processed Transparent Coordination Polymer Electrode for Photovoltaic Solar Cells. *Nano Energy* **2017**, 40, 376-381.

[15] Hoshiko, K.; Kambe, T.; Sakamoto, R.; Takada, K.; Nishihara, H. Fabrication of Dense and Multilayered Films of a Nickel Bis(dithiolene) Nanosheet by Means of the Langmuir-Schäfer Method. *Chem. Lett.* **2014**, 43, 252-253.

[16] Campbell, M. G.; Sheberla, D.; Liu, S. F.; Swager, T. M.; Dinca. M. Cu_3(hexaiminotriphenylene)$_2$: An Electrically Conductive 2D Metal-Organic Framework for Chemiresistive Sensing. *Angew. Chem., Int. Ed.* **2015**, 54, 4349-4352.

[17] Dong, R.; Pfeffermann, M.; Liang, H.; Zheng, Z.; Zhu, X.; Zhang, J.; Feng, X. Large-Area, Free-Standing, Two-Dimensional Supramolecular Polymer Single-Layer Sheets for Highly Efficient Electrocatalytic Hydrogen Evolution. *Angew. Chem. Int. Ed.* **2015**, 54, 12058-12063.

[18] Dong, R.; Zheng, Z.; Tranca, D. C.; Zhang, J.; Chandrasekhar, N.; Liu, S.; Zhuang, X.; Seifert, G.; Feng, X. Immobilizing Molecular Metal Dithiolene-Diamine Complexes on 2D Metal-Organic Frame- works for Electrocatalytic H_2 Production. *Chem. - Eur. J.* **2017**, 23, 2255-2260.

[19] Hmadeh, M.; Lu, Z.; Liu, Z.;Gandara, F. ; Furukawa, H.;Wan, S.; Augustyn, V.; Chang, R.; Liao, L.; Zhou, F.; Perre, E.; Ozolins, V.; Suenaga, K.; Duan, X.; Dunn, B.; Yamamto, Y.; Terasaki, O.; Yaghi, O. M. New Porous Crystals of Extended Metal-Catecholates. *Chem. Mater.* **2012**, 24, 3511-3513.

[20] Sheberla, D.; Sun, L.; Blood-Forsythe, M. A.; Er, S.; Wade, C. R.; Brozek, C. K.; Aspuru-Guzik, A.; Dinca, M. High Electrical Conductivity in Ni_3(2,3,6,7,10,11-Hexaiminotriphenylene)$_2$, a Semi-conducting Metal-Organic Graphene Analogue. *J. Am. Chem. Soc.* **2014**, 136, 8859-8862.

[21] Hoppe, B.; Hindricks, K. D. J.; Warwas, D. P.; Schulze, H. A.; Mohmeyer, A.; Pinkvos, T. J.; Zailskas, S.; Krey, M. R.; Belke, C.; König, S.; Fröba, M.; Haug, R. J.; Behrens, P. Graphene-Like Metal- Organic Frameworks: Morphology Control, Optimization of Thin Film Electrical Conductivity and Fast Sensing Applications. *CrystEngComm* **2018**, 20, 6458-647.

[22] Yao, M.-S.; Lv, X.-J.; Fu, Z.-H.; Li, W.-H.; Deng, W.-H.; Wu, G.-D.; Xu, G. Layer-By-Layer Assembled Conductive Metal-Organic Framework Nanofilms for Room-Temperature Chemiresistive Sens- ing. *Angew. Chem. Int. Ed.* **2017**, 56, 16510-16514.

[23] Liu, X.-H.; Hu, W.-L.; Jiang, W.-J.; Yang, Y.-W.; Niu, S.; Sun, B.; Wu, J.; Hu, J.-S. Well-Defined Metal-O6 in Metal-Catecholates as a Novel Active Site for Oxygen Electroreduction. *ACS Appl. Mater. Interfaces* **2017**, 9, 28473-28477.

[24] Li, Y.-L.; Zhou, J.-J.; Wu, M.-K.; Chen, C.; Tao, K.; Yi, F.-Y.; Han, L. Hierarchical Two-Dimensional Conductive Metal-Organic Framework/Layered Double Hydroxide Nanoarray for a High- Performance Supercapacitor. *Inorg. Chem.* **2018**, 57, 6202-6205.

[25] Li, W.-H.; Ding, K.; Tian, H.-R.; Yao, M.-S.; Nath, B.; Deng, W.-H.; Wang, Y.; Xu, G. Conductive Metal-Organic Framework Nanowire Array Electrodes for High-Performance Solid-State Super- capacitors. *Adv. Funct. Mater.* **2017**, 27, 1702067.

[26] Rubio-Gimenez, V.; Galbiati, M.;Castells-Gil, J.; Almora-Barrios, N.;Navarro-Sanchez, J.; Escorcia-Ariza, G.;Mattera, M.; Arnold, T.; Rawle, J.; Tatay, S.; Coronado, E.; Marti-Gastaldo, C. Bottom-Up Fabrication of Semiconductive Metal-Organic Framework Ultrathin Films. *Adv. Mater.* **2018**, 30, 1704291.

[27] Liu, J.; Wöll, C. Surface-Supported Metal-Organic Framework Thin Films: Fabrication Methods, Applications, and Challenges. *Chem. Soc. Rev.* **2017**, 46, 5730-5770.

[28] Jia, H.; Yao, Y.; Zhao, J.; Gao, Y.; Luo, Z.; Du, P. A Novel Two- Dimensional Nickel Phthalocyanine-Based Metal-Organic Framework for Highly Efficient Water Oxidation Catalysis. *J. Mater. Chem. A* **2018**, 6, 1188-1195.

[29] AlKaabi, K.; Wade, C. R.; Dinca, M. Transparent-To-Dark Electrochromic Behavior in Naphthalene-Diimide-Based Mesoporous MOF-74 Analogs. *Chem.* **2016**, 1, 264-272.

[30] Talin, A. A.; Centrone, A.; Ford, A. C.; Foster, M. E.; Stavila, V.; Haney, P.; Kinney, R. A.; Szalai, V.; El Gabaly, F.; Yoon, H. P.; Leonard,F.; Allendorf, M.D.Tunable Electrical Conductivity in Metal-Organic Framework Thin-Film Devices. *Science* **2014**, 343, 66-69.

[31] Allendorf, M. D.; Schwartzberg, A.; Stavila, V.; Talin, A. A. A Roadmap to Implementing Metal-Organic Frameworks in Electronic Devices: Challenges and Critical Directions. *Chem. Eur. J.* **2011**, 17, 11372-11388.

[32] Hod, I.; Bury, W.; Karlin, D. M.; Deria, P.; Kung, C.-W.; Katz, M. J.; So, M.; Klahr, B.; Jin, D.; Chung, Y.-W.; Odom, T. W.; Farha, O. K.; Hupp, J. T. Directed Growth of Electroactive Metal-Organic Framework Thin Films Using Electrophoretic Deposition. *Adv. Mater.* **2014**, 26, 6295-6300.

[33] Virmani,E.; Rotter, J. M.; Märinger, A.; von Zons,T.; Godt, A.; Bein, T.; Wuttke, S.; Medina, D. D. On-Surface Synthesis of Highly Oriented Thin Metal-Organic Framework Films Through Vapor-Assisted Conversion. *J. Am. Chem. Soc.* **2018**, 140, 4812-4819.

[34] Medina, D. D.; Rotter, J. M.; Hu, Y.; Dogru, M.; Werner, V.; Auras, F.; Markiewicz, J. T.; Knochel, P.; Bein, T. Room Temperature Synthesis of Covalent-Organic Framework Films Through Vapor- Assisted Conversion. *J. Am. Chem. Soc.* **2015**, 137, 1016-1019.

[35] Möller, K.; Yilmaz, B.; Jacubinas, R. M.; Müller, U.; Bein, T. One-Step Synthesis of Hierarchical Zeolite Beta via Network Formation of Uniform Nanocrystals. *J. Am. Chem. Soc.* **2011**, 133, 5284-5295.

[36] Changjean, W.-C.; Chiang, A. S.T.; Tsai, T.-C. Anti-Corrosion Zeolite Film by The Dry-Gel-Conversion Process. *Thin Solid Films* **2013**, 529, 327-332.

[37] Matsukata, M.; Ogura, M.; Osaki, T.; Hari Prasad Rao, P. R.; Nomura, M.; Kikuchi, E. Conversion of Dry Gel to Microporous Crystals in Gas Phase. *Top. Catal.* **1999**, 9, 77-92.

[38] Majano, G.; Mintova, S.; Ovsitser, O.; Mihailova, B.; Bein, T. Zeolite Beta Nanosized Assemblies. *Microporous Mesoporous Mater.* **2005**, 80, 227-235.

[39] Shi, Q.; Chen, Z.; Song, Z.; Li, J.; Dong, J. Synthesis of ZIF-8 and ZIF-67 by Steam-Assisted Conversion and an Investigation of Their Tribological Behaviors. *Angew. Chem. Int. Ed.* **2011**, 50, 672-675.

[40] Tatsumi, T.; Jappar, N. Properties of Ti-Beta Zeolites Synthesized by Dry-Gel Conversion and Hydrothermal Methods. *J. Phys. Chem. B* **1998**, 102, 7126-7131.

[41] Medina, D. D.; Werner, V.; Auras, F.; Tautz, R.; Dogru, M.; Schuster, J.; Linke, S.; Döblinger, M.; Feldmann, J.; Knochel, P.; Bein, T. Oriented Thin Films of a Benzodithiophene Covalent Organic Framework. *ACS Nano* **2014**, 8, 4042-4052.

[42] Medina, D. D.; Petrus, M. L.; Jumabekov, A. N.; Margraf, J. T.; Weinberger, S.; Rotter, J. M.; Clark, T.; Bein, T. Directional Charge-Carrier Transport in Oriented Benzodithiophene Covalent Organic Framework Thin Films. *ACS Nano* **2017**, 11, 2706-2713.

[43] Wu, G.; Huang, J.; Zang, Y.; He, J.; Xu, G. Porous Field-Effect Transistors Based on a Semiconductive Metal-Organic Framework. *J. Am. Chem. Soc.* **2017**, 139, 1360-1363.

[44] Lahiri, N.; Lotfizadeh, N.; Tsuchikawa, R.; Deshpande, V. V.; Louie, J. Hexaaminobenzene As a Building Block for a Family of 2D Coordination Polymers. *J. Am. Chem. Soc.* **2017**, 139, 19-22.

[45] Hinterholzinger, F. M.; Wuttke, S.; Roy, P.; Preusse, T.; Schaate, A.; Behrens, P.; Godt, A.; Bein, T. Highly Oriented Surface- Growth and Covalent Dye Labeling of Mesoporous Metal-Organic Frameworks. *Dalton Trans.* **2012**, 41, 3899-3901.

3.5. Appendix

3.5.1. Characterization

X-ray spectroscopy X-ray diffraction (XRD) analyses were performed on a *Bruker D8* diffractometer in Bragg- Brentano geometry with Ni-filtered Cu K_α ($\lambda = 1.54060$ Å) radiation operating at 40 kV and 30 mA with a position-sensitive detector (*LynxEye*). X-ray diffraction analysis in a detector scan mode was carried out in reflection mode using a *Bruker D8 Discover* with Ni-filtered Cu K_α radiation (1.5406 Å) and a position-sensitive detector (*LynxEye*). X-ray data were collected by fixing the X-ray source at a grazing incidence angle of 0.6° while the detector scans a 2-30° 2θ range. Two-dimensional grazing-incident wide angle X-ray scattering (2D GIWAXS) data were collected using an *Anton-Paar SAXSpace* system equipped with a Cu K_α microfocus source operated at 50 kV and 1 mA and an *Eiger Dectris R 1M* 2D detector.

Scanning electron microscopy (SEM) SEM images were recorded on an *FEI Helios NanoLab G3 UC* electron microscope with an acceleration voltage of 2 kV from a field emission gun. For the cross-section analysis substrates were partially cut and broken manually to reveal fresh cross-sections. *Prior* to SEM analysis the samples were coated with a thin carbon layer by carbon fiber flash evaporation in high vacuum.

Transmission electron microscopy (TEM) TEM images were collected on an *FEI Titan Themis 60-300* microscope at an acceleration voltage of 300 kV. Powder samples were prepared by crushing the particles with a razor blade and subsequently depositing the powder onto a copper grid supporting a thin electron transparent carbon film. TEM film samples were prepared by carefully removing the film layer on top of the substrate with a sharp blade and mounting it onto the sample grid.

Atomic force microscopy (AFM) AFM measurements were performed using a *NANOINK* atomic force microscope in tapping mode with a scanning rate of 0.2 Hz, a proportional gain of 50 and an integral gain of 32. The scanned area was 5.02×5.02 µm at 282×282 pixels.

Van der Pauw measurements Van der Pauw measurements were conducted on an *ECOPIA Model HMS 3000* Hall measurement setup. The samples were fixed in an *SPCB-1* spring clip board without any additional contacts. Distances between the single probes were adjusted to be 5 mm.

UV-VIS spectroscopy Photophysical characterization of as-prepared MOF thin films on 2.0×1.5 cm quartz substrates was performed in transmission mode with a *PERKIN ELMER UV VIS/NIR Lambda 1050* spectrophotometer equipped with an integrating sphere.

Photoluminescence (PL) spectroscopy PL measurements were performed on a *PicoQuant FluoTime 300* time-correlated single photon counting (TCSPC) setup. Steady-state spectra and time-resolved histograms were acquired using a 378 nm laser (*PicoQuant LDH-P-C-375*). Residual laser scattering was removed using a 400 nm dielectric longpass (*Thorlabs FELH0400*) in the beam path of the emitted light, which was detected under magic angle (54.7°) on a photomultiplying tube (*PicoQuant PMA 192*).

Optoelectronic Characterization Current-voltage (J-V) curves were recorded on a *Keithley 2400 SourceMeter* under illumination from an AM 1.5G solar simulator (*Solar Light Model 16S*), which was calibrated to 100 mW cm^{-2} with a *Fraunhofer ISE* certified KG5 filtered silicon cell. External quantum efficiencies (EQE) were measured at short circuit without bias illumination. Monochromatic light was obtained from a 150 W xenon lamp in combination with a monochromator and order-sorting filters. The slits were adjusted such that the FWHM was 5 nm at a light intensity of approximately 2 mW cm^{-2}. All light intensities were calibrated with a *Fraunhofer ISE* certified silicon reference cell equipped with a KG5 filter. The monochromatic light was modulated using an optical chopper at a frequency of 83 Hz. For signal detection, a Signal Recovery 7265 lock-in amplifier combined with a low-noise current amplifier (*Femto DLPCA-200*) was employed.

Nitrogen sorption Ad- and desorption measurements were performed at 77.3 K on an *Autosorb-1* (*Quantachrome instruments*, Florida, USA) with nitrogen of 99.9999% purity. The samples were activated under high vacuum at 120°C for at least 12 h. Evaluation of ad- and desorption isotherms was carried out with the program *AsiQwin v.3.01* (*Quantachrome instruments*, Florida, USA).

For BET calculations, pressure ranges of the nitrogen isotherms were chosen with the help of the BET assistant in the *ASiQwin* software. In accordance with ISO recommendations, multipoint BET tags equal to or below the maximum in $V \cdot (1 - p/p_0)$ were chosen.

Thermogravimetric analysis Thermogravimetric analysis of the samples was performed using a *NETZSCH STA 449C* with a heating rate of 2.35°C/min and a heating range up to 600°C under a stream of synthetic air.

3.5.2. Experimental

General All materials were purchased from *Sigma Aldrich, Acros* or *TCI Europe* in the common purities *purum, puriss* or reagent grade. The materials were used as received without additional purification and handled in air unless otherwise noted. The water utilized in the synthesis was subjected to a *Merck-Milipore Mili-Q* purification system *prior* to use.

Substrates The preparation of the gold substrates was based on the procedure described by Hinterholzinger *et al.* Seven microscope glass slides (*Menzel*, 76 mm × 26 mm) in a support made of Teflon were cleaned by ultrasonic treatment in acetone, followed by sequential washing steps with 2-propanol, a 1:100 mixture of *Hellmanex III* and water, water, and finally 2-propanol (*Chromasolv*). Oxygen plasma cleaning (*Diener electronic*, Plasma-Surface- Technology) for 30 min was conducted, previous to the mounting of the glass slides in a vacuum deposition unit installed in a glove box (*MBraun Labmaster Pro SP* equipped with an *Inficon SQC-310C* deposition controller). 10 nm of titanium and 40 nm of gold were thermally deposited under high vacuum onto the microscope glass slides.

The respective substrates were prepared by cutting commercially available microscope slides (*Menzel*, 76 mm × 26 mm), gold coated glass slides and indium-doped tin-oxide (ITO, *TEC7, Pilkington*) into pieces of 1.2 × 1.0 cm, while quartz substrates were cut into dimensions of 2.0 × 1.5 cm.

ITO, microscope slides (glass), and quartz substrates were cleaned with a detergent (*Hellmanex III*, 2 vol%), rinsed with water, followed by ethanol and dried in nitrogen flow *prior* to use.

3.5.3. Bulk synthesis

Ni-CAT-1 In a 5 mL culture tube, a solid mixture of 2,3,6,7,10,11-hexahydroxytriphenylene (0.0107 mmol, 3.5 mg) and nickel(II) acetate tetrahydrate (0.0201 mmol, 5 mg) was suspended in 1 mL 1-propanol and 1 mL distilled water (1:1 v:v). The loading of the culture tube was carried out under ambient atmosphere and the resulting blue solution was sonicated for 10 s at maximum power. Subsequently, the culture tube was tightly capped and heated at 85°C for 18 h in a preheated oven. The resulting black solution was washed three times with 10 mL dry acetone and isolated by centrifugation. The obtained dark blue microcrystalline product was dried under dynamic vacuum *prior* to analysis.

Co-CAT-1 In a 5 mL culture tube, a solid mixture of 2,3,6,7,10,11-hexahydroxytriphenylene (0.0107 mmol, 3.5 mg) and cobalt(II) acetate tetrahydrate (0.0207 mmol, 5 mg) was suspended in 1 mL of 1-propanol and 1 mL of distilled water (1:1 v:v). The loading of the culture tube was carried out under ambient atmosphere and the resulting blue solution was sonicated for 10 s at maximum power. Subsequently, the culture tube was tightly capped and heated at 85°C for 18 h in a preheated oven. The resulting black solution was washed three times with 10 mL of dry acetone and isolated by centrifugation. The obtained dark blue microcrystalline product was dried under dynamic vacuum *prior* to analysis.

Cu-CAT-1 In a 5 mL culture tube, a solid mixture of 2,3,6,7,10,11-hexahydroxytriphenylene (0.0107 mmol, 3.5 mg) and copper(II) trifluoroacetylacetonate (0.0162 mmol, 6 mg) was suspended in 1 mL of 1-propanol and 1 mL of distilled water (1:1 v:v). The loading of the culture tube was carried out under ambient atmosphere and the resulting blue solution was sonicated for 10 s at maximum power. Subsequently, the culture tube was tightly capped and heated at 85°C for 18 h in a preheated oven. The resulting black solution was washed three times with 10 mL dry acetone and isolated by centrifugation. The obtained dark blue microcrystalline product was dried under dynamic vacuum *prior* to analysis.

Preparation of Ni-, Co-, Cu-CAT-1 pellets Ni- (110.5 mg), Co- (95.8 mg) and Cu- (110.3 mg) CAT-1 pellets (obtained from several of the above described batches) for electrical conductivity measurements were fabricated with a standard Paul-Weber KBr Press by applying moderate pressure of 45 kg cm^{-2}.

3.5.4. Film formation *via* vapor-assisted conversion (VAC)

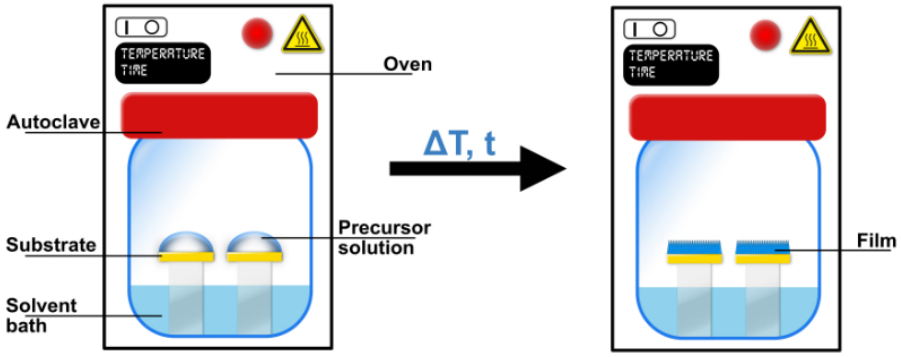

Figure 3.6 – Desired substrates were placed on top of the glass spacers above the solvent bath in a reaction vessel, typically an autoclave. A droplet containing the organic linker, inorganic precursor, and further additives such as modulators was deposited onto the substrate in a way that the whole substrate was evenly covered. The autoclave was tightly sealed and placed in a preheated oven for the adjusted time. During the reaction, the liquid layer was converted into a thin film covering the whole surface.

For the film formation using VAC, a glass bottle (*Schott Duran*, borosilicate 3.3, ISO4796, 100 mL) with a PBT cap equipped with a Teflon seal was used. The bottom part of the bottle was filled with 14 Raschig-rings (10 mm × 10 mm, soda-lime glass) to obtain an elevated flat platform for the substrate. A mixture of water and 1-propanol was filled into the bottle. Afterwards, a substrate (1.2 cm × 1 cm) was placed on top of the Raschig-rings and fully coated with a liquid layer of a freshly prepared MOF precursor solution. The bottle was closed and transferred into a

preheated oven where it was kept for the specified time. Afterwards, the autoclave was removed from the oven and cooled down for 10 min before the substrate was rinsed with dry acetone.

3.5.5. Synthesis of Ni-, Co- and Cu-CAT-1 films on gold surfaces

The HHTP precursor (2.69×10^{-3} mmol; 0.875 mg) and the metal precursors nickel acetate (5.0×10^{-3} mmol; 1.25 mg), cobalt acetate (5.0×10^{-3} mmol; 1.25 mg) or copper trifluoroacetylacetonate (5.0×10^{-3} mmol; 1.25 mg) were mixed in a defined ratio (1:2) and dissolved in a solvent mixture of water and 1-propanol (1.5 mL : 1.5 mL) by sonication for 20 s at maximum power. The obtained precursor solution was filtered through a syringe filter to remove any remaining particles. Subsequent, 40 µL of the solution (HHTP: 0.899 mmol L^{-1}; MOAc: 1.674 mmol L^{-1}) were deposited onto a clean 1.2×1.0 cm gold substrate. Four of these set-ups were placed onto glass spacers in an autoclave loaded with a solvent mixture of water and 1-propanol (2.5 mL : 2.5 mL). The autoclave was sealed immediately and placed into a preheated oven at 85°C for 3.5 h. The experimental set-up of the VAC is shown in Fig. 3.6. Afterwards, the autoclave was removed from the oven and cooled down for 10 min before the substrate was rinsed with dry acetone.

3.5.6. Synthesis of Ni-CAT-1 films on ITO substrates

The HHTP precursor (5.4×10^{-3} mmol; 1.75 mg) and the nickel acetate (10×10^{-3} mmol; 2.5 mg) were mixed in a defined ratio (1:2) and dissolved in a solvent mixture of water and 1-propanol (1 mL : 1 mL) with the addition of modulator acetic acid (50 µL). 40 µL of the respective precursor solution (HHTP: 5.35 mmol L^{-1}; NiAc: 10.7 mmol L^{-1}; HOAc: 1.745 mol L^{-1}) were deposited onto a clean 1.2×1.0 cm ITO substrate. Four of these set-ups were placed onto glass spacers in an autoclave loaded with a solvent mixture of water and 1-propanol (2.5 mL : 2.5 mL). The autoclave was sealed immediately and placed into a preheated oven at 85°C for 18 h. Afterwards, the autoclave was removed from the oven and cooled down for 10 min before the substrates were rinsed with dry acetone.

3.5.7. Synthesis of Ni-1 CAT-1 films on glass substrates

The HHTP precursor (5.4×10^{-3} mmol; 1.75 mg) and the nickel acetate (10×10^{-3} mmol; 2.5 mg) were mixed in a defined ratio (1:2) and dissolved in a solvent mixture of water and 1-propanol (1 mL : 1 mL) with the addition of modulator acetic acid (50 µL). 40 µL of the respective precursor solution (HHTP: 5.35 mmol L^{-1}; NiAc: 10.7 mmol L^{-1}; HOAc: 1.745 mol L^{-1}) were deposited onto a clean 1.2×1.0 cm ITO substrate. Four of these set-ups were placed onto glass spacers in an autoclave loaded with a solvent mixture of water and 1-propanol (2.5 mL : 2.5 mL). The

autoclave was sealed immediately and placed into a preheated oven at 85°C for 18 h. Afterwards, the autoclave was removed from the oven and cooled down for 10 min before the substrates were rinsed with dry acetone.

3.5.8. Synthesis of Co-CAT-1 films on glass substrates

The HHTP precursor (5.4×10^{-3} mmol; 1.75 mg) and the cobalt acetate (10×11.0^{-3} mmol; 3 mg) were mixed in a defined ratio (1 : 2.5 n : n) and dissolved in a solvent mixture of water, 1- propanol (1 mL : 1 mL) with addition of 50 µL of a salicylic acid (0.89 mmol; 125 mg) containing solution in a water, 1-propanol mixture (1 mL : 1 mL). 40 µL of the respective precursor solution (HHTP: 5.35 mmol L^{-1}; CoAc: 12.85 mmol L^{-1}; salicylic acid: 11.23 mmol L^{-1}) were deposited onto a clean 1.2×1.0 cm glass substrate. Four of these set-ups were placed onto glass spacers in an autoclave loaded with a solvent mixture of water and 1-propanol (2.5 mL : 2.5 mL). The autoclave was sealed immediately and placed into a preheated oven at 85°C for 18 h. Afterwards, the autoclave was removed from the oven and cooled down for 10 min before the substrates were rinsed with dry acetone.

3.5.9. Solar Cell device fabrication

Photovoltaic devices were fabricated in accordance with the architecture shown in Fig. 3.7. Herein, ITO was used as the bottom electrode on which Ni-CAT-1 MOF was grown as described in the synthesis protocol. As top electrode and electron contact, 40 nm of aluminum were thermally evaporated.

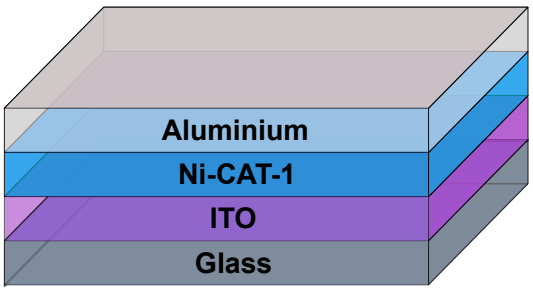

Figure 3.7 – Glass supported ITO was used as substrate for the solar cell fabrication. On top Ni-CAT-1 was synthesized by VAC and aluminum as top-electrode was evaporated.

3.5.10. Characterization of the M-CAT-1 bulk material

XRD, SEM and TEM analysis of the M-CAT-1 bulk material

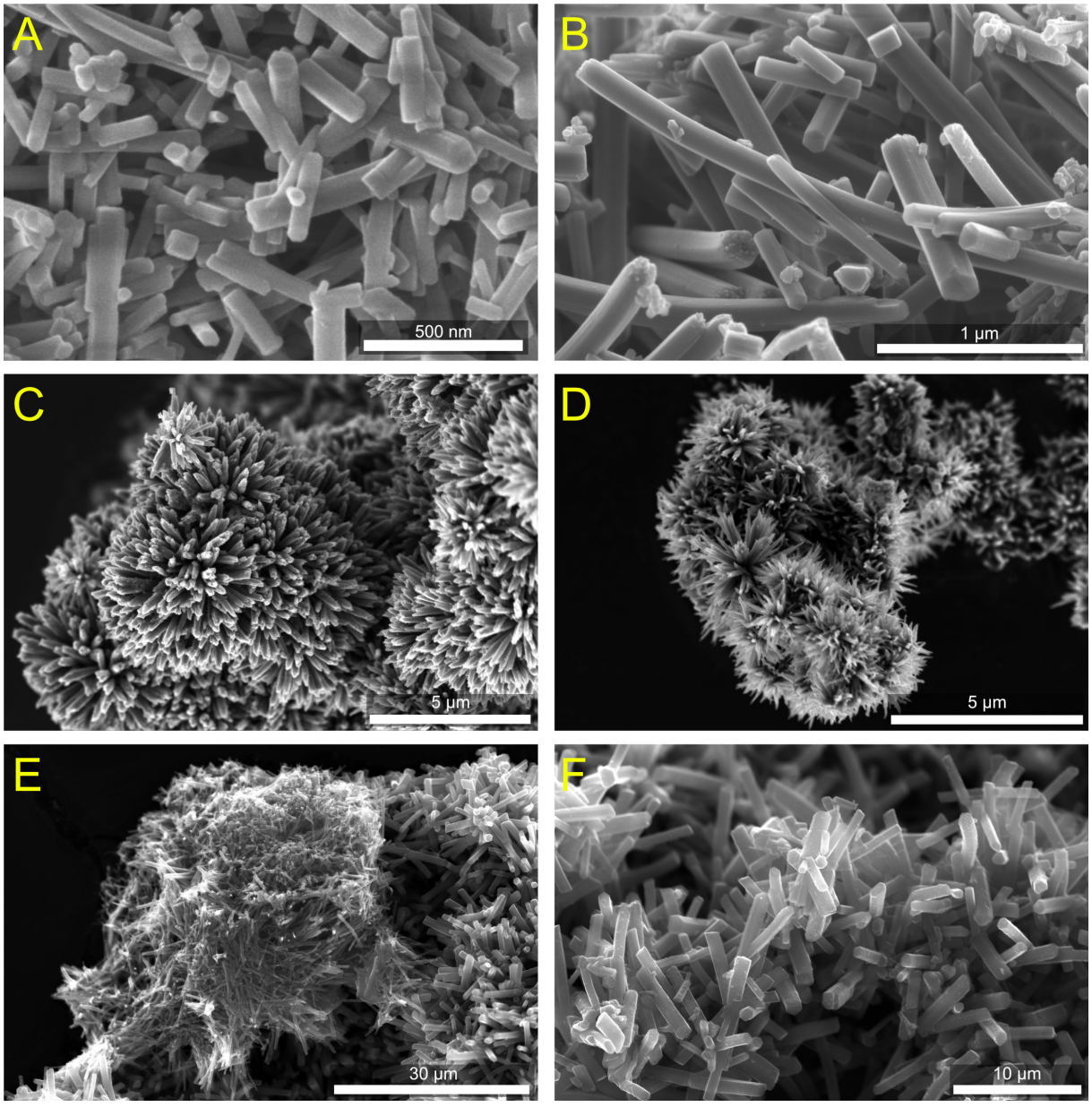

Figure 3.8 – SEM micrographs of the M-CAT-1 bulk materials prepared from a solution of water/1-propanol (v:v; 1:1). A., B. display crystallites of Ni-CAT-1, C and D of Co-CAT-1, while E. and F. show the Cu-CAT-1 bulk material. The typical needle-like morphology of the M-CAT series can be observed in all three cases. Note that the length of the needles increases systematically from 1-2 µm for the Ni-CAT-1 to 3-4 µm of the Co-CAT-1 up to 10 µm for the Cu-CAT-1 MOF.

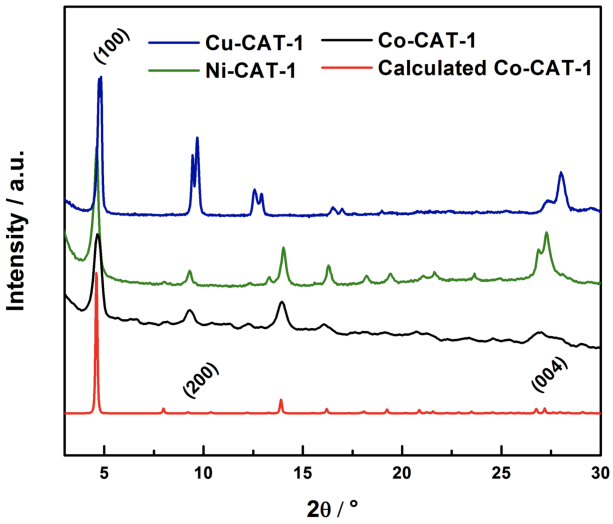

Figure 3.9 – PXRD of the Cu-, Ni-, Co- CAT-1 bulk materials and the simulated PXRD of the Co-CAT-1 displayed in blue, green, black, and red, respectively. As reported before, the Cu-CAT-1 structure differs slightly from the structure of the other two MOFs, resulting in split reflections in the XRD patterns.

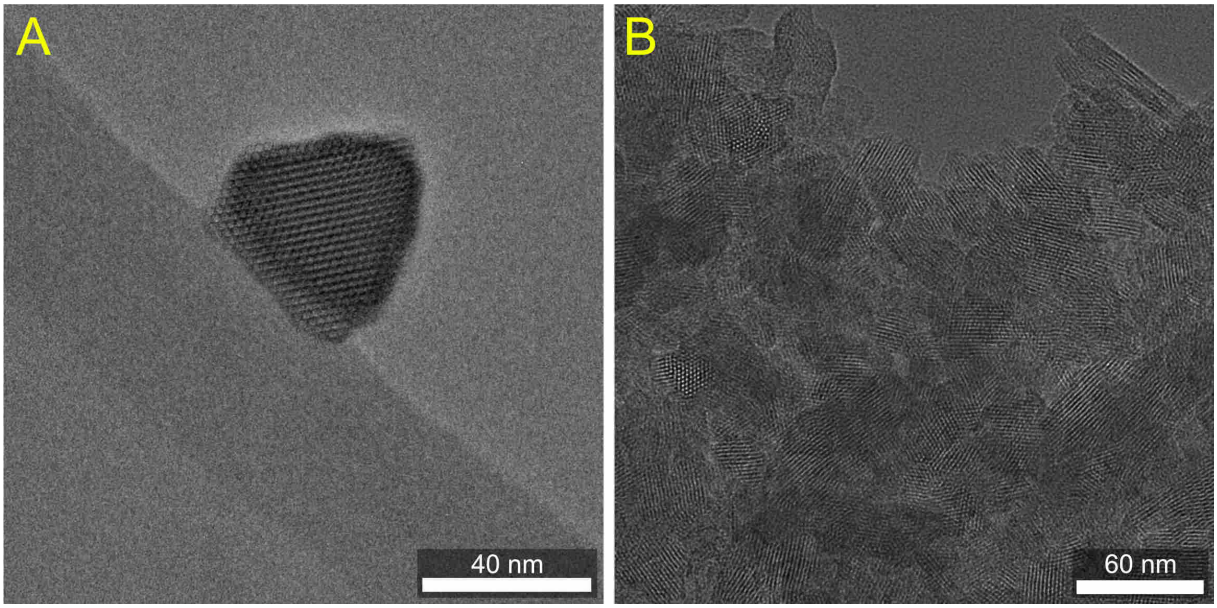

Figure 3.10 – TEM micrographs of the Ni-CAT-1 bulk material. A. Displays the characteristic honeycomb structure of the Ni-CAT-1 MOF. B. Shows randomly distributed crystal domains with sizes in the range of 5-40 nm.

Table 1 – Measurement parameters and electrical conductivity values obtained from van der Pauw analysis of the Ni-, Co-, Cu-CAT-1 pellets.

	Ni-CAT-1	Co-CAT-1	Cu-CAT-1
σ [S cm^{-1}]	6.8×10^{-3}	3.2×10^{-2}	2.7×10^{-2}
d [µm]	550	500	500
I [µA]	100	100	1000

Nitrogen sorption of Ni-, Co and Cu-CAT-1 bulk material

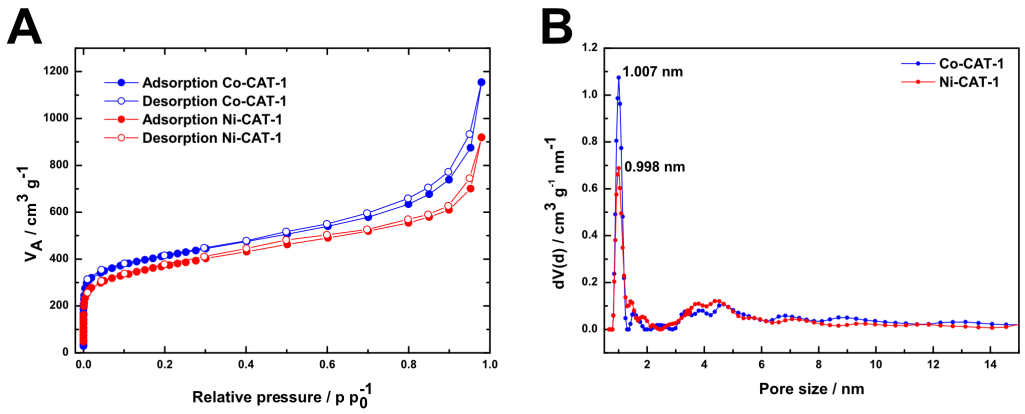

Figure 3.11 – A. Nitrogen adsorption and desorption isotherms of activated Ni- and Co-CAT-1 samples measured at 77.3 K. The process is reversible for both materials and represents a Type I(a) isotherm according to IUPAC. B. The corresponding calculated pore size distributions obtained by DFT.

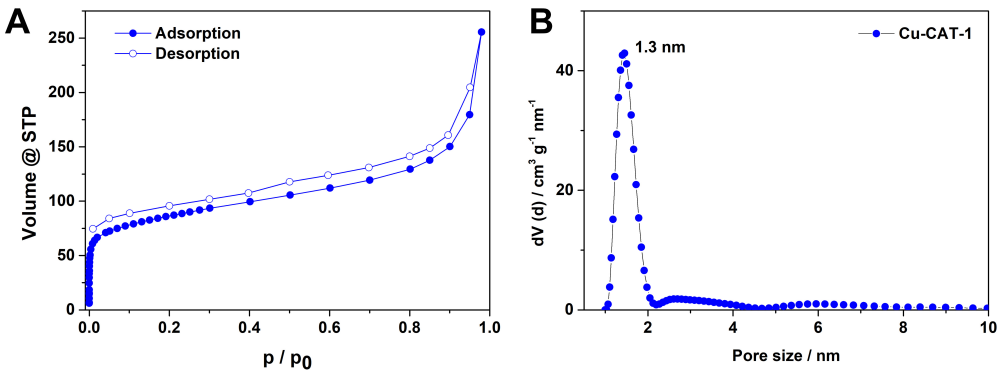

Figure 3.12 – A. Nitrogen ad-and desorption experiments of activated Cu-CAT-1 measured at 77.3 K representing a Type I(a) isotherm according to IUPAC. B. The corresponding calculated pore size distribution obtained by DFT.

M-CAT-1 Pellet Characterization

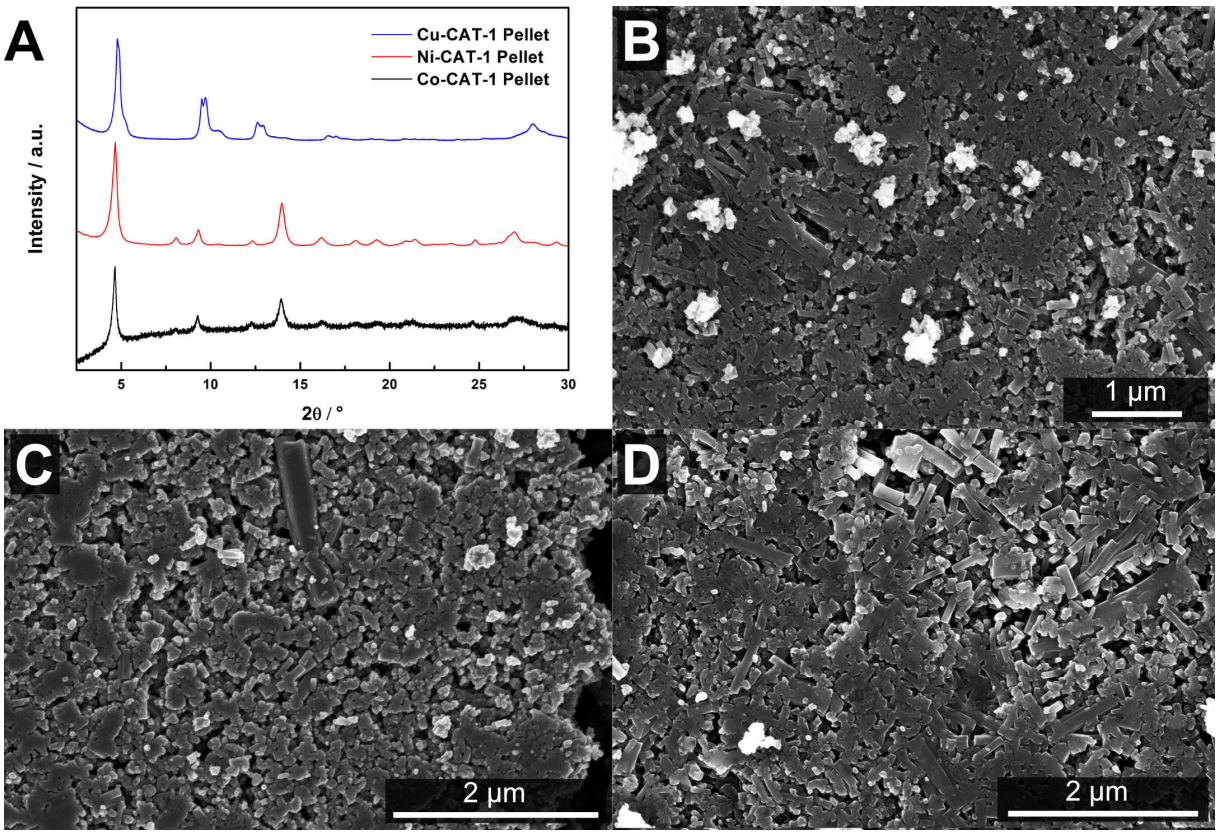

Figure 3.13 – Structural analysis of the as-prepared M-CAT pellets. A. shows the recorded XRD patterns. B., C. and D. display top-view SEM micrographs of the Ni-, Co-, and Cu-CAT-1 pellets, respectively.

3.5.11. Characterization of M-CAT-1 thin films

Analysis of M-CAT-1 thin films grown on gold substrates

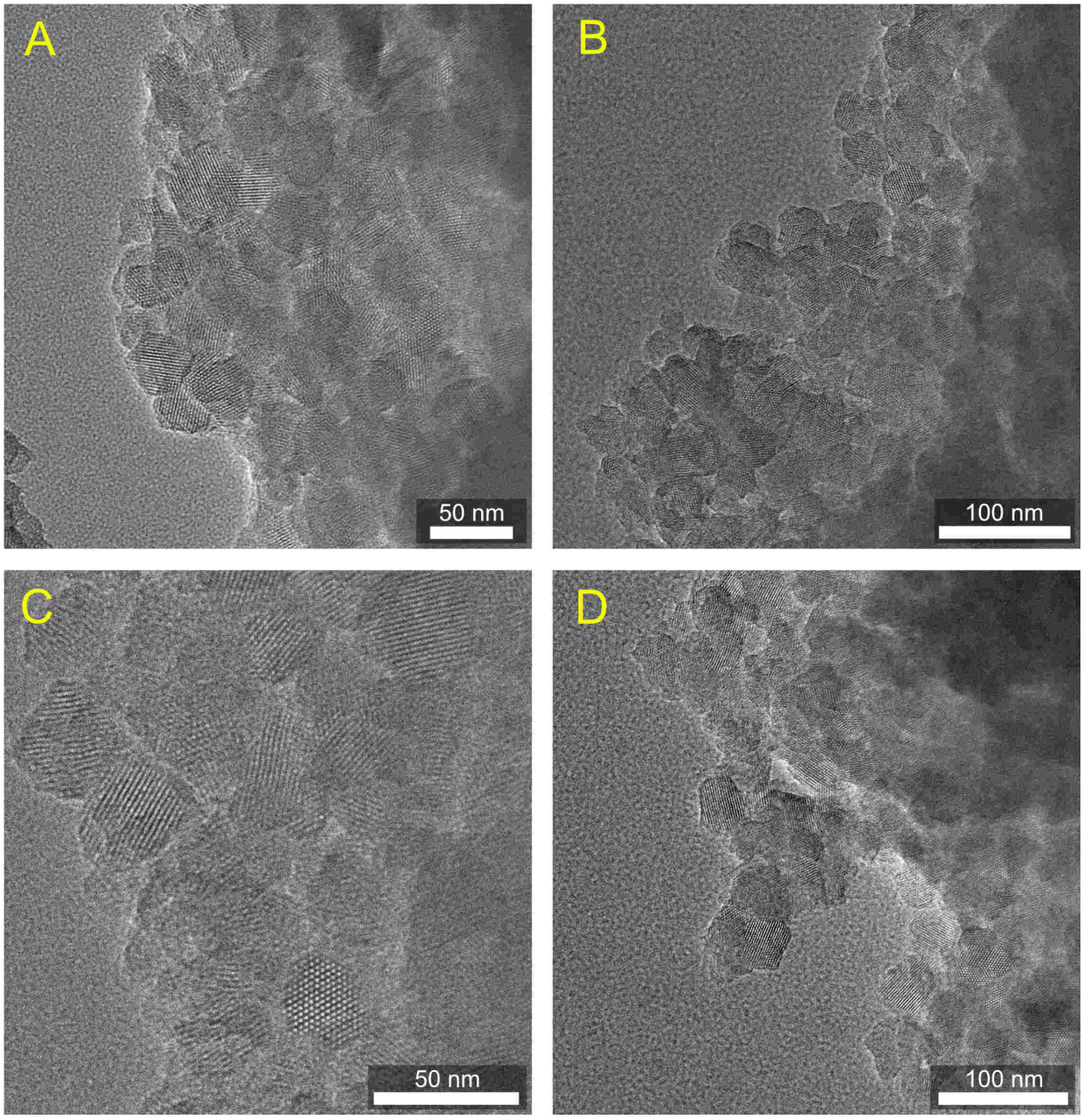

Figure 3.14 – TEM micrographs of Ni-CAT-1 materials grown on gold substrates (removed from substrate). The sample exhibits a crystalline cross-section domain size of up to 50 nm.

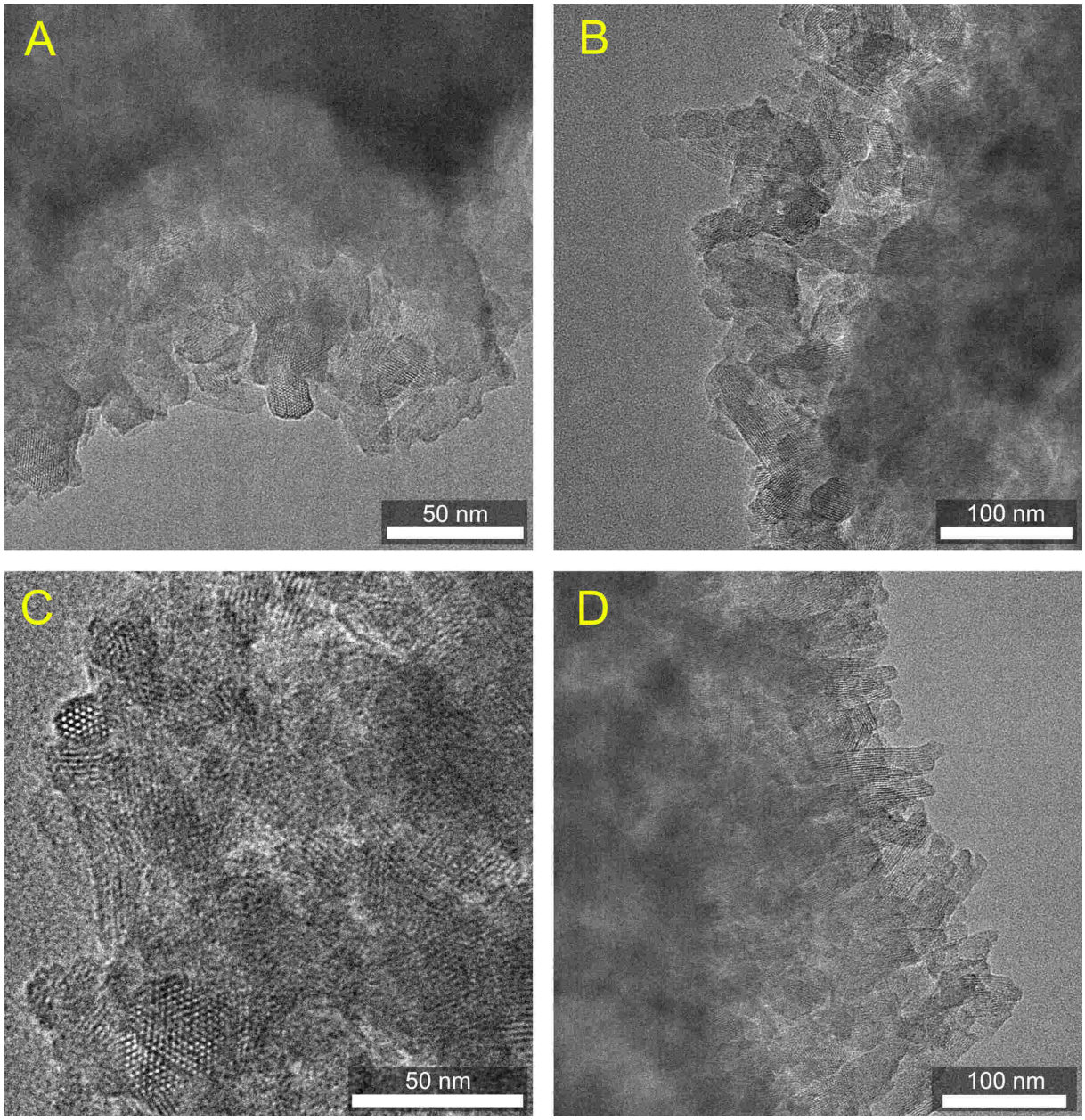

Figure 3.15 – TEM micrographs of Co-CAT-1 materials grown on gold substrates (removed from substrate). The sample exhibits a crystalline cross-section domain size of about 30 nm.

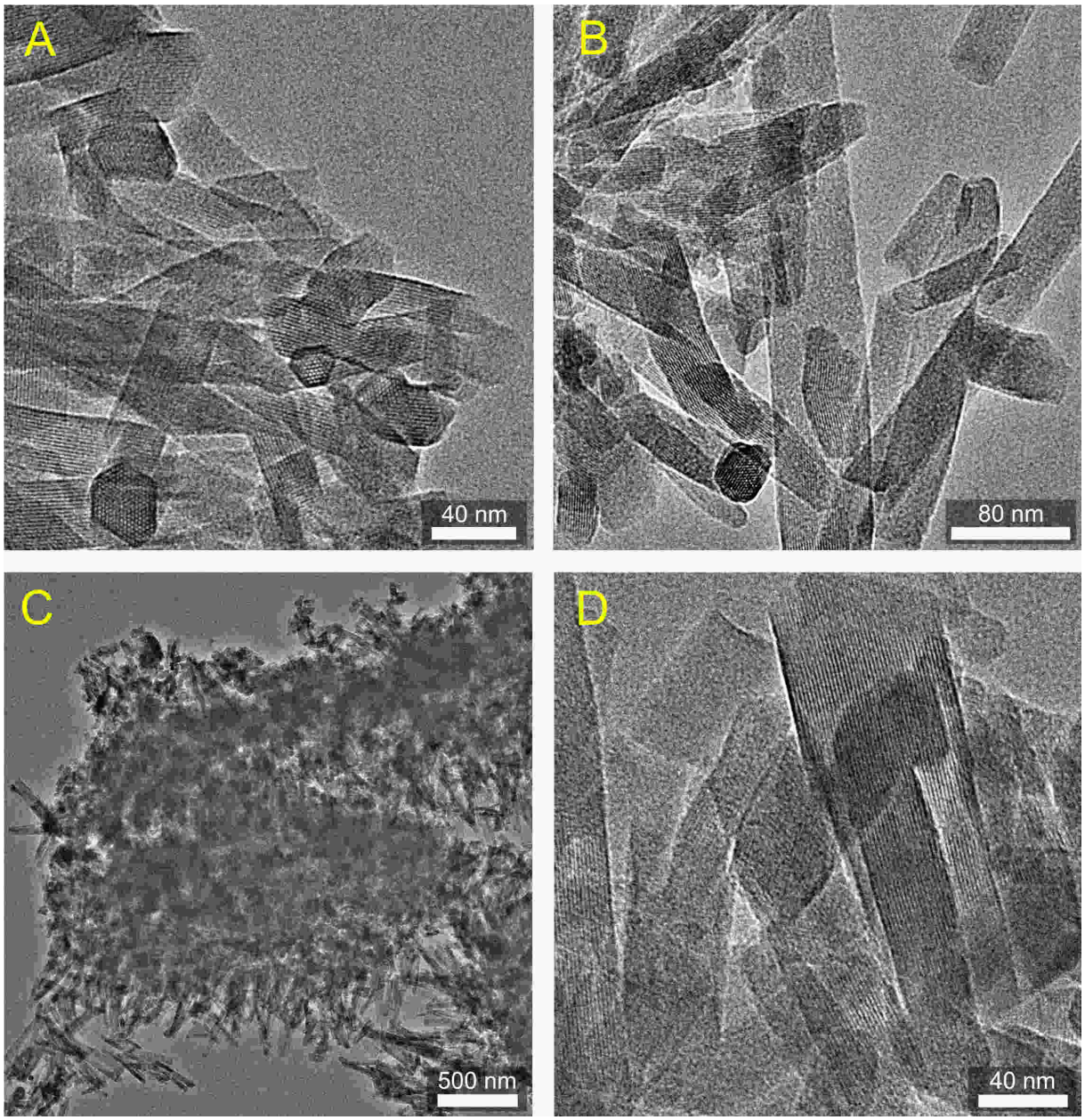

Figure 3.16 – TEM micrographs of Cu-CAT-1 materials grown on gold substrates (removed from substrate). The sample exhibits crystal domains sized about 45 nm and crystal lengths of about 100 nm.

Grazing incidence X-ray detector scan analysis

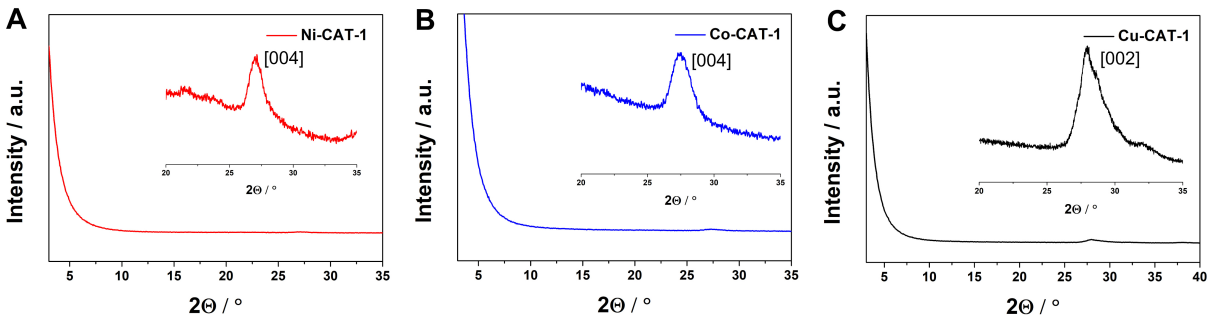

Figure 3.17 – A., B. and C. depicting the XRD detector scans of Ni-, Co and Cu-CAT-1 films on gold substrates showing the high degree of orientation obtained. The strongest reflections at about 27° are attributed to the stacking distance of the MOF layers and are shown as insets.

Data reduction plots of the 2D GIWAXS diffraction analysis

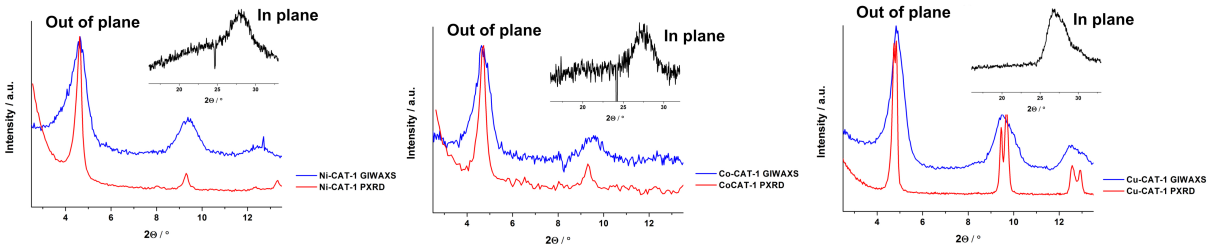

Figure 3.18 – Out of plane and in plane data reduction plots of the 2D GIWAXS diffraction patterns given in Figure 3.2 in the main manuscript, and the powder patterns of corresponding the bulk materials. The patterns confirm that in all experiments M-CAT materials are obtained as the crystalline phase on the substrate surface.

Additional SEM analysis

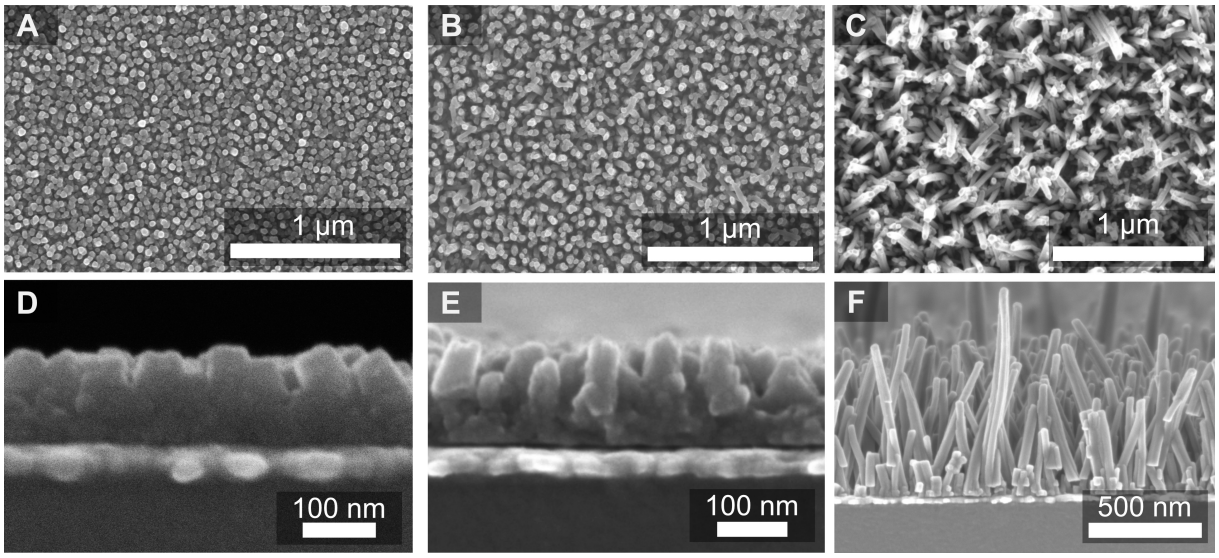

Figure 3.19 – A., B. and C. SEM top-view micrographs of Ni-, Co- and Cu-CAT-1 films on gold substrates at high magnifications. D., E. and F. SEM cross-section images of the same three samples obtained at high magnifications.

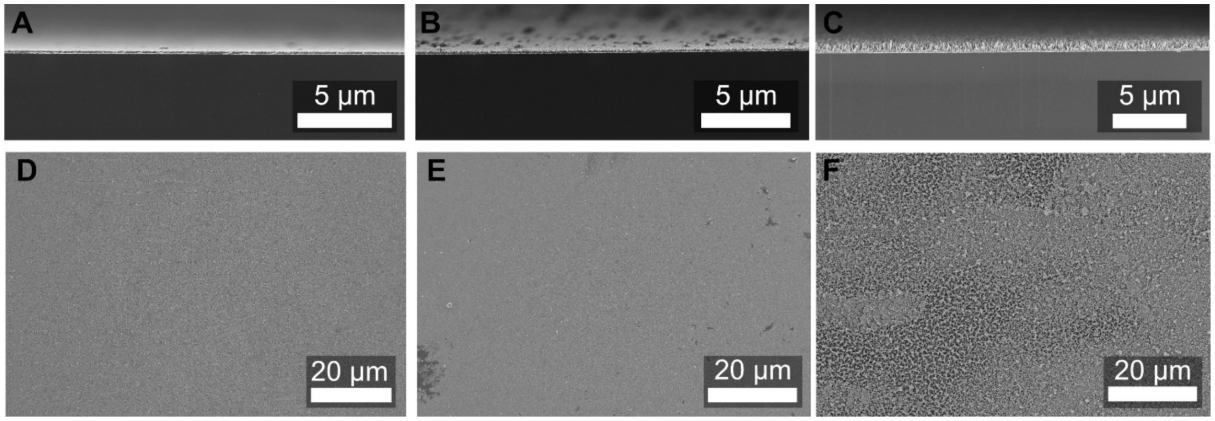

Figure 3.20 – A., B. and C., Large scale SEM cross-section micrographs of the Ni-, Co- and the Cu-CAT-1 thin films on gold substrates. D., E. and F., corresponding large scale SEM top-view micrographs of the same samples.

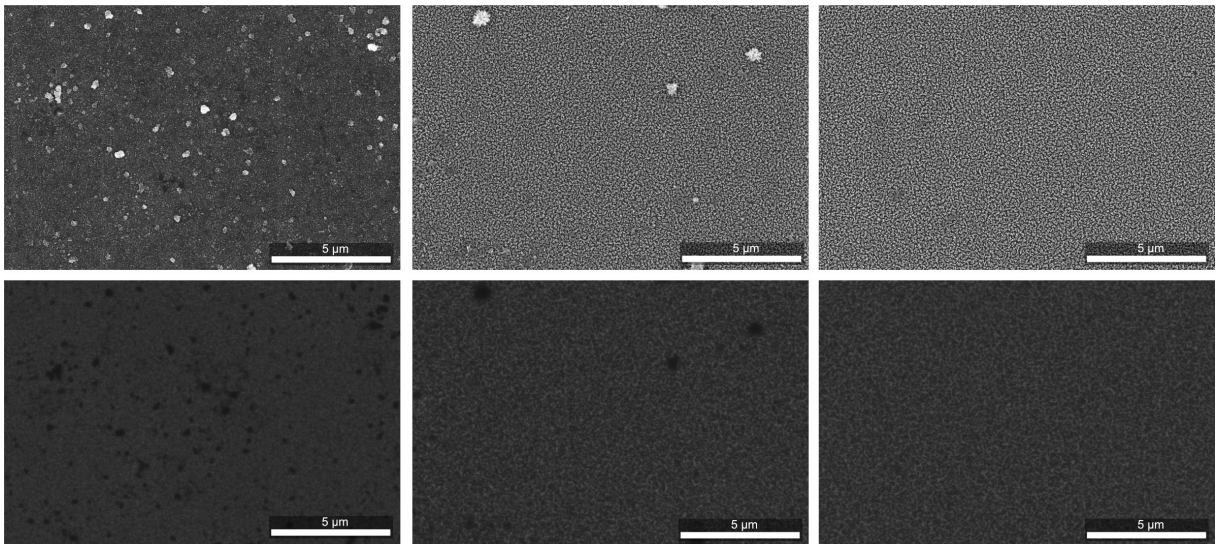

Figure 3.21 – A., B. and C., SEM top-view micrographs of the Ni-, Co and Cu-CAT-1 films on gold substrates. D., E., and F., back-scattered electron analysis at the same sample position.

Additional AFM analysis

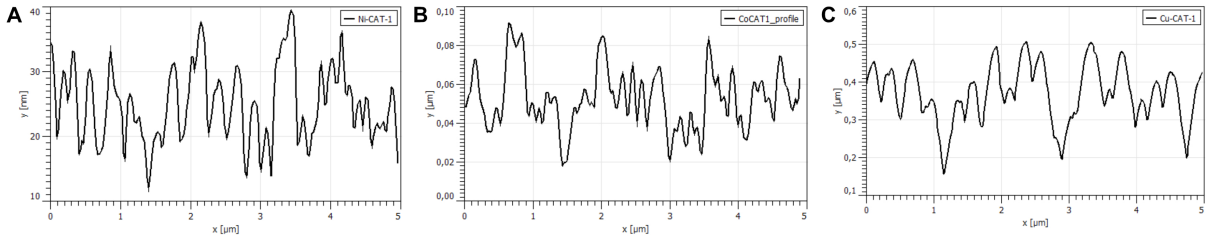

Figure 3.22 – Height profile analysis of the Ni- A., Co- B. and Cu-CAT-1 C., samples grown on gold substrates, respectively. The height profiles correspond to the 3D AFM topography images of Figure 3E., D. and F. presented in the main text.

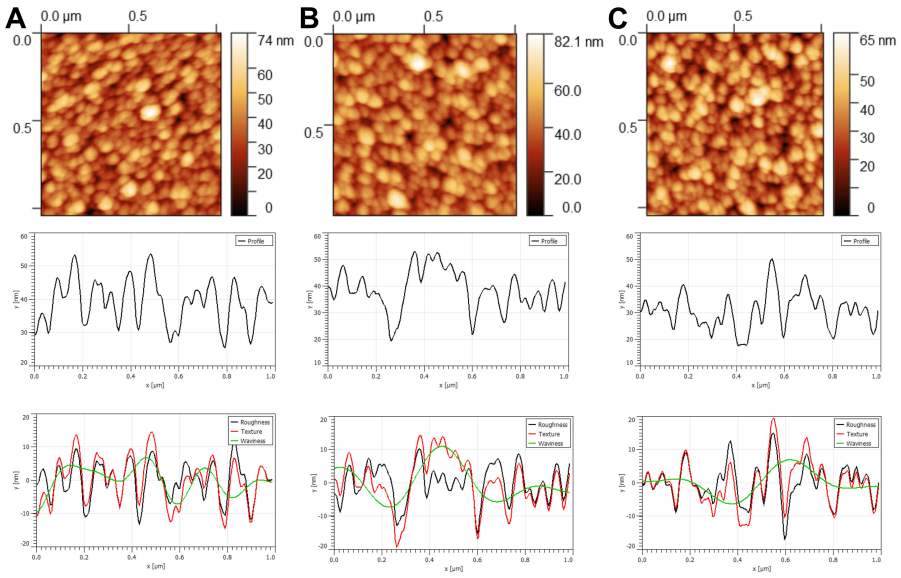

Figure 3.23 – AFM measurements performed on a 1 µm × 1 µm area of Ni-CAT-1 films on gold substrates. A., B. and C, displaying AFM topography images with the corresponding height profile and roughness analysis collected from three different Ni-CAT-1 thin film samples to obtain more accurate statistics on the surface roughness parameters. The average RMS (S_q) and R_q were calculated to be 8 and 7 nm.

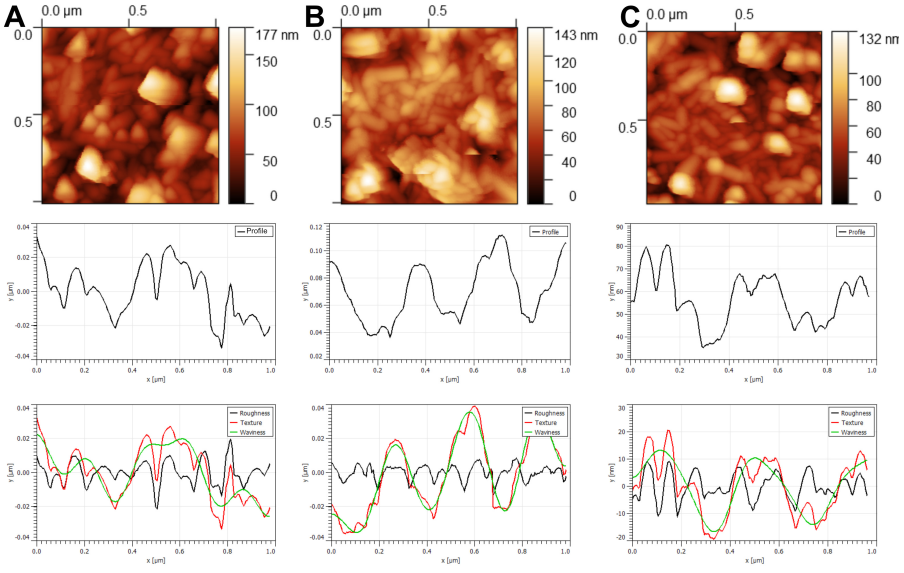

Figure 3.24 – AFM measurements performed on a 1 µm × 1 µm area of Co-CAT-1 films on gold substrates. A., B. and C., displaying AFM topography images with the corresponding height profile and roughness analysis collected from three different Co-CAT-1 thin film samples for more accurate statistics on the surface roughness parameters. The average RMS (S_q) and R_q were calculated to be 19 and 9 nm.

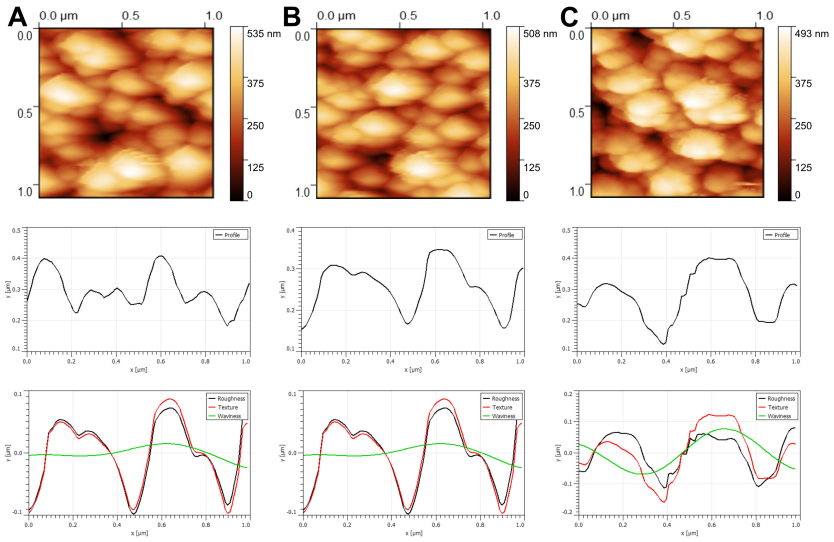

Figure 3.25 – AFM measurements performed on a 1 µm × 1 µm area of Cu-CAT-1 films on gold substrates obtained with copper acetylacetonate as precursor. A., B. and C., displaying AFM topography images with the corresponding height profile and roughness analysis collected from three different Cu-CAT-1 thin film samples for more accurate statistics on the surface roughness parameters. The average RMS (S_q) and R_q were calculated to be 91 and 51 nm.

Cu-CAT-1 film obtained from copper nitrate trihydrate as a precursor

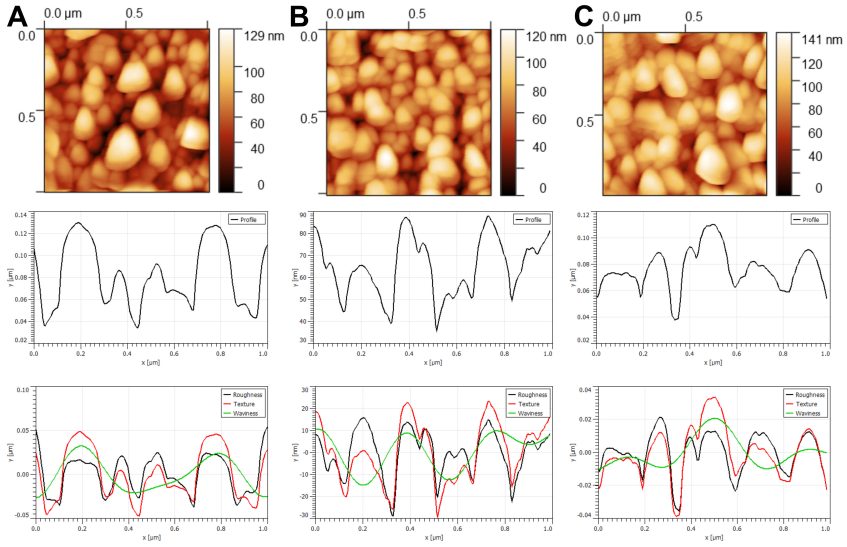

Figure 3.26 – AFM measurements performed on a 1 µm × 1 µm area of Cu-CAT-1 films on gold substrates obtained with copper nitrate as a precursor. A., B. and C. displaying AFM topography images with the corresponding height profile and roughness analysis collected from three different Cu-CAT-1 thin film samples for more accurate statistics on the surface roughness parameters. The average RMS (S_q) and R_q were calculated to be 20 and 10 nm.

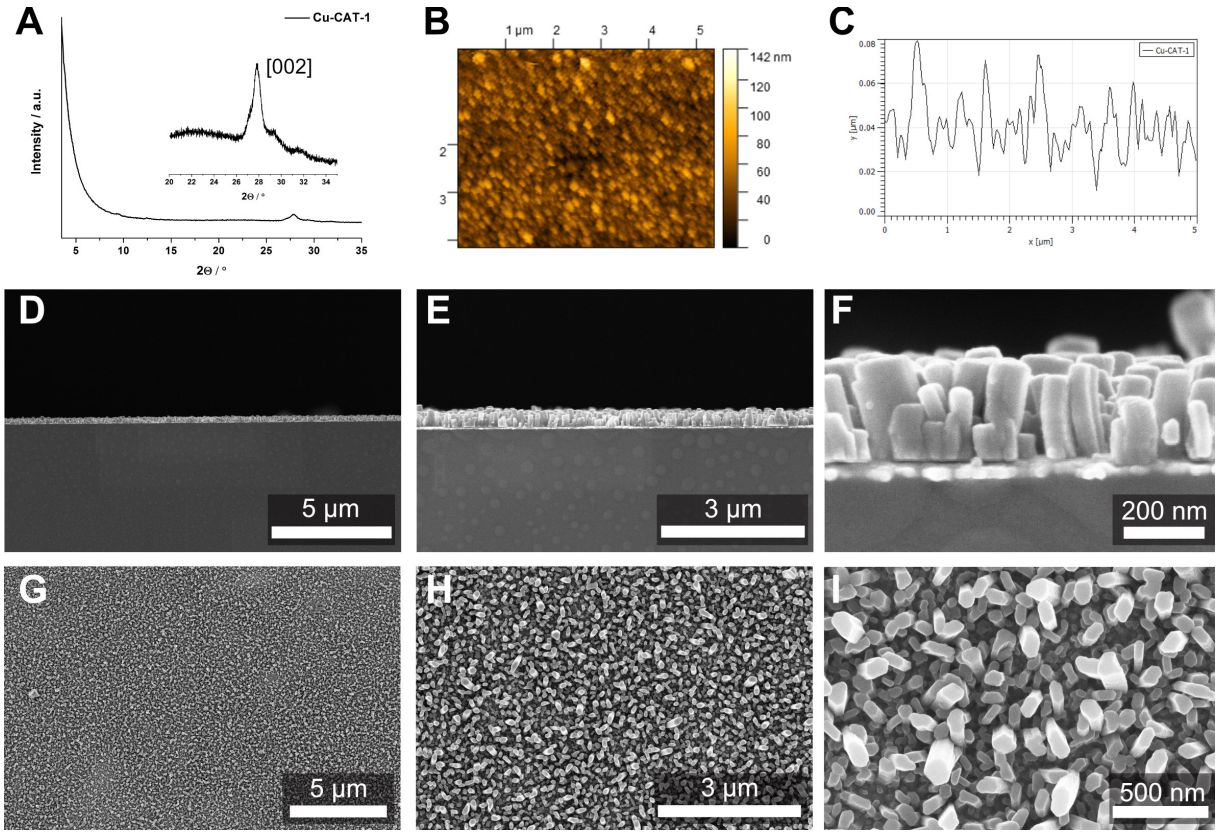

Figure 3.27 – A. XRD detector scan pattern of the Cu-CAT-1 thin film on gold showing a high degree of orientation. High resolution scan of the [002] reflection depicted as an inset. B. 5.2 µm × 4.2 µm AFM topographic scan of the related thin film and C showing corresponding height profile analysis. D. E., and F. cross section analysis of the Cu-CAT-1 film at different magnifications. G. H. and I. top view analysis of the identical sample at different magnifications.

Analysis of M-CAT-1 films grown on oxide surfaces

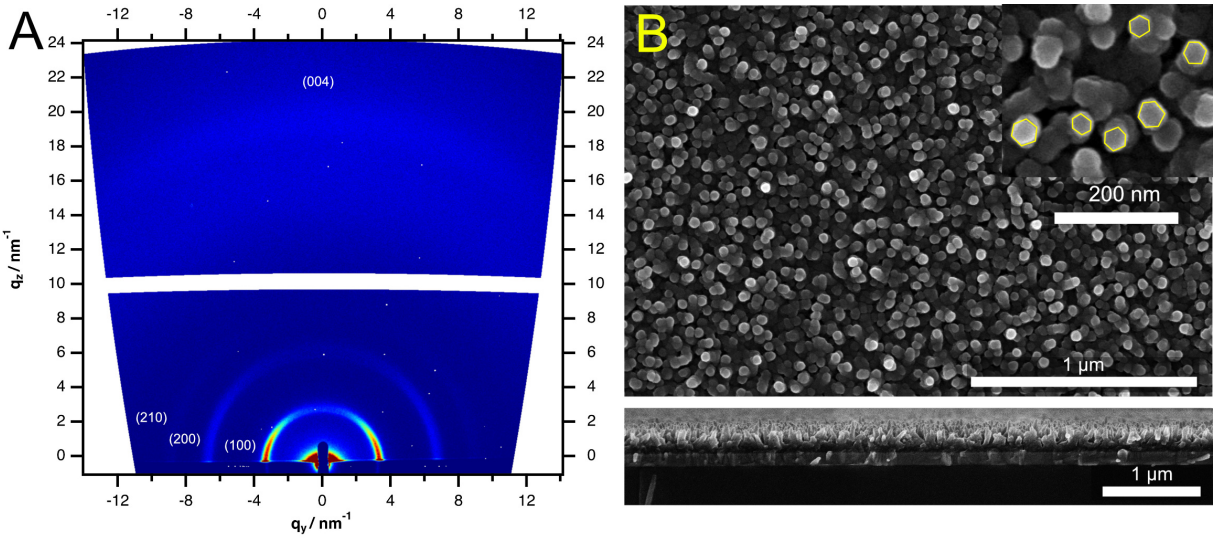

Figure 3.28 – A. GIWAXS analysis of a preferentially oriented Ni-CAT-1 film grown on an ITO substrate. B. Top and cross-section SEM analyses of the Ni-CAT-1 thin film grown on ITO.

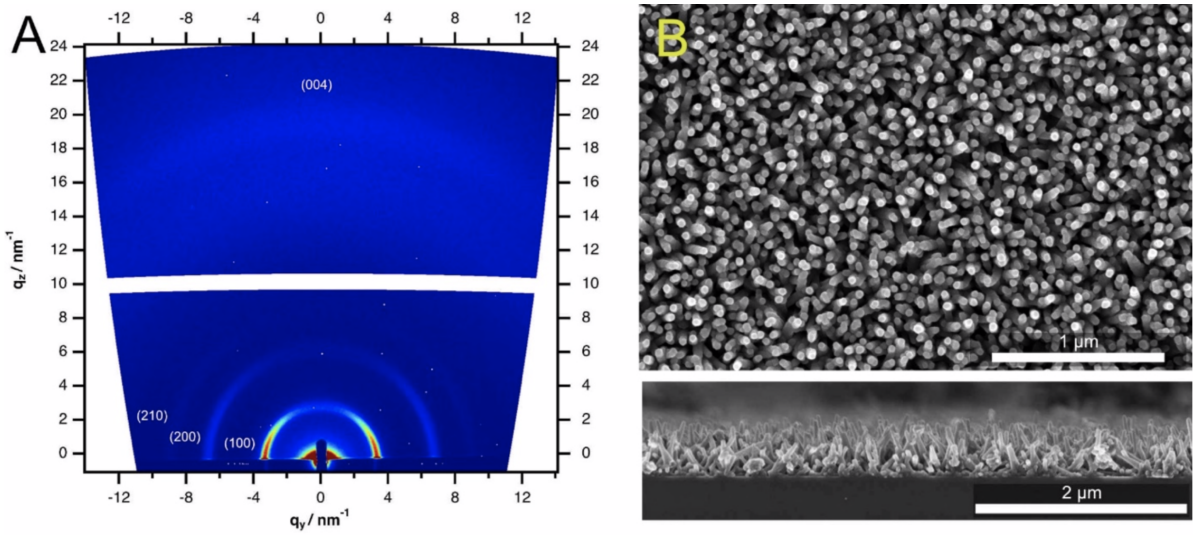

Figure 3.29 – A. GIWAXS analysis of a preferentially oriented Ni-CAT-1 film grown on a glass substrate. B. SEM top-view and cross-section analysis of Ni-CAT-1 films grown on glass. The needle-like crystals exhibit lengths of about 200 nm.

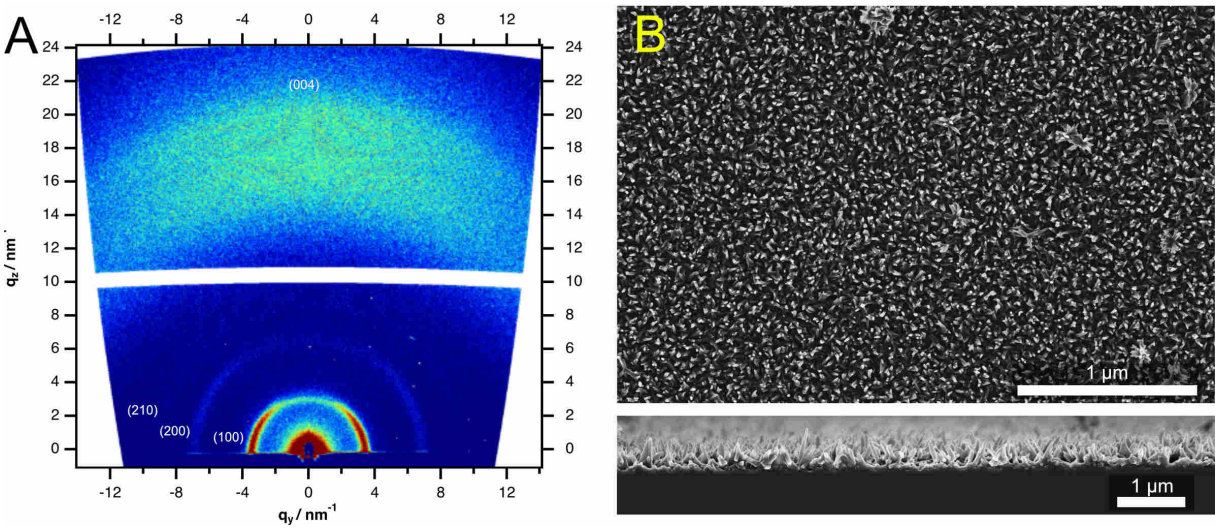

Figure 3.30 – A. GIWAXS analysis of a preferentially oriented Co-CAT-1 film grown on a glass substrate. B. SEM top-view and cross-section analysis of Co-CAT-1 films grown on glass.

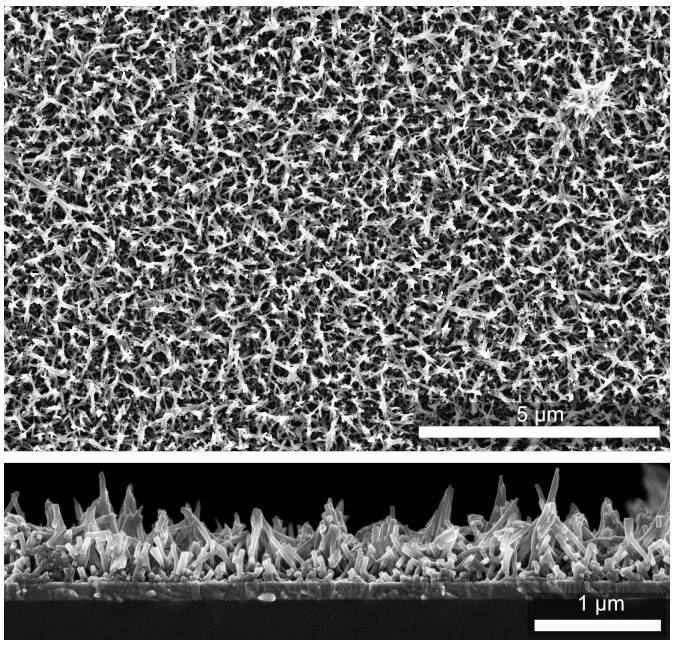

Figure 3.31 – SEM top-view and cross-section analysis of a Co-CAT-1 film grown on an ITO substrate. The needle- like crystallites display lengths of about 1 µm.

Additional AFM analysis

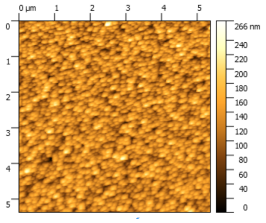

Figure 3.32 – AFM scan of a representative 5 µm × 5 µm Ni-CAT-1 thin film grown on ITO. The RMS roughness was calculated to be 28 nm.

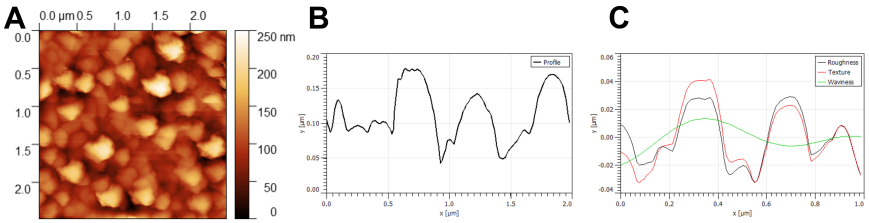

Figure 3.33 – AFM measurements performed on a 2.5 µm × 2.5 µm area of Ni-CAT-1 film on an ITO substrate with the corresponding height profile and roughness analysis. The average RMS (S_q) and R_q were calculated to be 28 and 19 nm.

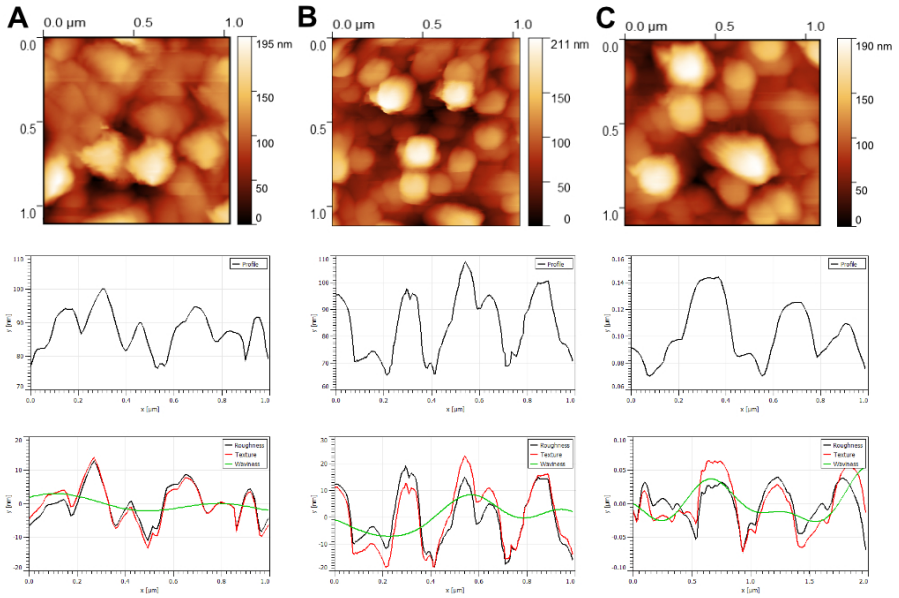

Figure 3.34 – AFM measurements performed on a 1 µm × 1 µm area of Ni-CAT-1 films on ITO substrates. A., B. and C. displaying AFM topography images with the corresponding height profile and roughness analysis collected from three different Ni-CAT-1 thin film samples for accurate statistics on the surface roughness parameters. The average (S_q) and R_q were calculated to be 25 and 18 nm.

Electrical conductivity measurements of Ni- and Co-CAT-1 films on glass substrates

Table 2 – Measurement parameters and electrical conductivity values obtained from van der Pauw analysis of the Ni- and Co -CAT-1 films grown on glass substrates.

	Ni-CAT-1	Co-CAT-1
σ [S cm^{-1}]	1.1×10^{-3}	3.3×10^{-2}
d [µm]	0.2	0.2
I [µA]	25	25

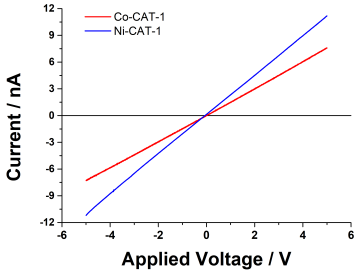

Figure 3.35 – Two-probe I-V measurements of the Ni- and Co-CAT-1 films grown on 1.0 cm × 1.2 cm quartz substrates. Electrodes were positioned at a distance at around 5 mm on the sample. Analysis gives electrical conductivity values of around 2.5 and 3.3×10^{-4} S cm^{-1} for the Ni- and the Co-CAT-1 samples.

Control Experiments

SEM of M-CAT-1 films grown on ITO substrates without acetic acid modulator

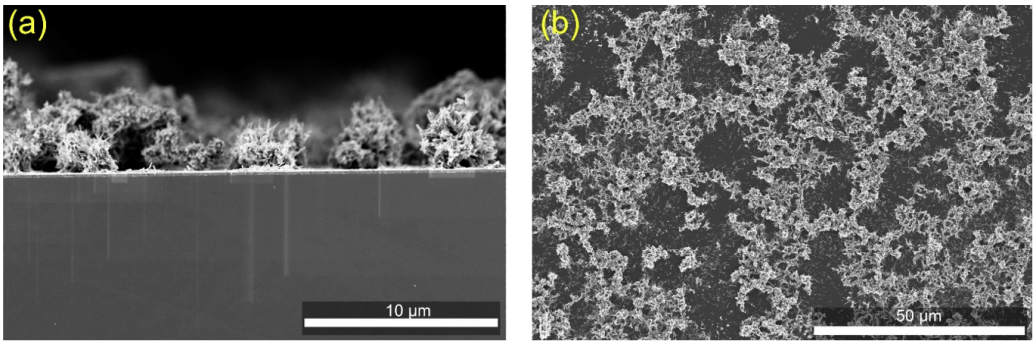

Figure 3.36 – A. SEM cross-section of scattered Ni-CAT-1 crystals on an ITO surface. B. The corresponding SEM top-view analysis of the sample showing that the formed material is deposited as agglomerates on the surface.

SEM and GIWAXS analysis of Cu-CAT-1 grown on an ITO surface

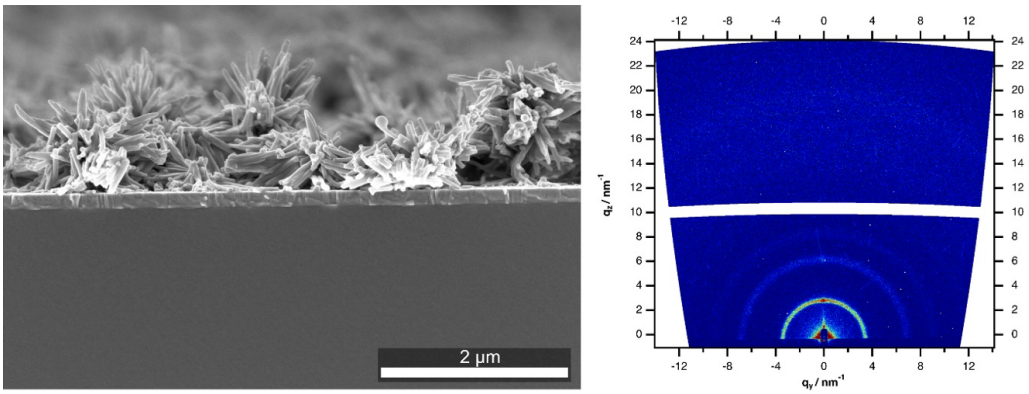

Figure 3.37 – A. SEM cross-section of scattered Cu-CAT-1 crystals on an ITO surface. B. The corresponding GIWAXS analysis of the sample showing that the formed material is deposited as non-oriented crystalline agglomerates on the surface.

Macroscopic photographs of the Ni- and Co-CAT-1 films on quartz substrates

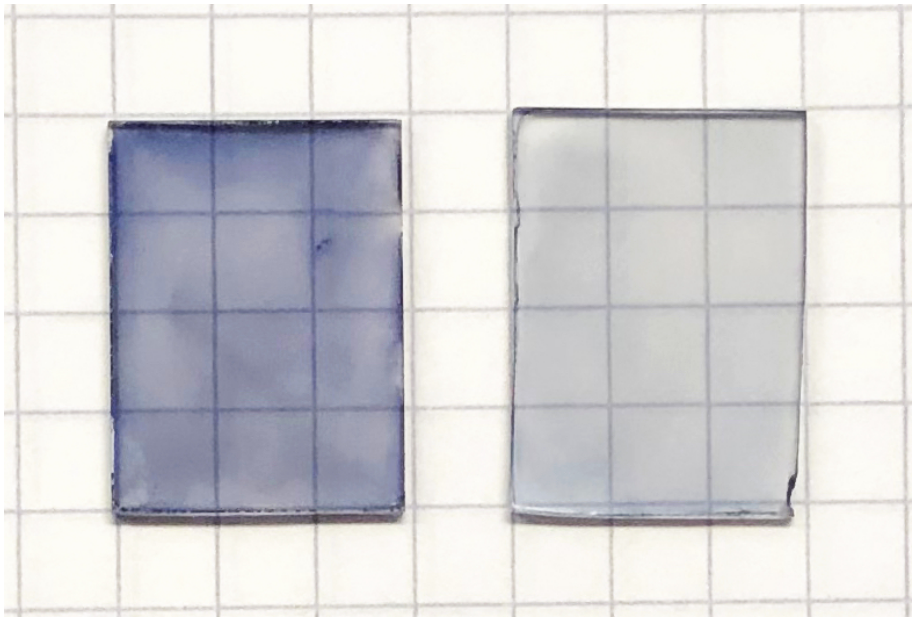

Figure 3.38 – Macroscopic photographs of Ni-CAT-1 (left) and Co-CAT-1 films (right) on quartz substrates.

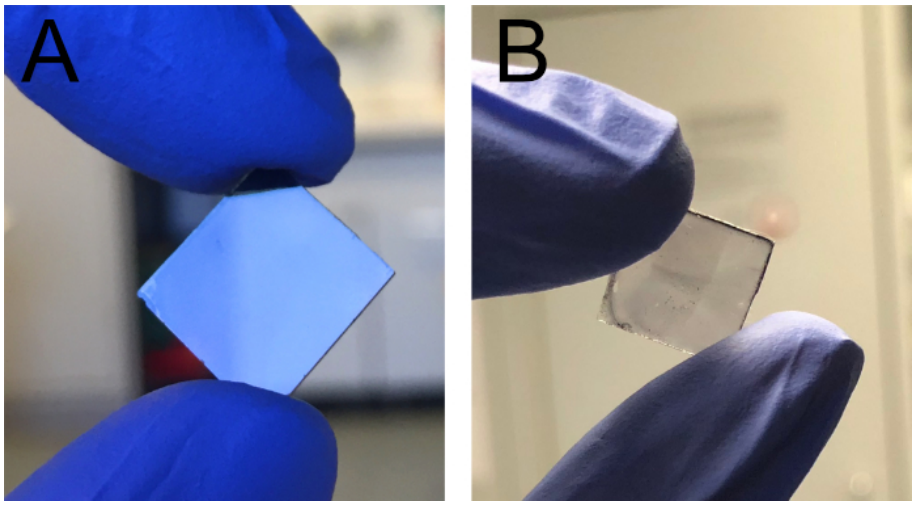

Figure 3.39 – Macroscopic photographs of A. Ni-CAT-1 and B. Co-CAT-1 films on ITO substrates.

3.5.12. Additional analysis

UV-Vis spectra of precursors and reference compounds

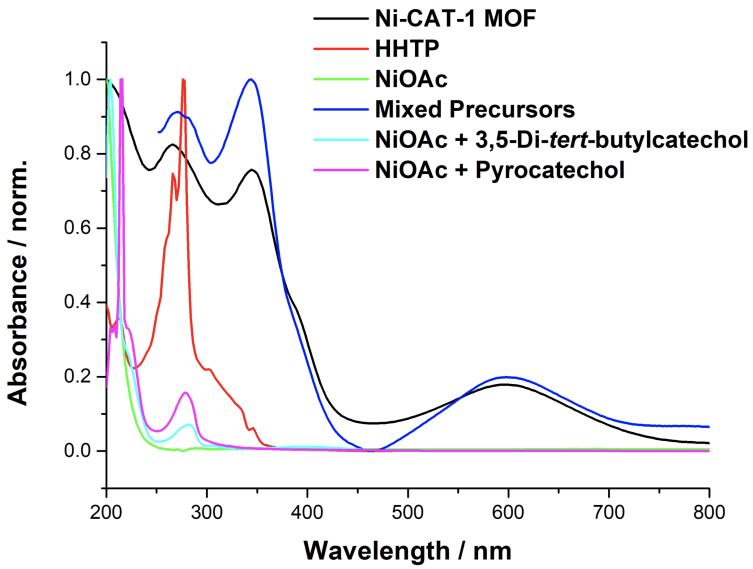

Figure 3.40 – UV-Vis spectra for HHTP, $Ni(OAc)_2$, the mixed precursors, $Ni(OAc)_2$ + 3,5-di-*tert*-butylcatechol and $Ni(OAc)_2$ + pyrocatechol dissolved in ethanol displayed in red, green, blue, cyan, and magenta, respectively. The mixed precursor solution contains the drop-cast solution (HHTP + $Ni(OAc)_2$) for the Ni-CAT-1 thin film synthesis on gold substrates. $Ni(OAc)_2$ + 3,5-di-*tert*-butylcatechol and $Ni(OAc)_2$ + pyrocatechol represent model complexes.

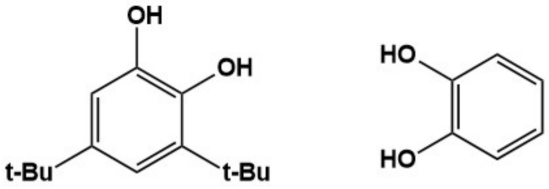

Figure 3.41 – Left: 3,5-di-*tert*-butylcatechol. Right: Pyrocatechol.

Cyclic voltammetry (CV) analysis of Ni-CAT-1 films grown on gold substrates

CV experiments were performed on a *Metrohm Autolab PGStat302N* in a sealed borosilicate glass cell in a three-electrode configuration with the MOF film grown on fluorine-doped tin oxide (FTO) as the working electrode, a platinum wire counter electrode and a silver wire as the reference. The cell was assembled in an argon-filled glove box. The electrolyte was 0.1 M NBu_4PF_6 (Aldrich, 99.9%) in methylene chloride (Aldrich, anhydrous, inhibitor-free). The MOF films were activated in vacuum at 120°C for several hours *prior* to use. The potential of the Ag reference vs. ferrocene (Aldrich, 95% resublimed) was established by adding ferrocene to the electrolyte after the first measurement and recording a second cyclic voltammogram. CV was performed at potentials between -0.2 and 1.4 V vs. ferrocene and a scan rate of 20 mV s^{-1}.

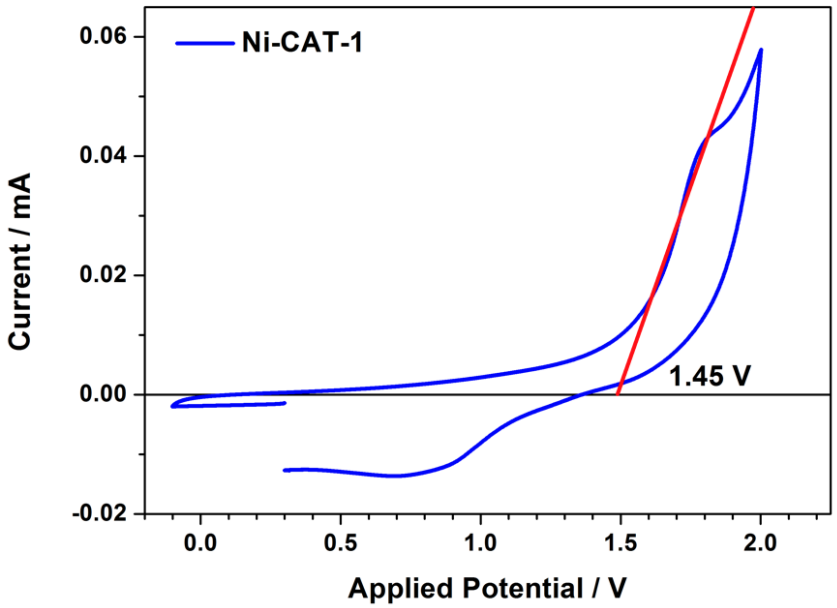

Figure 3.42 – Cyclic voltammogram of Ni-CAT-1 grown on fluorine-doped tin oxide (FTO). Scan direction from 0.2 V to higher potentials ending at 0.3 V. The red line indicates the onset potential of the Ni-CAT-1 film.

TCSPC data of Ni- and Co-CAT-1 films grown on quartz substrates

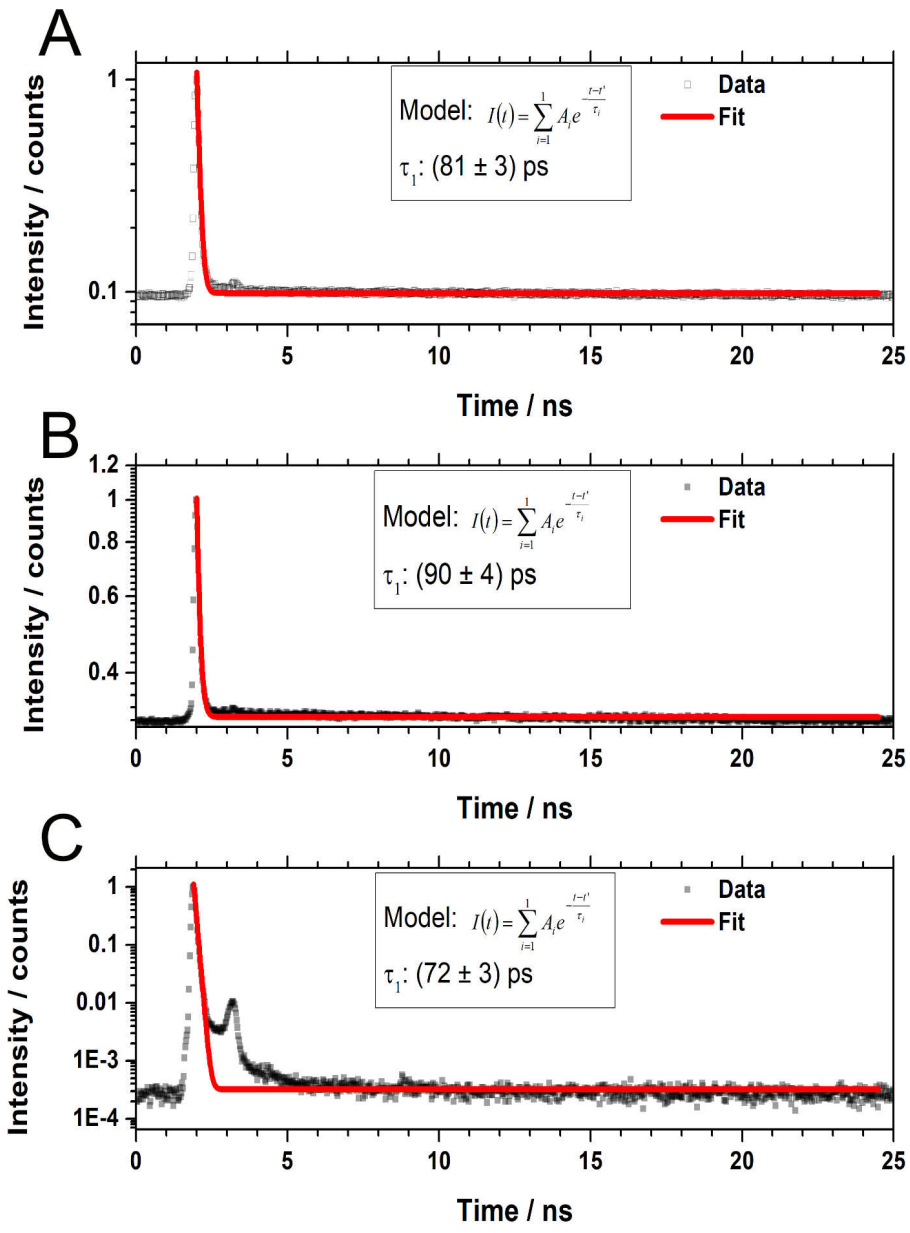

Figure 3.43 – TCSPC histograms (black dots) and monoexponential fits (red lines) of A. Ni-CAT-1 and B. Co-CAT-1 films grown on quartz substrates. C. Recorded IRF of the 378 nm laser.

Energy level alignment of an ITO/Ni-CAT-1/Al device

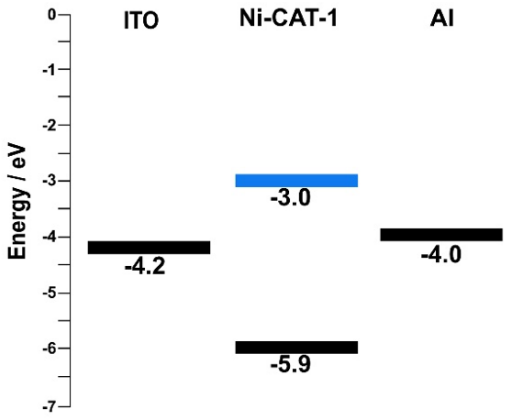

Figure 3.44 – Energy level alignment of an ITO/Ni-CAT-1/Al device.

Transient absorption plots of Ni-CAT-1 for an excitation wavelength of 350 nm

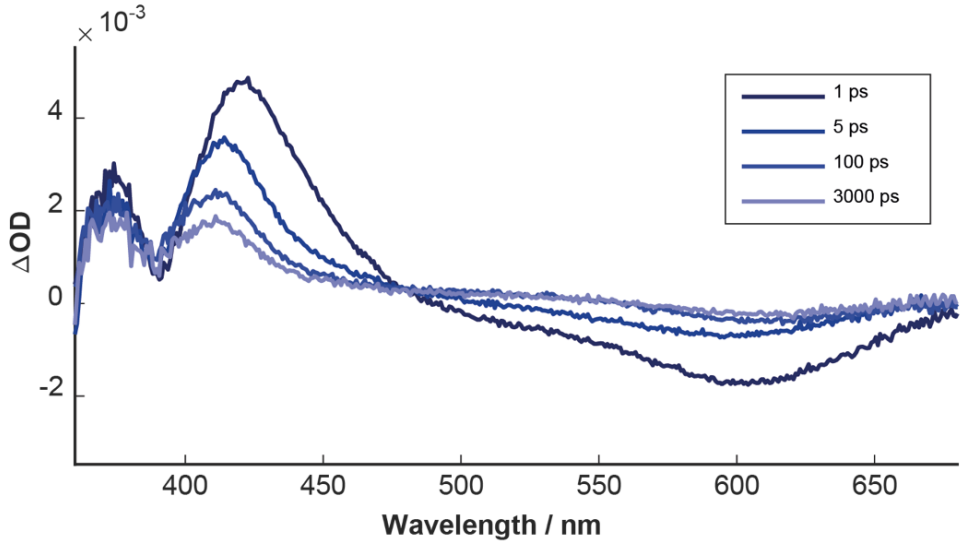

Figure 3.45 – Transient absorption spectra of a Ni-CAT-1 film on a quartz substrate for different pump-probe time delays, excited at 350 nm with an excitation density of 29 µJ cm^{-2}. At this excitation wavelength the full width of the broad photo-induced absorption feature from 360-480 nm is observable. The actual bleaching of the band edge state of the MOF film is superimposed on this signal and appears as a dip at around 390 nm within the broad positive above-mentioned feature. Interestingly, the bottom of the dip stays approximately constant over the whole transient, indicating that the rates of decay of the band edge bleach and the broad photo-induced signal are similar. This means that the signal between 415 and 450 nm can represent the band edge bleach due to this proportionality.

TSCPC data of Ni-CAT-1 grown on quartz

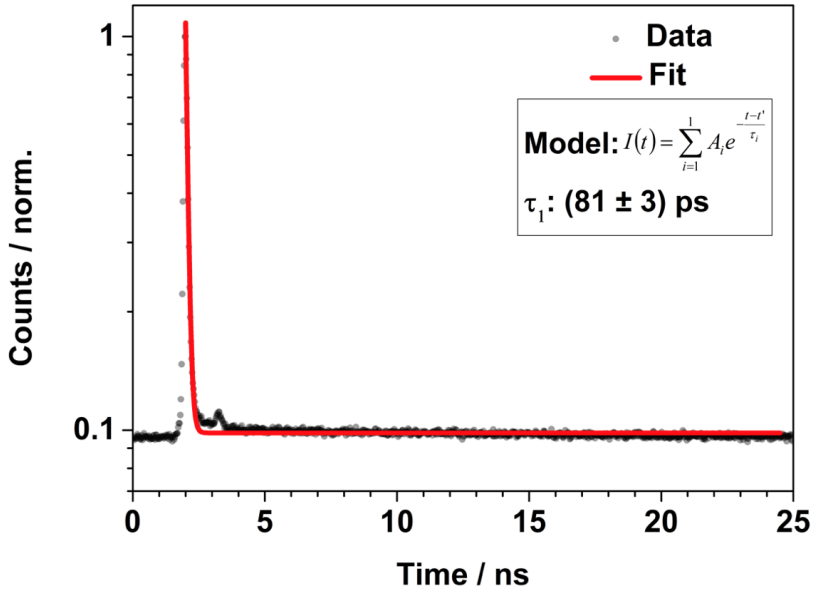

Figure 3.46 – Time-correlated single photon counting histogram (black dots) and respective fit (red) of Ni-CAT-1, excited at 378 nm and measured at 545 nm. The fitted mono-exponential decay lifetime is 81 ps, which is very similar to the instrument response.

4. Nanostructured and oriented metal-organic framework films enabling extreme surface wetting properties

This chapter is based on the following publication:

Andre Mähringer[†,§], Julian M. Rotter[†,§] and Dana D. Medina[*,†,§], *Beilstein J. Nanotechnol.* **2019,** *10,* 1994-2003.

[†]Department of Chemistry, Ludwig-Maximilians-Universität (LMU), Butenandtstr. 11 (E), 81377 Munich, Germany.

[§]Nanosystems Initiative Munich (NIM) and Center for NanoScience (CeNS), Schellingstr. 4, 80799 Munich, Germany.

[*]Corresponding Author

This manuscript was awarded with the *Beilstein young investigator award*, Beilstein Symposium "New directions for nanoporous materials", Rüdesheim, Germany.

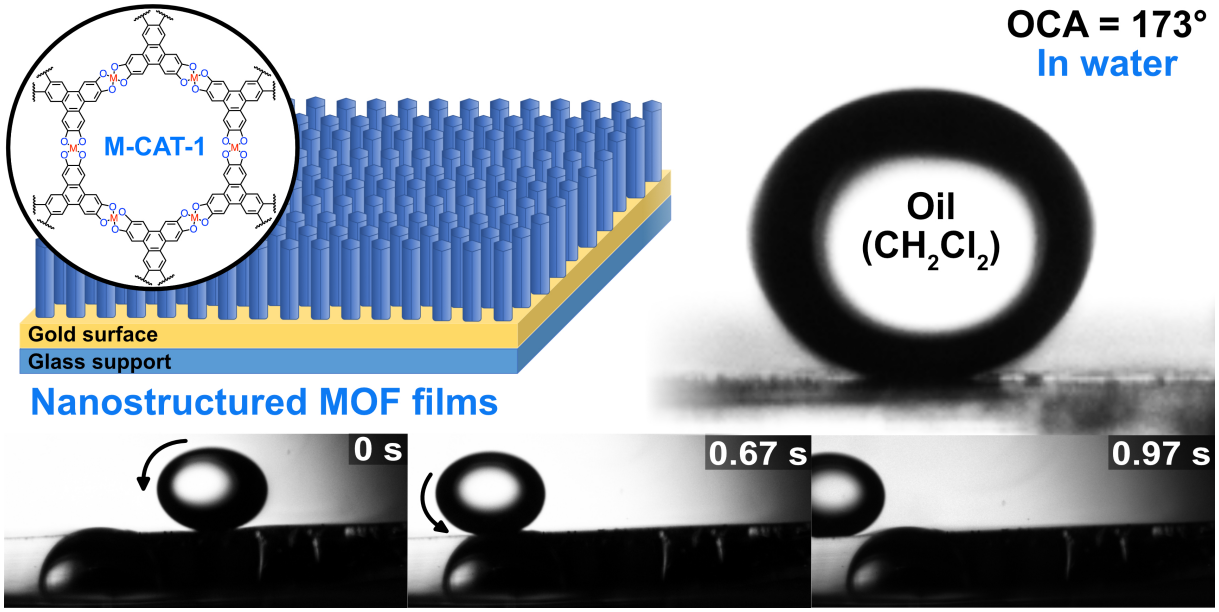

DOI: 10.3762/bjnano.10.196

Abstract

We report on the synthesis of highly oriented and nanostructured metal-organic framework (MOF) films featuring extreme surface wetting properties. The Ni- and Co- derivatives of the metal-catecholate series (M-CAT-1) were synthesized as highly crystalline bulk materials and thin films. Oriented pillar-like nanostructured M-CAT-1 films exhibiting pronounced needle-like morphology on gold substrates were established by incorporating a crystallization promoter into the film synthesis. These nanostructured M-CAT-1 MOF films feature extreme wetting phenomena, specifically superhydrophilic and underwater superoleophobic properties with water and underwater oil-contact angles of 0° and up to 174°, respectively. The self-cleaning capability of the nanostructured, needle-like M-CAT-1 films was illustrated by measuring time-dependent oil droplet rolling-off a tilted surface. The deposition of the nanostructured Ni-CAT-1 film on a large glass substrate allowed for the realization of an efficient, transparent, antifog coating, enabling a clear view even at extreme temperature gaps up to 120°C. This work illustrates the strong link between MOF film morphology and surface properties based on these framework materials.

4.1. Introduction

Over millions of years, plants and animals have evolved a spectrum of surface designs enabling specific wetting properties tailored for their survival in extreme conditions [1–4]. In plants, the unique surface architecture of the lotus leaf enables superhydrophobic and self-cleaning properties for sustaining efficient photosynthesis, even in polluted environments [5–7]. In the realm of animals, mosquitos utilize an antifog coating covering their eyes for clear vision in high humidity regions [8]. The fogstand beetles employ an antifog coating for enhancing water vapor harvesting abilities in dry climates [9]. In marine life, fish protect themselves from oil-polluted environments or avoid biofouling due to oil-repellent designs and self-cleaning capabilities of their skin [10–12]. These intriguing superhydrophilic or superoleophobic surface characteristics are obtained by the combination of a precise chemical composition and hierarchical microstructuring of the surface [13–16]. Nowadays, modern surface technologies such as antifog or antifouling, oil-repellant coatings, self-cleaning surfaces and water-harvesting systems are inspired by nature's designs [17–26]. The synthesis of artificial superhydrophilic surfaces can be achieved by a variety of routes, for example, sol-gel synthesis, electrochemical deposition, anodization, electrochemical polymerization, electrospinning, plasma treatment, chemical or hydrothermal methods, vapor deposition, layer-by-layer assembly or laser ablation [19,27–39]. However, the development of a straightforward

and versatile bottom-up synthesis scheme enabling tunable surface morphologies for controlled wetting properties is still challenging and highly desired.

Metal-organic frameworks (MOFs) are porous, crystalline materials featuring a great structural and chemical diversity[40–45]. Thereby, they are attractive synthesis targets for a large variety of applications, including gas storage and separation, chemical sensing, thermoelectrics, capacitors, transistors or photovoltaics[46–52]. Due to their exceptional variety of structural properties and functions, MOFs are intriguing candidates for the design and synthesis of coatings combining a superhydrophilic, superhydrophobic, superoleophilic or superoleophobic character with desired features such as light filtering, hosting cavities, electrical conductivity, etc. In the literature, the synthesis procedures of MOF powders with encoded wetting properties have been reported[53–60]. Typically, the desired wetting properties in MOFs were chemically induced by a post- synthesis modification or by including building blocks deco- rated with hydrocarbon side chains[58,61–64]. Very recently, a copper mesh decorated with hybrid $Cu(OH)_2$/MOF-nanobrushes showed underwater contact angles suggesting superoleophobic properties[65]. However, the use of well- defined MOF films for encoding on-surface wetting properties is yet to be revealed.

Here we report the synthesis of highly oriented, nanostructured MOF films that mimic architectures observed in nature, resulting in highly unusual, extreme surface wetting properties. For the synthesis, the Ni- and Co-derivatives of the metal-catecholate series (M-CAT-1) were selected[66]. First, these M-CAT-1 derivatives were synthesized as highly crystalline bulk materials. The M-CAT-1 surface energy was estimated by contact angle measurements using pellet samples exposing nonoriented crystallites on the surface. Next, oriented and compact Co- and Ni-CAT-1 films were deposited on gold surfaces by vapor-assisted conversion (VAC). These films showed enhanced hydrophilic and underwater oleophobic properties compared to the corresponding pressed pellet samples. Oriented, nanostructured M-CAT-1 films exhibiting a pronounced needle-like morphology on gold substrates were obtained by adding a crystallization promotor into the VAC pre- cursor solution. These nanostructured M-CAT-1 MOF films feature extreme wetting phenomena, specifically superhydrophilic and underwater superoleophobic properties with water and underwater oil-contact angles of 0° and up to 174°, respectively. The self-cleaning capability of the nanostructured, needle-like Ni- and Co-CAT-1 films was illustrated by measuring time-dependent oil droplet rolling-off a tilted surface. The deposition of the nanostructured Ni-CAT-1 film on large glass substrates allowed for the realization of an efficient anti-fog coating. These anti-fog coatings enabled clear vision, even at large temperature differences of up to 120°C.

4.2. Results and discussion

The M-CAT-1 MOFs are crystalline, microporous structures obtained by a solvothermal reaction of metal precursors and the organic building block 2,3,6,7,10,11-hexahydroxytriphenylene (HHTP) as a dark precipitate. The M-CAT-1 crystallites exhibit a hexagonally faceted, needle-like morphology with crystal cross-sections of 30-40 nm and several micrometers in length (Figure 4.1). In addition, the M-CAT-1 materials are electroactive featuring electrical conductivity values of up to 10^{-2}-10^{-3} S cm^{-1} for pressed powder pellets and oriented thin films, respectively[67]. However, the wetting properties of these MOFs both as pristine powders and as films have not been explored.

For our study, we focused on Ni- and the Co-CAT-1, since their structure is well-characterized and elucidated by diffraction methods, serving as a good basis for understanding their growth behavior and morphology. To assess the wetting properties of Ni- and Co-CAT-1, we investigated the interaction of the bulk materials pressed as compact pellets with different polar and apolar liquids. For this purpose, we synthesized M-CAT-1 bulk materials following our recently reported solvothermal synthesis procedure (for more details see Figure S4.6, Appendix)[67]. Subsequently, the obtained MOF powders were collected, activated under dynamic vacuum and pressed into crystalline pellet samples (1 cm diameter, thickness 500 µm; 100 mg activated MOF, roughness (RMS): 37 nm). Scanning electron microscope (SEM) micrographs reveal densely packed and randomly oriented MOF crystallites throughout the sample (see Figure S4.7, Appendix). For the contact angle (CA) measurements at the solid/air interface we chose diiodomethane as a nonpolar organic liquid, which exhibits a relatively high surface tension, and water as a polar liquid (see Figure 4.1). CA measurements on M-CAT-1 pellets reveal shallow angles of about 12° for diiodomethane and WCA values of about 46°. This illustrates that in air the M-CAT-1 materials feature an amphiphilic character, namely hydrophilic and superolephilic properties. This amphiphilic wetting property can be attributed to the high surface energy of the MOF materials. To estimate the corresponding MOF surface energy, we applied Fowker's theory, where the observed CA between a liquid and a solid is related to the sum of a polar and dispersive components of the liquid's surface tension[68]. Utilizing the measured CAs of diiodomethane exhibiting solely a dispersive component and water, having a dispersive and polar components, enabled the calculation of the overall surface energy for Ni- and Co-CAT-1 (for detailed discussion see Appendix, Table S4). We obtained a surface energy of 64.02 and 62.38 mN/m for the Ni- and Co-CAT-1 pellet samples, respectively, as summarized in Table 3. These values are higher than the surface energy reported for oleophilic polymers which exhibit a surface energy in the range of 20-50 mN/m. However, the estimated MOF surface energy and WCAs are in good agreement with systems such as modified carbonaceous layers, showing values of about 60 mN/m

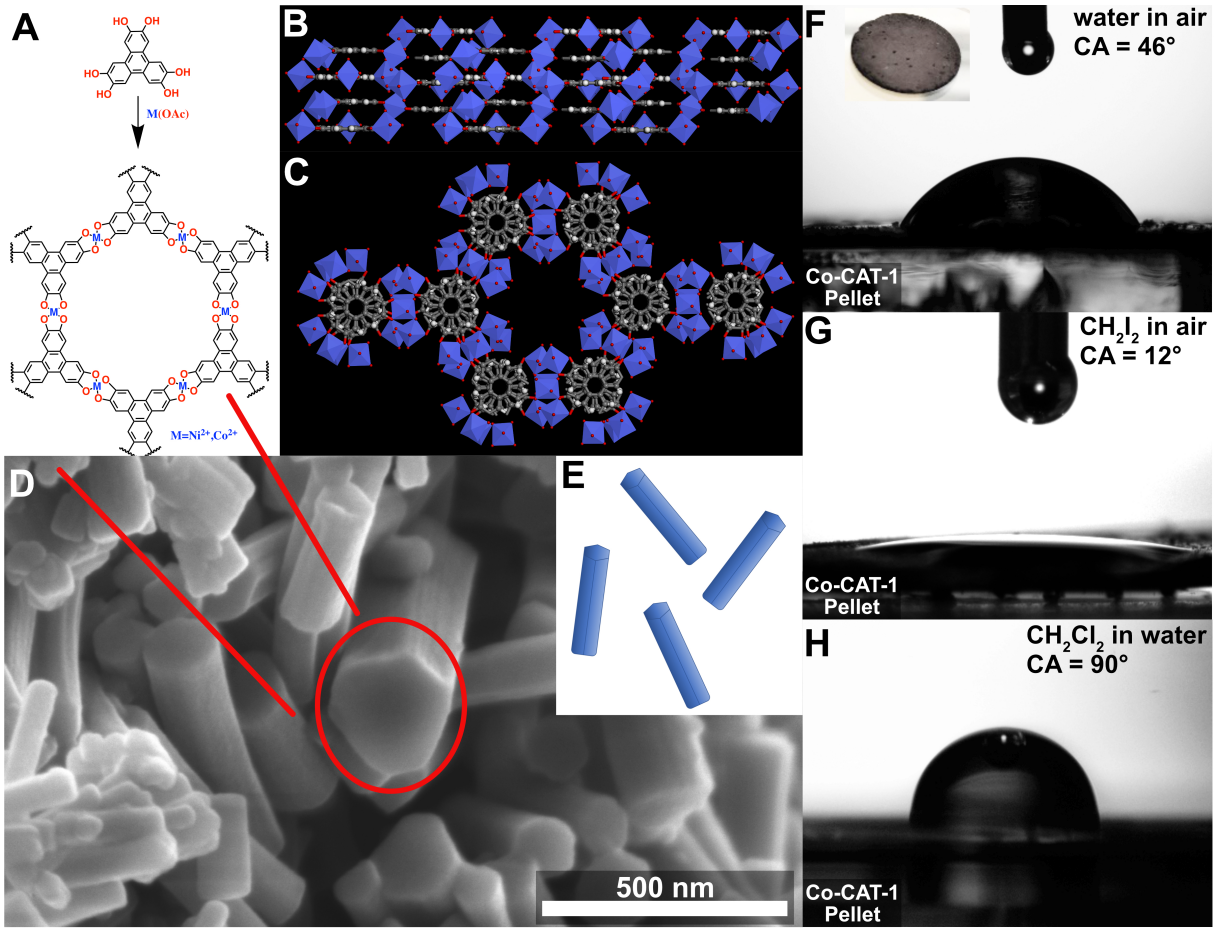

Figure 4.1 – A) Synthesis scheme of M-CAT-1 using 2,3,6,7,10,11-hexahydroxytriphenylene (HHTP) and the respective metal acetate under solvothermal conditions. B) Side view of the Co-CAT-1 crystal structure illustrating infinite layers of $HHTP_2Co_3$. C) View along the crystallographic *c*-axis highlighting the hexagonal pore channels. D) SEM micrograph showing the needle-like crystallite morphology, which is sketched in E) as elongated hexagonally shaped monoliths. F) Water contact angle (WCA) measured at the solid/air interface of a Co-CAT-1 pellet. G) Diiodomethane CA measured on the same pellet. H) Underwater CA measured at the solid/water interface on the identical pelletized sample.

and WCAs of 50°[69]. Superoleophilic wetting properties were also detected for chlorinated oils such as dichloromethane on M-CAT-1 pellets (see Figure S4.8, Appendix). This further illustrates the amphiphilic nature of the M-CATs, showing hydrophilic as well as superoleophilic behavior towards several different oils. Interestingly, the underwater oil contact angle (OCA) of diiodomethane on these pellets reveals an inverse wetting phenomenon. Under these conditions, the M-CAT-1 materials reject oil and turn oleophobic with an OCA of 90° (Figure 4.1H).

Table 3 – Surface energy σ_S and the respective dispersive $\sigma_S{}^D$ and polar $\sigma_S{}^P$ components estimated for Ni- and Co-CAT-1 pellet samples.

M-CAT-1	σ_S [mN/m]	$\sigma_S{}^D$ [mN/m]	$\sigma_S{}^P$ [mN/m]
Ni-CAT-1	64.02	49.69	14.06
Co-CAT-1	62.38	50.30	12.08

Constructing nanostructured M-CAT-1 surfaces

According to Wenzels model, film topography has a strong impact on the wetting properties of a surface[70]. Following this line of thought, we aimed at constructing M-CAT-1 thin films featuring distinct surface morphologies, allowing for the desired surface wetting properties to be achieved. However, on-surface control of MOF film morphology is a challenging task due to the required growth conditions for maintaining key features such as homogeneity, crystallinity and crystal orientation on the surface. In our previous reports, we have demonstrated that the use of a modulator in combination with the choice of a substrate play a crucial role in VAC synthesis and the formation of a crystalline MOF film[71]. In the present study, we introduce the use of a crystallization promoter in the VAC process, solely for inducing distinct film morphology while maintaining crystallinity and crystal orientation on a preselected substrate.

Accordingly, we employed VAC methods for producing both compact and nanostructured M-CAT-1 films (see Figure S4.13, Appendix). Briefly, oriented thin films of Ni- and Co-CAT-1 were synthesized on gold substrates by depositing a thin layer of a precursor solution onto a gold substrate. Then, the gold substrate was placed on a glass platform above a solvent bath inside a glass autoclave. Subsequently, the reactor was sealed and placed at 85°C in a preheated oven. After 12 h of reaction time, the reactor was removed from the oven and allowed to cool down to room temperature. The substrates were recovered, washed and dried under a N_2 stream, revealing a colored film on the gold substrate. These films typically exhibit thickness of about 150 nm, consisting of highly intergrown oriented crystallites (see Figure S4.13, Appendix).

Next, nanostructured pillar-like M-CAT-1 films were synthesized by including carboxylic acids, which served as crystallization promotors in the drop-cast precursor solution layer. Specifically, we introduced acetic acid in the Ni-CAT-1 and salicylic acid in the Co-CAT-1 synthesis (see Figure 4.2A). Top-view SEM images show a homogenous film and a long-range ordered array of pillar-like structures with a cross-section of 20-30 nm and evident gaps between the pillars of about 150 nm for both samples (see Figure 4.2B, C).

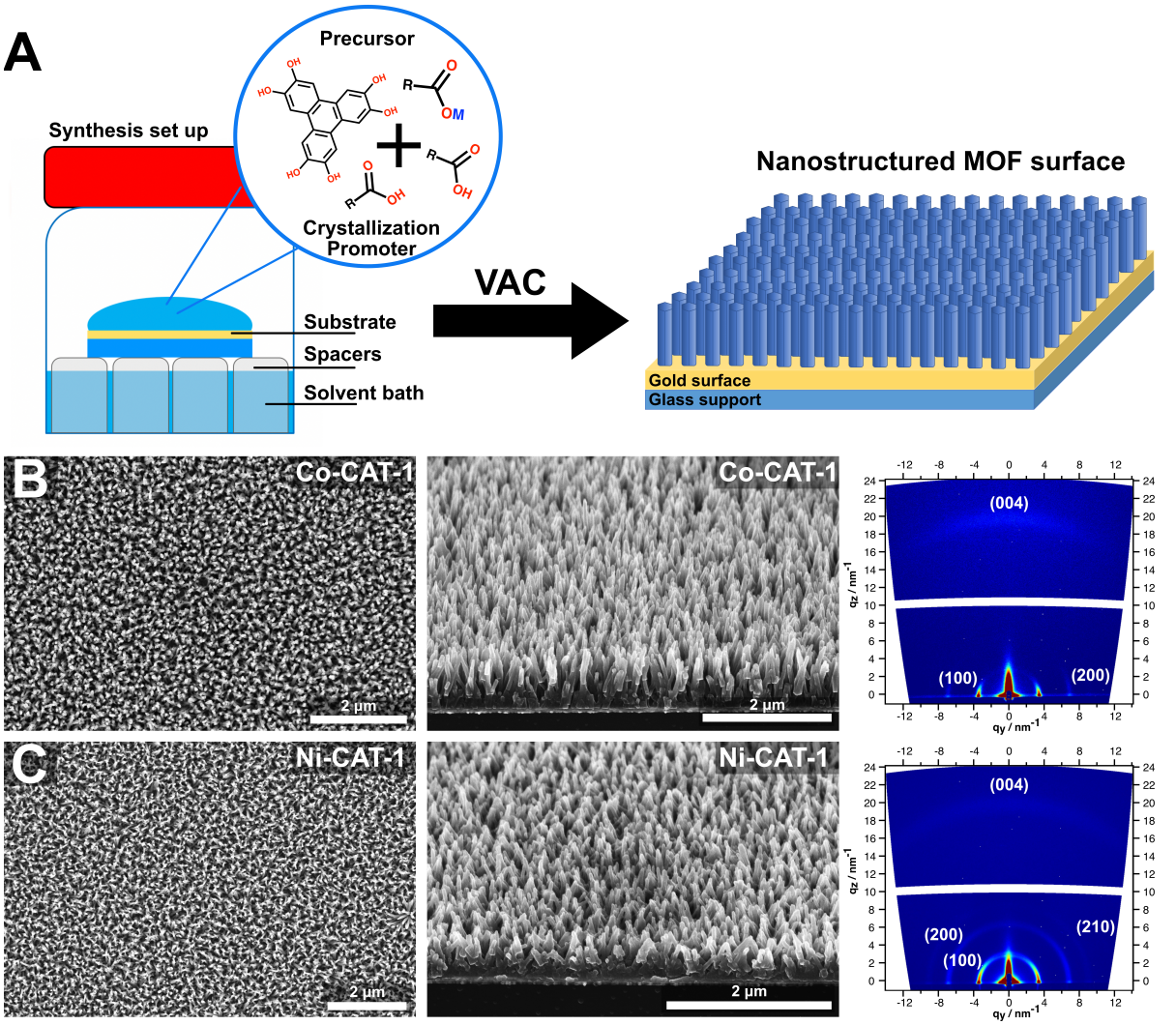

Figure 4.2 – A) A scheme of the vapor-assisted conversion (VAC) set up and the resulting nanostructured films. B) SEM top view, 30°tilted cross-section and the related GIWAXS pattern of the Co-CAT-1 film. C) SEM top view, 30° tilted cross-section micrographs and the related GIWAXS pattern of the Ni-CAT-1.

Cross-section SEM micrographs clearly visualize an array of vertically aligned MOF needles on the surface plane. In addition, a uniform film thickness of about 800 nm is observed throughout the cross-section of both Ni- and Co-CAT-1 samples, indicating a self-terminating growth under the employed conditions (Figure 4.2). To confirm that the defined nanostructured film is indeed crystalline and the crystallites are well-aligned orthogonal to the surface plane, X-ray grazing incidence wide-angle scattering (GIWAXS) experiments were performed (see Figure 4.2B, C). GIWAXS analysis of the obtained films confirmed the successful on-surface deposition of crystalline M-CAT-1 materials. The collected out-of-plane reflections at $q_y = 3.9\,nm^{-1}$ (100),

$q_y = 7.1\,nm^{-1}$ (200) and $q_y = 9.2\,nm^{-1}$ (210) near $q_z = 0$ were indexed according to the powder X-ray diffraction pattern of Co-CAT-1. The (004) reflection, referred to as the in-plane reflection, is visible as a diffuse arc at $q_z = 19\,nm^{-1}$(for further details see Appendix). The latter corresponds to an interlayer distance of 3.3 Å. This points toward the preferential orientation of the M-CAT-1 crystals on the surface, where the crystallographic *c*-axis is positioned normal to the surface plane.

These data show that by employing the VAC synthesis approach in the presence of a specific crystallization promotor, the fabrication of crystalline nanostructured and oriented M-CAT-1 films on gold substrates is feasible. Deviating from these optimal conditions resulted in a poorly crystalline or inhomogeneous film (see Figure S4.22, Appendix).

Superhydrophilic and underwater superoleophobic MOF-based surfaces

Following Wenzels equation[70], an increased surface roughness results in a decreased WCA and in an enhanced OCA. To study the impact of roughness on the wetting properties of the M-CAT-1 films, we performed WCA and underwater OCA measurements for the compact and the nanostructured M-CAT-1 films (see Figure 4.3 and S4.17, Appendix).

Oriented and compact films demonstrated CAs of 32° and 26° for Ni- and Co-CAT-1, respectively, whereas oriented and nanostructured films featured a drastic decrease in the WCA (see Figures S4.17, S4.19, Appendix). Strikingly, we observed complete water spreading on the M-CAT-1 films and a WCA of 0° for both films, thus these surfaces can be considered superhydrophilic (Figure 4.3D and S4.17, Appendix). These observed surface properties were further confirmed by measuring the underwater OCA with a droplet of dichloromethane (DCM). The oriented and compact films showed enhanced oleophobic properties with an underwater OCA of about 130° and 133° for Ni-CAT-1 and Co-CAT- 1, respectively (see Figure 4.3 and S4.17, Appendix). Remarkably, for the oriented and nanostructured films, we observed a strong increase in the OCA and extreme values of 174° and 173° were determined for Ni-CAT-1 and Co-CAT- 1, respectively (see Figure S4.17, Appendix). On these films, a nearly perfect oil sphere was formed, which is hardly in contact with the surface (see Figure S4.19, Appendix). These surface properties resemble those of surface designs found in nature. For example, referring to marine life, fish scales in air show an amphiphilic behavior due to their high surface energy, but under water they turn super- oleophobic, which is of great advantage for protection against hazardous environments, for example, oil-polluted water.

The self-cleaning properties of these extremely oleophobic M-CAT-1 nanostructured surfaces were demonstrated by casting a DCM oil droplet on a marginally tilted substrate (*e.g.*, by 1.4°). Subsequently, the motion of the droplet was recorded by a high-speed camera with 3 frames per second (see Figure 4.3G and S4.18, Appendix). The obtained image series reveals that the

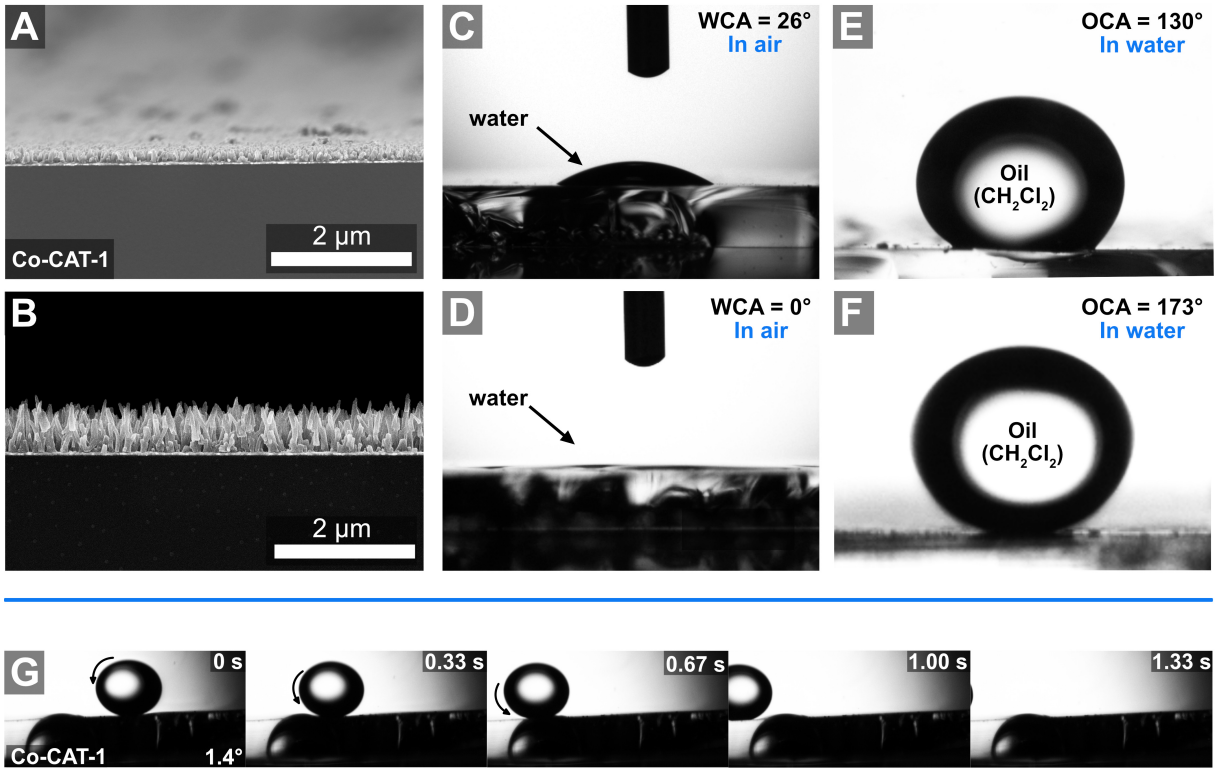

Figure 4.3 – Cross-section SEM micrographs of A) an oriented and compact Co-CAT-1 film and B) an oriented (pillar-like) nanostructured Co-CAT-1 film. WCA of the C) compact (WCA = 26°) and the D) nanostructured (WCA = 0°) films. Underwater OCA (dichloromethane (DCM)) of the E) compact (CA = 130°) and the F) nanostructured films (CA = 173°). G) An image series of a self-cleaning surface experiment (3 frames per second) with DCM as an oil droplet placed on the nanostructured Co-CAT-1 film performed at a substrate tilt angle of 1.4°.

droplet crosses the substrate and rolls out of the detection range of the high-speed camera in about 1.3 s. According to the Cassi-Baxter theory, the combination of the very low tilt-angle that is required for the droplet to roll off the substrate and the extreme underwater OCA angle suggests that the DCM sphere is in contact only with the tips of the crystalline needles, whereas the intercrystallite areas only interact with water[72]. To exclude the contribution of the gold surface to the wetting properties of the MOF films, we carried out control experiments with blank gold substrates giving a WCA of 94° and underwater OCA of 52° (see Figure S4.11, Appendix). This confirms that the observed superhydrophilic and superoleophobic behavior arises from the MOF film.

To illustrate the stability of the MOF under harsh conditions, the films were subjected to an acidic environment (pH 5, 12 h), a basic environment (pH 9, 12 h), high temperature (150°C, 12 h), and mechanical impact (sonication in water, 20 min). GIWAXS analysis in addition to WCA

and OCA measurements after the respective treatment confirmed that the crystallinity, crystal orientation and extreme wetting properties were preserved (see Figures S4.26, S4.27, Appendix).

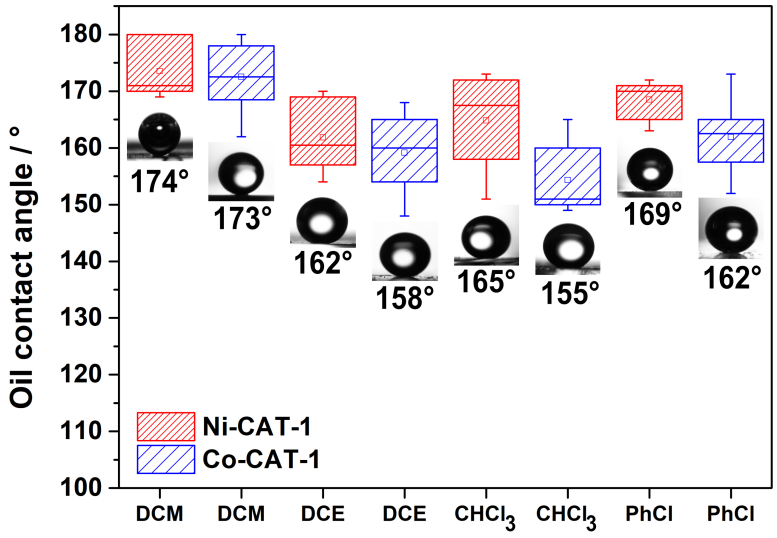

Figure 4.4 – Box and whisker plot of the measured underwater OCAs for the nanostructured Ni-CAT-1 and Co-CAT-1 films. The employed liquids are dichloromethane (DCM), dichloroethane (DCE), chloroform ($CHCl_3$) and chlorobenzene (PhCl). For all the tested liquids, a superoleophobicity is observed with underwater OCAs $> 150°$.

To establish these MOF films as superoleophobic surfaces applicable to a wide range of oils, we examined the interactions of other high-density oils with the oriented and nanostructured MOF surfaces. For this purpose, we determined the underwater OCA for different chlorinated liquids, such as dichloromethane (DCM), dichloroethane (DCE), chloroform ($CHCl_3$) and chlorobenzene (PhCl). The OCAs were recorded using the exact same described procedure for DCM, and the results are plotted as box and whisker plots in Figure 4.4. For all the measured oils, superoleophobic behavior was observed with extreme OCAs ranging from 155° (DCE) for Co-CAT-1 to 169° (PhCl) for Ni-CAT-1 films. Specifically, the Ni-CAT-1 film exhibits the following OCAs: 174° (DCM), 162° (DCE), 165°($CHCl_3$) and 169°(PhCl), whereas the Co-CAT-1 film exhibits 173°(DCM), 158° (DCE), 155°($CHCl_3$) and 162°(PhCl). These results confirm that the MOF films efficiently repel a large variety of oily liquids, hence constituting an intriguing platform for underwater superoleophobic properties.

Since MOFs are crystalline materials featuring crystal facets with distinct surface energies, the orientation of these crystallites on a surface is expected to impact the wetting properties. In the following, we discuss the case of Ni-CAT-1 as a model for the M-CAT-1 series. In the context of crystal orientation on the surface, we analyzed the Ni-CAT-1 WCAs measured for pressed pellet samples and those of oriented and compact films. Interestingly, pressed pellet samples

consisting of randomly distributed crystallites on the surface exhibit greater WCAs than oriented films, although the latter shows a slightly increased surface roughness (see Figures S4.14, S4.15, S4.8, S4.9, Appendix). We attribute this difference to the different surface character which directly impacts the surface energy, and hence, the wetting properties (see Table S4, Appendix). We therefore conclude that the observed wetting properties are due to a combination of two different significant contributions which can be controlled by the VAC process, namely the surface roughness and the crystallite orientation on the substrate.

Anti-fog coating with MOF films

Water condensation on surfaces is a known phenomenon occurring at the dew point on substrates such as glass, which serves as a favorable nucleation site for water droplets. This process leads to a substantial reduction in the transparency of the glass and the vision though the glass becomes extremely limited. To avoid condensation, modifications of the glass surface with different classes of functional coatings are necessary. Motivated by the superhydrophilic properties obtained by growing nanostructured M-CAT-1 films on gold substrates, we investigated the synthesis of such films as transparent coatings on glass substrates, thereby altering their wetting character towards superhydrophilic properties. Through this approach, a thin water layer decorating the textured MOF surface is expected to form, hindering the nucleation of water droplets on the glass surface. For this purpose, we employed the newly developed methodology for the synthesis of nanostructured Ni-CAT-1 films on gold substrates with a slightly modified synthesis procedure in order to address larger substrate dimensions such as 2.5 cm × 2.5 cm. The resulting MOF films on glass substrates reveal a blue-tinted, yet transparent coating (see Figure 4.5 C, F). A top view SEM micrograph revealed the typical orthogonally aligned needle-like nanostructures on the surface, similar to the M-CAT-1 films grown on gold surfaces. The preferential orientation of the MOF crystals on the glass substrate was further confirmed by GIWAXS measurements (see Figure S4.20, Appendix). The WCA measurements showed superhydrophilic properties similar to those observed for gold substrates (Figure 4.5C). Further control experiments confirmed that the superhydrophilic wetting properties originate from the presence of the nanostructured MOF film. Blank glass substrates showed WCA of 11° and OCA of 81° (see Figure S4.12, Appendix). Furthermore, the MOF films endow the glass substrates with light-absorbing properties while maintaining transparency (see Figure S4.20, Appendix). In addition, we found that these MOF films are stable in acidic (pH 5, 12 h) and basic conditions and at high temperature (150°C, 12 h) (see Figure S4.28, Appendix).

To test the anti-fog properties of the Ni-CAT-1 film, a glass vessel containing a reservoir of boiling water (= 100°C) was placed above an LMU seal, and a non-modified glass substrate was positioned on top of the open vessel (see Figure 4.5D, F and S4.23, Appendix). Within seconds,

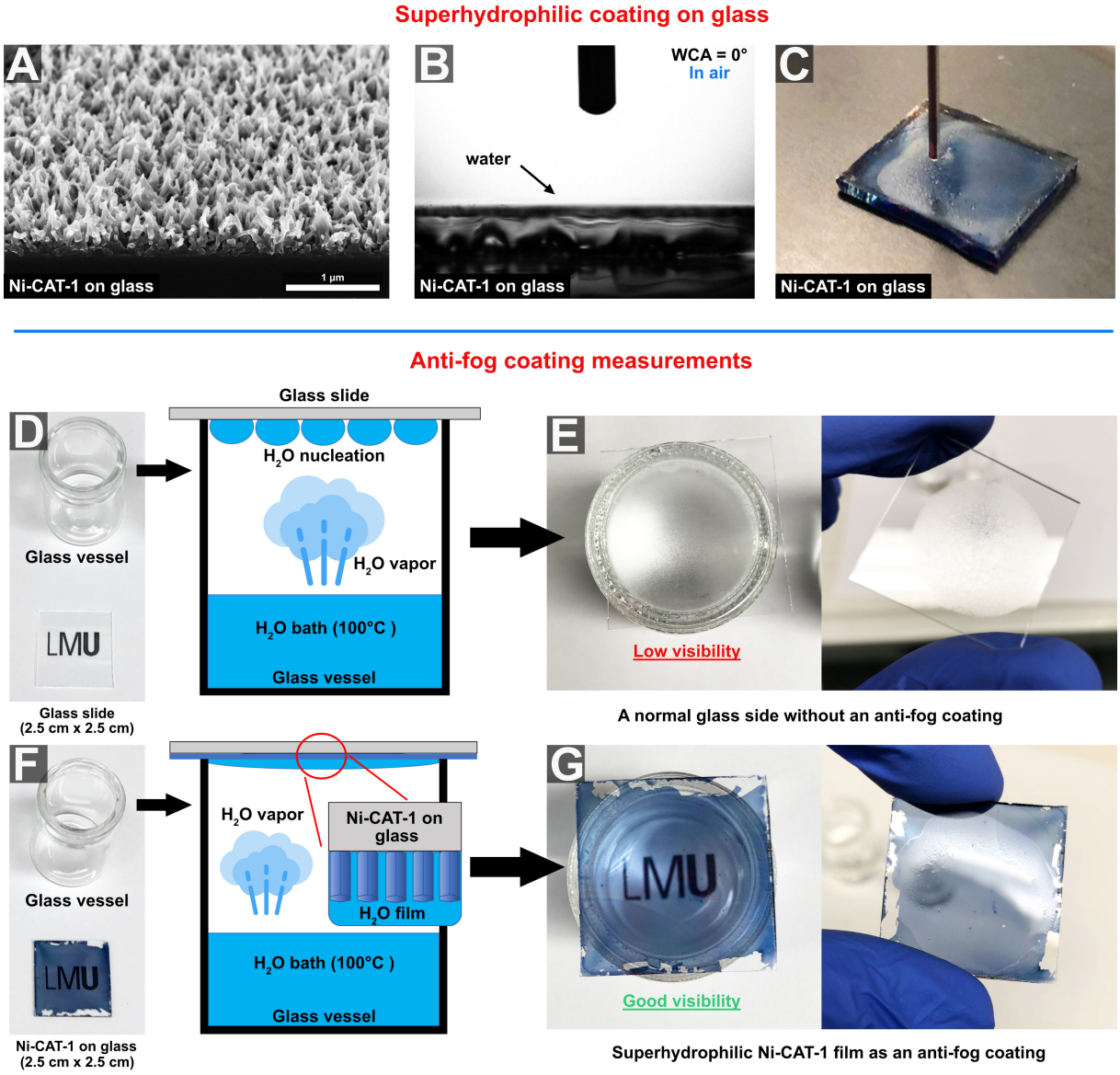

Figure 4.5 – A) A 30° tilted SEM top view micrograph of Ni-CAT-1 film grown on glass. B) WCA on the superhydrophilic and nanostructured Ni-CAT-1 film. C) Macroscopic image of the Ni-CAT-1 on a glass substrate, showing a complete spreading of the water droplet. D) An anti-fog coating experiment performed with a bare glass slide that is placed above a glass vessel containing a reservoir of hot water at boiling temperature. E) The LMU seal obscured by water condensation on the bare glass. F) An anti-fog coating experiment performed with a MOF-coated glass above a glass vessel containing a reservoir of hot water at boiling temperature. G) High transparency and visibility through the substrate and a visible LMU seal is demonstrated.

the seal was no longer visible, obscured by the water droplets generated by the condensation of steam on the glass surface (Figure 4.5E). In contrast, using a MOF-coated glass substrate, high

transparency and clear visibility through the substrate were enabled, and the seal was visible even after longer exposure times (Figure 4.5F, G). To examine the behavior of the anti-fog coating under extreme temperature differences, the MOF-modified glass substrates were cooled down to −20°C and subsequently placed on top of the hot water reservoir. Under all examined conditions, clear vision through the glass was maintained and water vapor nucleation was not observed (see Figure S4.24, Appendix). This striking effect is attributed to the formation of a thin water layer on the MOF films which spreads out completely on the surface. This thin water layer is clearly visible by turning the substrate upside down (Figure 4.5G). This set of experiments establishes the pillar-like nanostructured Ni-CAT-1 films as highly efficient, anti-fog coatings featuring additional desired properties such as light absorbance. Furthermore, it underlines the power of VAC in enabling controlled bottom-up fabrication of MOF films with well-defined nanoscale morphologies and associated functionality.

4.3. Conclusion

In this study, we demonstrated the controlled on-surface synthesis of crystalline, highly oriented and nanostructured M-CAT-1 films by employing a crystallization promoter in a VAC synthesis. First, the free surface energy of M-CAT-1 was calculated for pressed pellet samples, shedding light on the amphiphilic wetting properties (both hydrophilic and oleophilic) of the materials in air. Oriented and compact M-CAT-1 films exhibited enhanced wetting properties where shallower contact angles were deter-mined for water (about 32°) and a large underwater OCA (130°), indicating oleophobic properties. The correspond- ing oriented and nanostructured M-CAT-1 films exhibited extreme wetting properties with a WCA of 0° and an under- water OCA of 174°, and are thus demonstrated as being superhydrophilic and superoleophobic in water. The underwater self-cleaning ability of these films was demonstrated by depositing an oil droplet on a substrate tilted at a shallow angle of 1.4°. The effective underwater oil-repelling properties of the M-CAT-1 films were confirmed by employing a variety of different chlorinated oily liquids. Under ambient atmosphere, the water wetting properties of these systems could be drastically altered by changing the film morphology from compact to pillar-like nanostructures. This effect was also transferred onto transparent substrates such as glass, resulting in an efficient, transparent, MOF-based, anti-fog coating. Hence, we demonstrate that on-surface alteration of the MOF film morphology by versatile solution-based bottom-up methods such as VAC is a powerful tool for realizing the potential of MOFs in surface-based technologies such as oil-water separation systems, anti-oil coatings, or self-cleaning surfaces. Furthermore, the use of a MOF allows for encoding further desired surface properties such as light absorption and electrical conductivity.

This can be valuable for applications such as photo-electrocatalysis water splitting where a high textural surface area, water contact and light absorption are required.

References

[1] Yong, J.; Chen, F.; Yang, Q.; Jiang, Z.; Hou, X. *Adv. Mater. Interfaces* **2018,** *5,* 1701370. doi:10.1002/admi.201701370
[2] Yong, J.; Chen, F.; Yang, Q.; Huo, J.; Hou, X. *Chem. Soc. Rev.* **2017,** *46,* 4168-4217. doi:10.1039/c6cs00751a
[3] Helbig, R.; Nickerl, J.; Neinhuis, C.; Werner, C. *PLoS One* **2011,** *6,* e25105. doi:10.1371/journal.pone.0025105
[4] Hernandez, A.; Brebbia, C. A. *Design and Nature IV: Comparing Design in Nature With Science and Engineering; WIT Press:* Ashurst, 2012.
[5] Feng, L.; Zhang, Y.; Xi, J.; Zhu, Y.; Wang, N.; Xia, F.; Jiang, L. *Langmuir* **2008**, *24,* 4114-4119. doi:10.1021/la703821h
[6] Neinhuis, C.; Barthlott, W. *Ann. Bot. (Oxford, U. K.)* **1997**, *79,* 667-677. doi:10.1006/anbo.1997.0400
[7] Rich, B. B.; Pokroy, B. *Soft Matter* **2018,** *14,* 7782-7792. doi:10.1039/c8sm01115j
[8] Gao, X.; Yan, X.; Yao, X.; Xu, L.; Zhang, K.; Zhang, J.; Yang, B.; Jiang, L. *Adv. Mater. (Weinheim, Ger.)* **2007,** *19,* 2213-2217. doi:10.1002/adma.200601946
[9] Parker, A. R.; Lawrence, C. R. *Nature* **2001,** *414,* 33-34. doi:10.1038/35102108
[10] Waghmare, P. R.; Gunda, N. S. K.; Mitra, S. K. *Sci. Rep.* **2014,** *4,* 7454. doi:10.1038/srep07454
[11] Bixler, G. D.; Bhushan, B. *Nanoscale* **2013,** *5,* 7685-7710. doi:10.1039/c3nr01710a
[12] Liu, M.; Wang, S.; Wei, Z.; Song, Y.; Jiang, L. *Adv. Mater. (Weinheim, Ger.)* **2009,** *21,* 665-669. doi:10.1002/adma.200801782
[13] Bhushan, B.; Jung, Y. C.; Koch, K. Philos. *Trans. R. Soc., A* **2009,** *367,* 1631-1672. doi:10.1098/rsta.2009.0014
[14] Feng, L.; Li, S.; Li, Y.; Li, H.; Zhang, L.; Zhai, J.; Song, Y.; Liu, B.; Jiang, L.; Zhu, D. *Adv. Mater. (Weinheim, Ger.)* **2002,** *14,* 1857-1860. doi:10.1002/adma.200290020
[15] Darmanin, T.; Guittard, F. *Mater. Today* **2015,** *18,* 273-285. doi:10.1016/j.mattod.2015.01.001
[16] Kota, A. K.; Li, Y.; Mabry, J. M.; Tuteja, A. Adv. Mater. (Weinheim, Ger.) 2012, 24, 5838-5843. doi:10.1002/adma.201202554
[17] Wen, L.; Tian, Y.; Jiang, L. *Angew. Chem.* **2015,** *127,* 3448-3462. doi:10.1002/ange.201409911
[18] Jiang, L.; Zhao, Y.; Zhai, J. *Angew. Chem., Int. Ed.* **2004,** *43,* 4338-4341. doi:10.1002/anie.200460333
[19] Jiang, T.; Guo, Z.; Liu, W. J. **Mater. Chem. A** *2015,* **3,** 1811-1827. doi:10.1039/c4ta05582a
[20] Koch, K.; Bhushan, B.; Barthlott, W. *Prog. Mater. Sci.* **2009,** *54,* 137-178. doi:10.1016/j.pmatsci.2008.07.003
[21] Liu, X.; Zhou, J.; Xue, Z.; Gao, J.; Meng, J.; Wang, S.; Jiang, L. *Adv. Mater. (Weinheim, Ger.)* **2012,** *24,* 3401-3405. doi:10.1002/adma.201200797
[22] Nishimoto, S.; Bhushan, B. *RSC Adv.* **2013,** *3,* 671-690. doi:10.1039/c2ra21260a
[23] Xu, L.-P.; Peng, J.; Liu, Y.; Wen, Y.; Zhang, X.; Jiang, L.; Wang, S. *ACS Nano* **2013,** *7,* 5077-5083. doi:10.1021/nn400650f
[24] Cai, Y.; Lin, L.; Xue, Z.; Liu, M.; Wang, S.; Jiang, L. *Adv. Funct. Mater.* **2014,** *24,* 809-816. doi:10.1002/adfm.201302034
[25] Tahk, D.; Kim, T.-i.; Yoon, H.; Choi, M.; Shin, K.; Suh, K. Y. Langmuir 2010, 26, 2240-2243. doi:10.1021/la904768e
[26] Williams, D. E.; Dolgopolova, E. A.; Pellechia, P. J.; Palukoshka, A.; Wilson, T. J.; Tan, R.; Maier, J. M.; Greytak, A. B.; Smith, M. D.; Krause, J. A.; Shustova, N. B. *J. Am. Chem. Soc.* **2015,** *137,* 2223-2226. doi:10.1021/ja5131269
[27] Barthwal, S.; Kim, Y. S.; Lim, S.-H. J. *Colloid Interface Sci.* **2013,** *400,* 123-129. doi:10.1016/j.jcis.2013.02.037
[28] Chang, C.-J.; Wang, C.-F.; Chen, J.-K.; Hsieh, C.-C.; Chen, P.-A. *Appl. Surf. Sci.* **2013,** *286,* 280-286. doi:10.1016/j.apsusc.2013.09.071
[29] Choi, H.-J.; Choo, S.; Shin, J.-H.; Kim, K.-I.; Lee, H. *J. Phys. Chem. C* **2013,** *117,* 24354-24359. doi:10.1021/jp4070399
[30] Ellinas, K.; Pujari, S. P.; Dragatogiannis, D. A.; Charitidis, C. A.; Tserepi, A.; Zuilhof, H.; Gogolides, E. *ACS Appl. Mater. Interfaces* **2014,** *6,* 6510-6524. doi:10.1021/am5000432
[31] Ganesh, V. A.; Dinachali, S. S.; Nair, A. S.; Ramakrishna, S. *ACS Appl. Mater. Interfaces* **2013,** *5,* 1527-1532. doi:10.1021/am302790d
[32] Hayase, G.; Kanamori, K.; Hasegawa, G.; Maeno, A.; Kaji, H.; Nakanishi, K. *Angew. Chem., Int. Ed.* **2013,** *52,* 10788-10791. doi:10.1002/anie.201304169
[33] Liu, J.-Q.; Bai, C.; Jia, D.-D.; Liu, W.-L.; He, F.-Y.; Liu, Q.-Z.; Yao, J.-S.; Wang, X.-Q.; Wu, Y.-Z. RSC Adv. 2014, 4, 18025-18032. doi:10.1039/c4ra01505c
[34] Deng, X.; Mammen, L.; Butt, H.-J.; Vollmer, D. *Science* **2012,** *335,* 67-70. doi:10.1126/science.1207115
[35] Onda, T.; Shibuichi, S.; Satoh, N.; Tsujii, K. *Langmuir* **1996,** *12,* 2125-2127. doi:10.1021/la950418o
[36] Wang, R.; Hashimoto, K.; Fujishima, A.; Chikuni, M.; Kojima, E.; Kitamura, A.; Shimohigoshi, M.; Watanabe, T. *Nature* **1997,** *388,* 431-432. doi:10.1038/41233
[37] Fujishima, A.; Rao, T. N.; Tryk, D. A. Electrochim. *Acta* **2000,** *45,* 4683-4690. doi:10.1016/s0013-4686(00)00620-4
[38] Nakajima, A.; Fujishima, A.; Hashimoto, K.; Watanabe, T. *Adv. Mater. (Weinheim, Ger.)* **1999,** *11,* 1365-1368. doi:10.1002/(sici)1521-4095(199911)11:16<1365::aid-adma1365>3.3.c o;2-6
[39] Gordon, V.; Marom, G.; Magdassi, S. *Int. J. Pharm.* **2015,** *478,* 172-179. doi:10.1016/j.ijpharm.2014.11.038
[40] Ferey, G. *Chem. Soc. Rev.* **2008,** *37,* 191-214. doi:10.1039/b618320b
[41] Furukawa, H.; Cordova, K. E.; O Keeffe, M.; Yaghi, O. M. *Science* **2013,** *341,* 1230444. doi:10.1126/science.1230444
[42] Cook, T. R.; Zheng, Y.-R.; Stang, P. *J. Chem. Rev.* **2013,** *113,* 734-777. doi:10.1021/cr3002824
[43] Evans, J. D.; Garai, B.; Reinsch, H.; Li, W.; Dissegna, S.; Bon, V.; Senkovska, I.; Fischer, R. A.; Kaskel, S.; Janiak, C.; Stock, N.; Volkmer, D. Coord. *Chem. Rev.* **2019,** *380,* 378-418. doi:10.1016/j.ccr 2018.10.002
[44] Haraguchi, T.; Otsubo, K.; Kitagawa, H. *Eur. J. Inorg. Chem.* **2018,** 1697-1706. doi:10.1002/ejic.201701234
[45] Ko, M.; Mendecki, L.; Mirica, K. A. *Chem. Commun.* **2018,** *54,* 7873-7891. doi:10.1039/c8cc02871k
[46] Meek, S. T.; Greathouse, J. A.; Allendorf, M. D. *Adv. Mater. (Weinheim, Ger.)* **2011,** *23,* 249-267. doi:10.1002/adma.201002854
[47] Qiu, S.; Zhu, G. *Coord. Chem. Rev.* **2009,** *253,* 2891-2911. doi:10.1016/j.ccr.2009.07.020
[48] Rowsell, J. L. C.; Yaghi, O. M. *J. Am. Chem. Soc.* **2006,** *128,* 1304-1315. doi:10.1021/ja056639q
[49] Usman, M.; Mendiratta, S.; Lu, K.-L. *Adv. Mater. (Weinheim, Ger.)* **2017,** *29,* 1605071. doi:10.1002/adma.201605071

[50] Sun, L.; Campbell, M. G.; Dinca, M. *Angew. Chem., Int. Ed.* **2016,** *55,* 3566-3579. doi:10.1002/anie.201506219
[51] Allendorf, M. D.; Schwartzberg, A.; Stavila, V.; Talin, A. *A. Chem. - Eur. J.* **2011,** *17,* 11372-11388. doi:10.1002/chem.201101595
[52] Dolgopolova, E. A.; Shustova, N. B. *MRS Bull.* **2016,** *41,* 890-896. doi:10.1557/mrs.2016.246
[53] Liu, M.; Tie, L.; Li, J.; Hou, Y.; Guo, Z. *J. Mater. Chem. A* **2018,** *6,* 1692-1699. doi:10.1039/c7ta09711e
[54] Ma, D.; Peh, S. B.; Han, G.; Chen, S. B. *ACS Appl. Mater. Interfaces* **2017,** *9,* 7523-7534. doi:10.1021/acsami.6b14223
[55] Sun, H.; Tang, B.; Wu, P. *ACS Appl. Mater. Interfaces* **2017,** *9,* 21473-21484. doi:10.1021/acsami.7b05504
[56] Du, J.; Zhou, C.; Yang, Z.; Cheng, J.; Shen, Y.; Zeng, X.; Tan, L.; Dong, L. *Surf. Coat. Technol.* **2019,** *363,* 282-290. doi:10.1016/j.surfcoat.2019.02.062
[57] Zhang, X.; Zhao, Y.; Mu, S.; Jiang, C.; Song, M.; Fang, Q.; Xue, M.; Qiu, S.; Chen, B. *ACS Appl. Mater. Interfaces* **2018,** *10,* 17301-17308. doi:10.1021/acsami.8b05137
[58] Tan, T. T. Y.; Reithofer, M. R.; Chen, E. Y.; Menon, A. G.; Hor, T. S. A.; Xu, J.; Chin, J. M. *J. Am. Chem. Soc.* **2013,** *135,* 16272-16275. doi:10.1021/ja407896m
[59] Padial, N. M.; Quartapelle Procopio, E.; Montoro, C.; Lopez, E.; Oltra, J. E.; Colombo, V.; Maspero, A.; Masciocchi, N.; Galli, S.; Senkovska, I.; Kaskel, S.; Barea, E.; Navarro, J. A. R. *Angew. Chem., Int. Ed.* **2013**, *52,* 8290-8294. doi:10.1002/anie.201303484
[60] Ko, M.; Aykanat, A.; Smith, M. K.; Mirica, K. A. *Sensors* **2017,** *17,* 2192. doi:10.3390/s17102192
[61] Du, J.; Zhang, C.; Pu, H.; Li, Y.; Jin, S.; Tan, L.; Zhou, C.; Dong, L. *Colloids Surf., A* **2019,** *573,* 222-229. doi:10.1016/j.colsurfa.2019.04.064
[62] Jayaramulu, K.; Datta, K. K. R.; Rösler, C.; Petr, M.; Otyepka, M.; Zboril, R.; Fischer, R. A. *Angew. Chem., Int. Ed.* **2016,** *55,* 1178-1182. doi:10.1002/anie.201507692
[63] Gao, M.-L.; Zhao, S.-Y.; Chen, Z.-Y.; Liu, L.; Han, Z.-B. *Inorg. Chem.* **2019,** *58,* 2261-2264. doi:10.1021/acs.inorgchem.8b03293
[64] Jayaramulu, K.; Datta, K. K. R.; Rösler, C.; Petr, M.; Otyepka, M.; Zboril, R.; Fischer, R. A. *Angew. Chem.* **2016,** *128,* 1193-1197. doi:10.1002/ange.201507692
[65] Ma, Q.; Yin, P.; Zhao, M.; Luo, Z.; Huang, Y.; He, Q.; Yu, Y.; Liu, Z.; Hu, Z.; Chen, B.; Zhang, H. *Adv. Mater. (Weinheim, Ger.)* **2019,** *31,* 1808249. doi:10.1002/adma.201808249
[66] Hmadeh, M.; Lu, Z.; Liu, Z.; Gandara, F.; Furukawa, H.; Wan, S.; Augustyn, V.; Chang, R.; Liao, L.; Zhou, F.; Perre, E.; Ozolins, V.; Suenaga, K.; Duan, X.; Dunn, B.; Yamamto, Y.; Terasaki, O.; Yaghi, O. M. *Chem. Mater.* **2012,** *24,* 3511-3513. doi:10.1021/cm301194a
[67] Mähringer, A.; Jakowetz, A. C.; Rotter, J. M.; Bohn, B. J.; Stolarczyk, J. K.; Feldmann, J.; Bein, T.; Medina, D. D. *ACS Nano* **2019,** *13,* 6711-6719. doi:10.1021/acsnano.9b01137
[68] Fowkes, F. M. *J. Phys. Chem.* **1963,** *67,* 2538-2541. doi:10.1021/j100806a008
[69] Turri, R. G.; Santos, R. M.; Rangel, E. C.; da Cruz, N. C.; Bortoleto, J. R. R.; Dias da Silva, J. H.; Antonio, C. A.; Durrant, S. F. *Appl. Surf. Sci.* **2013,** *280,* 474-481. doi:10.1016/j.apsusc.2013.05.013
[70] Wenzel, R. N. *Ind. Eng. Chem.* **1936,** *28,* 988-994. doi:10.1021/ie50320a024
[71] Virmani, E.; Rotter, J. M.; Mähringer, A.; von Zons, T.; Godt, A.; Bein, T.; Wuttke, S.; Medina, D. D. *J. Am. Chem. Soc.* **2018,** *140,* 4812-4819. doi:10.1021/jacs.7b08174
[72] Cassie, A. B. D.; Baxter, S. *Trans. Faraday Soc.* **1944,** *40,* 546-551. doi:10.1039/tf9444000546

4.4. Appendix

4.4.1. Characterization

X-ray spectroscopy

X-ray diffraction (XRD) analyses were performed on a *Bruker D8* diffractometer in Bragg-Brentano geometry with Ni-filtered Cu K_α ($\lambda = 1.54060\,Å$) radiation operating at 40 kV and 30 mA with a position-sensitive detector (*LynxEye*). Two-dimensional grazing-incident wide angle X-ray scattering (2D GIWAXS) data were collected using an *Anton-Paar SAXSpace* system equipped with a Cu-K_α microfocus source operated at 50 kV and 1 mA and an *Eiger Dectris R 1M* 2D detector.

Scanning electron microscopy (SEM)

SEM images were recorded on a *FEI Helios NanoLab G3 UC* electron microscope with an acceleration voltage of 2 kV from a field emission gun. For the cross-section analysis substrates were partially cut and broken manually to reveal fresh cross-sections. *Prior* to SEM analysis the samples were coated with a thin carbon layer by carbon fiber flash evaporation in high vacuum.

Contact angle measurements Contact-angle measurements were performed on an attension from *Biolin Scientific*. A droplet with the sessile drop method. A droplet of liquid was placed on the substrate, while recording images with 1 fps for 10 s, while the dynamic measurements (self-cleaning surfaces) were recorded with 3 fps for 10 s. The image analysis was carried out with the software ImageJ using the manual mode and fitting the contour of the droplets manually.

Atomic force microscopy (AFM) AFM measurements were performed using a *NANOINK* atomic force microscope in tapping mode with a scanning rate of 0.2 Hz, a proportional gain of 50 and an integral gain of 32. The scanned area was $5.02 \times 5.02\,\mu m$ at 282×282 pixels.

4.4.2. Experimental

General

All materials were purchased from *Sigma Aldrich, Acros or TCI Europe* in the common purities *purum, puriss* or *reagent grade*. The materials were used as received without additional purification and handled in air unless otherwise noted. The water utilized in the synthesis was subjected to a *Merck-Milipore Mili-Q* purification system *prior* to use.

Substrates

Analogous as described in[1]. The preparation of the gold substrates was based on the procedure described by Hinterholzinger *et al.* Seven microscope glass slides (*Menzel,* 76 mm × 26 mm) in a support made of Teflon were cleaned by ultrasonic treatment in acetone, followed by sequential washing steps with 2-propanol, a 1:100 mixture of *Hellmanex III* and water, and finally 2-propanol (*Chromasolv*). Oxygen plasma cleaning (*Diener electronic*, Plasma-Surface-Technology) for 30 min was conducted, previous to the mounting of the glass slides in a vacuum deposition unit installed in a glove box (*MBraun Labmaster Pro SP* equipped with an *Inficon SQC-310C* Deposition controller). 10 nm of titanium and 40 nm of gold were thermally deposited under high vacuum onto the microscope glass slides. The respective substrates were prepared by cutting commercially available microscope slides (*Menzel*, 76 mm × 26 mm), gold coated glass slides into pieces of 1.2 cm × 1.0 cm and 2.5 cm × 2.5 cm.

Bulk Synthesis Ni-CAT-1

Analogous as described in[1]. In a 5 mL culture tube, a solid mixture of 2,3,6,7,10,11-hexahydroxytriphenylene (0.0107 mmol, 3.5 mg) and nickel(II) acetate tetrahydrate (0.0201 mmol, 5 mg) was suspended in 1 mL 1-propanol and 1 mL distilled water (1:1 v:v). The loading of the culture tube was carried out under ambient atmosphere and the resulting blue solution was sonicated for 10 s at maximum power. Subsequently, the culture tube was tightly capped and heated at 85°C for 18 h in a preheated oven. The resulting black solution was washed three times with 10 mL dry

acetone and isolated by centrifugation. The obtained dark blue microcrystalline product was dried under dynamic vacuum *prior* to analysis.

Co-CAT-1

Analogous as described in[1]. In a 5 mL culture tube, a solid mixture of 2,3,6,7,10,11- hexahydroxytriphenylene (0.0107 mmol, 3.5 mg) and cobalt(II) acetate tetrahydrate (0.0207 mmol, 5 mg) was suspended in 1 mL of 1-propanol and 1 mL of distilled water (1:1 v:v). The loading of the culture tube was carried out under ambient atmosphere and the resulting blue solution was sonicated for 10 s at maximum power. Subsequently, the culture tube was tightly capped and heated at 85°C for 18 h in a preheated oven. The resulting black solution was washed three times with 10 mL of dry acetone and isolated by centrifugation. The obtained dark blue microcrystalline product was dried under dynamic vacuum *prior* to analysis.

Preparation of Ni- and Co-CAT-1 pellets

Analogous as described in[1]. Ni- (110.5 mg) and Co- (95.8 mg) CAT-1 pellets (obtained from several of the above described batches) for electrical conductivity measurements were fabricated with a standard *Paul-Weber KBr* Press.

Film formation *via* vapor-assisted conversion (VAC)

Analogous as described in[1]. For the film formation using VAC, a glass bottle (*Schott Duran*, borosilicate 3.3, ISO4796, 100 mL) with a PBT cap equipped with a Teflon seal was used. The bottom part of the bottle was filled with 14 Raschig-rings (10 mm × 10 mm, soda-lime glass) to obtain an elevated flat platform for the substrate. A mixture of water and 1-propanol was filled into the bottle. Afterwards, a substrate (1.2 cm × 1 cm) was placed on top of the Raschig-rings and fully coated with a liquid layer of a freshly prepared MOF precursor solution. The bottle was closed and transferred into a preheated oven where it was kept for the specified time. Afterwards, the autoclave was removed from the oven and cooled down for 10 min before the substrate was rinsed with dry acetone.

Synthesis of compact Ni- and Co-CAT-1 films on gold surfaces

Analogous as described in[1]. The HHTP precursor (2.69×10^{-3} mmol; 0.875 mg) and the metal precursors nickel acetate (5.0×10^{-3} mmol; 1.25 mg), cobalt acetate (5.0×10^{-3} mmol; 1.25 mg) or copper trifluoroacetylacetonate (5.0×10^{-3} mmol; 1.25 mg) were mixed in a defined ratio (1:2) and dissolved in a solvent mixture of water and 1-propanol (1.5 mL : 1.5 mL) by sonication for 20 s at maximum power. The obtained precursor solution was filtered through a syringe filter to remove any remaining particles. Subsequent, 40 µL of the solution (HHTP: 0.899 mmol L^{-1}; MOAc: 1.674 mmol L^{-1}) were deposited onto a clean 1.2 cm × 1.0 cm gold substrate. Four of these set-ups were placed onto glass spacers in an autoclave loaded with a solvent mixture of

water and 1-propanol 2.5 cm × 2.5 cm. The autoclave was sealed immediately and placed into a preheated oven at 85°C for 3.5 h. Afterwards, the autoclave was removed from the oven and cooled down for 10 min before the substrate was rinsed with dry acetone.

Synthesis of nanostructured Ni-CAT-1 films on gold substrates

The precursor solution was prepared by providing a hexahydroxytriphenylene (HHTP) precursor (5.4×10^{-3} mmol; 1.75 mg) as the organic building blocks and nickel acetate (10×10^{-3} mmol; 2.5 mg) as the metallic precursor in a defined ratio (1:2 n:n) and dissolving them in a solvent mixture of water and 1-propanol (1 mL : 1 mL) with the addition of a modulator acetic acid (50 µL). 40 µL of the respective precursor solution (HHTP: 2.75 mmol L^{-1}; NiAc: 5 mmol L^{-1}; HOAc: 0.41 mol L^{-1}) was dropcasted onto the surface of a clean 1.2 cm × 1.0 cm gold coated glass substrate. Four of such substrates, each carrying a thin layer of precursor solution, were placed onto glass spacers as substrate holders in an autoclave partly filled with a solvent bath consisting of water and 1-propanol (2.5 cm × 2.5 cm). The autoclave was sealed immediately and placed into a preheated oven at 85°C for 12 hours. Afterwards, the autoclave was removed from the oven and cooled down for 10 min, before the substrates were rinsed with dry acetone.

Synthesis of nanostructured Co-CAT-1 films on gold substrates

The precursor solution was prepared by providing an HHTP precursor (5.4×10^{-3} mmol; 1.75 mg) as the organic building blocks and cobalt acetate (11.0×10^{-3} mmol; 3 mg) as the metallic precursors in a defined ratio (1:2 n:n) and dissolving them in a solvent mixture of water, 1-propanol (1 mL : 1 mL) with addition of 50 µL of a water, 1-propanol solution (1 mL : 1 mL) containing salicylic acid as a modulator (0.89 mmol; 125 mg). 40 µL of the respective precursor solution (HHTP: 2.75 mmol L^{-1}; CoAc: 6 mmol L^{-1}; salicylic acid: 0.01 mmol L^{-1}) was dropcasted onto a clean 1.2 cm × 1.0 cm gold coated substrate. Four of such substrates, each carrying a thin layer of precursor solution, were placed onto glass spacers as substrate holders in an autoclave partly filled with a solvent bath consisting of water and 1-propanol (2.5 cm × 2.5 cm). The autoclave was sealed immediately and placed into a preheated oven at 85°C for 12 h. Afterwards, the autoclave was removed from the oven and cooled down for 10 min, before the substrates were rinsed with dry acetone.

Synthesis of nanostructured Ni-CAT-1 films on glass substrates

Analogous as described in [1]. The HHTP precursor (5.4×10^{-3} mmol; 1.75 mg) and the nickel acetate (10.0×10^{-3} mmol; 2.5 mg) were mixed in a defined ratio (1:2) and dissolved in a solvent mixture of water and 1-propanol (1 mL : 1 mL) with the addition of the modulator acetic acid (50 µL). 100 µL of the respective precursor solution (HHTP: 2.75 mmol L^{-1}; NiAc: 6 mmol L^{-1}; HOAc: 0.41 mol L^{-1}) were deposited onto a clean 2.5 × 2.5 cm glass substrate. One of this set-ups was placed onto glass spacers in an autoclave loaded with a solvent mixture of water and

1-propanol (2.5 cm × 2.5 cm). The autoclave was sealed immediately and placed into a preheated oven at 85°C for 18 h. Afterwards, the autoclave was removed from the oven and cooled down for 10 min before the substrates were rinsed with dry acetone.

4.4.3. Characterization of the M-CAT-1 bulk material

PXRD and SEM analysis of Ni- and Co-CAT-1 bulk materials

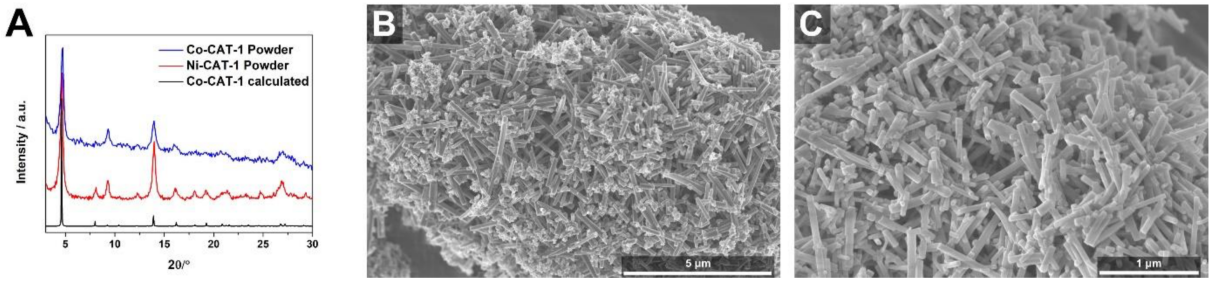

Figure 4.6 – PXRD pattern of the Ni- and Co-CAT-1 (red and blue) powders compared to the calculated Co-CAT-1 pattern (black). B) and C) show the needle-like bulk morphology of the Ni- and Co-CAT-1 crystal, respectively.

PXRD and SEM analysis of pelletized Ni- and Co-CAT-1 samples

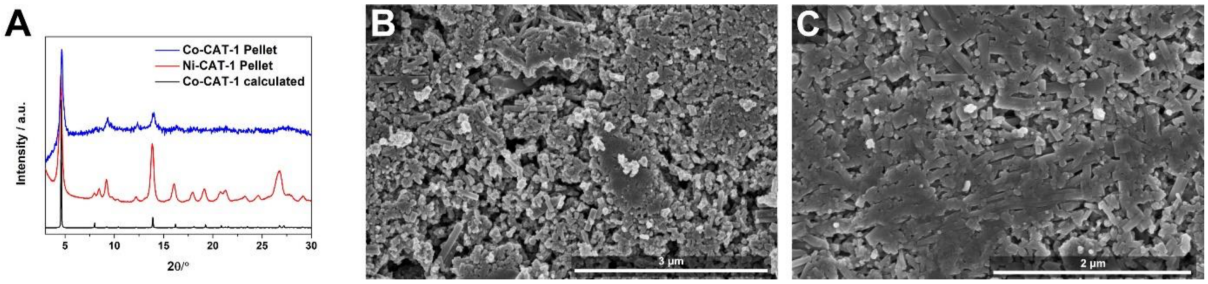

Figure 4.7 – A) PXRD pattern of the Ni- and Co-CAT-1 (red and blue) pelletized materials compared to the calculated Co-CAT-1 pattern (black). B) and C) show the dense needle-like bulk surface of the Ni- and Co-CAT-1 pelletized samples, respectively.

Water and Oil-contact angles of Ni- and Co-CAT-1 pellets in water

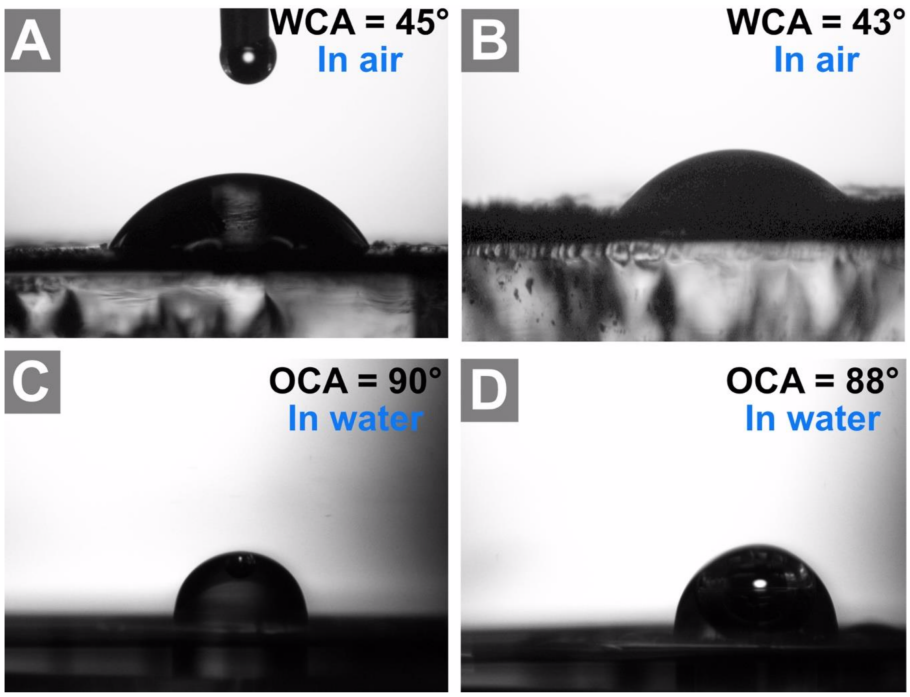

Figure 4.8 – A) and B) Water contact angle of Ni- and Co-CAT-1 pellet samples in air, respectively. C) and D) underwater dichloromethane contact angle of Ni- and Co-CAT-1 pellet samples, respectively.

Atomic force microscopy (AFM) of M-CAT-1 Pellets

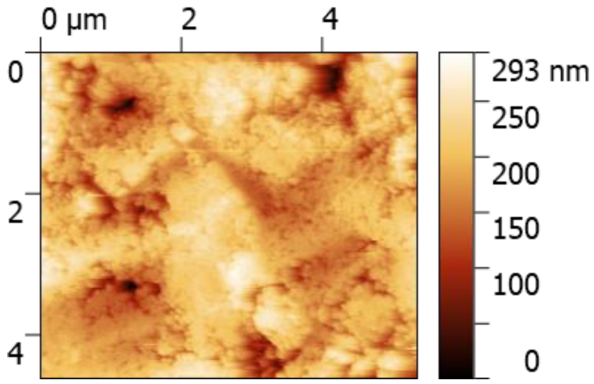

Figure 4.9 – AFM topographic measurement of a Ni-CAT-1 pelletized sample (4.5 µm × 4.7 µm). The surface roughness values were calculated to be 37 nm (R_{ms}).

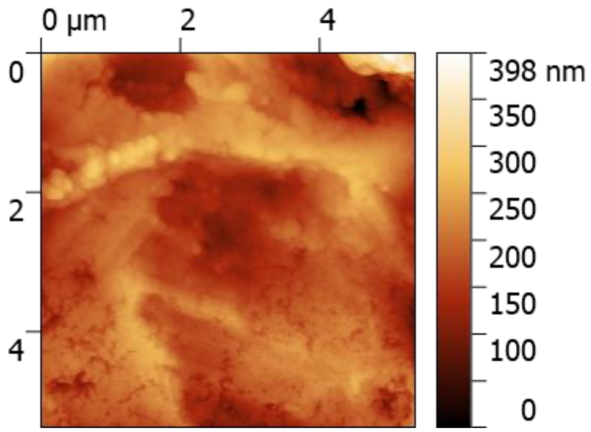

Figure 4.10 – AFM topographic measurement of a Co-CAT-1 pelletized sample (4.5 µm × 4.7 µm). The surface roughness values were calculated to be 44 nm (R_{ms}).

Surface energy of M-CATs

The wetting properties of the M-CAT-1 were estimated by the following procedure. First, M-CAT-1 bulk materials were prepared according to a literature procedure. Subsequently, the obtained microcrystalline powders were pressed to pelletized samples (1 cm diameter, thicknesses 500 µm; 100 mg material). The samples exhibit an even surface composed of densely packed and randomly oriented crystallites. This was confirmed by scanning-electron microscopy (SEM) and X-ray diffraction (XRD) analysis and atomic force microscopy (AFM). On the as-prepared pelletized samples we performed contact angle (CA) measurements to estimate the free solid surface energy, especially the dispersive and polar components. The free surface energy of a solid cannot be directly measured, but it can be calculated from a set of steady state liquid/solid contact angles. Therefore, we used a common method for estimating the free surface energy, the Fowkes theory. This theory describes the surface energy of a solid as composed of a dispersive component, and "non"-dispersive part (polar). It is therefore based on the Young's equation and the Dupre's definition of adhesion energy showing that the adhesive energy between a solid and a liquid can be separated into dispersive interactions and the non-dispersive (polar) interactions between the two phases. These two energy expressions, *e.g.,* Young's and the Dupre's equations can be combined to yield the Fowkes' surface energy equation:

$$(\sigma_L^D)^{1/2}(\sigma_S^D)^{1/2} + (\sigma_L^P)^{1/2}(\sigma_S^P)^{1/2} = \frac{\sigma_L(cos\theta + 1)}{2} \tag{4.1}$$

σ_L^D = surface tension liquid (dispersive); σ_S^D = surface tension solid (dispersive); σ_S^P = surface tension solid (polar); σ_L^P = surface tension liquid (polar); σ_L = overall surface tension liquid; θ = measured contact angle at the liquid/solid interface.

In order to determine the surface energy, we tested the solid surface using a liquid which exhibits only a dispersive component to its overall surface tension ($\sigma_L = \sigma_L^D = 50.8\,\mathrm{mN/m}$) featuring a high surface tension, hence diiodmethane ($\sigma_L^P = 0$) was the solvent of choice. Straightforwardly, eq. 4.1 can be expressed as:

$$\sigma_S^D = \frac{\sigma_L(cos\theta + 1)^2}{4} \tag{4.2}$$

σ_S^D can be directly determined from the measured CA of diiodmethane. In the next step, we proceeded with measuring the CA of distilled water showing one polar and one dispersive component to its overall surface tension ($\sigma_L^P = 46.4\,\mathrm{mN/m}$, and $\sigma_L^D = 26.4\,\mathrm{mN/m}$). Knowing these components, we calculated σ_S^P as the only unknown parameter in eq. 4.1. By adding the dispersive and the polar components of the solid, we finally obtained the σ_S overall surface energy of the M-CAT-1 materials (eq. 4.3).

$$\sigma_S^D + \sigma_S^P = \sigma_S \tag{4.3}$$

Table 4 – Overall surface energies (σ_S) and the respective dispersive (σ_S^D) and polar component (σ_S^P) estimated for Ni- and Co-CAT-1 oriented and compact films (OCF) and oriented and nanostructured films (ONF).

M-CAT-1	σ_S [mN/m]	$\sigma_S{}^D$ [mN/m]	$\sigma_S{}^P$ [mN/m]
Ni-CAT-1(OCF)	71.3	50.8	20.4
Co-CAT-1(OCF)	73.6	50.8	22.8
Ni-CAT-1(ONF)	79.5	50.8	28.5
Co-CAT-1(ONF)	79.5	50.8	28.5

4.4.4. Reference contact angle measurements

Contact angle (CA)

The contact angle (CA) describes the measured angle between a liquid-vapor interface in direct contact with a solid surface. From the obtained CA the wettability of the solid surface can be analyzed.

CA measurements on gold substrates

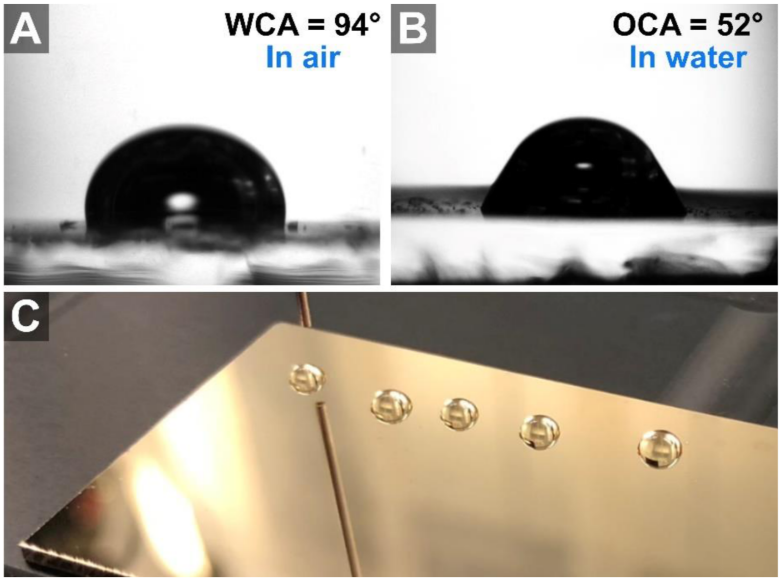

Figure 4.11 – A) CA measurements of a bare gold surface (right after deposition) in air. B) OCA measurements of a bare gold surface in water with dichloromethane as an oil test liquid C) Macroscopic photographs of water droplets on a bare gold surface used for WCA measurements in air.

CA measurements on glass substrates

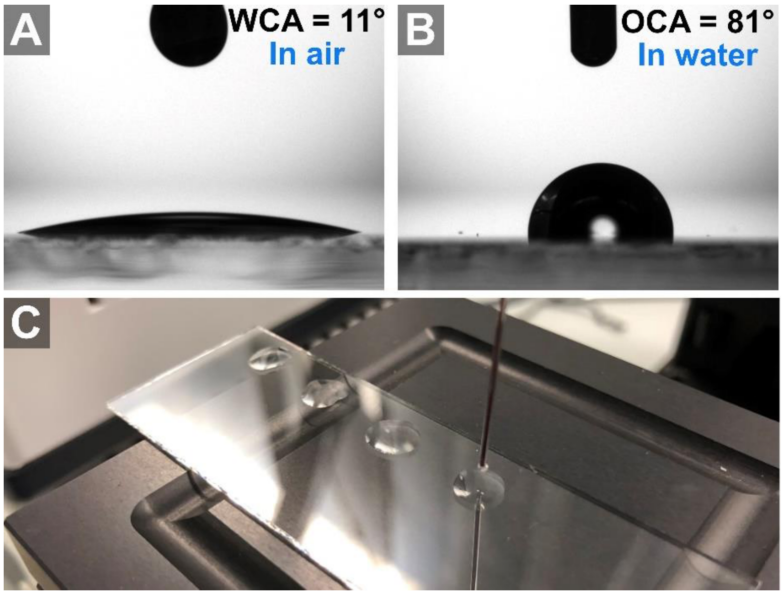

Figure 4.12 – A) WCA on a bare glass surface in air. B) Under water OCA of dichloromethane droplet on a bare glass surface C) Macroscopic photographs of water droplets placed on a bare glass surface in air.

4.4.5. Characterization of M-CAT-1 thin films

GIWAXS and SEM of oriented and compact Ni- and Co-CAT-1 thin films

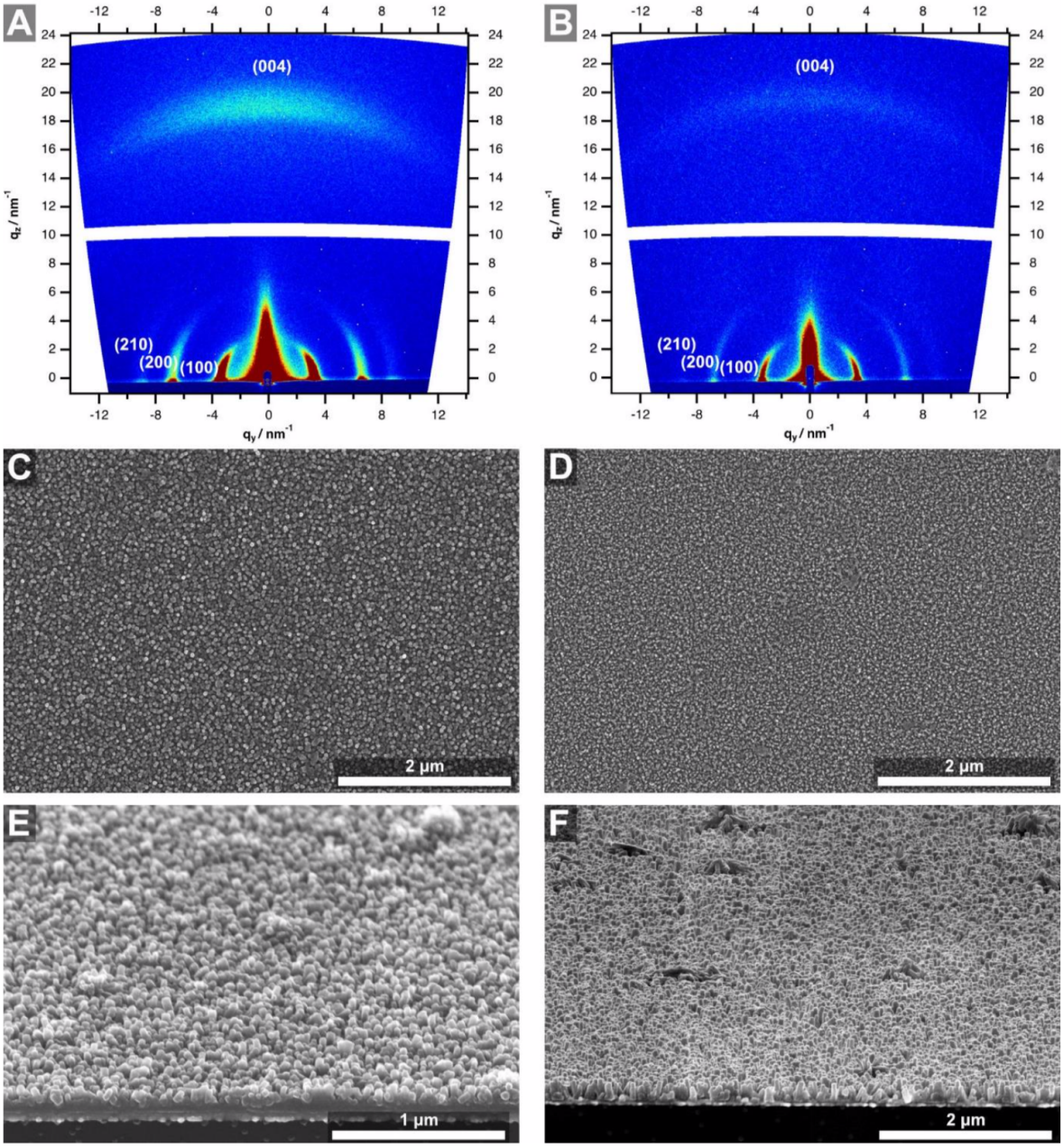

Figure 4.13 – A), C) and E) Depict a the GIWAXS measurement of an oriented and compact Ni- CAT-1 film on gold, top-view SEM and 30° tilted SEM cross-section images of the same sample, respectively. B), D) and F) Depict a GIWAXS measurement of an oriented and compact Co-CAT- 1 film on gold, top-view SEM and 30° tilted SEM cross-section images of the same sample, respectively.

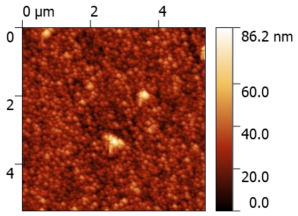

Figure 4.14 – Atomic force microscopy topographic image of an oriented and compact Ni- CAT-1 thin film (4.5 µm × 4.7 µm). Measured roughness (R_{ms}) of 10.2 nm.

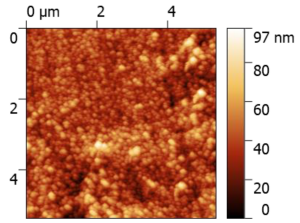

Figure 4.15 – Atomic force microscopy topographic image of an oriented and compact Co-CAT-1 film (4.5 µm × 4.7 µm). Measured roughness (R_{ms}) of 14.1 nm.

Nanostructured Ni- and Co-CAT-1 thin films on gold substrates

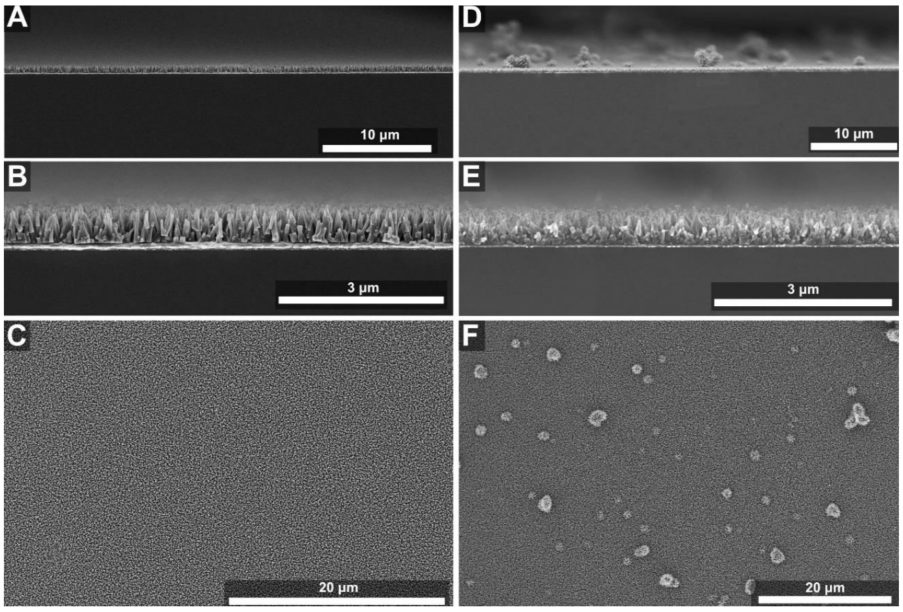

Figure 4.16 – A), B) and C) Depict the cross-section, a magnified cross-section image, and a top- view micrograph of Co-CAT-1 grown on gold as a nanostructured film, respectively. D), E) and F) Depict the cross-section, a magnified cross-section image, and a top-view micrograph of Ni- CAT-1 grown on gold as a nanostructured film, respectively.

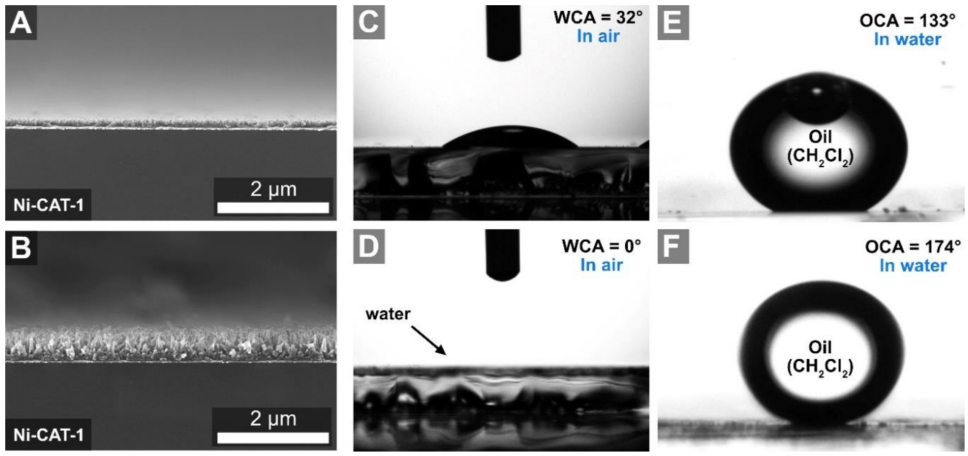

Figure 4.17 – Cross-section SEM micrographs of A) an oriented and compact Ni-CAT-1 film and B) an oriented (pillar-like) nanostructured Ni-CAT-1 film. C) and D) WCA obtained for the compact (WCA = 32°) and the nanostructured (WCA = 0°) films, respectively. E) and F) Underwater OCA obtained for the compact (CA = 133°) and the nanostructured film (CA = 173°) with dichloromethane (DCM), respectively.

Figure 4.18 – An image series of a self-cleaning surface experiment (3 fps) with DCM as an oil droplet placed on a tilted nanostructured Ni-CAT-1 film (tilt angle of 1.4°).

Photographs of the WCA and OCA measurements

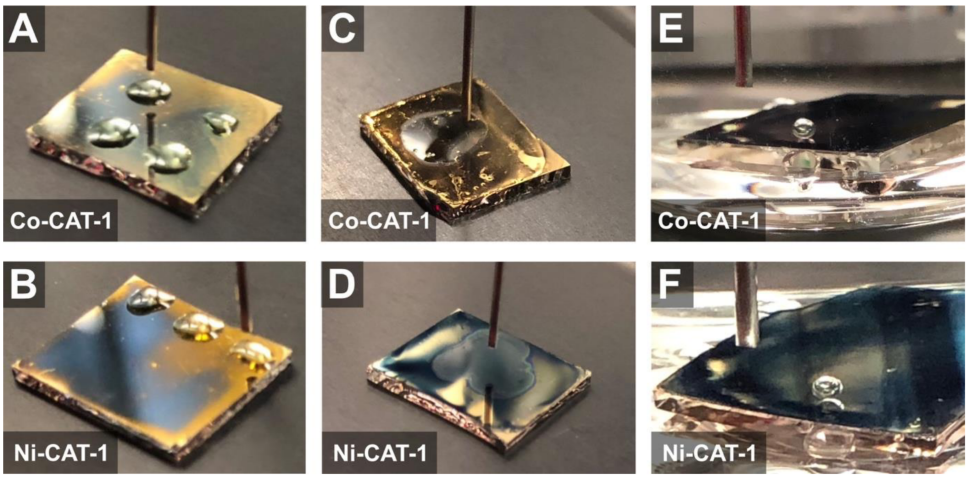

Figure 4.19 – A) and B) Macroscopic macrographs of the WCA experiments on compact Co- and Ni-CAT-1 films. C) and D) WCA experiments on nanostructured Co- and Ni-CAT-1 films in water. E) and F) OCA experiments on nanostructured Co- and Ni-CAT-1 films in water.

GIWAXS and SEM analysis of nanostructured films grown on glass substrates

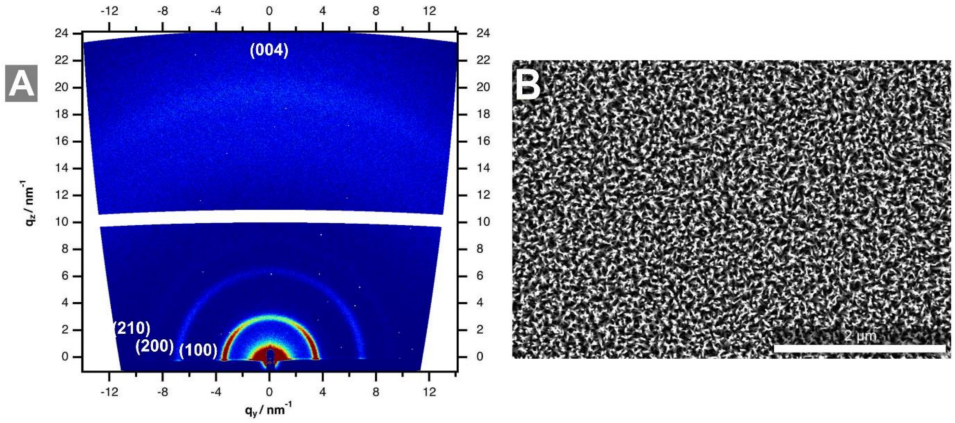

Figure 4.20 – A) GIWAXS pattern of a Ni-CAT-1 film featuring preferred crystal orientation on a glass substrate. B) Corresponding top-view SEM micrograph of the film.

UV-vis of nanostructured Ni-CAT-1 films grown on quartz

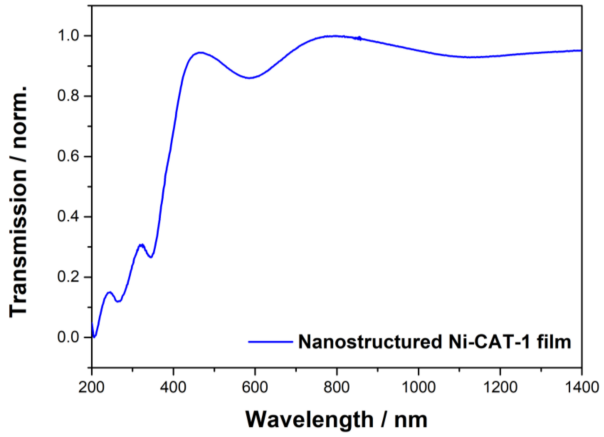

Figure 4.21 – Transmission UV-vis spectrum of Ni-CAT-1 film grown on a quartz substrate. The material exhibits a strong absorbance with an onset at 425 nm.

Impact of precursor and crystallization promotor concentration on the film growth

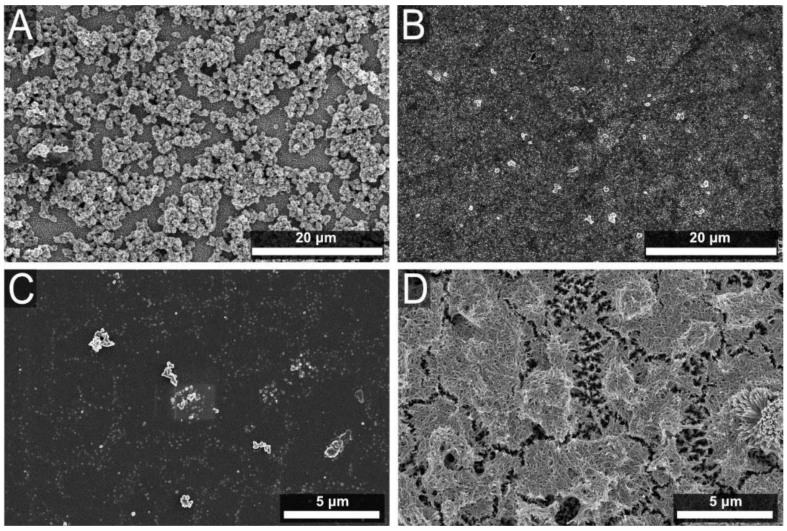

Figure 4.22 – Reducing the concentration of the crystallization promotor with respect to the optimal conditions led to uncontrolled formation of bulk material on top of the film (A). A higher concentration of the additive led to the formation of an amorphous phase (B). Reducing the precursor material concentration led to the formation of an amorphous material precipitation on the surface (C), while higher concentrations led to the precipitation of residual powder on the MOF film (D).

4.4.6. Anti-fog coating experiments

Macroscopic photograph of the anti-fog coating experiment

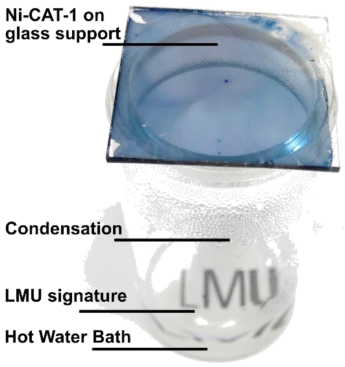

Figure 4.23 – In a glass vessel a hot water bath is provided. The hot steam rising from the hot water reservoir is condensing on the upper part of the glass vessel, while the Ni-CAT-1 coated glass support remains free of water droplets. Therefore, vision through the glass support is enabled.

Temperature-dependent anti-fog coating experiments

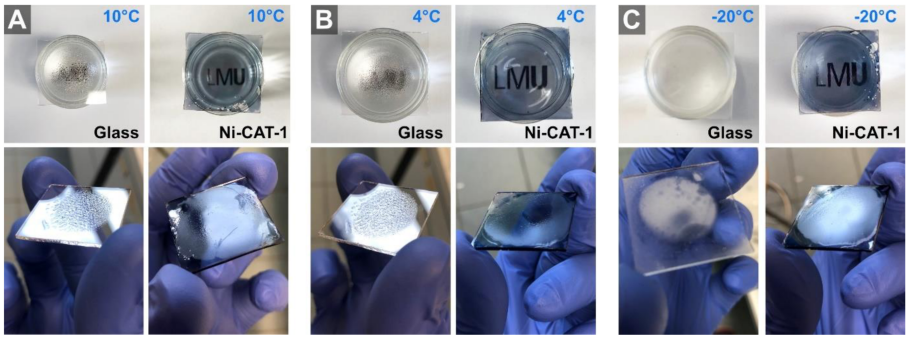

Figure 4.24 – Temperature-dependent anti-fog experiment series. Here, glass reference and the Ni-CAT-1 film on glass were cooled down to temperature of 10°C, 4°C and −20°C. After cooling, the substrates were placed on top of the hot water reservoir. It can be seen that in all cases the hot vapor steam is not condensing on the Ni-CAT-1 glass supported samples.

4.4.7. Wetting models

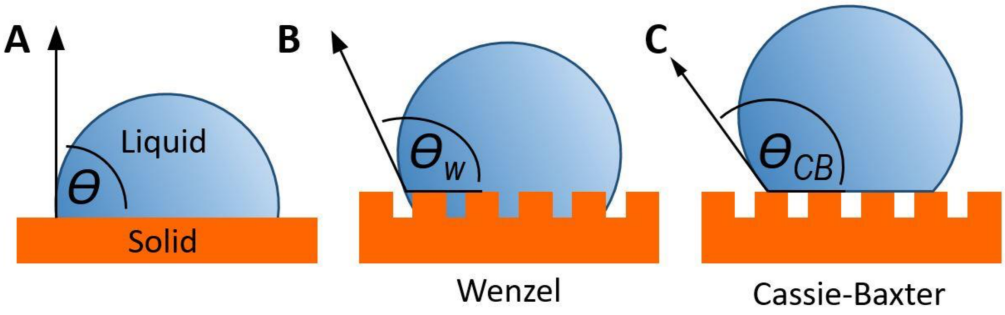

Figure 4.25 – A Scheme of possible wetting models for a liquid of a structured solid surface. A) Displays the wetting angle θ of a theoretical flat surface. B) The change of the wetting angle to θ_w according to the Wenzel equation: $\cos\theta_w = \mathrm{r}\cos\theta$. In this model, the structuring of the solid enhances the inherent existing wetting properties of the surface. The liquid is homogenously wetting the surface. C) a Cassie and Baxter description of the contact angle θ_{CB} referring to a heterogeneous wetting of the surface by interacting solely with the elevated structured surface.

4.4.8. Stability tests

Ni-CAT-1 oriented and nanostructured films on gold substrates

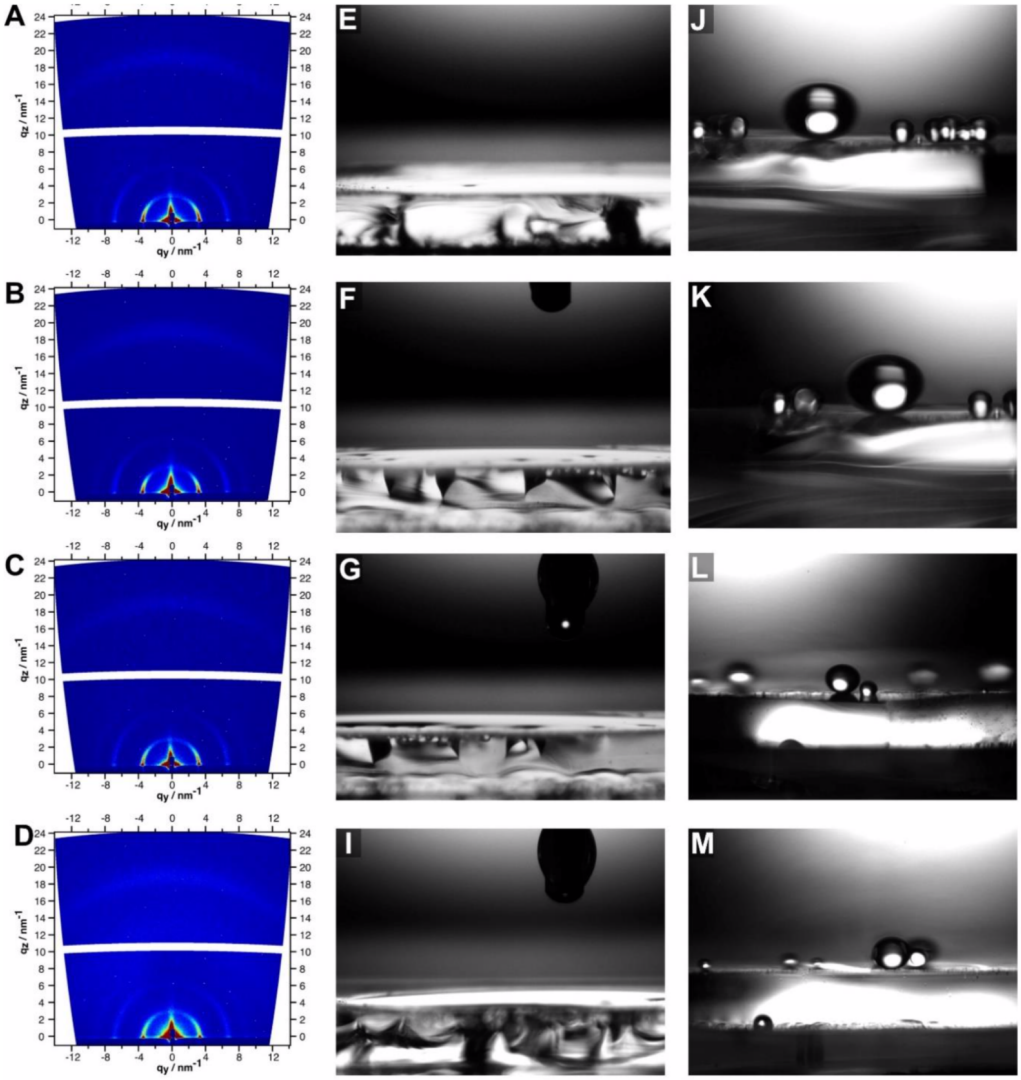

Figure 4.26 – A), B), C) and D) GIWAXS patterns of nanostructured Ni-CAT-1 thin films on gold substrates after immersion in an acidic (hydrochloric acid) aqua solution (pH 5, 12 h), basic (sodium hydroxide) aqua solution (pH 9, 12 h), exposure to high temperatures (150°C, 12 h), and mechanical impact (sonication in a water bath, 20 min), respectively. E), F), G) and H) WCA of Ni-CAT-1 nanostructured thin films after immersion in an acidic (hydrochloric acid) aqua solution (pH 5, 12 h), in basic (sodium hydroxide) aqua solution (pH 9, 12 h), exposure to high temperatures (150°C, 12 h), and mechanical impact (sonication in a water bath, 20 min), respectively. J), K), L) and M) OCA of Ni-CAT-1 nanostructured thin films after immersion in an acidic (hydrochloric acid) aqua solution (pH 5, 12 h), in basic (sodium hydroxide) aqua solution (pH 9, 12 h), exposure to high temperatures (150°C, 12 h), and mechanical impact (sonication in a water bath, 20 min), respectively.

Co-CAT-1 oriented and nanostructured films on gold substrates

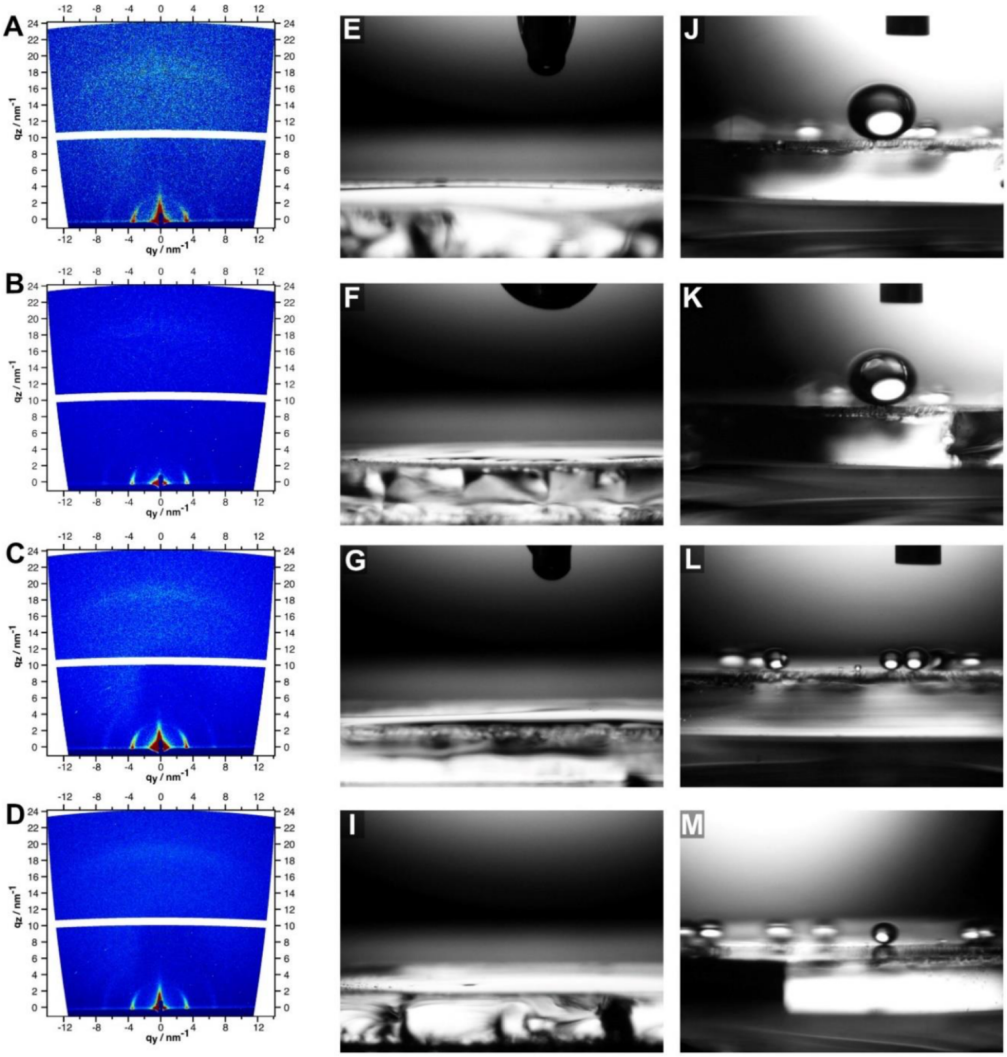

Figure 4.27 – A), B), C) and D) GIWAXS patterns of nanostructured Co-CAT-1 thin films on gold substrates after immersion in an acidic (hydrochloric acid) aqua solution (pH 5, 12 h), basic (sodium hydroxide) aqua solution (pH 9, 12 h), exposure to high temperatures (150°C, 12 h), and mechanical impact (sonication in a water bath, 20 min), respectively. E), F), G) and H) WCA of Ni-CAT-1 nanostructured thin films after immersion in an acidic (hydrochloric acid) aqua solution (pH 5, 12 h), in basic (sodium hydroxide) aqua solution (pH 9, 12 h), exposure to high temperatures (150°C, 12 h), and mechanical impact (sonication in a water bath, 20 min), respectively. J), K), L) and M) OCA of Ni-CAT-1 nanostructured thin films after immersion in an acidic (hydrochloric acid) aqua solution (pH 5, 12 h), in basic (sodium hydroxide) aqua solution (pH 9, 12 h), exposure to high temperatures (150°C, 12 h), and mechanical impact (sonication in a water bath, 20 min), respectively.

Nanostructured Ni-CAT-1 films on glass substrates

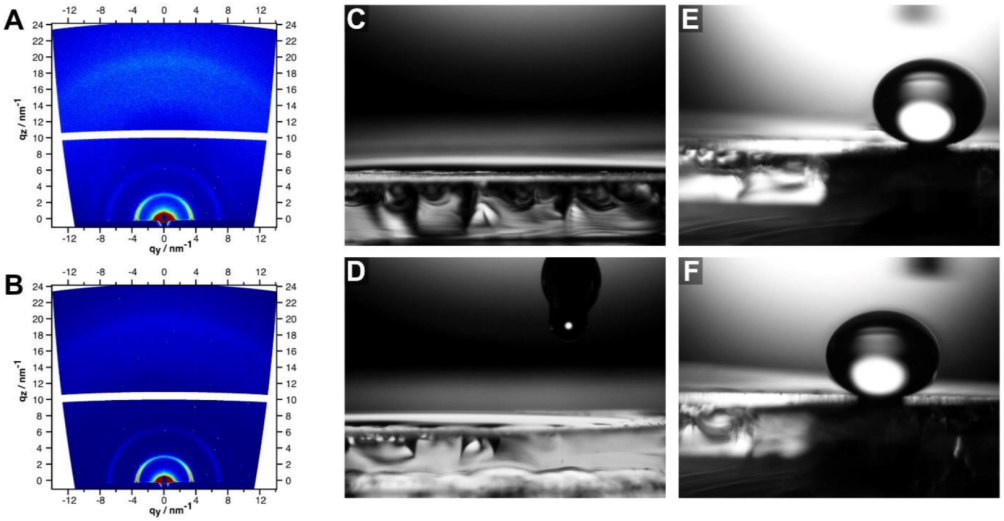

Figure 4.28 – A), B) GIWAXS patterns of nanostructured Ni-CAT-1 thin films grown on gold substrates after immersion in an acidic (hydrochloric acid) aqua solution (pH 5, 12 h) and exposure to high temperatures (150°C, 12 h), respectively. C), D) WCA of Ni-CAT-1 nanostructured thin films after immersion in an acidic (hydrochloric acid) aqua solution (pH 5, 12 h) and exposure to high temperatures (pH 5, 12 h), respectively. E) and F) OCA of Ni-CAT- 1 nanostructured thin films after immersion in acidic (hydrochloric acid) aqua solution (pH 5, 12 h) and exposure to high temperatures (150°C, 12h), respectively.

References

[1] Mähringer, A.; Jakowetz, A. C.; Rotter, J. M.; Bohn, B. J.; Stolarczyk, J. K.; Feldmann, J.; Bein, T.; Medina, D. D. *ACS Nano* **2019,** *13,* 6711-6719. doi:10.1021/acsnano.9b01137

5. Energy efficient, ultrahigh flux separation of oily pollutants from water with superhydrophilic nanoscale metal-organic framework architectures

This chapter is based on the following publication:

Andre Mähringer[a], Matthias Hennemann[b], Timothy Cark[b], Thomas Bein[a] and Dana D. Medina*[,a],
Angew. Chem. Int. Ed. **2021,** 60, 2-10.

[a]Department of Chemistry, Ludwig-Maximilians-Universität (LMU), Butenandtstr. 11 (E), 81377 Munich, Germany.

[b]Computer-Chemistry-Center, Department of Chemistry and Pharmacy, Friedrich-Alexander-University Erlangen-Nuremberg, Naegelsbachstr. 25, 91052 Erlangen, Germany.

*Corresponding Author.

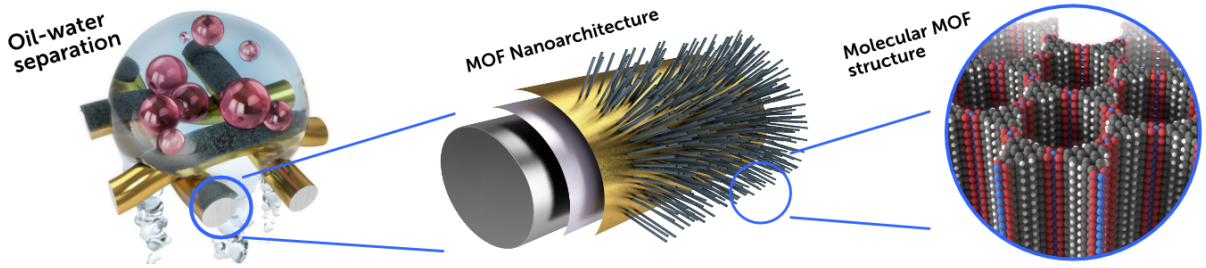

DOI: 10.1002/anie.202012428

Abstract

The rising demand for clean water for a growing and increasingly urban global population is one of the most urgent issues of our time. Particularly, the increasing generation of wastewater by cities and industrial sources requires the development of novel platforms for separating contaminants such as oils. Here, we introduce the synthesis of a unique nanoscale architecture of pillar-like Co-CAT-1 metal-organic framework (MOF) crystallites on gold-coated woven stainless steel meshes with large, 50 µm apertures. These nanostructured mesh surfaces feature superhydrophilic and underwater superoleophobic wetting properties, allowing for gravity-driven, highly efficient oil-water separation featuring water fluxes of up to nearly one million $L\,m^{-2}\,h^{-1}$. Water physisorption experiments reveal the hydrophilic nature of Co-CAT-1 with a total water uptake at room temperature of $470\,cm^3\ g^{-1}$. Furthermore, semiempirical molecular orbital calculations shed light on water affinity of the inner and outer pore surfaces. The MOF-based membranes enable high separation efficiencies for a number of liquids tested, including the notorious water pollutant, crude oil, affording chemical oxygen demand (COD) concentrations below $25\,mg\ L^{-1}$ of the effluent. Our results demonstrate the great impact of suitable nanoscale surface architectures as a means of encoding on-surface extreme wetting properties, yielding energy-efficient water-selective large-aperture membranes. The extremely low resistance to flow and the resulting enormous flux capabilities hold great promise for water cleanup on a massive scale and for the design of practical, low-cost water purification devices that can be operated without external power source and without moving parts.

5.1. Introduction

Adequate wastewater management is of great significance for a global sustainable and green economic development. By definition, wastewater is regarded as any human-affected water and can originate from a variety of diverse sources, e.g., domestic, industrial or agricultural.[1] In 2017, the United Nations released the world water development report entitled "Wastewater, the untapped resource" highlighting that 80% of the globally produced wastewater flows back into the ecosystem without adequate treatment or being reused.[2] Since two thirds of the world's population currently lives in areas that experience water scarcity for at least one month per year, the collection, separation, and recycling of wastewater will become a matter of vital importance.[3] One important pathway for improving water-resource management is recovering vital organic substances from waste water, enabling both to be reused after recycling processes.[2,4]

Generally, oil-water separation includes a broad range of applications such as removing oil leaks and spills, industrial wastewater treatment in oil refineries, petrochemical plants or chemical

plants, or reusing wastewater for agriculture.[5] To date, several approaches for the separation of oil and water have been developed, the most prominent being the American Oil Petroleum Institute (API) oil-water separators, which are based on Stokes' law, harnessing the density difference and size of oil droplets in water for the separation.[6] Alternatively, traces of oils in water can be removed by passing the wastewater through absorber tanks containing organoclays.[7] Nowadays, membrane-based filters with nanometer pore apertures such as MOFs are emerging.[8] The separation principle of these systems is based on chemical functionalization of the membrane with hydrophobic or hydrophilic moieties.[8] By using particular functional groups, either the incoming water or oil flow is hindered according to the specific wetting properties of the membrane. A major advantage of this technique is a high separation efficiency. However, the need of applying significant backpressure to achieve sufficient flux, the chemical stability of the filter, time-consuming production, or sieving of high-profile contaminants such as crude oil are still serious challenges.[10]

In addition to employing chemical functional groups, extreme wetting properties can also be controlled through morphology.[11] According to the Wenzel or Cassie-Baxter models, rough surfaces feature enhanced wetting properties, depending on their intrinsic polarity.[12] To achieve ultrahigh flux in separations, nanowires and nanorods have been synthesized on the backbone of meshes with large apertures.[8,13] While several reports deal with oil-water separations by this approach, deterministic control over the morphology and orientation of crystalline selective layers on the mesh wires is still lacking. In additions, due to the utilization of large pore membranes the issue of water effluent quality remains largely elusive.[10]

Herein, we report highly efficient, gravity-driven and ultrahigh flux oil-water separations using an open mesh decorated with a well-defined nanoscale MOF architecture. We utilized vapor-assisted conversion (VAC) for crafting pillar-like Co-CAT-1 (Co triphenylene catecholate) MOF architectures exclusively on the mesh backbone.[14,15] Three-dimensional periodic semiempirical molecular-orbital (MO) calculations of the Co-CAT-1 water stabilization energy and water sorption experiments illustrate the high affinity of this compound towards water. According to these findings, MOF-coated mesh membrane, several oil-water separation studies were performed. To determine the water quality after separation, the water effluent was collected, and the chemical oxygen demand (COD) concentrations were measured. Based on the COD values, we further elucidated the separation efficiencies, which ranged up to 99.98%, and the MOF-based filtration system. Furthermore, we have illustrated the efficient separation of water and crude oil, driven by gravity alone and yielding cleaned water within minutes, with COD levels much below typical wastewater reuse standards.[16] The chemical and mechanical stability of the mesh were tested under different separation conditions, filtering water with acidic and basic pH and seawater. Remarkably, the MOF-based membrane features extremely high fluxes up to nearly one million

$L\,m^{-2}\,h^{-1}$, higher than a bare mesh, combined with superior water quality (COD greater as $25\,mg\,L^{-1}$).[17]

5.2. Results and discussion

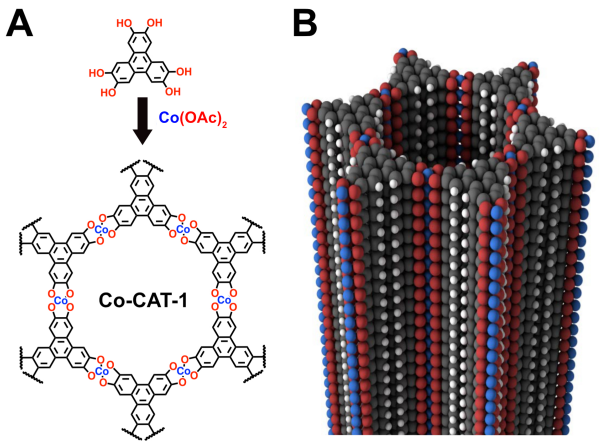

Figure 5.1 – **A)** Reaction scheme of 2,3,6,7,11,12 hexahydroxytriphenylene (HHTP) and cobalt acetate tetrahydrate to form Co-CAT-1. **B)** The planar layers of Co-CAT-1 are stacked, forming hexagonal micropore alignments.

The metal-organic Co-CAT-1 framework is a microporous material consisting of the organic building block 2,3,6,7,10,11-hexahydroxytriphenylene (HHTP) connected *via* cobalt catecholate complex nodes forming a layered structure (Figure5.1). A previous pioneering report elucidated the Co-CAT-1 crystal structure and the incorporation of water molecules in the crystal through complexation to the metal nodes (Figure 5.13 S8). This intriguing structural property points to a highly polar pore environment, essentially increasing the effective hydrophilic surfaces. Very recently, we reported the synthesis of nanostructured and pillar-like M-CAT-1 coatings that make superhydrophilic, underwater superoleophobic and self-cleaning properties on continuous surfaces possible.[18] Thereby, the combination of well-defined and -aligned water-containing nanoporous cavities and a deterministic control of the film roughness created extreme wetting properties (Figure 5.14).

Here, the concept of crafting nanostructured MOF surfaces was transferred to 3D-shaped permeable objects, aimed at separating oil and water by the fundamental principle of selective flow on the basis of extreme hydrophilicity at polar surfaces. In the first part of the study, Co-CAT-1 coating was exclusively grown on the wires of stainless steel meshes (SSMs). To enable high flux and efficient oil-water separations, SSMs with large apertures of 50 µm were chosen as a preferred type of substrate (Figure 5.2A). According to our previous reports, M-CAT-1 materials

grow as crystalline and oriented thin films preferably on gold surfaces. To provide gold-supported membranes, (Figure 5.2B) a thin layer of 40 nm gold was deposited on the bare SSMs *via* physical vapor deposition (PVD) (Figure 5.10). A cost estimate for the gold deposition process is given in the SI. The Au@SSM obtained was used as a substrate in a VAC synthesis of Co-CAT-1 film on the mesh surface (Figure 5.2C, 5.7, 5.9). In short, a gold-coated mesh was immersed into a MOF precursor solution in a Teflon cavity holder (Figure 5.6). This setup was positioned on top of a glass platform in a glass autoclave. At the bottom of the autoclave, a solvent mixture bath of 1-propanol and water (5 mL; 1:1; v/v) was placed. Subsequently, the autoclave was sealed and transferred to a preheated oven at 85°C. In the course of the reaction, the solvent of the precursor solution in the small cavity was slowly evaporated, enabling a homogenous growth of the Co-CAT-1 onto the mesh wires. After 12 h, the Co-CAT-1@Au@SSM mesh was retrieved and rinsed with acetone *prior* to analysis.

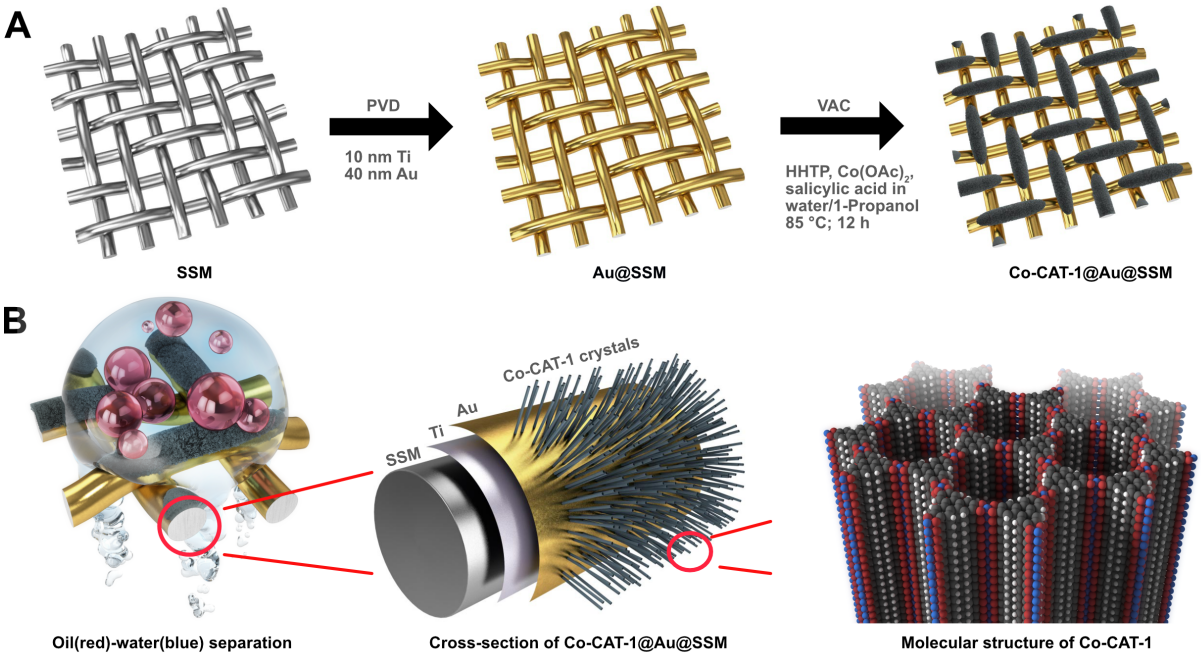

Figure 5.2 – **A)** A schematic illustration of the fabrication process of a MOF-based mesh. A stainless-steel mesh (SSM) with apertures of 50 µm is coated with a thin 40 nm layer of gold *via* physical vapor deposition (PVD). The obtained Au@SSM is used as a substrate for VAC film synthesis, resulting in the desired Co-CAT-1@Au@SSM. **B)** Schematic illustration of the oil-water separation by the Co-CAT-1@Au@SSM membrane blocking oil flux and allowing only water to pass through the apertures. Cross-sectional visualization of a fabricated Co-CAT-1@Au@SSM string. The Co-Cat-1 crystals are comprised of metal-ions in-plane coordinated by 2,3,6,7,10,11-hexahydroxytriphenylene units forming hexagonally structured 2D layers. Finally, the MOF forms needle-like crystallites on the gold patterns encoding superhydrophilic properties on the mesh.

The fabrication process of the Co-CAT-1@Au@SSMs was monitored by energy dispersive X-ray spectroscopy (EDX) mapping and back-scattered electron (BSE) microscopy (Figure 5.7-5.8). Here, continuous cobalt-containing patches exclusively covering the gold-coated parts of the mesh were observed (Figure 5.7). The coating is further visualized in the BSE image as a dark area (Figure 5.3A) which precisely overlaps with the cobalt distribution EDX maps (Figure 5.7-5.8). Furthermore, SEM micrographs reveal a distinct textured layer on the mesh's wires following the gold pattern, however in the proximity of the nodes where gold is absent, the MOF coating ceases. After the synthesis, the apertures of the mesh appear accessible and residual precursor or extraneous MOF material is not detected (see Figure 5.8). A high magnification SEM micrograph of the Co-CAT-1@Au@SSM reveals a nanostructured surface composed of needle-like crystallites (Figure 5.3B), which are preferentially aligned perpendicular to the surface (Figure 5.9). To confirm the formation of Co-CAT-1, the mesh surface was scratched off with a sharp razor blade and the substance obtained was transferred to a conducting copper grid for transmission electron microscopy (TEM) analysis. The electron diffraction pattern and corresponding d-spacing values of the removed material are in good agreement with the calculated ones of the Co-CAT-1. Using these d-spacing values, the corresponding 1D diffraction pattern was calculated and the reflections were indexed according to the reported Co-CAT-1 powder X-ray diffraction (PXRD) pattern (Figure 5.3E, Table 5).[14] These findings confirm the formation of a highly crystalline Co-CAT-1 material on the gold-coated mesh surface. Moreover, TEM micrographs of the scratched-off substance revealed a highly crystalline material, as indicated by the visualization of lattice fringes of the needle-like MOF crystallites and their cross-section honeycomb structure in projections along the crystal c-axis (Figure 5.3). Notably, using higher or lower concentrations in the reaction mixture for the VAC synthesis led to uncontrolled growth of Co-CAT-1 on the mesh backbone (see Figure 5.11).

Next, we were intrigued to determine the wetting properties of the large pore aperture MOF-coated mesh. To assess the underwater superoleophobic properties, the underwater static oil-contact angles (OCAs) were determined for dichloromethane (DCM). Strikingly, placing a droplet of DCM on the MOF-coated open mesh surface resulted in a nearly perfect oil sphere with OCA = 174° (see Figure 5.3E and Table 7). Static water-contact angle measurements reveal strong interactions of water with the mesh indicated by WCAs of 0° (Figure 5.3F). Using a high-speed camera, the time for a complete spread of the water droplet on the mesh was determined to be approximately 0.01 s (Figure 5.3G). These findings confirm that the superhydrophilic and underwater superoleophobic properties can also be encoded into large pore aperture meshes through the installation of nanostructured MOF architectures exclusively on the mesh wires.

To investigate the affinity of Co-CAT-1 towards water further, we explored the water-host interactions by employing water vapor physisorption analysis and quantum chemical calculations.

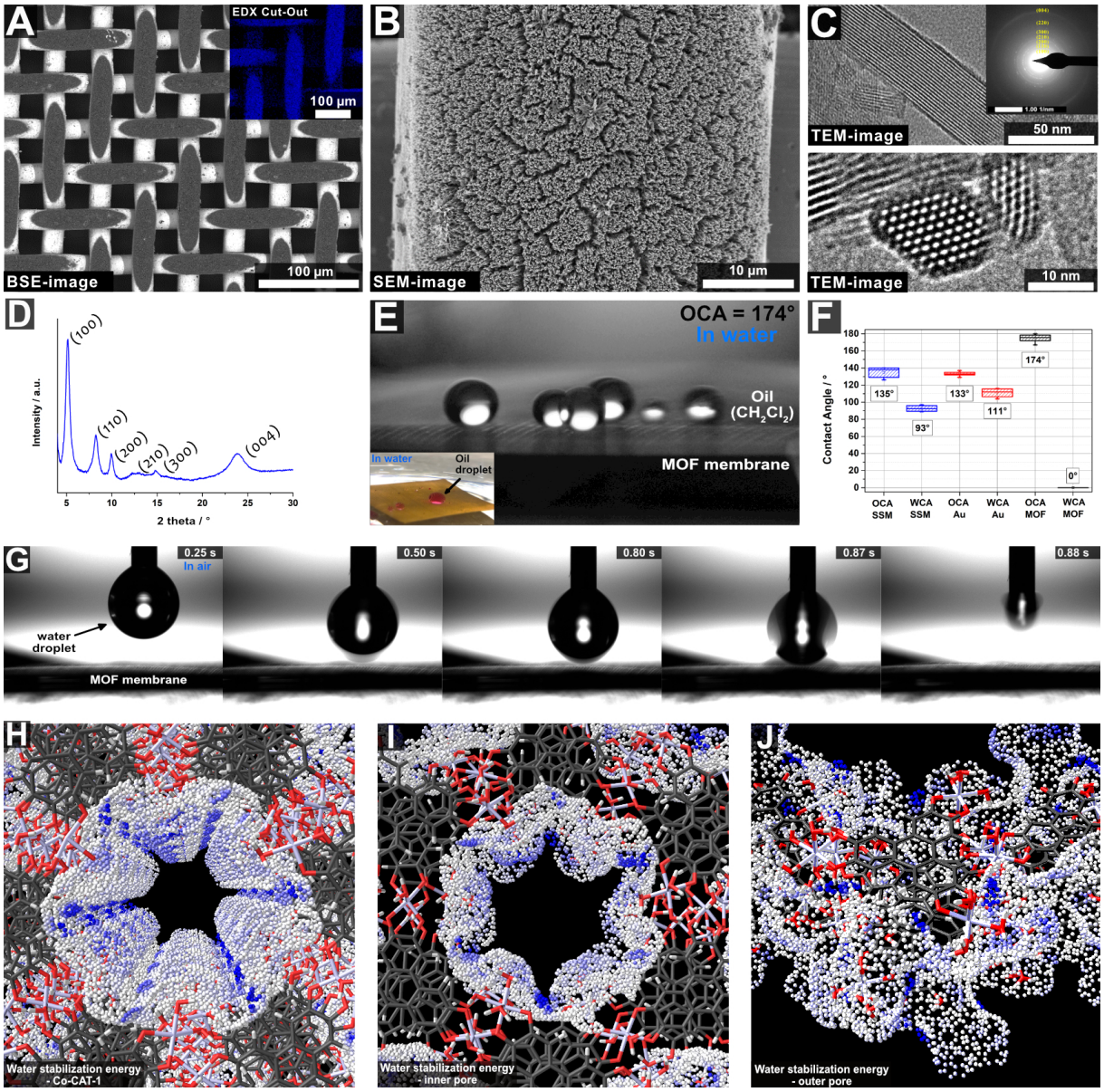

Figure 5.3 – **A)** Back-scattered electron (BSE) micrograph and inset with color-coded EDX mapping of cobalt atoms (dark blue). **B)** High-magnification SEM micrograph showing pillar-like crystallites. **C)** TEM images of the needle-shaped MOF crystallites displaying lattice fringes and the expected Co-CAT-1 honeycomb-like cross-section structure along the crystallite c-axis. **D)** Reconstructed 1D diffraction pattern from the TEM diffraction image shown as inset in **C)** of surface-removed MOF crystallites. **E)** Underwater OCA experiment using DCM as oil droplet on Co-CAT-1@Au@SSM. Inset: Colored DCM oil droplets in water on the MOF-coated mesh. **F)** Statistics of CA for the SSM (WCA=93°; OCA=135°), Au@SSM (WCA=111°; OCA=133°), and Co-CAT-1@Au@SSM (WCA=0°; OCA=174°) samples. **G)** High-speed camera recording of the WCA of Co-CAT-1@Au@SSM showing the water droplet spread in air occurring in a time course of about 0.01 second (last two images). **H)** Calculation of water-pore interaction-energy surface. Color scale: Blue high interaction energy and white less interaction energy. Multiple cells along the *c*-direction. **I)** Inner and **J)** outer surface of the Co-CAT-1 crystallite with water-surface interaction energy.

Using water vapor as an adsorptive at room temperature, a water uptake as high as $470\,cm^3\,g^{-1}$ was measured for Co-CAT-1 powder, confirming that Co-CAT-1 is a highly hydrophilic material (Figure 5.23). Furthermore, hysteresis in the desorption curve is observed, implying strong adsorbate-adsorbate and adsorbate-adsorbent interactions. To elucidate the polar nature of the Co-CAT-1 molecular structure, calculations of the water stabilization energy inside and outside the pore were carried out. First, three-dimensional periodic AM1* [19] semiempirical molecular-orbital (MO) geometry optimizations were set up on the experimental Co-CAT-1 crystal structure reported by Yaghi and coworkers. [14] These calculations used the in-house version of EMPIRE [20] within the unrestricted Hartree-Fock (UHF) formalism using a unit cell in which all loosely bound crystal water inside the pore was omitted. Subsequently, the hydration of the pore in the optimized periodic structure was investigated using an extension of the published self-consistent reaction field (SCRF) polarizable continuum model [21] for periodic systems. These calculations gave an electrostatic water stabilization energy of $-50\,kcal\,mol^{-1}$ for the inner pore and $-68\,kcal\,mol^{-1}$ for outer surface of the crystals per lattice cell. Both surfaces show a significant electrostatic stabilization upon hydration of the exposed surface, which agrees well with the high water uptake measured by water-vapor physisorption. Interestingly, the outer surface shows a more hydrophilic character of $-18\,kcal\,mol^{-1}$ compared with the pore surface. These findings are visualized in Figures 5.3H-J, which show the molecular surface color coded according to the electrostatic stabilization energy for the two systems, ranging from $0.0\,kcal\,mol^{-1}\,Å^{-2}$ (white) to $-1.0\,kcal\,mol^{-1}\,Å^{-2}$ (blue). Here, the blue areas with higher stabilizing interactions between Co-CAT-1 and water are located at the catechol-oxygen atoms of the intercalated molecular units. In contrast, at the outer surface of the crystal additional catechol-oxygen atoms of these units are exposed, leading to a higher water affinity. These findings support our previously reported results on 2D nanostructured M-CAT-1 thin films describing that nanostructuring is essential for achieving superhydrophilic properties. In these systems, the outer crystal surface area in combination with Wenzel's law plays a crucial role.

To unlock the potential of the MOF-based mesh membrane for oil-water separations, we constructed a filtration setup based on a 3×3 cm large Co-CAT-1@Au@SSM mounted in a 25 mm glass microanalysis vacuum filter compartment (see Figure 5.4 A). Notably, the Co-CAT-1@Au@SSM filter was treated with doubly distilled water *prior* to use. Proof-of-principle oil-water separation experiments were conducted by filtering colored (Sudan-red) n-hexane and (methylene blue) water (Figure 5.4). For the separation, 10 mL of red-colored n-hexane was mixed with 10 mL of water, yielding two distinct phases. This mixture was poured into a glass column and subsequently onto the MOF-based membrane (Figure 5.17). Remarkably, water easily flowed and passed the filter while the red-colored n-hexane liquid was blocked on the filter opening, resulting in a standing red oil column. Furthermore, adding an additional 30 mL of water to the oil-containing glass

tube resulted in water percolation through the red-colored oil. The water easily passed through the MOF-based filter membrane and was subsequently collected in the collecting vessel, while the oil column remained intact. To the naked eye, the filtered water was clear and red-colored oil residue contaminants were not visible. To target a wide range of water contaminants, the MOF-based membrane was subjected to different oil-water compositions where the separation efficiencies, residual oil-content in the water effluent and the water flux were determined (for further information see Materials and Methods). Hereby, light weight oils such as n-hexane and n-pentane, 1-dodecene (as an example for diesel fuel resembling the general sum formula $C_{12}H_{24}$)[22] paraffin oils such as polydimethylsiloxane, cycloalkanes, aromatic hydrocarbons, economically relevant oils such as xylene (mixture of ortho-, meta-, and para-isomers) and crude oil were investigated. The water quality after filtration of the different oil-water mixtures was determined by chemical oxygen demand (COD) measurements. This indirect measurement is widely used for the quantitative detection of organic residuals in waste and drinking water and is an important indicator of water quality.[16] The COD value is displayed as the equivalent amount of oxygen required for the oxidation of the organic pollutant in one liter of the analyzed water (for further information about the COD analysis see the Appendix). For evaluating the resulting water quality, a liquid mixture (3:1; v:v; 150 mL) of water and oil was filtered with the MOF-based membrane as shown exemplarily in Figure 5.17. After filtration, the effluent was collected, and its COD was determined. For each of the oil-contaminated water samples, water was collected from five filtration batches and subsequently subjected to the COD test (Figure 5.4C and Table 8).

Notably, all the tested water samples exhibit low COD values ranging from 0.6 mg L^{-1} to 24.3 mg L^{-1} (averaged values after 5 cycles). To put these results in perspective, the COD values of tap water and surface water samples are in the range of 20 mg L^{-1}.[23] These findings confirm that the MOF-based membrane filtration system is suitable for the high-quality separation of a wide range of oily liquids from water. Importantly, water and industrially relevant substances such as 1-dodecene are separated most efficiently by the MOF-based filtration system. So far, we had investigated the separation of poorly soluble oils in the water phase. We therefore analyzed a xylene-water mixture as a model for an oily contaminant featuring increased solubility in water. For comparison, the solubility of xylene in water is 20 times greater than that of n-hexane. Here, slightly higher average COD concentrations of 155.3 mg L^{-1} were determined for the water effluent (corresponding to a xylene conc. of 48.9 mg L^{-1}). It is important to emphasize that the COD value requirements for safe wastewater disposal for the chemical industry in Germany lie between 75 mg L^{-1} and 2500 mg L^{-1}; the specific COD value depends on the pollutant concentrations at the site of occurrence in the industrial process.[16] In this work, the large majority of the tested water samples after one single cycle of filtration were well below this limit and would be suitable

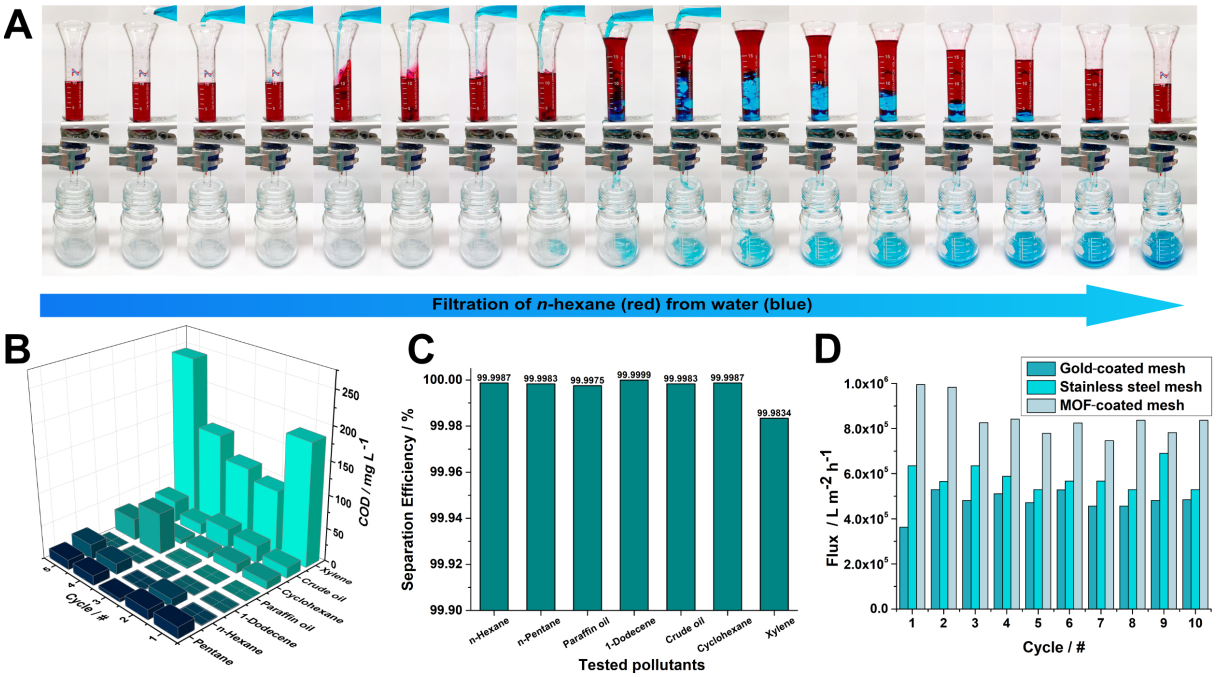

Figure 5.4 – **A)** Image sequence illustrating the course of filtration of water through the MOF-based filter setup. As oily liquid, colored (sudan-red) n-hexane was used. **B)** 3D bar diagram of the measured COD values for the filtrated water samples. **C)** Water and oil separation efficiencies of n-pentane, n-hexane, 1-dodecene, paraffin oil, cyclohexane, xylene and crude oil. **D)** Measured water flux through SSM (cyan) Au@SSM (turquois), and Co-CAT-1@Au@SSM (light cyan) filter systems. The experimental work shown in Figure 5.3 is supported by further statistical data (see Figure 5.18-5.19).

for disposal without further treatment. Even in the case of more water-soluble contaminants such as xylene isomers, the COD concentrations are still within the safe range for wastewater disposal (Figure 5.4B).

The oil-water separation efficiency was determined by calculating the molar amount of pollutant in water before and after filtration (Figure 5.4D). Assuming a stoichiometric reaction of oxygen and the organic pollutant and using the COD values afforded the molar amount of organic pollutant per liter of water. To obtain the separation efficiencies, this value was placed in relation to oil fraction amount before filtration of the oil-water mixture For the different oil-water mixtures, separation-efficiency values of up to 99.99% were calculated. Water-xylene isomers gave slightly lower efficiencies of 99.98% due to the greater solubility of the aromatic compound in water (see Table 5.10). Control experiments for the SSM and Au@SSM are shown in Figure 5.15-5.16.

The gravity-driven water flux measurements were conducted by allowing a 10 cm high water column to run through the Co-CAT-1@Au@SSM until completion (for further details see Appendix). The water flux through the MOF-coated mesh was compared to that of the analogous SSM and

Au@SSM filters (see Figure 5.4D). Hereby, the exceptionally high average water flux increased in the order Au@SSM ($3.8 \times 10^5\,\mathrm{L\,m^{-2}\,h^{-1}}$) < SSM ($6.2 \times 10^5\,\mathrm{L\,m^{-2}\,h^{-1}}$ < Co-CAT-1@Au@SSM ($8.4 \times 10^5\,\mathrm{L\,m^{-2}\,h^{-1}}$). These flux values are conservative estimates due to the progressing reduction of water column height during the process. Nevertheless, to the best of our knowledge the Co-CAT-1@Au@SSM offers the highest flux reported for MOF-modified open meshes/citeA17 (for further information see Tables S 10-12). The results illustrate that the MOF nanostructure even enhances the water flux (ca. 1.3 factor) through the membrane compared to the bare stainless steel mesh, while adding the important property of oil blocking. We attribute this striking increase of the flux to the superhydrophilic nature of the nanostructured MOF, which leads to a complete wetting of the surface of the mesh with water, thereby reducing the forces acting on the mesh during the flow, similar to natural phenomena observed, for example, at the surface of shark skin.[24]

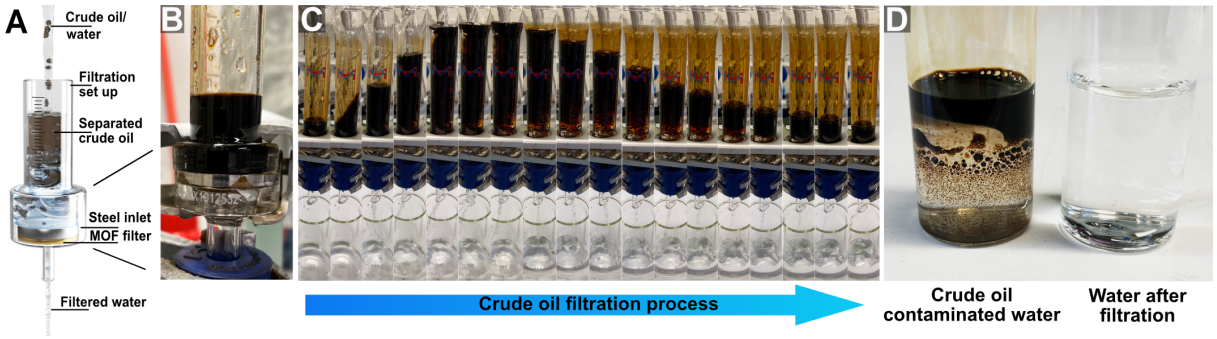

Figure 5.5 – **A)** Experimental setup for the separation of crude oil from double-distilled (dd) water. **B)** Magnified depiction of the crude oil and MOF filter interface in the separation set up. **C)** Image series monitoring the separation of water from crude oil. **D)** Image showing the qualitative result of the separation. Left side depicts the crude oil contaminated water sample before filtration. Right side illustrates the same water after filtration with the Co-CAT-1@Au@SSM filter setup. The measured average COD value is below $25\,\mathrm{mg\,L^{-1}}$.

To illustrate the impact of filtration based purely on surface wetting and gravity further, we focused on the separation of water and crude oil (Figure 5.5). Crude oil is responsible for severe environmental damage and catastrophic oil leaks or spills on the open sea or in rivers. It consists of different alkanes, cycloalkanes and various aromatic hydrocarbons containing different traces of metals, bacteria and sulfur. It typically forms a dark viscous suspension, which is very challenging to extract or to separate from water. Using the MOF-based filtration system, the separation of water and a crude oil pollutant mixture was demonstrated, yielding an apparently clear and clean extract (Figure 5.5D). Remarkably, the measured COD value for the collected water was determined to be as low as $24.3\,\mathrm{mg\,L^{-1}}$ (average value after five filtration cycles; see Table 8), making the filtered water ready for disposal as harmless wastewater without further cleanup.

The integrity of the MOF filter system is of paramount importance for filtration of water from industrial processes or emerging from natural sources. Therefore, we verified the stability of the MOF-membrane by measuring the OCA and WCA after every fifth cycle of a total of 25 filtration cycles in doubly distilled (dd) water as reference, saltwater (exemplary for sea water, 3.5 wt.% NaCl) and water of pH 6 and 8 (see Table 5.15 and Figure 5.21-5.22). Here, the extreme wetting properties of the membrane were maintained throughout these filtration cycles. (Figure 5.22). Furthermore, 25 liters of water were filtered in total through the MOF-based filter in a total of 50 filtration iterations. Subsequently, effluent samples were collected after every fifth cycle and tested using inductively coupled plasma optical emission spectrometry (ICP-AES; limit of detection = 10 ng mL^{-1}, Table 5.16). Importantly, no traces of cobalt ions were detected in the effluents. These findings suggest that the MOF film is stable during the filtration process and that no harmful metal ions are released from the filter to the collected water. Furthermore, the breakthrough time of a 10 cm oil column (150 mL n-hexane) on a 7.065 mm^2 sized Co-CAT-1@Au@SSM filter fused to the bottom (1.5 cm in diameter) of a polyester vessel was found to be ca. 6 h (see Figure 5.21). After breakthrough, the underwater superoleophobic behavior can be recovered by simple re-wetting of the Co-CAT-1@Au@SSM filter with dd-water.

5.3. Conclusion

Summarizing, the combination of a specifically designed nanoscale architecture with aligned and accessible polar nanocavities in MOF crystal needles endows the membrane with outstanding, wetting capabilities. The superhydrophilic nature of Co-CAT-1 crystallites was elucidated by water physisorption measurements and quantum mechanical modeling, confirming the high affinity of the molecular structure towards water. Subsequently, a proof-of-principle water filtration setup was constructed using 3 ×3 cm large MOF-functionalized meshes. With this setup, several oily fluids including the notorious water pollutant crude oil were successfully separated from water. The key point is that the aqueous phase freely passes the superhydrophilic mesh with only gravity as the driving force, while the flow of the hydrophobic oily phase is completely blocked. Oil-water separation efficiencies were measured by calculating the concentration of pollutant before and after filtration in one liter of water. For the oily substances tested, efficiencies of 99.99-99.98% were reached. Importantly, low COD values ranging from 0.6 mg L^{-1} to 24.3 mg L^{-1} were determined for the filtered water effluents, depending on the nature of the oily phase. Therefore, the water quality obtained after filtration is in every tested case very close to tap water quality and can therefore be reused for different purposes.[16,25] These outstanding filtration abilities are based purely on highly unusual wetting properties induced by the nanoscale MOF architecture on the mesh. Moreover, the accessible 50 µm mesh apertures allow for extremely

high water flux reaching nearly one million $\mathrm{L\,m^{-2}\,h^{-1}}$, driven simply by gravity, which eliminates the need for applying backpressure. Therefore, these MOF-based filters are highly suitable for applications where a high water flux and low driving force are needed, such as large-scale separations or water purification in remote areas without the need for any moving parts. The stability of the MOF-based filters was verified at different pH values and environmental factors such as salt-water. These findings show that the MOF-modified meshes can operate even under substantially different and challenging conditions. Furthermore, the chemical integrity of the MOF coating was studied by ICP-AES, showing no traces of cobalt ions in the filtered water after filtration of 25 liters of water. Finally, we note that this MOF-based separation system can serve as a structural blueprint for additional nanoscale porous architectures suitable for morphology-based separations. Thereby, other features of interest such as rapid production methods, desirable mechanical properties or stability against fouling could be engineered into the open mesh system while maintaining the highly efficient separation capabilities.

References

[1] T. Asano, *Water reuse. Issues, technology, and applications,* McGraw-Hill, New York, NY, **2007.**

[2] *Wastewater. The untapped resource,* UNESCO, Paris, **2017.**

[3] H. Kim, S. R. Rao, E. A. Kapustin, L. Zhao, S. Yang, O. M. Yaghi, E. N. Wang, *Nat. com.* **2018,** *9,* 1191.

[4] a) S. Sengupta, T. Nawaz, J. Beaudry, *Curr Pollution Rep* **2015,** *1,* 155; b) A. Alsbaiee, B. J. Smith, L. Xiao, Y. Ling, D. E. Helbling, W. R. Dichtel, *Nature* **2016,** *529,* 190.

[5] a) E. Ankyu, R. Noguchi, *Procedia. Agric. Ecosyst. Environ.* **2014,** *2,* 67; b) S. Munirasu, M. A. Haija, F. Banat, *Process Saf Environ* **2016,** *100,* 183; c) A. Fakhru'l-Razi, A. Pendashteh, L. C. Abdullah, D. R. A. Biak, S. S. Madaeni, Z. Z. Abidin, *J. Hazard* **2009,** *170,* 530; d) M. Sarcletti, D. Vivod, T. Luchs, T. Rejek, L. Portilla, L. Müller, H. Dietrich, A. Hirsch, D. Zahn, M. Halik, *Adv. Funct. Mater.* **2019,** *29,* 1805742.

[6] *American Petroleum Institute.,* Division of Refining., Design and operation of oil-water separators, American Petroleum Institute, Washington, D.C., **1990**.

[7] G. R. Alther, *Water Eng. Manag.* **2001,** *148,* 27.

[8] R. K. Gupta, G. J. Dunderdale, M. W. England, A. Hozumi, *J. Mater. Chem. A* **2017,** *5,* 16025.

[9] a) L. Feng, Z. Zhang, Z. Mai, Y. Ma, B. Liu, L. Jiang, D. Zhu, *Angew. Chem. Int. Ed.* **2004,** *43,* 2012; b) G. J. Dunderdale, M. W. England, T. Sato, C. Urata, A. Hozumi, *Macromol. Mater. Eng.* **2016,** *301,* 1032; c) J. G. Nguyen, S. M. Cohen, *J. Am. Chem. Soc.* **2010,** *132,* 4560; d) K. He, H. Duan, G. Y. Chen, X. Liu, W. Yang, D. Wang, *ACS Nano* **2015,** *9,* 9188; e) K. P. Rao, M. Higuchi, K. Sumida, S. Furukawa, J. Duan, S. Kitagawa, *Angew. Chem. Int. Ed.* **2014,** *53,* 8225; f) K. Jayaramulu, K. K. R. Datta, C. Rösler, M. Petr, M. Otyepka, R. Zboril, R. A. Fischer, *Angew. Chem. Int. Ed.* **2016,** *55,* 1178.

[10] B. Wang, W. Liang, Z. Guo, W. Liu, *Chem. Soc. Rev.* **2015,** *44,* 336.

[11] a) R. N. Wenzel, *Ind. Eng. Chem.* **1936,** *28,* 988; b) A. B. D. Cassie, S. Baxter, *Trans. Faraday Soc.* **1944,** *40,* 546; M. Liu, S. Wang, L. Jiang, *Nat. Rev. Mat.* **2017,** *2,* 17036.

[12] a) J. Yong, F. Chen, Q. Yang, J. Huo, X. Hou, *Chem. Soc. Rev.* **2017,** *46,* 4168; b) L. Wen, Y. Tian, L. Jiang, *Angew. Chem.* **2015,** *127,* 3448; c) S. Wang, K. Liu, X. Yao, L. Jiang, *Chem. Rev.* **2015,** *115,* 8230.

[13] a) F. Zhang, W. B. Zhang, Z. Shi, D. Wang, J. Jin, L. Jiang, *Adv. Mater.* **2013,** *25,* 419; b) Q. Wen, J. Di, L. Jiang, J. Yu, R. Xu, *Chem. Sci.* **2013,** *4,* 591; c) J. Zeng, Z. Guo, *Colloids Surf. A* **2014,** *444,* 283; d) Q. Ma, P. Yin, M. Zhao, Z. Luo, Y. Huang, Q. He, Y. Yu, Z. Liu, Z. Hu, B. Chen et al., *Adv. Mater.* **2019,** *31,* 1808249.

[14] M. Hmadeh, Z. Lu, Z. Liu, F. Gandara, H. Furukawa, S. Wan, V. Augustyn, R. Chang, L. Liao, F. Zhou et al., *Chem. Mater.* **2012,** *24,* 3511.

[15] a) V. Rubio-Gimenez, M. Galbiati, J. Castells-Gil, N. Almora-Barrios, J. Navarro-Sanchez, G. Escorcia-Ariza, M. Mattera, T. Arnold, J. Rawle, S. Tatay et al., *Adv. Mater.* **2018,** *30*; b) M. K. Smith, K. E. Jensen, P. A. Pivak, K. A. Mirica, *Chem. Mater.* **2016,** *28,* 5264.

[16] Federal Environmental Ministry of Germany Federal *Law Gazette BGBl. I* p. 1108.

[17] X. Zhang, H. Li, W. Miao, Q. Shen, J. Wang, D. Peng, J. Liu, Y. Zhang, *AIChE J* **2019,** *65,* e16596.

[18] A. Mähringer, J. M. Rotter, D. D. Medina, *Beilstein J. Nanotechnol.* **2019,** *10,* 1994.

[19] a) M. J. S Dewar, E. G. Zoebisch, E. F. Healy, J. J. P. Stewart, *J. Am. Chem. Soc.* **1985,** *107,* 3902-3909; b), P. Winget, , A. H. C. Horn, C. Selcuki, B. Martin, T. Clark, *J. Mol. Model.* **2003,** *9,* 408-414; c) H. Kayi, T. Clark, *J. Mol. Model.* **2010,** *16,* 29-47.

[20] a) M. Hennemann, T. Clark, *J. Mol. Model.* **2014,** *20,* 2331; b) J. T. Margraf, M. Hennemann, B. Meyer, T. Clark, *J. Mol. Model.* **2015,** *21,* 144.

[21] G. Rauhut, T. Clark, T. Steinke, *J. Am. Chem. Soc.* **1993,** *115,* 9174-9181.

[22] C. Soares in *Gas turbines. A handbook of air, land and sea applications* (Ed.: C. Soares), Butterworth-Heinemann is an imprint of Elsevier, Kidlington, Oxford, UK, 2015, pp. 317-411.
[23] D. Chapman, Water Quality Assessments, Taylor and Francis, Abingdon, UK, 1992.
[24] G. D. Bixler, B. Bhushan, *Nanoscale* **2013,** *5,* 7685.
[25] W. H. Organization, *Guidelines for Drinking-water Quality,* World Health Organization, Geneva, **2011.**

5.4. Appendix

5.4.1. Materials and methods

All materials were purchased from Sigma Aldrich, Across or TCI Europe in the common purities *purum, puriss* or reagent grade. The materials were used as required without further purification and handled in air unless otherwise noted. The water used in the experiments was subjected to a Merck-Milipore Mili-Q purification system *prior* to use.

Au@SSM preparation

The SSMs were cut into 18×6 cm large pieces and cleaned by ultrasonic treatment in acetone followed by ethanol and water. SSMs were positioned in a rotating vacuum deposition unit installed in a glovebox (*MBraun Labmaster Pro SP* equipped with an *Inficon SQC-310C* deposition controller). 10 nm titanium as adhesion layer and subsequently 40 nm of gold were thermally deposited under high vacuum on the mesh. The evaporation procedure was conducted for both sides of the SSM.

For the VAC synthesis the meshes were cut into 3×3 cm pieces and cleaned under nitrogen flow.

Scanning electron microscopy (SEM)

SEM micrographs were collected with an *FEI Helios Nanolab G3 UC* electron microscope with an acceleration voltage of 2 kV from a field emission gun. For the analysis, the respective samples were cut into sizes of 1×1 cm and mounted on carbon pad-modified stainless steel sample holders. No carbon layer was evaporated in high vacuum *prior* to analysis.

Transmission electron microscope (TEM)

TEM imaging and electron diffraction was conducted on an *FEI Titan Themis 60-300* microscope at an acceleration voltage of 300 keV. Samples were prepared by carefully removing film material from the mesh with a sharp razor blade and mounting it onto conducting copper grids.

Static contact angle measurements

Contact-angle measurements were collected using *attension* from *Biolin Scientific*. A small amount of the respective liquid was placed on the substrate by a precision syringe, while recording images with a camera speed of 1 frame per second (fps) for 10 s. The high-speed images for recording the superhydrophilic properties and water spreading were performed using 40 fps for 1 s. The image analysis was carried out with the software ImageJ using the manual mode and fitting the contour of the droplets manually.

Inductively coupled plasma optical emission spectrometer (ICP-AES)

ICP-AES was conducted using water aliquots of 10 mL after each filtration cycle with 50 cycles in total. The Co ion content was determined using a *Varian Vista RL ICP-AES* instrument with a limit of detection (LOD) of 10 ng mL^{-1}.

Cost estimation for the gold deposition process

We use gold for physical vapor deposition (PVD) in the common purity 99.99%. One evaporation cycle employs one gold pellet (0.3 g). According to the gold prize at the global market (1 g = 51 Euro) one evaporation cycle cost ca. 16 Euro. In our evaporation chamber, we were able to deposit gold from one pellet on 4 meshes (392 cm^2) at once. Covering both sides of the mesh via two cycle we calculate a total cost of 0.04 Euro cm^{-2} or 400 Euro cm^{-2}.

5.4.2. Vapor-assisted conversion

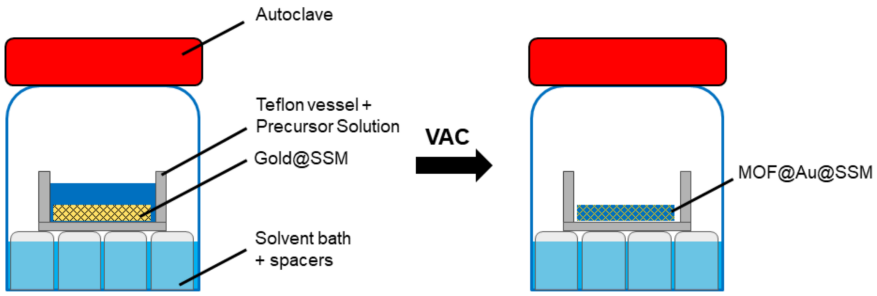

Figure 5.6 – An illustration scheme of the vapor-assisted conversion setup for the fabrication of MOF@Au@SSM. The as- prepared Au@SSM substrates are placed in a teflon vessel, which is located on top of glass spacers in an autoclave. On the bottom of the autoclave a solvent bath is filled. Subsequently, a precursor solution is added to the substrate containing teflon vessel. The autoclave is sealed and placed in a preheated oven for adjusted time. After the course of the synthesis, the solvent mixture dried and in the end of the reaction, the MOF@Au@SMM can be retrieved and subjected to various work-up routines.

A 3×3 cm Au@SSM sample was placed into glass supported petri dishes with 3 cm in diameter. A MOF precursor solution was prepared by mixing HHTP precursor (10.8×10^{-3} mmol; 3.5 mg) and cobalt acetate (22.0×10^{-3} mmol; 6 mg) in a defined ratio (1:2 n:n) in a solvent mixture of water and 1-propanol (1.5 mL : 1.5 mL). To the precursor solution, 100 µL were added from a fresh prepared solution comprising a salicylic acid modulator (0.89 mmol; 125 mg) in a water, 1-propanol (1 mL : 1 mL). 1 mL of the respective precursor solution (HHTP: 3.6 mmol L^{-1}; CoAc: 7.33 mmol L^{-1}; salicylic acid: 0.29 mmol L^{-1}) were filled into the petri dishes, evenly covering the mesh. The setup was transferred to a polypropylene autoclave with a cap equipped with a Teflon seal. At the bottom, the autoclave was filled with 14 Raschig rings (10×10 mm, soda lime glass) to create an elevated flat platform for the petri dish. A liquid mixture of 1-propanol and water;

1:1 ; v/v) was placed as a solvent bath at the bottom of the autoclave. The autoclave was sealed and subsequently transferred to a preheated oven (85°C) for 12 h. After the synthesis, the set-up was removed from the oven and cooled down to room temperature. The Co-CAT-1@Au@SSM meshes were rinsed with acetone and dried under nitrogen flow *prior* to use.

5.4.3. Analysis of SSM, Au@SSM and MOF@Au@SSM meshes

EDX analysis of the respective meshes

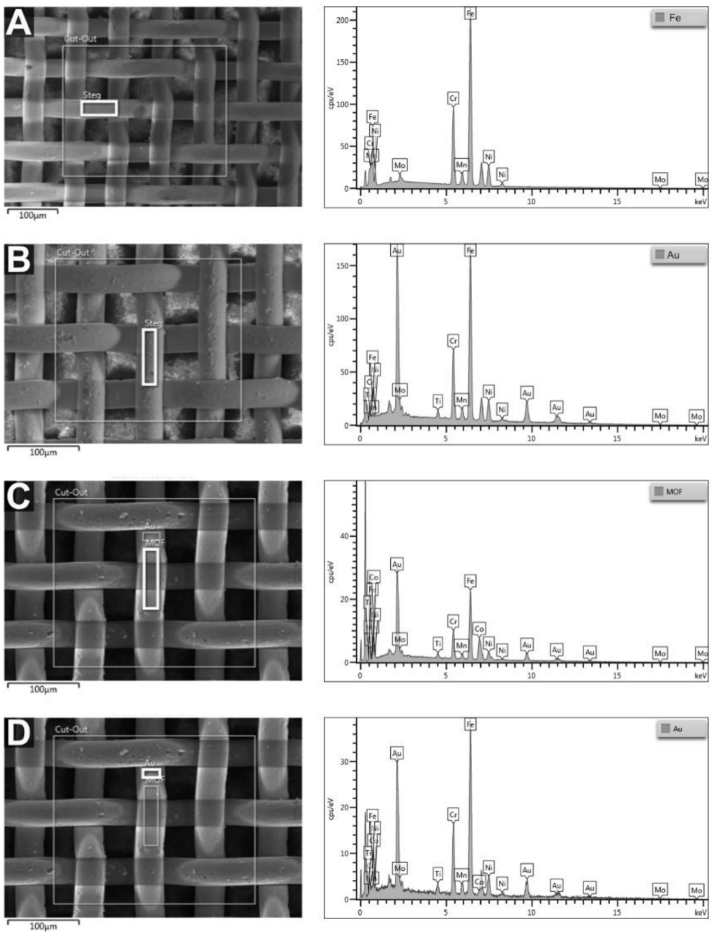

Figure 5.7 – EDX analysis of the fabricated meshes. **A** SEM of the SSM substrate and the corresponding EDX spectrum of the selected area showing the elemental composition of the alloy. **B** SEM of the Au@SSM substrate and the corresponding EDX spectrum of the selected area confirming the presence of the deposited metals Ti and Au. **C** SEM of the MOF@Au@SSM substrate and the corresponding EDX spectrum obtained at the highlighted area (center of the mesh backbone) in the SEM image. **D** SEM of the MOF@Au@SSM substrate and the corresponding EDX spectrum recorded at the highlighted area (area close to the mesh node) in the SEM image.

EDX mapping of the respective meshes

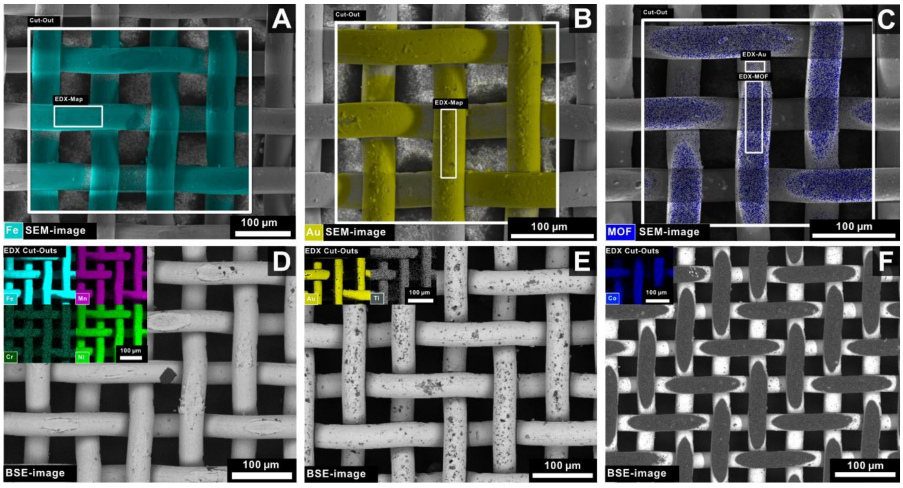

Figure 5.8 – **A, B** and **C** SEM micrographs of SSM, Au@SSM and Co-CAT-1@Au@SSM samples with cut-outs containing color- coded EDX mapping of the elements iron (turquois), gold (yellow), and cobalt (dark blue), respectively. **D, E** and **F** display the corresponding back-scattered electron (BSE) micrographs. The respective element EDX maps of the above-depicted cut-outs of the respective elements manganese (violet), chromium (dark green), nickel (light green), titanium (grey) are shown as insets.

SEM analysis of MOF@Au@SSM

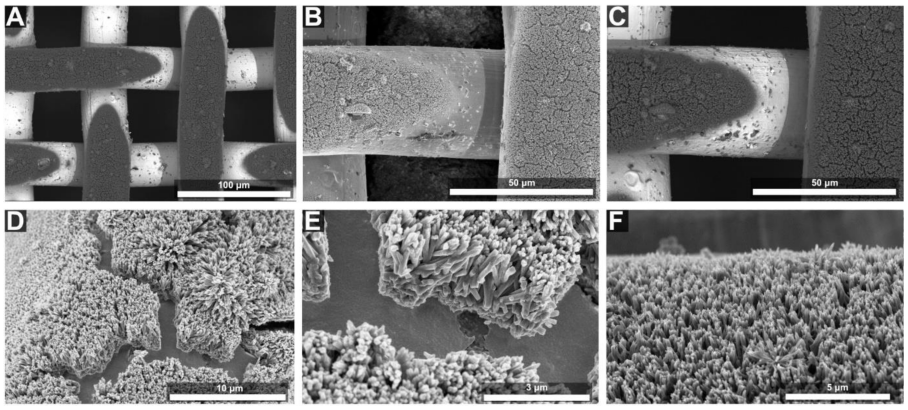

Figure 5.9 – Additional SEM analysis of the MOF@Au@SSM. **A** BSE image of the mesh showing the MOF patches in darker contrast and the uncovered metal parts in bright contrast. **B** Magnified SEM micrograph of a mesh node and **C** the corresponding BSE image. Here, the transition between MOF film, blank gold parts and stainless steel alloy are clearly visible. **D** Image of the pillar-like crystallite orientation on the mesh surface growing orthogonally to the curvature of the surface. **E** Corresponding magnified SEM image on a film crack highlighting the orientation of the MOF crystallites on the surface. **F** A representative SEM image of a dense array of MOF pillar-like crystallites on the mesh surface.

Macroscopic photographs of the respective meshes

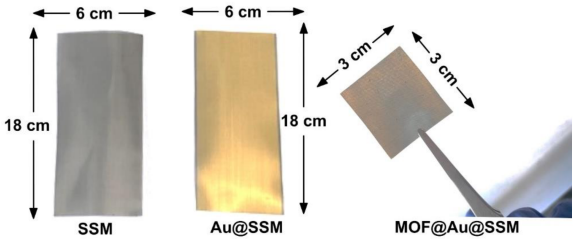

Figure 5.10 – Macroscopic photographs of the stainless-steel mesh, gold coated mesh and the cut MOF membrane (from left to right).

TEM analysis

Table 5 – Observed and calculated indices of the TEM analysis.

Observed (nm)	Calculated (nm)	Index
1.72	1.75	(100)
1.01	1.01	(110)
0.84	0.88	(200)
0.66	0.66	(210)
0.56	0.58	(300)
0.48	0.51	(220)
0.29	0.32	(004)

.

Impact of the synthesis conditions on the Co-CAT-1 growth

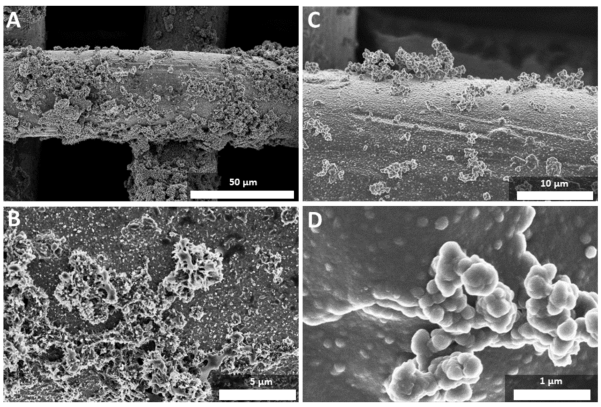

Figure 5.11 – Scanning-electron microscopy images of Co-CAT@Au@SSM samples. **A-B** the mesh was synthesized using higher and **C-D** lower concentrations of precursor material compared to the optimum concentration described in the experimental part.

5.4.4. Characterization of surface wetting properties

Reference contact angle measurements

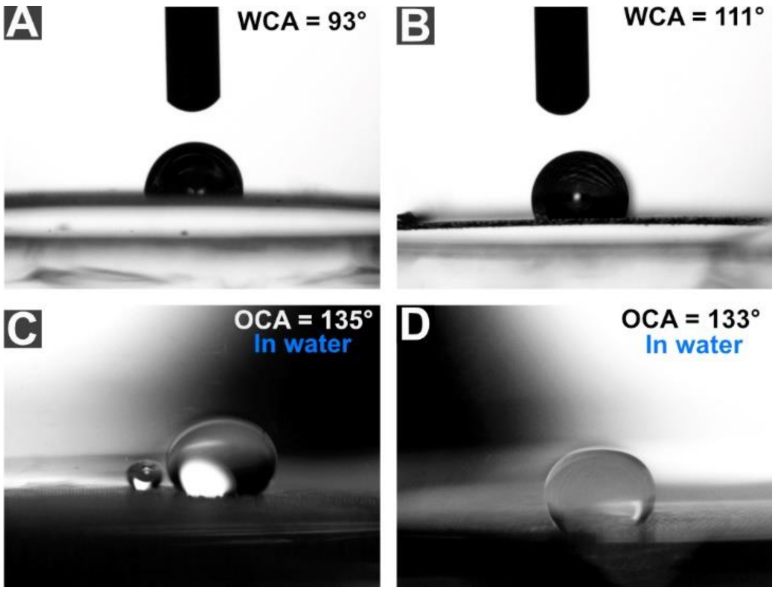

Figure 5.12 – Reference contact angle measurements of the SSM and Au@SSM substrates and the averaged WCAs and OCAs. **A** Representative WCA of SSM and **B** of Au@SSM. Representative OCAs in water for **C** SSM and **D** of Au@SSM.

Measured WCAs and OCAs

Table 6 – Measured WCAs and underwater OCAs using DCM as a probe of Au@SSM and SSM substrates.

Repeat	OCA(°)/Au@SSM	WCA(°)/Au@SSM	OCA(°)/SSM	WCA(°)/SSM
1	134	115	138	90
2	134	116	140	95
3	137	104	129	97
4	135	109	140	89
5	133	111	126	93

Table 7 – Measured underwater OCAs using DCM as a probe for MOF@Au@SSM substrates.

Repeat	OCA(°)	Repeat	OCA(°)
1	177	13	167
2	173	14	174
3	170	15	167
4	175	16	168
5	180	17	180
6	180	18	180
7	171	19	180
8	176	20	172
9	176	21	176
10	180	22	177
11	175	23	176
12	172	24	173

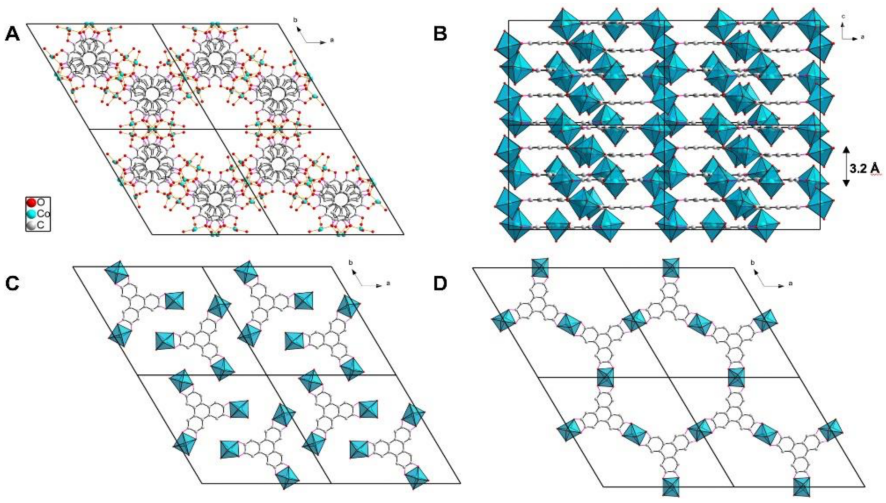

Figure 5.13 – Crystal structure of Co-CAT-1 (for better illustration, the loosely bound crystal water was omitted). **A** View along the *c*-axis. **B** View along the *b*-axis. **C** Layered structure comprised of $HHTP(H_2O)_{12}$ complexes. **D** Continuous layer of HHTP in-plane coordinated by Co ions.

Crystal shape and pore alignment of Co-CAT-1@Au@SSM

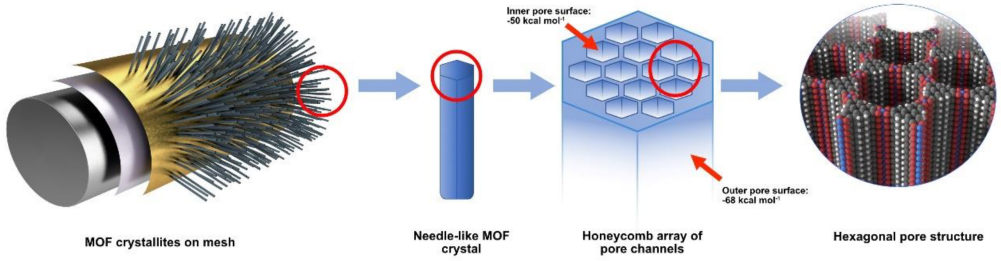

Figure 5.14 – Arrangement of Co-CAT-1 crystallites on the mesh backbone. MOF crystallites feature a needle-like crystallite shape. These crystallites show a honeycomb array of pore channels built up from hexagonal HHTP subunits coordinated in- plane by Co-ions.

5.4.5. Characterization of oil-water separation

Chemical oxygen demand determination

After filtration, an aliquot of 2 mL was taken from the filtrated water phase and subjected to a *Merck Spectroquant CID* cell test (Hg-free). The reaction cell contained sulfuric acid, potassium dichromate and silver sulfate catalyst. After the addition, the solution was mixed vigorously using a vortexer and the reaction cell was transferred to a preheated oven (148°C) for 2 h. Afterwards, the vials were cooled down to room temperature, homogenized by a vortexer, and transferred to 10 mm quartz cuvettes for analysis by UV-vis spectroscopy. The same routine was performed with a COD standard test solution (100 mg L^{-1}) from *VWR* in water and a blank water sample. The spectroscopic investigation was carried out using a *Perkin Elmer UV/VIS/NIR Lambda 1050* spectrometer equipped with a 150 nm integrating sphere. After recording the blank measurement, the UV-vis spectrum of the standard solution was collected to determine the absorbance at 445 nm. After that, a formula was set up to calculate the COD for the following samples by measuring the absorbance at 445 nm:

$$Abs\,445\,nm \cdot 297.7 = COD\,(mg\,L^{-1}) \tag{5.1}$$

$Abs\,445\,nm$ = represents the absorbance of the tested water sample at 445 nm; $factor\,297.7$ = determined by measuring the absorbance of a COD standard solution (100 mg L^{-1}).

Table 8 – COD values and the related absorbance values at 445 nm for the filtrated water samples. The values were recorded for five filtration cycles.

Cycle	Absorbance	COD (mg/L)
n-hexane		
1 Cycle	0.005	14.8
2 Cycle	0.043	12.80
3 Cycle	0.0045	1.339
4 Cycle	0.055	16.37
5 Cycle	0.077	22.92
n-pentane		
1 Cycle	0.057	16.96
2 Cycle	0.051	15.18
3 Cycle	0.017	5.06
4 Cycle	0.049	14.58
5 Cycle	0.05	14.88
1-Dodecene		
1 Cycle	0.004	1.19
2 Cycle	0.003	0.89
3 Cycle	0.001	0.29
4 Cycle	0.0026	0.77
5 Cycle	0.0003	0.08
Xylene		
1 Cycle	0.62	184.57
2 Cycle	0.32	95.26
3 Cycle	0.37	110.14
4 Cycle	0.48	142.89
5 Cycle	0.82	244.11
Parrafin Oil		
1 Cycle	0	0
2 Cycle	0	0
3 Cycle	0.009	2.67
4 Cycle	0.21	62.51
5 Cycle	0.11	32.74
Cyclohexane		
1 Cycle	0.041	12.20
2 Cycle	0.048	14.28
3 Cycle	0.029	8.63

Table 8 – COD values and the related absorbance values at 445 nm for the filtrated water samples. The values were recorded for five filtration cycles.

Cycle	Absorbance	COD (mg/L)
4 Cycle	0.023	6.84
5 Cycle	0.049	14.53
Crude oil		
1 Cycle	0.055	16.37
2 Cycle	0.087	25.89
3 Cycle	0.1	29.77
4 Cycle	0.057	16.96
5 Cycle	0.11	32.74

Separation efficiency results

$$\mathrm{aCxHy + bO_2 \longrightarrow cH_2O + dCO_2} \tag{5.2}$$

The stochiometric ratio r(O_2) between the organic pollutant aC_xH_y and oxygen bO_2 (measured oxygen demand) was set according to equation (5.2). With the following equations the concentrations of the respective pollutants were calculated:

$$\frac{COD}{1000 \cdot 32\, g\, mol^{-1}} = x\, mol[O_2] \tag{5.3}$$

$$x\, mol[O_2] \times r(O_2) = y\, mol[pollutant] \tag{5.4}$$

$$y\, mol[pollutant] \times M[pollutant] = m[pollutant] \tag{5.5}$$

The obtained m [pollutant] was converted with the respective density of the tested pollutants to V_{after} filtration [pollutant]. The V_{after} filtration [pollutant] was finally set in relation to the V_{before} filtration [pollutant] being 333 mL [pollutant] per liter filtered. The results for the respective pollutants are summarized in table 9.

Table 9 – Separation efficiencies for the respective tested oil contaminated water samples.

Tested Pollutant	Concentration [mg L^{-1}]
n-Hexane	3.08
n-Pentane	3.52
PDMS	8.2
1-Dodecene	0.18
Crude oil	6.92
Xylene	48.9
Cyclohexane	3.3

.

Separation efficiency - control experiments

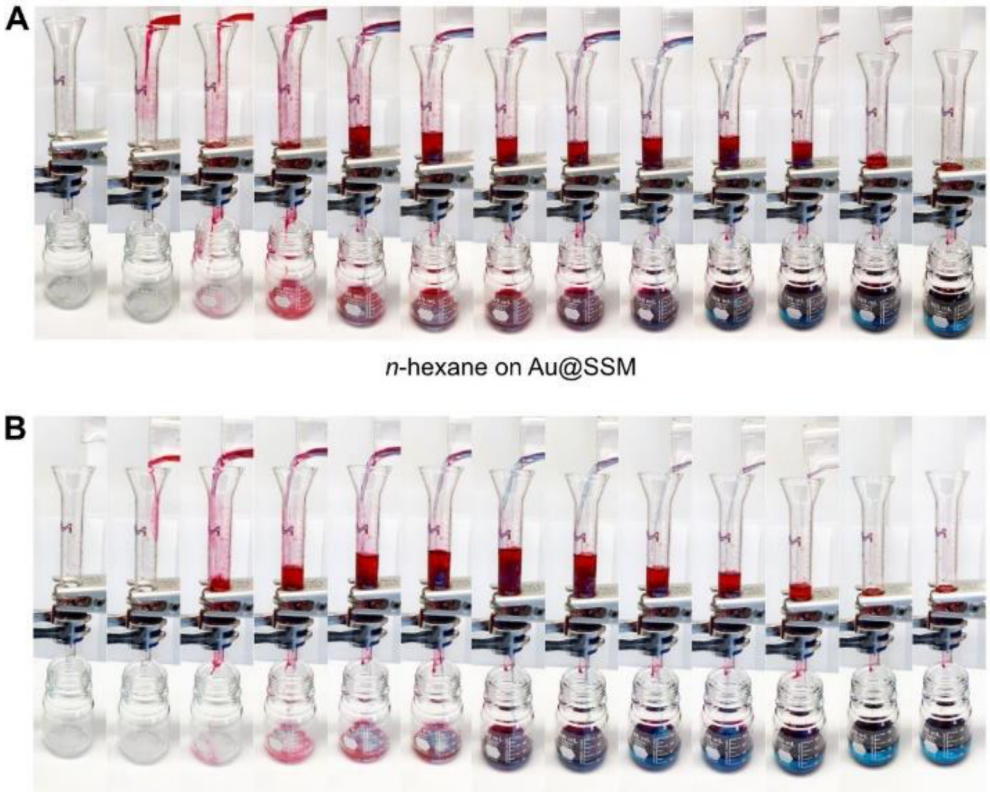

Figure 5.15 – Separation efficiency control experiments shown for the **A** Au@SSM, **B** SSM, respectively. For the tested pollutant n-hexane was chosen and false colored with Sudan red. The water was false colored by methylene blue.

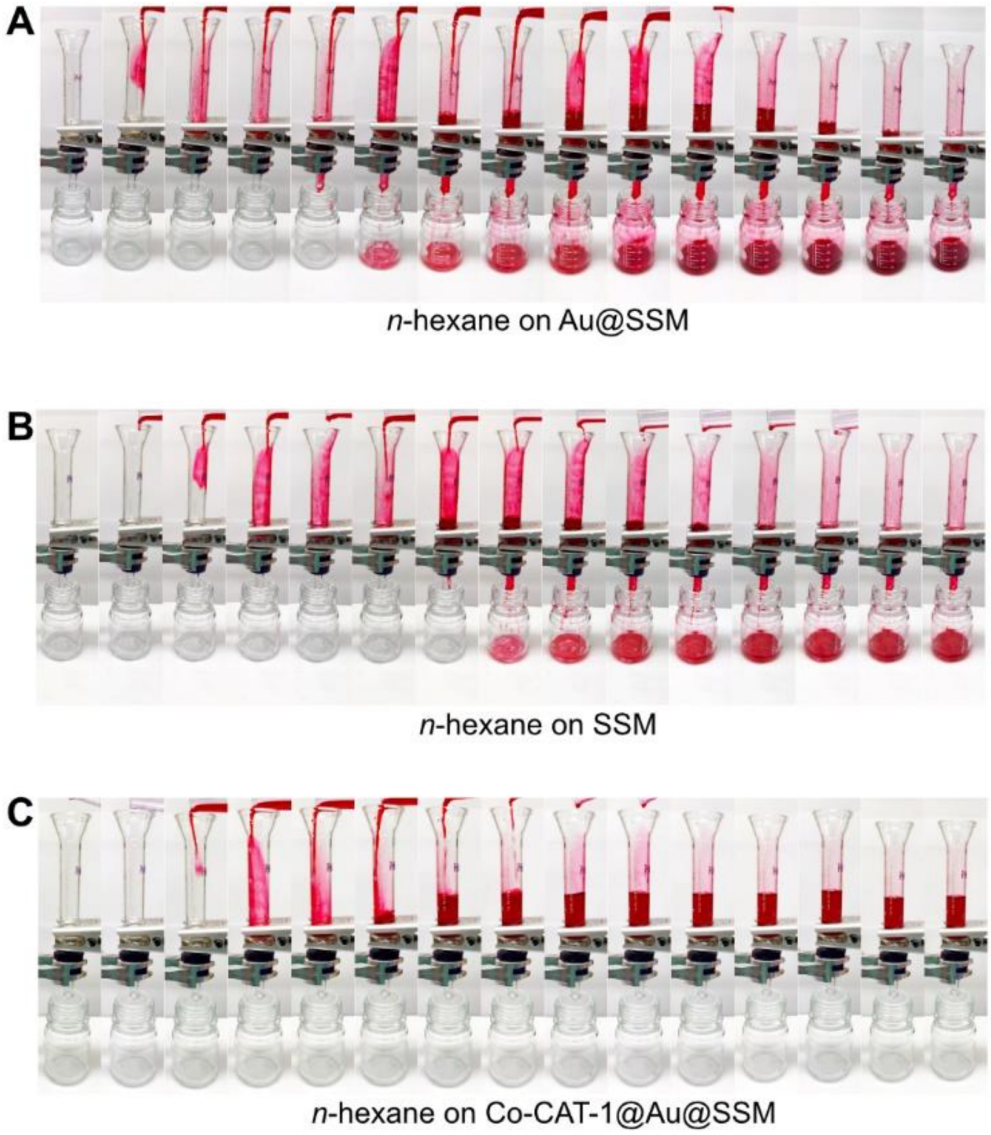

Figure 5.16 – Ability of **A** Au@SSM, **B** SSM, **C** Co-CAT-1@Au@SSM to hold back incoming oil. For the tested oil n-hexane was chosen and false colored with Sudan red.

Figure 5.17 – Separation experiment of a mixture of oil (n-hexane) and water. For better visualization, the water and oil components were colored with methylene blue and Sudan red, respectively.

Table 10 – Flux analysis of the respective mesh types for 10 runs with dd water.

	MOF/Au/SSM Flux (L m^{-2} h^{-1})	**Au/SSM Flux (L m^{-2} h^{-1})**	**SSM Flux (L m^{-2} h^{-1})**
1 Run	995,026	362,426	634,920
2 Run	982,835	565,280	529,100
3 Run	825,805	480,536	634,920
4 Run	841,763	510,924	587,889
5 Run	778,631	471,517	529,100
6 Run	824,558	528,067	566,893
7 Run	746,005	456,517	566,893
8 Run	836,415	456,517	529,100
9 Run	781,355	480,536	690,131
10 Run	836,673	484,874	529,100

Flux analysis

The water flux of the respective meshes was calculated by the given formula:

$$\frac{V}{A \cdot t} = flux \tag{5.6}$$

Where V represents the filtrated water volume, A the area of the filter and the t the testing time. It should be noted that the height of the water column was not constant. We measured the flow of 50 mL (0.05 L) of water passing the filter. The diameters of the circular filters were in the range of 1.5 mm to 4 mm. The flux was only driven by gravity. For demonstration we added an example calculation of the MOF-based membrane flux:

$$A = \pi \cdot r^2 \tag{5.7}$$

$$A = \pi \cdot (1.5\,mm)^2 = 7.065\,mm^2 = 7.065 \times 10^{-6}\,m^2 \tag{5.8}$$

We measured 50 mL (0.05 L) passing the filter in 21 s (5.8×10^{-3} h)

$$Flux = \frac{V}{A \cdot t} = \frac{0.05\,L}{7.065 \times 10^{-6}\,m^2 \cdot 5.8 \times 10^{-3}\,h} \tag{5.9}$$

Yielding a flux of 1,025672 L m^2 h^{-1}.

Table 11 – Flux analysis of four MOF/Au/SSM filters with 10 cycles respectively.

Cycle	Time (s)	Flux (L m^{-2} h^{-1})	Time (s)	Flux (L m^{-2} h^{-1})
	MOF/Au/SSM (⌀ 3 mm)		**MOF/Au/SSM (⌀ 4 mm)**	
1.	23	1127373	16	925000
2.	26	997292	13	1138462
3.	26	997292	21	704762
4.	26	997292	20	740000
5.	28	926056	21	704762
6.	24	1080399	19	778947
7.	24	1080399	23	643478
8.	25	1037183	16	925000
9.	25	1037183	20	740000
10.	20	1296479	22	672727
	MOF/Au/SSM (⌀ 4 mm)		**MOF/Au/SSM (⌀ 4 mm)**	
1.	14	1057143	17	870588
2.	17	870588	16	925000
3.	19	778947	18	822222
4.	21	704762	16	925000
5.	21	704762	19	778947
6.	24	616667	18	822222
7.	24	616667	23	643478
8.	20	740000	23	643478
9.	21	704762	23	643478
10.	21	704762	22	672727

Table 12 – Flux analysis of four SSM filters with 10 cycles respectively.

Cycle	Time (s)	Flux (L m^{-2} h^{-1})	Time (s)	Flux (L m^{-2} h^{-1})
	SSM (⌀ 3.8 mm)		**SSM (⌀ 4 mm)**	
1.	27	587889	23	690131
2.	28	566893	28	566893
3.	31	512033	25	634921
4.	29	547345	28	566893

Table 12 – Flux analysis of four SSM filters with 10 cycles respectively.

Cycle	Time (s)	Flux (L m^{-2} h^{-1})	Time (s)	Flux (L m^{-2} h^{-1})
5.	32	496032	32	496032
6.	32	496032	27	587889
7.	33	481000	34	466853
8.	33	481000	34	466853
9.	34	466853	35	453515
10.	34	473821	29	544529
	SSM (⌀ 4 mm)		**SSM (⌀ 3.8 mm)**	
1.	14	1057143	37	432507
2.	17	870588	37	424412
3.	19	778947	36	437273
4.	21	704762	39	404408
5.	21	704762	29	544529
6.	24	616667	37	429000
7.	24	616667	35	453515
8.	20	740000	40	396825
9.	21	704762	35	453515
10.	21	704762	27	593162

Table 13 – Flux analysis of four Au/SSM filters with 10 cycles respectively.

Cycle	Time (s)	Flux (L m^{-2} h^{-1})	Time (s)	Flux (L m^{-2} h^{-1})
	Au/SSM (⌀ 3 mm)		**Au/SSM (⌀ 4 mm)**	
1.	55	463034	38	378947
2.	48	530560	34	423529
3.	57	446788	37	389189
4.	47	541849	30	480000
5.	55	463034	36	400000
6.	47	541849	33	436364
7.	55	463034	43	334884
8.	55	463034	46	313043
9.	57	446788	49	293878
10.	52	489748	48	300000
	Au/SSM (⌀ 4 mm)		**Au/SSM (⌀ 3.8 mm)**	
1.	55	261818	44	327273
2.	24	600000	36	400000
3.	28	514286	39	369231
4.	30	480000	44	327273
5.	30	480000	43	334884
6.	28	514286	49	293878
7.	32	450000	42	342857
8.	32	450000	43	334884

Table 13 – Flux analysis of four Au/SSM filters with 10 cycles respectively.

Cycle	Time (s)	Flux (L m^{-2} h^{-1})	Time (s)	Flux (L m^{-2} h^{-1})
9.	28	514286	44	327273
10.	30	480000	49	293878

Statistics

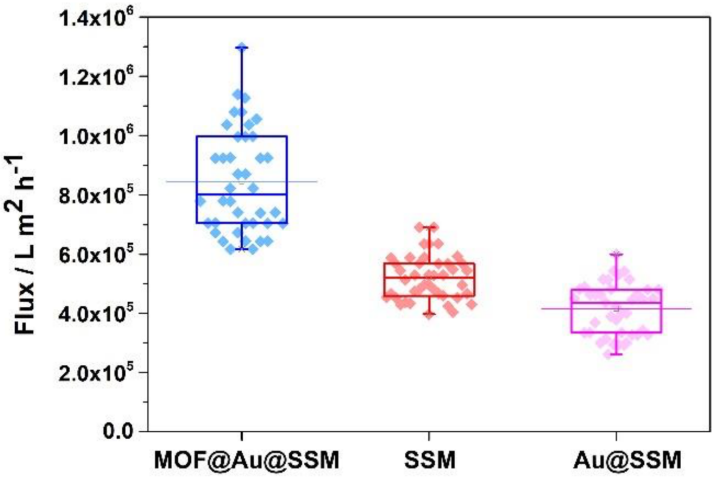

Figure 5.18 – Flux analysis of MOF@Au@SSM, SSM, and Au@SSM. For each flux analysis 40 data points were collected and plotted for the respective mesh.

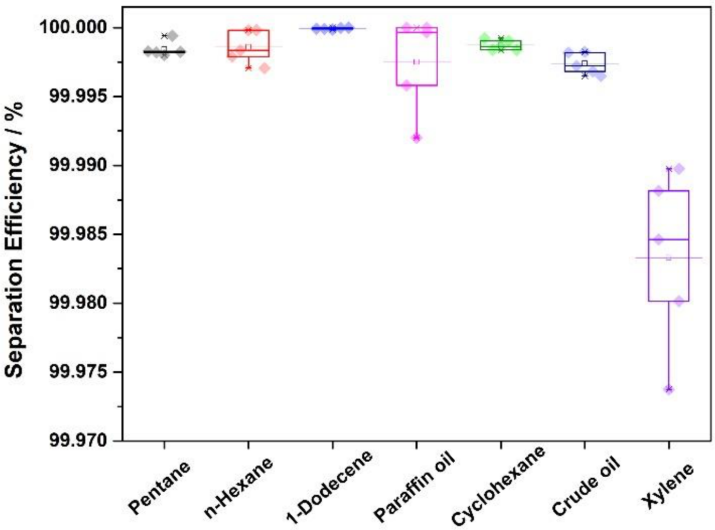

Figure 5.19 – Separation efficiency for each tested pollutant plotted in chart diagrams. For each separation efficiency 5 data points were collected and plotted as box-chart diagrams for the respective tested pollutant.

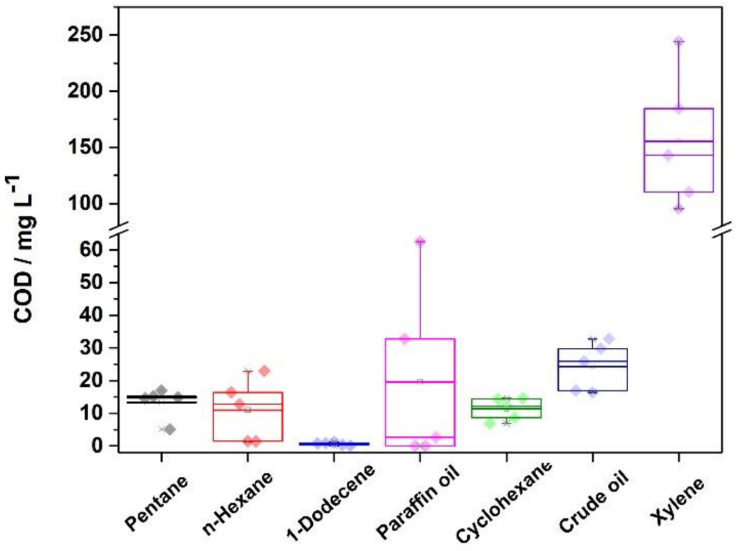

Figure 5.20 – COD value for each tested pollutant plotted in chart diagrams. For each COD determination 5 data points were collected and plotted as box-chart diagrams for the respective tested pollutant.

5.4.6. Stability tests of the MOF@Au@SSM

WCAs and OCAs of the stability tests

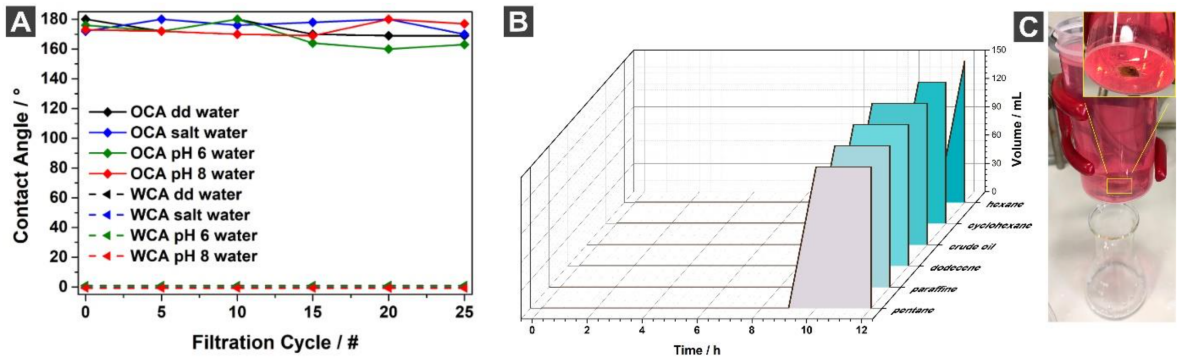

Figure 5.21 – **A)** Stability test of the Co-CAT-1@Au@SSM filter towards different kinds of water. The figure depicts the development of the WCA and underwater OCA measured after every 5th cycle with 25 filtration cycles in total. For the stability test, n-hexane was mixed with the saltwater (3.5 wt% NaCl; blue), water of pH 6 (green), water of pH 8 (red) and water (black) as reference prior to filtration, respectively. **B)** Durability of water activated filter measured using the breakthrough times of 150 mL of the respective oily liquids. **C)** Exemplary depiction of a MOF filter resisting the gravimetric pressure of 150 mL colored (Sudan red) n-hexane.

Table 14 – Measured WCAs and OCAs for the MOF@AU@SSM after every 5th filtration cycle. The WCAs and OCAs were measured using dd water, while the filtration was conducted under the respective aqueous medium.

dd. water						
Cycle	0	5	10	15	20	25
OCA (°)	180	172	180	170	169	169
WCA (°)	0	0	0	0	0	0
NaCl solution						
Cycle	0	5	10	15	20	25
OCA (°)	172	180	176	178	180	170
WCA (°)	0	0	0	0	0	0
HCl solution						
Cycle	0	5	10	15	20	25
OCA (°)	176	172	180	164	160	163
WCA (°)	0	0	0	0	0	0
NaOH solution						
Cycle	0	5	10	15	20	25
OCA (°)	173	172	170	169	180	177
WCA (°)	0	0	0	0	0	0

Table 15 – The ICP analysis of the filtrated water. ICP tests for the presence of cobalt ions were conducted after the filtering of every 5th filtration cycle. 500 mL dd water were filtered by each cycle.

Co(238,89 nm)	
Sample No.	Conc. (µg/ml)
1	< LOD
5	< LOD
10	< LOD
15	< LOD
20	< LOD
25	< LOD
30	< LOD
35	< LOD
40	< LOD
45	< LOD
50	< LOD
LOD (µg/ml)	**0.01**

OCA and OCA records of the stability tests

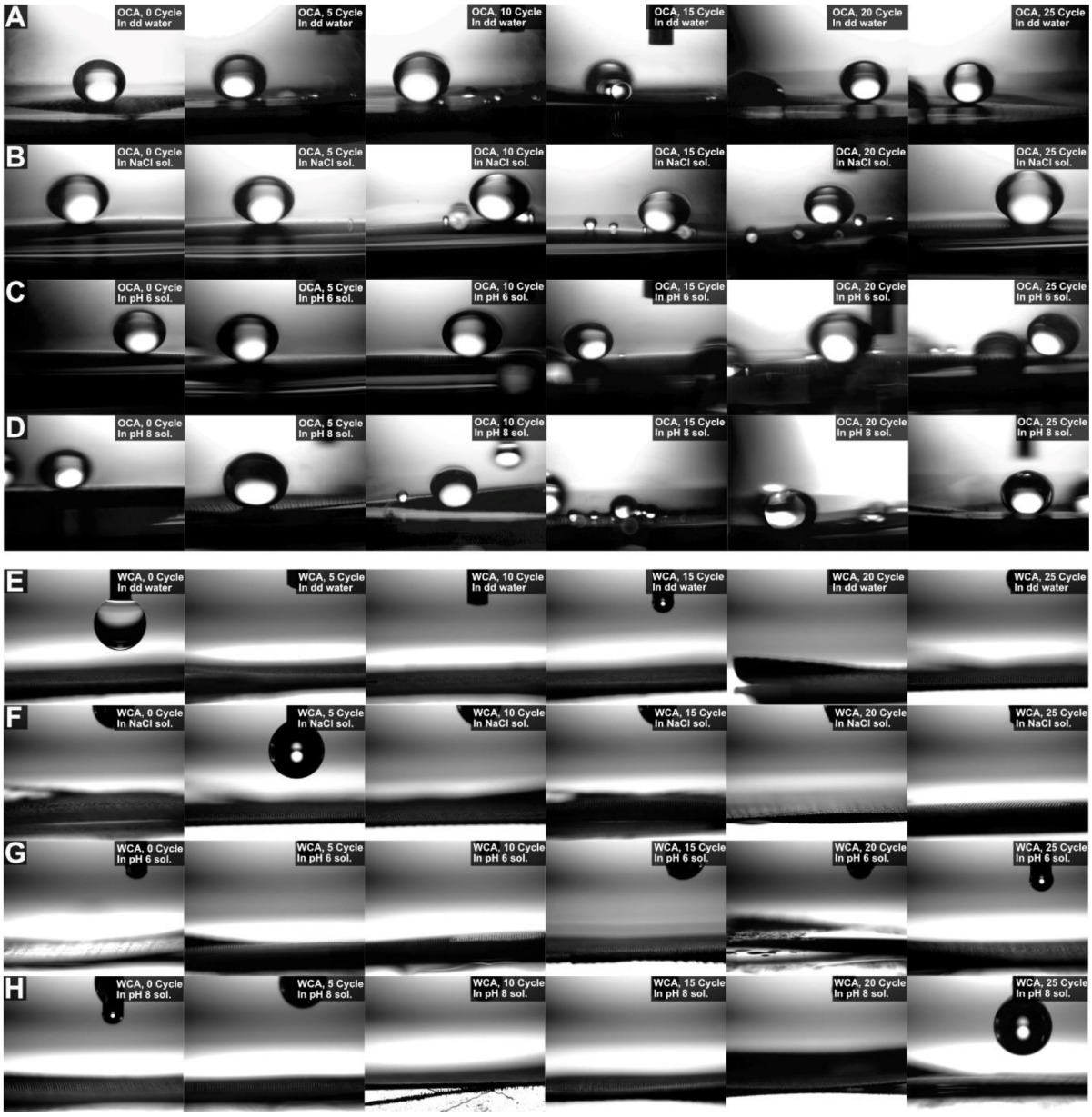

Figure 5.22 – Contact angle measurements of the MOF-modified mesh under different conditions. The OCAs and WCAs were measured after each filtration with the respective aqueous media. **A** OCA for 25 filtration cycles in dd water as reference. **B** OCA for 25 filtration cycles in NaCl solution. **C** OCA for 25 filtration cycles in water of pH 6. **D** OCA for 25 filtration cycles in water of pH 8. **E** WCA for 25 filtration cycles in dd water as reference. **F** WCA for 25 filtration cycles in NaCl solution. **G** WCA for 25 filtration cycles in water of pH 6. **H** WCA for 25 filtration cycles in water of pH 8. Dichloromethane was used as an organic solvent for testing the OCAs.

Water sorption

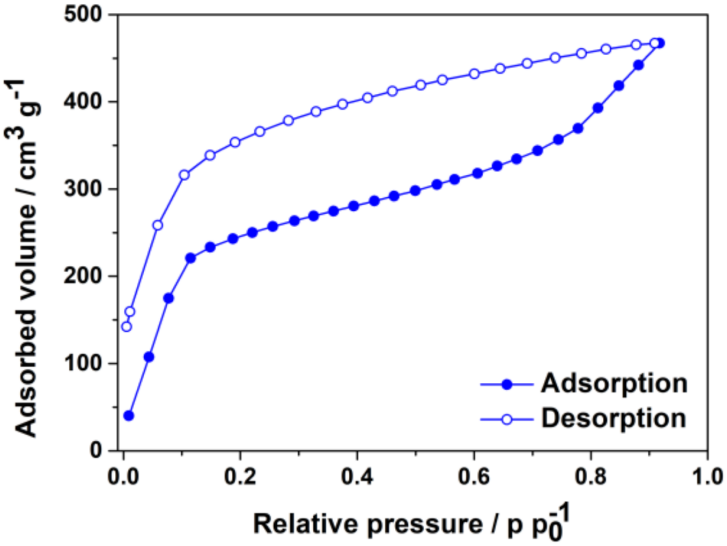

Figure 5.23 – Water isotherm of Co-CAT-1 bulk material at 120°C.

5.4.7. Electrostatic hydration stabilization calculation

Three-dimensional periodic AM1* semiempirical molecular-orbital (MO) geometry optimizations using the in-house version of *EMPIRE* and starting from the experimentally suggested unit cell without the crystal water were performed within the unrestricted Hartree-Fock(UHF) formalism. The screening radius for the periodic calculations was 40 Å. The formal high-spin multiplicity of 59 (18×3 unpaired electrons on Co plus 4 unpaired electrons on the HHTP(-3) ligands of the covalently extended layers) for a $C_{144}H_{168}O_{108}Co_{18}$ lattice cell gave a −168 kcal mol^{-1} more stable structure (Structure 1, see 5.24) than the formal low spin multiplicity of 23 (18+4+1; Structure 2, see 5.25). Details of the optimized structure are given below. Subsequently, the hydration of the pore in the optimized periodic structure was investigated using an extension of the reported self-consistent reaction field (SCRF) polarizable continuum model for periodic systems. These calculations gave an electrostatic stabilization energy of −50 kcal mol^{-1} per lattice cell for the high spin structure. The hydration of the outer surface of the crystals was investigated using two-dimensional periodic calculations on a $C_{144}H_{164}O_{104}Co_{16}$ repeat unit that was constructed by cutting the three-dimensional periodic structure at the catechol ligands. A formal high spin multiplicity of 53 (16×3+4+1) resulted in a −73 kcal mol^{-1} more stable structure (Structure 3, see 5.26) than a low spin multiplicity of 21 (16+4+1; Structure 4, see 5.27) and gave an electrostatic stabilization energy of −67 kcal mol^{-1} for the repeat unit.

```
                 ***  Summary of AM1* Calculation  ***
                 ***   EMPIRE'20 (Revision 2815)   ***

<><><>
```

```
                  ***  Summary of AM1* Calculation  ***
                  ***   EMPIRE'20 (Revision 2815)   ***

<><><>
```

6. A highly crystalline anthracene-based MOF-74 series featuring electrical conductivity and luminescence

This chapter is based on the following publication:

Patricia I. Scheurle[†,a,b], Andre Mähringer[†,a,b], Andreas C. Jakowetz[a,b], Pouya Hosseini[c], Alexander F. Richter[b,d], Gunther Wittstock[c], Dana D. Medina[*,a,b], and Thomas Bein[*,a,b] *Nanoscale.* **2019,** *11,* 20949.

[a]Department of Chemistry, Ludwig-Maximilians-Universität (LMU), Butenandtstr. 11 (E), 81377 Munich, Germany.

[b]Nanosystems Initiative Munich (NIM) and Center for NanoScience (CeNS), Schellingstr. 4, 80799 Munich, Germany.

[c]Institute of Chemistry, Carl von Ossietzky Universität Oldenburg, 26111 Oldenburg, Germany

[d]Chair for Photonics and Optoelectronics, Nano-Institute Munich, Department of Physics, Ludwig-Maximilians-Universität (LMU), Königinstr. 10, 80539 Munich, Germany

[†] The authors contributed equally to this work.

[*]Corresponding Author.

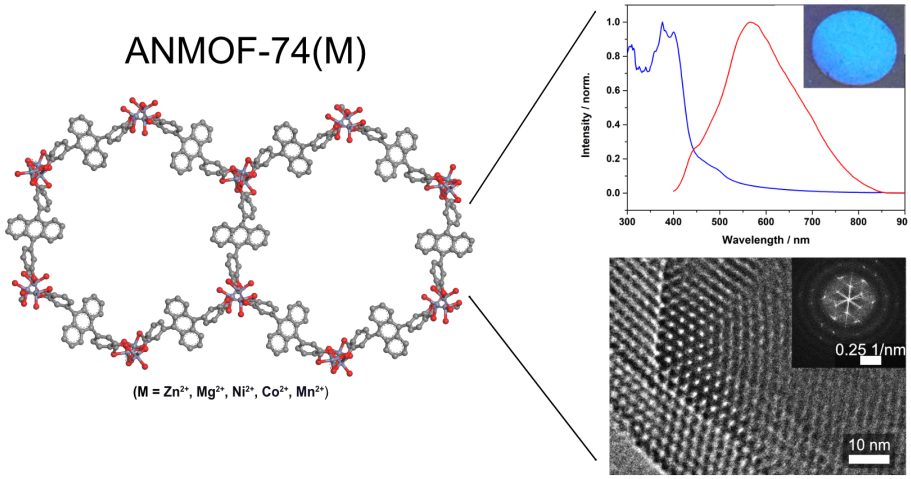

Andre Mähringer took part in the design and synthesis of the organic linker. He performed the structural simulations, Rietveld refinements and electrical conductivity studies.

DOI: 10.1039/c9nr05431f

Abstract

Recently, a small group of metal-organic frameworks (MOFs) has been discovered featuring substantial charge transport properties and electrical conductivity, hence promising to broaden the scope of potential MOF applications in fields such as batteries, fuel cells and supercapacitors. In combination with light emission, electroactive MOFs are intriguing candidates for chemical sensing and optoelectronic applications. Here, we incorporated anthracene-based building blocks into the MOF-74 topology with five different divalent metal ions, that is, Zn^{2+}, Mg^{2+}, Ni^{2+}, Co^{2+} and Mn^{2+}, resulting in a series of highly crystalline MOFs, coined ANMOF-74(M). This series of MOFs features substantial photoluminescence, with ANMOF-74(Zn) emitting across the whole visible spectrum. The materials moreover combine this photo- luminescence with high surface areas and electrical conductivity. Compared to the original MOF-74 materials constructed from 2,5-dihydroxy terephthalic acid and the same metal ions Zn^{2+}, Mg^{2+}, Ni^{2+}, Co^{2+} and Mn^{2+}, we observed a conductivity enhancement of up to six orders of magnitude. Our results point towards the importance of building block design and the careful choice of the embedded MOF topology for obtaining materials with desired properties such as photoluminescence and electrical conductivity.

6.1. Introduction

Metal-organic frameworks (MOFs) are composed of metal ions or clusters that are interconnected by rigid organic building blocks forming crystalline porous structures.[1] Based on their well-defined and tunable pore spaces and high surface areas, many MOFs are attractive candidates for gas separation and storage applications.[2,3] Depending on the organic building blocks and the respective metal species, MOFs can be synthesized with diverse chemical composition, connectivity and functionality. Therefore, a large variety of different chemical and physical properties can be attained.[2–6] Recently, the intriguing property of electrical conductivity was added to this portfolio.[2,7–12] Hereby, an increasing number of MOFs were investigated with a view towards applications in the fields of charge storage, semiconductors, chemical sensing, energy con- version or electrocatalysis.[11,13–20]

To date, only a few MOFs have been reported exhibiting the desired property of electrical conductivity in combination with ultrahigh surface area, which is viewed to be essential for sensing or charge storage applications.[21] Recently, structures based on the MOF-74 topology constructed with 2,5-dihydroxy terephthalic acid were introduced as electrically conducting platforms.[2,5,22,23] MOF-74 isostructures connected through phenoxidmetal nodes showed low conductivity values, whereas structures containing sulfur ligating functionalities in the linking

motif or mixed valence of the metal ions showed an increased electrical conductivity of up to $10^{-6}\,\mathrm{S\,cm^{-1}}$.[2,24]

Here, we present a series of MOF-74 analogs comprising an anthracene core in the linear organic linker. Anthracene and its derivatives are known for their high charge carrier mobility and electroluminescent properties.[10,21] We demonstrate that the incorporation of anthracene-containing building blocks can strongly enhance electrical conductivity in phenoxide-connected MOF-74 topology. Furthermore, we show that the anthracene core endows the MOFs with photoluminescent properties allowing for the realization of light emitting and electrically conducting MOFs. For constructing the framework, we first established the synthesis of an anthracene-based building block modified with ortho-hydroxy para-carboxylic functionalities enabling the required bonding to metal ions, namely 4,4'-(anthracene-9,10-diyl)bis(2-hydroxybenzoic acid), ABHB.

Using the anthracene building block and divalent metal ions, that is, Zn^{2+}, Mg^{2+}, Ni^{2+}, Co^{2+} and Mn^{2+}, five novel, highly crystalline and porous anthracene-based MOF-74-type (ANMOF-74) materials were synthesised under solvothermal conditions (Fig. 6.1). The ANMOF-74 series features an enhancement of electrical conductivity by several orders of magnitude compared to the respective original MOF-74 isostructures. Furthermore, the photoluminescence lifetimes and quantum yields were determined for the ANMOF-74 series.

6.2. Results and discussion

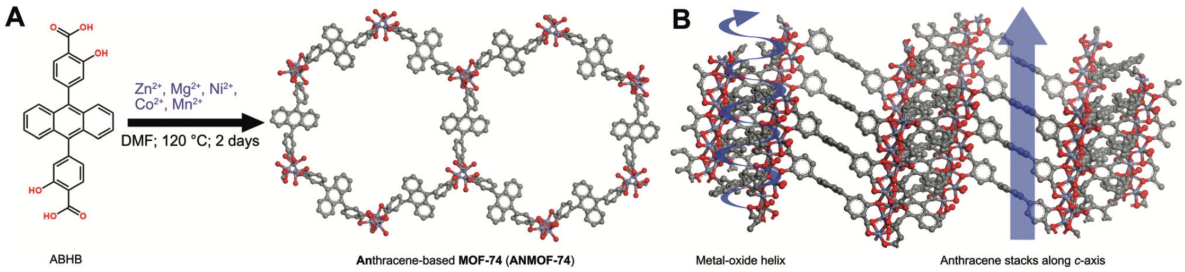

Figure 6.1 – (A) A synthesis scheme of the anthracene-based MOF-74 (ANMOF-74). The organic building block ABHB forms porous hexagonal frameworks with the respective metal ions. (B) View on the helical metal-oxo chains of the ANMOF-74 structure (left) and the anthracene moieties (right) stacked along the crystallographic *c*-direction.

The employed ABHB linker was synthesized via a three-step reaction procedure (see Schemes 6.7-6.9).[25,26] In short, the reaction of methyl 4-iodosalicylate and bis(pinacolato)diboron afforded a boronated intermediate product, which was sub- sequently coupled in a Suzuki reaction with the brominated anthracene core to the methyl protected ABHB linking motif. After

deprotection and purification, the final organic building block ABHB was obtained in a sufficient yield (ca. 70%) as a beige powder. For the MOF synthesis, the stoichiometric reaction of ABHB with the respective metal precursors (Zn^{2+}, Mg^{2+}, Ni^{2+}, Co^{2+} and Mn^{2+}) in different DMF/MeOH/EtOH/BnOH/H_2O mixtures at 120°C for 2 days led to the precipitation of colored powders. Here, the color of the obtained powders was strongly dependent on the utilized metal ion precursor (for further information see SI). The obtained powders were washed with DMF and methanol and subsequently dried under dynamic vacuum.

Powder X-ray diffraction (PXRD) data of the dried powders are shown in Fig. 6.2. All materials exhibit a high degree of crystallinity with pronounced reflections at 3.75°, 6.51°, 10.02°, 11.34°, 13.14° and 13.66° 2θ. Bragg reflections at up to 25° θ could be detected, underlining the high crystallinity of the obtained ANMOF-74 series. The collected diffractograms matched with the ones predicted from simulated model structures. The predicted model structures were obtained with *Accelrys Materials Studio 6.0* using the calculated MOF-74 crystal structure as a basis for the simulations.[2] After establishing the simulated unit cells, PXRD patterns were calculated, which were Rietveld-refined according to the respective experimental PXRD pattern (Rwp ranging from 3.94-6.96%). From the refinement, we conclude that the ANMOF-74 crystallizes in the trigonal space group, *R3*, with exemplary lattice constants of a=b=46.1 Å, c=5.8 Å, α=β=90° and γ=120° for the ANMOF-74(Zn), for further information see ESI. ANMOF-74(Zn). These findings are in good agreement with simulations performed for related MOF-74 structures.[10,27] All ANMOF-74 materials exhibit one-dimensional hexagonal channels with pore apertures of 2 nm. These channels are formed by the ABHB units that are interconnected in the c-direction by infinite helical metal-oxo chains. Furthermore, ANMOF-74 include infinite stacks of the anthracene core arranged along the c-direction, with interlayer distance between adjacent anthracene cores estimated to be 5.8 Å (Fig. 6.1B). For the ABHB unit, we determined a torsion angle of 60.7° between the para-positioned benzene rings and the anthracene core. Transmission electron microscopy (TEM) analysis of the ANMOF-74 series revealed highly crystalline materials (Fig. 6.12). For ANMOF-74(Co), hexagonally shaped crystal facets and large cross-section domain sizes of about 120 nm illustrate the high degree of crystallinity (Fig. 6.2F). The calculated diffraction pattern in the fast Fourier transform (FFT) of the TEM image shows angles of 120° in accordance with the proposed trigonal crystal system.

The synthesized powders were further investigated using X-ray photoelectron spectroscopy (XPS). As summarized in Fig. 6.22-6.26, XPS spectra of ANMOF-74(M) show the presence of the respective metal, C and O peaks attributed to the MOFs, as well as nitrogen, tentatively attributed to DMF residues coordinating to the metal ions in the structure. These findings are in accordance with the high-resolution analysis of the O 1s regions in the XPS spectra of all ANMOFs, indicating three types of oxygen atoms. The signals can be assigned to the functional

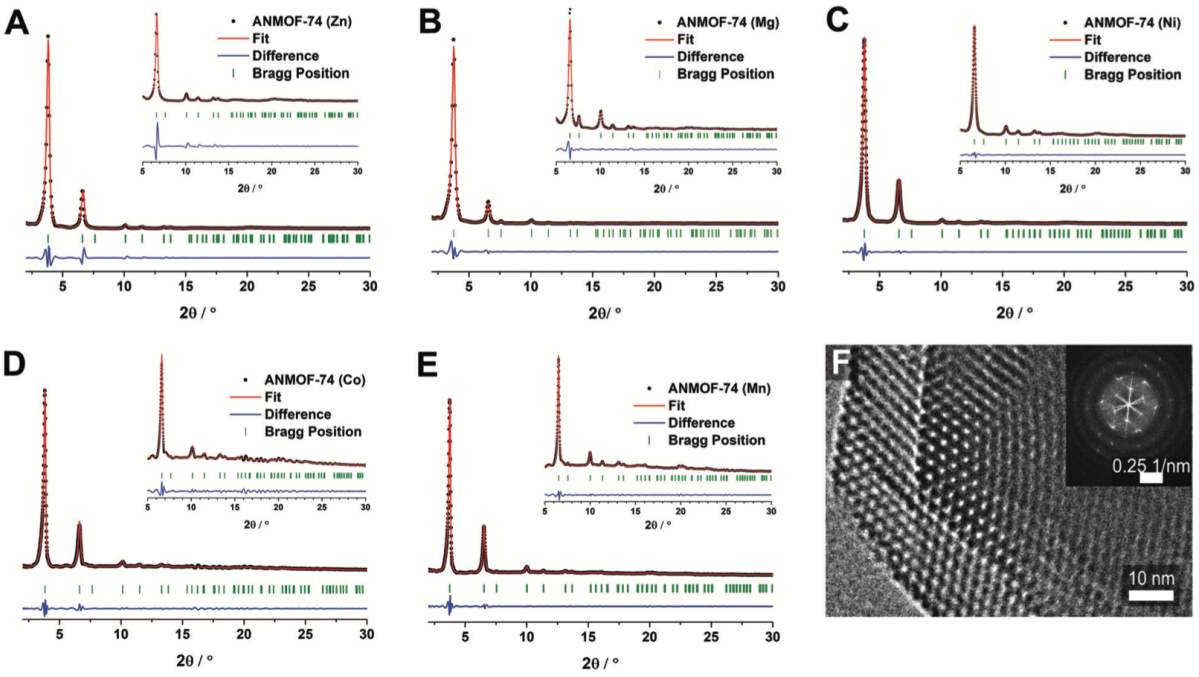

Figure 6.2 – Experimental powder X-ray diffraction patterns of the ANMOF-74(M) series showing (A) the Zn-, (B) Mg-, (C) Ni-, (D) Co- and (E) Mn-MOF derivatives, respectively (black). The simulated PXRD pattern were Rietveld-refined (red) according to the experimental data, whereby the difference plots are depicted in blue. The respective Bragg positions of the predicted hexagonal unit cell are shown as green bars. (F) A high resolution TEM image of an ANMOF-74 (Co) crystal oriented along the [001] axis with FFT of the entire image as inset.

groups (carboxy and hydroxy) of the ligating build-ing block and to the oxygen related to DMF. Only ANMOF-74 (Zn) has a second N 1s peak arising from residual NO_3^-, which apparently originates from the $Zn(NO_3)_2$ synthesis precursor. Importantly, Cl or additional N peaks related to impurities originating from the metal precursors were not observed for all other samples of the ANMOF-74 series. The purity of the obtained materials was further studied by energy dispersive X-ray spectroscopy (EDX) which showed no impurities arising from precursor anions (see Fig. 6.20). Thermogravimetric analysis (TGA) revealed that the ANMOF-74(M) materials were stable below 300°C under dynamic conditions (Fig. 6.19).

The pore accessibility of the activated samples was investigated by nitrogen physisorption experiments. The nitrogen isotherms (77 K) of all ANMOF-74(M) powders (Fig. 6.3) show IUPAC Type *I(b)*[28] sorption curves, indicating that the ANMOF-74(M) form micropores (2.5 nm). All examined MOFs show an initial uptake of about 200 $cm^3\,g^{-1}$ at low pressures and a second uptake at 0.02-0.05 p/p_0 of about 100 $cm^3\,g^{-1}$. The adsorption branch and the desorption branch merge at low relative pressures illustrating a reversible process. The Brunauer-Emmett-Teller (BET)

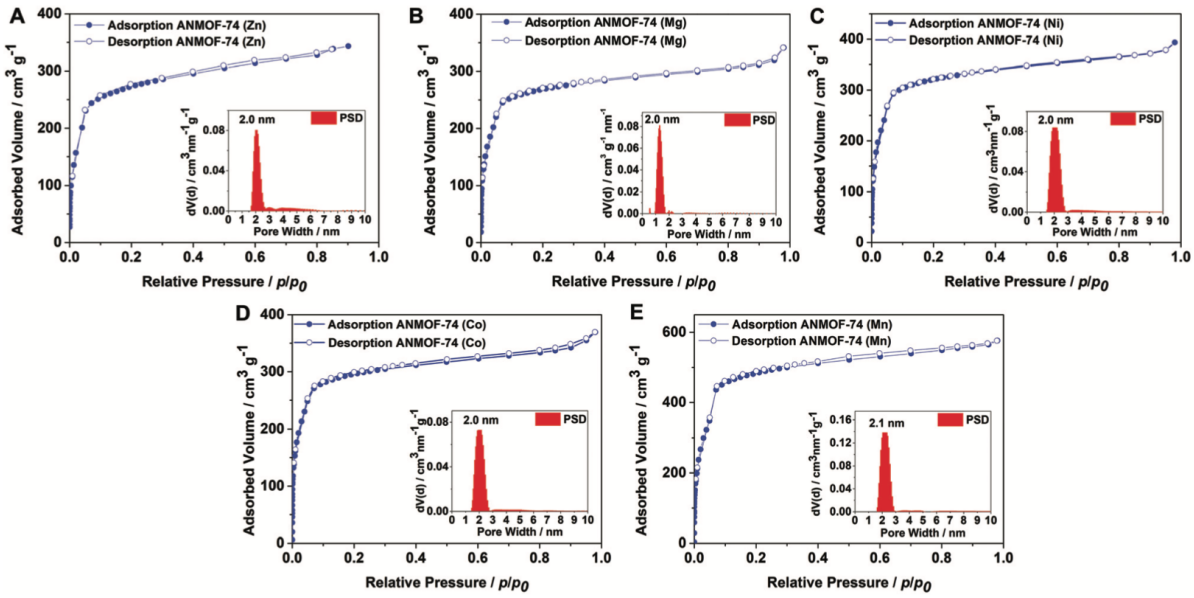

Figure 6.3 – Nitrogen physisorption isotherms of (A) ANMOF-74(Zn), (B) ANMOF-74(Mg), (C) ANMOF-74(Ni), (D) ANMOF-74(Co) and (E) ANMOF-74(Mn) showing Type I(b) isotherm curves. The ad- and desorption branches are depicted as blue and white colored circles, respectively. Pore size distributions (PSD) are included as insets.

surface areas and total pore volumes for the ANMOF-74(M) bulk materials series were calculated to be $1124\,m^2\,g^{-1}$ and $0.49\,cm^3\,g^{-1}$ for Zn, $1137\,m^2\,g^{-1}$ and $0.48\,cm^3\,g^{-1}$ for Mg, $1352\,m^2\,g^{-1}$ and $0.56\,cm^3\,g^{-1}$ for Ni, $1231\,m^2\,g^{-1}$ and $0.53\,cm^3\,g^{-1}$ for Co, $1748\,m^2\,g^{-1}$ and $0.83\,cm^3\,g^{-1}$ for Mn, respectively. The pore size distributions were calculated using quenched solid density functional theory (QSDFT), revealing pore sizes of 2.1 nm in ANMOF-74 (Mn) and 2.0 nm in all other ANMOF-74(M) structures, which match the predicted value of 2.0 nm obtained by the simulated structure. Connolly surface area calculations with nitrogen as a probe molecule (2.6 Å) predict a theoretical surface area of $1757\,m^2\,g^{-1}$, which matched best with the BET results obtained for the ANMOF-74(Mn) sample. Scanning electron microscopy (SEM) images of the ANMOF-74(M) powders showed needle-shaped crystallites forming spherical agglomerates (Fig. 6.4 and 6.11). In addition, high magnification SEM analysis revealed crystallites with a well-faceted hexagonal cross-section, further confirming the proposed trigonal crystal structures.

To elucidate the electrical properties of the ANMOF-74 series, we performed four-point probe van der Pauw measurements of crystalline and pelletized samples (for further details see Appendix). The obtained results are summarized in Table 16. The values obtained for ANMOF-74(M) range from 10^{-7} to $10^{-9}\,S\,cm^{-1}$, corresponding to a striking increase of up to six orders of magnitude with regard to the values obtained (and reported)[2] for the respective MOF-74. To validate

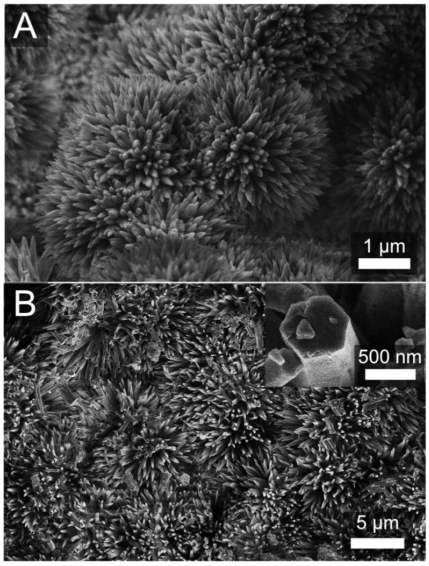

Figure 6.4 – SEM images of the ANMOF-74 bulk materials (A) ANMOF-74(Ni) and (B) ANMOF-74(Mn), with a high magnification of a hexagonally shaped crystal depicted as inset.

the impact of the anthracene core on the electrical conductivity, crystalline MOF-74 powders with the same set of metal ions were synthesized, activated (vacuum dried), compressed into pellets and their electrical conductivity was evaluated. The van der Pauw measurements of the MOF-74 pellets confirmed the ANMOF-74 series to be substantially more conducting than the MOF-74 isostructures. We attribute the enhanced electrical conductivity to the presence of the electron-rich anthracene core incorporated in the ANMOF-74 backbone, in contrast to the rather electron-poor 2,5-dihydroxy terephthalic acid building block embedded in MOF-74. Here, our strategy of embed- ding the electron-rich anthracene-based linker resulted in a remarkable increase in relative conductivity, however, the measured values are still modest compared to other conducting MOF platforms.[29,30] Due to the fairly large stacking distance between adjacent anthracene units we postulate that charge transport still occurs mostly through the metal-oxo chains by charge carrier hopping between metal nodes.

To further elucidate the impact of the MOF-embedded anthracene moiety, we examined the optical properties of the ANMOF-74(M) bulk materials by using UV-vis absorption and photoluminescence (PL) spectroscopy, summarized in Fig. 6.5. The UV-vis spectra were measured in diffuse reflectance geometry and obtained using the Kubelka-Munk equation. For all examined ANMOF-74 samples the absorption bands are located in the UV and blue spectral regions. ANMOF-74(Zn) has an absorption onset of around 528 nm and a second one at around 450 nm, and ANMOF-74(Mg; Ni; Co; Mn) at around 440 nm. Tauc plots were analyzed, assuming direct band gaps, yielding an optical band gap of 2.86 eV for ANMOF-74(Zn) and in case of

Table 16 – Electrical conductivity values of ANMOF-74(M) and MOF-74(M) samples obtained with pellets by using the four-point probe van der Pauw technique.

ANMOF-74(Zn)	MOF-74(Zn)	ANMOF-74(Mg)	MOF-74(Mg)	ANMOF-74(Ni)
$6 \times 10^{-8}\,\mathrm{S\,cm^{-1}}$	$6 \times 10^{-12}\,\mathrm{S\,cm^{-1}}$	$5 \times 10^{-9}\,\mathrm{S\,cm^{-1}}$	$6 \times 10^{-13}\,\mathrm{S\,cm^{-1}}$	$4 \times 10^{-7}\,\mathrm{S\,cm^{-1}}$
ANMOF-74(Co)	MOF-74(Co)	ANMOF-74(Mn)	MOF-74(Mn)	MOF-74(Ni)
$4 \times 10^{-8}\,\mathrm{S\,cm^{-1}}$	$6 \times 10^{-13}\,\mathrm{S\,cm^{-1}}$	$3 \times 10^{-8}\,\mathrm{S\,cm^{-1}}$	$4 \times 10^{-13}\,\mathrm{S\,cm^{-1}}$	$6 \times 10^{-13}\,\mathrm{S\,cm^{-1}}$

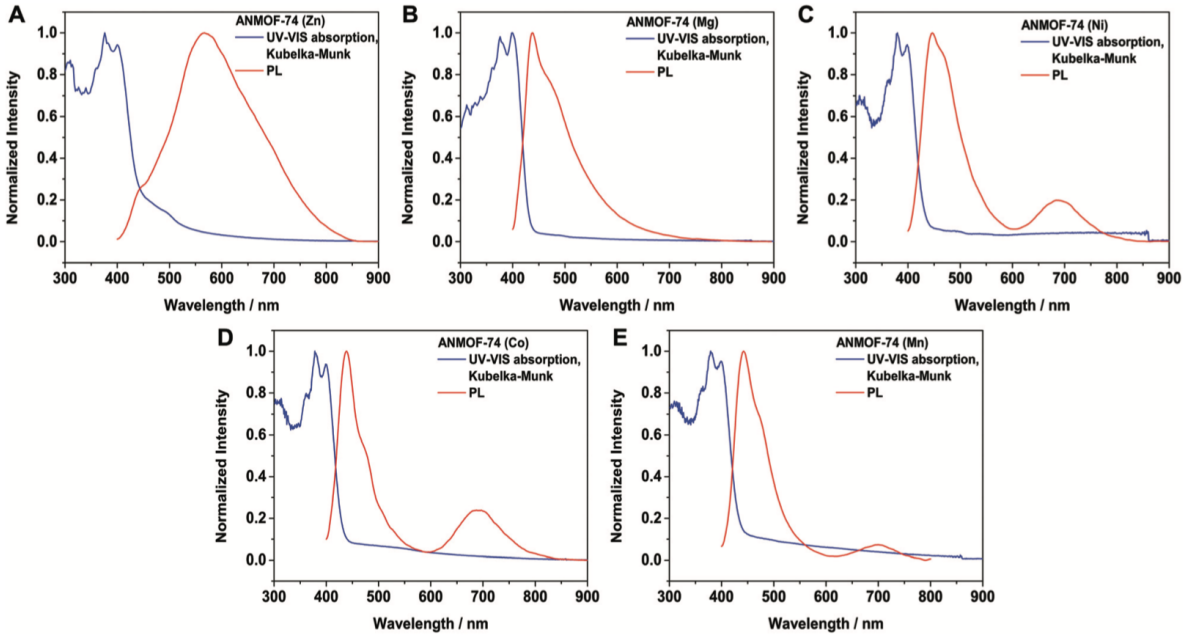

Figure 6.5 – Diffuse reflectance UV-vis absorption spectra of the ANMOF-74 powders (blue line) and the photoluminescence (PL) spectra of the pristine MOF bulk materials measured with 378 nm excitation (red line): (A) ANMOF-74(Zn), (B) ANMOF-74(Mg), (C) ANMOF-7(Ni), (D) ANMOF-74(Co) and (E) ANMOF-74(Mn).

ANMOF-74(Mg; Ni; Co; Mn) band gaps between 2.91 eV and 2.95 eV (Fig. 6.14). These five MOFs have two sharp absorption maxima at 400 nm and 380 nm, which originate from the integrated ABHB building blocks (see Fig. 6.13(A)). Photoluminescence (PL) of the ANMOF-74(M) bulk materials was measured with 378 nm excitation under argon atmosphere to protect the anthracene from degradation. The PL spectrum of ANMOF-74(Zn) shows a very broad emission band over the whole visible spectrum with a maximum at 570 nm and a large Stokes shift of 170 nm. ANMOF-74(Mg) and ANMOF-74(Co), as well as ANMOF-74 (Ni) and ANMOF-74(Mn) have a narrow emission band with a small shoulder and an emission maximum between 438 nm

and 444 nm, respectively. It is similar to the emission band at 441 nm of the ABHB linker monomer measured in solution (see Fig. 6.13(B)). These MOFs exhibit smaller Stokes shifts of 38-44 nm. ANMOF-74(Co) and ANMOF-74(Ni) also have a weaker emission band at 692 nm. ANMOF-74(Mn) has a weak emission band at 701 nm. Time-correlated single photon counting (TCSPC) traces of ANMOF-7(Zn) and ANMOF-74(Mg) were recorded at the respective emission maxima of 570 nm and 438 nm, shown in Fig. 6.6. Both MOFs exhibit very similar relaxation behavior, analyzed with a tri-exponential fit. Both exhibit fast decays of around $\tau_1 = 0.16$ ns, which is near the instrumental response limit. However, the instrument response function was not included during the fitting procedure. The medium component has a lifetime τ_2 of 0.79 ns and 1.03 ns while the third component has a lifetime τ_3 of 3.44 ns and 4.90 ns for Zn and Mg, respectively. The main difference between the two materials is the fractional distribution of lifetimes. While the medium-lifetime decay channel is contributing almost 60% to the overall emission in the ANMOF-74(Zn) and only 50% in the ANMOF-74(Mg), this difference is balanced by the longer lifetime components, i.e. 18% versus 29% in the Zn and Mg ANMOFs, respectively. This results in the faster overall decay of the ANMOF-74(Zn) as compared to the longer-lived ANMOF-7(Mg). Due to the bright emission and long lifetime of ANMOF-74(Mg), we also measured the photoluminescence quantum yield (PLQY), which reaches 2.5% (see Fig. 6.16). The ABHB linker molecules (as solid powder) show PLQY values of up to 13%, which is reduced by one order of magnitude upon incorporation into the framework. However, the luminescence is still detectable with the naked eye by irradiating the ANMOF(Mg) sample with a UV lamp (see Fig. 6.17 and 6.18).

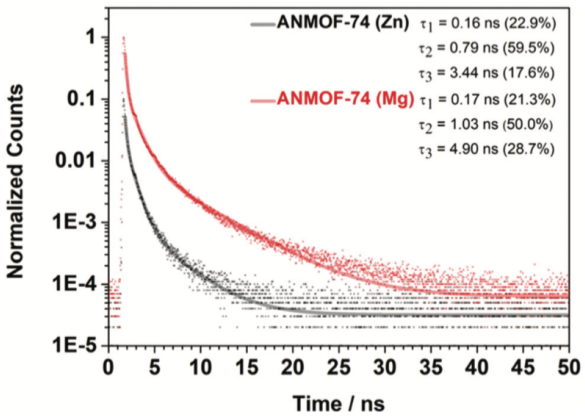

Figure 6.6 – The time-correlated single photon counting (TCSPC) traces corresponding to the PL spectra of ANMOF-74(Zn) (black) and ANMOF-74(Mg) (red), which were recorded at the respective emission maximum of each MOF. The lifetimes were obtained from triexponential fits (solid lines) to the data (scatter). The fractions of emitted photons corresponding to the respective lifetimes are stated in brackets.

TCSPC traces of ANMOF-74(Ni), ANMOF-74(Co) and ANMOF-74(Mn) show similar lifetime components with τ_1 around 0.06 ns, τ_2 between 0.79 ns and 0.89 ns and τ_3 in the range of 5-7 ns (see Fig. 6.15). The ABHB linker monomer has a monoexponential decay with a lifetime of 4.3 ns (see 6.15). The long PL lifetime of ANMOF-74(Mg) in comparison to the other ANMOFs might be related to the different emission spectrum. ANMOF-74(Mg), similar to the ABHB linker, does not have a second emission band at around 700 nm. But the PL lifetime of ANMOF-74(Mg) and of the ABHB linker are much longer compared to the other ANMOFs. Thus, in the ANMOF-74(Mg), the linkers might be similarly electronically 'isolated' as the monomer in solution while the emission band at around 700 nm might be related to electronic interactions between linkers (and transition metal ions), effectively decreasing the PL lifetime.

6.3. Conclusions

In our study, we present the successful synthesis of a novel series of metal-organic frameworks showing MOF-74 topology, coined ANMOF-74. The frameworks are built from anthracene-based linking motifs (ABHB) connected *via* helical metal-oxo chains, whereby a range of different metal ions could be incorporated (Zn, Mg, Co, Ni and Mn) into the framework. All ANMOF-74 materials feature a high degree of crystallinity and show BET surface areas exceeding 1000 $m^2\,g^{-1}$. Furthermore, all ANMOF-74 materials exhibit an enhancement of electrical conductivity of up to one-million fold compared to regular MOF-74. The ANMOF-74 materials feature direct optical band gaps of around 2.9 eV and most show photoluminescence in the blue spectral region. In contrast to the other derivatives, the ANMOF-74(Mg) shows a rather high quantum yield of 2.5%. Remarkably, ANMOF-74(Zn) emits photoluminescence across the entire visible spectrum. We believe that this promising combination of high crystallinity, defined porosity, luminescence as well as electrical conductivity embedded in a fixed MOF matrix will enable a range of possible applications such as sensing and charge storage. Our study highlights the great versatility of the MOF-74 topology, allowing for the integration of sterically demanding organic linker structures with interest- ing electrical and optical properties. In the future, we envision the integration of additional chromophores with interesting optoelectronic properties and a tunable degree of electronic coupling into this highly attractive MOF topology, to further broaden the field of MOF-74 based structures for optoelectronic applications.

References

[1] O. M. Yaghi and H. Li, *J. Am. Chem. Soc.*, 1995, **117,** 10401-10402.
[2] L. Sun, C. H. Hendon, M. A. Minier, A. Wals and M. Dinca, *J. Am. Chem. Soc.*, 2015, **137,** 6164-6167.
[3] S. T. Meek, J. A. Greathouse and M. D. Allendorf, *Adv. Mater.*, 2011, **23,** 249-267.
[4] E. A. Dolgopolova and N. B. Shustova, *MRS Bull.*, 2016, **41,** 890-896.

[5] M. T. Kapelewski, S. J. Geier, M. R. Hudson, D. Stück, J. A. Mason, J. N. Nelson, D. J. Xiao, Z. Hulvey, E. Gilmour, S. A. FitzGerald, M. Head-Gordon, C. M. Brown and J. R. Long, *J. Am. Chem. Soc.*, 2014, **136,** 12119-12129.
[6] N. L. Rosi, J. Kim, M. Eddaoudi, B. Chen, M. O'Keeffe and O. M. Yaghi, *J. Am. Chem. Soc.*, 2005, **127,** 1504-1518.
[7] M. Usman, S. Mendiratta, S. Batjargal, G. Haider, M. Hayashi, N. Rao Gade, J.-W. Chen, Y.-F. Chen and K.-L. Lu, |textitACS Appl. Mater. Interfaces, **2015,** 7, 22767-22774.
[8] L. Sun, M. G. Campbell and M. Dinca, *Angew. Chem. Int. Ed.,* 2016, **55,** 3566-3579.
[9] M. Usman, S. Mendiratta and K.-L. Lu, *Adv. Mater.,* 2017, **29,** 1605071.
[10] Y. Kobayashi, B. Jacobs, M. D. Allendorf and J. R. Long, *Chem. Mater.,* 2010, **22,** 4120-4122.
[11] J. D. Evans, B. Garai, H. Reinsch, W. Li, S. Dissegna, V. Bon, I. Senkovska, R. A. Fischer, S. Kaskel, C. Janiak, N. Stock and D. Volkmer, *Coord. Chem. Rev.,* 2019, **380,** 378-418.
[12] V. Stavila, A. A. Talin and M. D. Allendorf, *Chem. Soc. Rev.,* 2014, **43,** 5994-6010.
[13] M. G. Campbell, D. Sheberla, S. F. Liu, T. M. Swager and M. Dinca, *Angew. Chem. Int. Ed.,* 2015, **54,** 4349-4352.
[14] Z. Zhang, H. I. Yoshikawa and K. Awaga, *J. Am. Chem. Soc.,* 2014, **136,** 16112-16115.
[15] M. G. Campbell and M. Dinca, *Sensors,* 2017, **17,** 1106.
[16] L. E. Kreno, K. Leong, O. K. Farha, M. Allendorf, R. P. van Duyne and J. T. Hupp, *Chem. Rev.,* 2012, **112,** 1105-1125.
[17] Y. Watanabe, T. Haraguchi, K. Otsubo, O. Sakata, A. Fujiwara and H. Kitagawa, *Chem. Commun.,* 2017, **53,** 10112-10115.
[18] F.-Y. Yi, D. Chen, M.-K. Wu, L. Han and H.-L. Jiang, *ChemPlusChem,* 2016, **81,** 675-690.
[19] H. Kim, S. R. Rao, E. A. Kapustin, L. Zhao, S. Yang, O. M. Yaghi and E. N. Wang, *Nat. Commun.,* 2018, **9,** 1191.
[20] F. Gerard, F. Millange, M. Morcrette, C. Serre, M.-L. Doublet, J.-M. Greneche and J.-M. Tarascon, *Angew. Chem. Int. Ed.,* 2007, **46,** 3259-3263.
[21] D. Chen, H. Xing, Z. Su and C. Wang, *Chem. Commun.,* 2016, **52,** 2019-2022.
[22] H. Deng, S. Grunder, K. E. Cordova, C. Valente, H. Furukawa, M. Hmadeh, F. Gandara, A.-C. Whalley, Z. Liu, S. Asahina, H. Kazumori, M. O. Keeffe, O. Terasaki, J. F. Stoddart and O. M. Yaghi, *Science,* 2012, **336,** 1018-1023.
[23] A. F. Cozzolino, C. K. Brozek, R. D. Palmer, J. Yano, M. Li and M. Dinca, *J. Am. Chem. Soc.,* 2014, **136,** 3334-3337.
[24] L. Sun, T. Miyakai, S. Seki and M. Dinca, *J. Am. Chem. Soc.,* 2013, **135,** 8185-8188.
[25] A. M. Fracaroli, H. Furukawa, M. Suzuki, M. Dodd, S. Okajima, F. Gandara, J. A. Reimer and O. M. Yaghi, *J. Am. Chem. Soc.,* 2014, **136,** 8863-8866.
[26] M. Hirofumi, S. Akira, M. Yusuke and I. Yoshinori, Polycarboxylic Acid Containing Condensed Aromatic Ring, Crystalline Network Complex Using Same, and Gas Storage Material, WO2017006638A1, 2017.
[27] J. Zheng, R. S. Vemuri, L. Estevez, P. K. Koech, T. Varga, D. M. Camaioni, T. A. Blake, B. P. McGrail and R. K. Motkuri, *J. Am. Chem. Soc.*, 2017, **139,** 10601-10604.
[28] M. Thommes, K. Kaneko, A. V. Neimark, J. P. Olivier, F. Rodriguez-Reinoso, J. Rouquerol and K. S. W. Sing, *Pure Appl. Chem.,* 2015, **87,** 1051-1069.
[29] M. Ko, L. Mendecki and K. Mirica, *Chem. Commun.,* 2018, **54,** 7873-7891.
[30] A. Mähringer, A. C. Jakowetz, J. M. Rotter, B. J. Bohn, J. Feldmann, T. Bein and D. D. Medina, *ACS Nano*, 2019, **13,** 6711-6719.

6.4. Appendix

6.4.1. Characterization methods

Nuclear magnetic resonance (NMR)

NMR spectra were recorded on *Bruker AV400* and *AV400 TR* spectrometers. The chemical shifts are expressed in parts per million and calibrated using residual (undeuterated) solvent peaks as an internal reference (^{1}H-NMR: DMSO-d_6: 2.50; ^{13}C-NMR: DMSO-d_6: 39.52). The data for ^{1}H-NMR spectra are written as follows: s = singlet, d = doublet, t = triplet, q = quartet, m = multiplet.

X-ray analysis

X-ray diffraction (XRD) analyses were performed on a Bruker D8 diffractometer in Bragg-Brentano geometry with Ni-filtered Cu K_α (λ = 1.54060 Å) radiation operating at 40 kV and 30 mA with a position-sensitive detector (*LynxEye*).

Scanning electron microscopy (SEM)

SEM images were recorded on a *FEI Helios NanoLab G3 UC* electron microscope with an acceleration voltage of 2 kV from a field emission gun. For the cross-section analysis substrates were partially cut and broken manually to reveal fresh cross-sections. *Prior* to SEM analysis the samples were coated with a thin carbon layer by carbon fiber flash evaporation in high vacuum.

Transmission electron microscopy (TEM)

TEM images were collected on an *FEI Titan Themis 60-300* microscope at an acceleration voltage of 300 kV. Powder samples were prepared by crushing the particles with a razor blade and subsequently depositing the powder onto a copper grid supporting a thin electron transparent carbon film.

Nitrogen sorption

Ad- and desorption measurements were performed on an Autosorb 1 (Quantachrome instruments, Florida, USA) with nitrogen of 99.9999% purity at 77.3 K. The samples were activated (dried) under high vacuum at 120°C for at least 12 h. Evaluation of ad- and desorption isotherms was carried out with the *AsiQwin v.3.01* (*Quantachrome instruments*, Florida, USA) software.

For BET calculations, pressure ranges of the nitrogen isotherms were chosen with the help of the BET assistant in the *AsiQwin v.3.01* software. In accordance with the ISO recommendations, multipoint BET tags equal to or below the maximum in $V \times (1\text{-}p/p_0)$ were chosen.

Van der Pauw measurements

Van der Pauw measurements were conducted on a *ECOPIA Model HMS 3000* Hall measurement setup. The samples were fixed in an SPCB-1 spring clip board without any additional contacts. Distances between the single probes were adjusted to be 5 mm.

Preparation of ANMOF-74 and MOF-74 pellets

ANMMOF-74 and MOF-74 pellets with 1 cm diameter (obtained from several described batches) for electrical conductivity measurements were fabricated with 100 mg of the respective MOF bulk material with a standard *Paul-Weber KBr* Press with 45 kg/cm^2 pressure.

UV-VIS spectroscopy

UV-Vis spectra were recorded using a *PERKIN ELMER UV VIS/NIR Lambda 1050* spectrophotometer equipped with a 150 mm InGaAs integrating sphere. Diffuse reflectance spectra were collected with a Praying Mantis (Harrick) accessory and were referenced to barium sulphate powder as white standard.

Photoluminescence (PL) spectroscopy

PL measurements were performed on a *PicoQuant FluoTime* 300 time-correlated single photon counting (TCSPC) setup. Steady-state spectra and time-resolved histograms were acquired using a 378 nm laser (*PicoQuant LDH-P-C-375*). Residual laser scattering was removed using a 400 nm dielectric long pass (*Thorlabs FELH0400*) in the beam path of the emitted light, which was detected under magic angle (54.7°) on a photomultiplying tube (*PicoQuant PMA 192*).

For measuring the absolute photoluminescence quantum yield and CIE-values, we used a *Horiba FluoroLog 3* in combination with an integrating sphere by *Horiba*. The sample was prepared as follows: a small amount of powder of the MOF was sandwiched between two glass coverslips and sealed using Parafilm at the edges. A reference structure without sample was prepared as well. By relating the signal area change between sample and reference at the luminescence region and at the Rayleigh peak the absolute radiative quantum yield was calculated.

Thermogravimetric analysis

Thermogravimetric analysis (TGA) measurements were performed on a *Netzsch Jupiter ST 449 C* instrument equipped with a *Netzsch TASC 414/4* controller. The samples were heated from room temperature to 800°C under a synthetic air flow (25 mL min^{-1}) at a heating rate of 1 K min^{-1}.

X-ray photoelectron spectroscopy

XPS was performed using an *ESCALAB 250 Xi instrument (Thermo Fisher, East Grinsted, UK)* with monochromatized Al Kα ($h\nu$ = 1486.6 eV) radiation focused to a spot of 500 micron

diameter at the surface of samples. Spectra were measured with pass energies of 200 eV for survey scans and 10 eV for high-resolution regions. Charging was compensated by use of an internal electron flood gun. Peak fitting was performed by the software *Avantage,* version 5.9904 (*Thermo Fisher*) using a Shirley background ('Smart Shirley') and a convolution of Gaussian and Lorentzian functions for each signal component. All spectra were referenced to remaining adventitious carbon at 284.8 eV.

Elemental Analysis

The elemental analysis for carbon and hydrogen for ANMOF-74 (M) was performed on a *Vario MICRO* cube instrument (*Elementar Analysensysteme GmbH, Germany*). The metal detection for all samples was carried out on a *Varian Vista RL* ICP-OES spectrometer. All materials were treated under dynamic vacuum *prior* to analysis.

6.4.2. Experimental

General

All materials were purchased from *Sigma Aldrich, Acros* or *TCI Europe* in the common purities *purum, puriss* or reagent grade. The materials were used as received without additional purification and handled in air unless otherwise noted. The water utilized in the synthesis was subjected to a *Merck-Milipore Mili-Q* purification system *prior* to use.

Synthetic procesures

Methyl 2-hydroxy-4-(4,4,5,5-tetramethyl-1,3,2-dioxaborolan-2-yl)benzoate (compound 3) (adapted from Fracaroli, A. M.; Furukawat, H.; Suzuki, M.; Dodd, M.; Okajima, S.; Gandarat, F.; Reimer, J. A.; Yaghi, O. M. Metal-organic Frameworks with Preciseley Designed Interior for Carbon Dioxide Capture in the Presence of Water. *J. Am. Chem. Soc.* **2014,** 136, 8863-8866.)

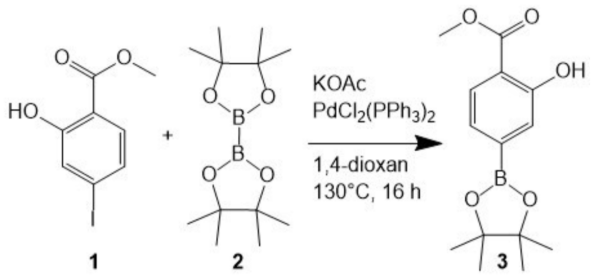

Figure 6.7 – Scheme 1.

Methyl 4-iodosalicylate (compound 1) (1.0 g, 3.6 mmol), bis(pinacolato)diboron (compound 2) (1.01 g, 3.98 mmol), KOAc (1.1 g, 10.8 mmol), and $PdCl_2(PPh_3)_2$ (50.7 mg, 0.072 mmol) were

dissolved in 18 mL anhydrous 1,4-dioxane in a 100 mL flask under nitrogen atmosphere. The resulting solution was heated to 130°C for 13 h under stirring. The solution was allowed to cool to room temperature and filtered through celite. It was washed with 1,4-dioxane, toluene and ethyl acetate. The filtrate was concentrated in vacuo. The obtained yellow solid was dissolved in ethyl acetate. The white solid was filtered off. The filtrate was concentrated under vacuum. The obtained yellow needles were recrystallized in methanol (2 mL), giving colorless crystals with 71% yield. ^{1}H NMR (400 MHz, DMSO-d_6) δ (*ppm*): 10.35 (s, 1H), 7.75 (d, 1H) 7.20 (s, 1H), 7.17 (d, 1H), 3.87 (s, 3 H), 1.26 (s, 12H).

Dimethyl 4,4'-(anthracene-9,10-diyl)bis(2-hydroxybenzoate) (compound 5) (adapted from Hirofumi M., Akira S., Yusuke M., Yoshinori I. Polycarboxylic acid containing condensed aromatic ring, crystalline network complex using same, and gas storage material. **2017.** WO 2017006638 A1.)

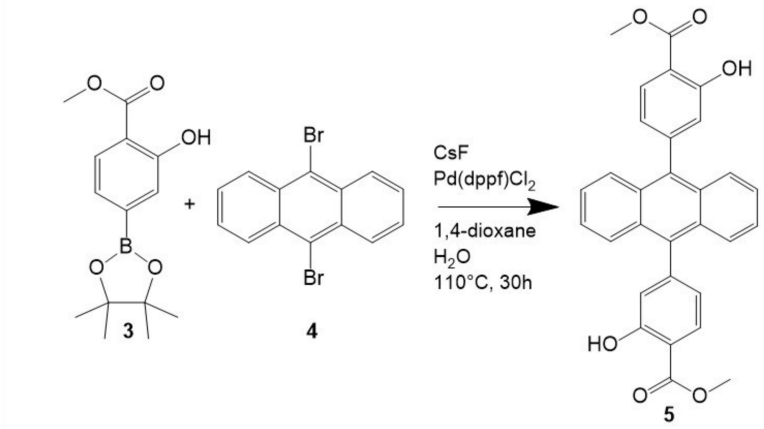

Figure 6.8 – Scheme 2.

Methyl 2-hydroxy-4-(4,4,5,5-tetramethyl-1,3,2-dioxaborolan-2-yl)benzoate (compound 3) (700 mg, 2.5 mmol), 9,10-dibromoanthracene (compound 4) (369 mg, 1.099 mmol), CsF (1.0 g, 65.8 µmol), Pd(dppf)Cl_2 (44.85 mg, 613 µmol) were dissolved in 12.8 mL 1,4-dioxane and 1.8 mL water in a 100 mL flask under nitrogen atmosphere. The resulting solution was heated to 110°C for 30 h. The solution was allowed to cool to room temperature and NH_4Cl (40 mL) and chloroform (40 mL) were added. It was filtered through celite and the residue was washed with chloroform (400 mL). The filtrate was separated and the aqueous layer was extracted with chloroform. The organic layer was washed with saturated sodium chloride solution (3 × 200 mL) and dried over $MgSO_4$. The filtrate was concentrated under vacuum, giving a brown powder with 72% yield. ^{1}H NMR (400 MHz, DMSO-d_6) δ (*ppm*): 8.04 (d, 2H), 7.64-7.59 (m, 4H), 7.49-7.45 (m, 4H), 7.09 (t, 2H), 7.06-7.03 (ddd, 2H), 3.99 (s, 6H).

4,4'-(anthracene-9,10-diyl)bis(2-hydroxybenzoic acid) (compound 6) ABHB linker, (adapted from Hirofumi M., Akira S., Yusuke M., Yoshinori I. (2017). WO 2017006638 A1.)

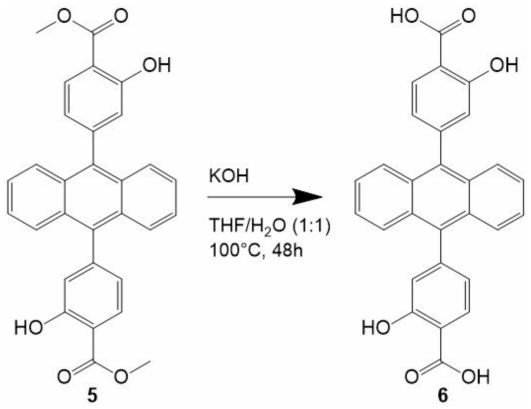

Figure 6.9 – Scheme 3.

Dimethyl 4,4'-(anthracene-9,10-diyl)bis(2-hydroxybenzoate) (compound 5) (300 mg, 0.63 mmol), potassium hydroxide (KOH) (500 mg, 8.9 mmol) and a mixture of THF/H_2O (1:1) (30 mL) were heated in a 100 mL flask under nitrogen atmosphere at 100°C for 48 h. The resulting solution was allowed to cool to room temperature and poured into HCl (200 mL). The solid was filtered off, washed with acetic acid (30 mL), water (500 mL) and MeOH (30 mL) and dried under vacuum, giving a beige powder with 70% yield. ^{1}H NMR (400 MHz, DMSO-d_6) δ (*ppm*): 8.03 (d, 2H), 7.64-7.59 (m, 4H), 7.48-7.43 (m, 4H), 7.03 (s, 2H), 7.02-6.97 (m, 2H), 3.99 (s, 6H). ^{13}C NMR (400 MHz, DMSO-d_6) δ (*ppm*): 171.73 (2C), 161.07 (2C), 145.75 (2C), 135.59 (2C), 130.60 (3C), 128.51 (3C), 126.13 (6C), 125.92 (3C), 122.11 (4C).

Anthracene-based MOF-74 (ANMOF-74) synthesis

ANMOF-74(Zn) 4,4'-(anthracene-9,10-diyl)bis(2-hydroxybenzoic acid) (10.00 mg, 0.022 mmol), $Zn(NO_3)_2 \cdot 4H_2O$ (22.07 mg, 0.084 mmol) and benzoic acid (2.7 mg, 0.022 mmol) were suspended in DMF (1.5 mL). The resulting mixture was sonicated until complete dissolution of the educts was achieved and it was kept in a culture tube at 120°C for 2 days. The resulting precipitate was washed with DMF (2×10 mL) and MeOH (1×10 mL) and activated at 120°C to remove the less volatile solvent to obtain a brownish crystalline powder. The PXRD pattern of the synthesized MOF matches the simulated ANMOF-74 PXRD pattern. Elemental Analysis (vacuum treated): Calculated for $Zn_{18}C_{252}H_{125}O_{63} \cdot$ DMF (%): Zn, 22.04; C, 56.70; H. 2.38; Found (%): Zn, 21.48; C, 56.91; H, 2.57, N, 0.71.

ANMOF-74(Mg) 4,4'-(anthracene-9,10-diyl)bis(2-hydroxybenzoic acid) (10.00 mg, 0.022 mmol) and $Mg(NO_3)_2 \cdot 6H_2O$ (21.60 mg, 0.084 mmol) were suspended in DMF (1.3 mL) and MeOH

(0.2 mL). The resulting mixture was sonicated until complete dissolution of the educts was achieved and it was kept in a culture tube at 120°C for 2 days. The resulting precipitate was washed with DMF (2 × 10 mL) and MeOH (1 × 10 mL) and activated at 120°C to remove the less volatile solvent to obtain a bright beige crystalline powder. The PXRD pattern of the synthesized MOF matches the simulated ANMOF-74 PXRD pattern. Elemental Analysis (vacuum treated): Calculated for $Mg_{18}C_{252}H_{125}O_{63}$ · DMF (%): Mg, 9.51; C, 65.81; H, 2.76; Found (%): Mg, 9.12; C, 66.12; H, 2.97, N, 0.59.

ANMOF-74(Zn) 4,4'-(anthracene-9,10-diyl)bis(2-hydroxybenzoic acid) (10.00 mg, 0.022 mmol), $NiCl_2$ (10.80 mg, 0.084 mmol) and benzoic acid (2.7 mg, 0.022 mmol) were suspended in benzyl alcohol (0.7 mL) and EtOH (0.7 mL) The resulting mixture was sonicated until complete dissolution of the educts was achieved and it was kept in a culture tube at 120°C for 2 days. The resulting precipitate was washed with DMF (2 × 10 mL) and MeOH (1 × 10 mL) and activated at 120°C to remove the less volatile solvent to obtain a green crystalline powder. The PXRD pattern of the synthesized MOF matches the simulated ANMOF-74 PXRD pattern. Elemental Analysis (vacuum treated): Calculated for $Ni_{18}C_{252}H_{125}O_{63}$ · DMF (%): Ni, 20.25; C, 58.00; H. 2.43; Found (%): Ni, 19.37; C, 58.84; H, 2.60, N 0.61.

ANMOF-74(Zn) 4,4'-(anthracene-9,10-diyl)bis(2-hydroxybenzoic acid) (10.00 mg, 0.022 mmol), $Co(NO_3)_2 \cdot 6H_2O$ (24.30 mg, 0.084 mmol) and benzoic acid (2.7 mg, 0.022 mmol) were suspended in DMF (1.1 mL), EtOH (0.3 mL) and H_2O (1 mL). The resulting mixture was sonicated until complete dissolution of the educts was achieved and it was kept in a culture tube at 120°C for 2 days. The resulting precipitate was washed with DMF (2 × 10 mL) and MeOH (1 × 10 mL) and activated at 120°C to remove the less volatile solvent to obtain a pink crystalline powder. The PXRD pattern of the synthesized MOF matches the simulated ANMOF-74 PXRD pattern. Elemental Analysis (vacuum treated): Calculated for $Co_{18}C_{252}H_{125}O_{63}$ · DMF (%): Co, 20.31; C, 57.96; H. 2.43; Found (%): Co, 19.78; C, 58.16; H, 2.79, N, 0.65.

ANMOF-74(Zn) 4,4'-(anthracene-9,10-diyl)bis(2-hydroxybenzoic acid) (10.00 mg, 0.022 mmol) and $MnCl_2 \cdot 4H_2$ O (22.60 mg, 0.084 mmol) were suspended in DMF (1.5 mL). The resulting mixture was sonicated until complete dissolution of the educts was achieved and it was kept in a culture tube at 120°C for 2 days. The resulting precipitate was washed with DMF (2 × 10 mL) and MeOH (1 × 10 mL) and activated at 120°C to remove the less volatile solvent to obtain a light beige crystalline powder. The PXRD pattern of the synthesized MOF matches the simulated ANMOF-74 PXRD pattern. Elemental Analysis (vacuum treated): Calculated for $Mn_{18}C_{252}H_{125}O_{63}$ · DMF (%): Mn, 19.20; C, 58.77; H. 2.47; Found (%): Mn, 18.07; C, 58.94, H, 2.67, N, 0.56.

6.4.3. Characterization

Unit cell parameters and atomic coordinates

ANMOF-74(Zn)

$R_{wp} = 6.74\%$, $R_p = 4.99\%$

R$\bar{3}$ (146) - trigonal

a = b = 46.06 Å, c = 5.78 Å

$\alpha = \beta = 90°$, $\gamma = 120°$

Table 17 – Atoms positions in the unit cell of ANMOF-74(Zn)

Atom	x/a	y/b	z/c
O1	0.6465	0.6054	-0.1318
O2	0.6262	0.6377	0.0040
O3	0.6388	0.6434	0.4834
O4	0.3912	0.3476	1.6885
O5	0.3647	0.3616	0.9242
O6	0.3606	0.3515	1.3502
Zn7	0.6542	0.6711	0.1483
O8	0.3593	0.389	1.5693
Zn9	0.3506	0.3453	1.6414
C10	0.6163	0.6077	0.4376
C11	0.5890	0.5870	0.5889
C12	0.5687	0.5518	0.5495
C13	0.5772	0.5377	0.3678
C14	0.6015	0.5577	0.2096
C15	0.4166	0.4155	0.8479
C16	0.3885	0.3933	0.9881
C17	0.4051	0.4386	1.2642
C18	0.4312	0.4604	1.1229
C19	0.4385	0.4493	0.9190
C20	0.4709	0.4741	0.8078
C21	0.5002	0.4726	0.8493
C22	0.5323	0.4991	0.7803
C23	0.5361	0.5282	0.6700
C24	0.5068	0.5299	0.6302
C25	0.4747	0.5033	0.6996
C26	0.4464	0.5063	0.6562
C27	0.4493	0.5342	0.5447
C28	0.4804	0.5598	0.4744
C29	0.5088	0.5088	0.5165
C30	0.5165	0.4961	0.8249

Table 17 – Atoms positions in the unit cell of ANMOF-74(Zn)

Atom	x/a	y/b	z/c
C31	0.5577	0.4681	0.9369
C32	0.5265	0.4426	1.0065
C33	0.4981	0.4448	0.9632
C34	0.6286	0.6102	0.0372
C35	0.6180	0.5924	0.2302
C36	0.3671	0.3823	1.3633
C37	0.3853	0.4053	1.1998

ANMOF-74(Mg)

$R_{wp} = 6.96\%$, $R_p = 5.16\%$

R$\mathcal{3}$ (146) - trigonal

a = b = 46.36 Å, c = 6.05 Å

$\alpha = \beta = 90°$, $\gamma = 120°$

Table 18 – Atoms positions in the unit cell of ANMOF-74(Mg)

Atom	x/a	y/b	z/c
O1	0.6465	0.6054	-0.1318
O2	0.6262	0.6377	0.0040
O3	0.6388	0.6434	0.4834
O4	0.3912	0.3476	1.6885
O5	0.3647	0.3616	0.9242
O6	0.3606	0.3515	1.3502
Mg7	0.6542	0.6711	0.1483
O8	0.3593	0.389	1.5693
Mg9	0.3506	0.3453	1.6414
C10	0.6163	0.6077	0.4376
C11	0.5890	0.5870	0.5889
C12	0.5687	0.5518	0.5495
C13	0.5772	0.5377	0.3678
C14	0.6015	0.5577	0.2096
C15	0.4166	0.4155	0.8479
C16	0.3885	0.3933	0.9881
C17	0.4051	0.4386	1.2642
C18	0.4312	0.4604	1.1229
C19	0.4385	0.4493	0.9190
C20	0.4709	0.4741	0.8078
C21	0.5002	0.4726	0.8493
C22	0.5323	0.4991	0.7803

Table 18 – Atoms positions in the unit cell of ANMOF-74(Mg)

Atom	x/a	y/b	z/c
C23	0.5361	0.5282	0.6700
C24	0.5068	0.5299	0.6302
C25	0.4747	0.5033	0.6996
C26	0.4464	0.5063	0.6562
C27	0.4493	0.5342	0.5447
C28	0.4804	0.5598	0.4744
C29	0.5088	0.5088	0.5165
C30	0.5165	0.4961	0.8249
C31	0.5577	0.4681	0.9369
C32	0.5265	0.4426	1.0065
C33	0.4981	0.4448	0.9632
C34	0.6286	0.6102	0.0372
C35	0.6180	0.5924	0.2302
C36	0.3671	0.3823	1.3633
C37	0.3853	0.4053	1.1998

ANMOF-74(Ni)

$R_{wp} = 3.94\%$, $R_p = 3.15\%$

R$\mathcal{3}$ (146) - trigonal

a = b = 46.36 Å, c = 6.05 Å

$\alpha = \beta = 90°$, $\gamma = 120°$

Table 19 – Atoms positions in the unit cell of ANMOF-74(Ni)

Atom	x/a	y/b	z/c
O1	0.6465	0.6054	-0.1318
O2	0.6262	0.6377	0.0040
O3	0.6388	0.6434	0.4834
O4	0.3912	0.3476	1.6885
O5	0.3647	0.3616	0.9242
O6	0.3606	0.3515	1.3502
Mg7	0.6542	0.6711	0.1483
O8	0.3593	0.389	1.5693
Mg9	0.3506	0.3453	1.6414
C10	0.6163	0.6077	0.4376
C11	0.5890	0.5870	0.5889
C12	0.5687	0.5518	0.5495
C13	0.5772	0.5377	0.3678
C14	0.6015	0.5577	0.2096

Table 19 – Atoms positions in the unit cell of ANMOF-74(Ni)

Atom	x/a	y/b	z/c
C15	0.4166	0.4155	0.8479
C16	0.3885	0.3933	0.9881
C17	0.4051	0.4386	1.2642
C18	0.4312	0.4604	1.1229
C19	0.4385	0.4493	0.9190
C20	0.4709	0.4741	0.8078
C21	0.5002	0.4726	0.8493
C22	0.5323	0.4991	0.7803
C23	0.5361	0.5282	0.6700
C24	0.5068	0.5299	0.6302
C25	0.4747	0.5033	0.6996
C26	0.4464	0.5063	0.6562
C27	0.4493	0.5342	0.5447
C28	0.4804	0.5598	0.4744
C29	0.5088	0.5088	0.5165
C30	0.5165	0.4961	0.8249
C31	0.5577	0.4681	0.9369
C32	0.5265	0.4426	1.0065
C33	0.4981	0.4448	0.9632
C34	0.6286	0.6102	0.0372
C35	0.6180	0.5924	0.2302
C36	0.3671	0.3823	1.3633
C37	0.3853	0.4053	1.1998

ANMOF-74(Co)

$R_{wp} = 3.94\%$, $R_p = 3.15\%$

R$\bar{3}$ (146) - trigonal

a = b = 46.36 Å, c = 6.05 Å

$\alpha = \beta = 90°$, $\gamma = 120°$

Table 20 – Atoms positions in the unit cell of ANMOF-74(Co)

Atom	x/a	y/b	z/c
O1	0.6465	0.6054	-0.1318
O2	0.6262	0.6377	0.0040
O3	0.6388	0.6434	0.4834
O4	0.3912	0.3476	1.6885
O5	0.3647	0.3616	0.9242
O6	0.3606	0.3515	1.3502
Mg7	0.6542	0.6711	0.1483

Table 20 – Atoms positions in the unit cell of ANMOF-74(Co)

Atom	**x/a**	**y/b**	**z/c**
O8	0.3593	0.389	1.5693
Mg9	0.3506	0.3453	1.6414
C10	0.6163	0.6077	0.4376
C11	0.5890	0.5870	0.5889
C12	0.5687	0.5518	0.5495
C13	0.5772	0.5377	0.3678
C14	0.6015	0.5577	0.2096
C15	0.4166	0.4155	0.8479
C16	0.3885	0.3933	0.9881
C17	0.4051	0.4386	1.2642
C18	0.4312	0.4604	1.1229
C19	0.4385	0.4493	0.9190
C20	0.4709	0.4741	0.8078
C21	0.5002	0.4726	0.8493
C22	0.5323	0.4991	0.7803
C23	0.5361	0.5282	0.6700
C24	0.5068	0.5299	0.6302
C25	0.4747	0.5033	0.6996
C26	0.4464	0.5063	0.6562
C27	0.4493	0.5342	0.5447
C28	0.4804	0.5598	0.4744
C29	0.5088	0.5088	0.5165
C30	0.5165	0.4961	0.8249
C31	0.5577	0.4681	0.9369
C32	0.5265	0.4426	1.0065
C33	0.4981	0.4448	0.9632
C34	0.6286	0.6102	0.0372
C35	0.6180	0.5924	0.2302
C36	0.3671	0.3823	1.3633
C37	0.3853	0.4053	1.1998

ANMOF-74(Mn)

$R_{wp} = 4.38\%$, $R_p = 2.80\%$

R$\mathcal{3}$ (146) - trigonal

a = b = 46.21 Å, c = 5.69 Å

$\alpha = \beta = 90°$, $\gamma = 120°$

Table 21 – Atoms positions in the unit cell of ANMOF-74(Mn)

Atom	**x/a**	**y/b**	**z/c**

Table 21 – Atoms positions in the unit cell of ANMOF-74(Mn)

Atom	**x/a**	**y/b**	**z/c**
O1	0.6465	0.6054	-0.1318
O2	0.6262	0.6377	0.0040
O3	0.6388	0.6434	0.4834
O4	0.3912	0.3476	1.6885
O5	0.3647	0.3616	0.9242
O6	0.3606	0.3515	1.3502
Mg7	0.6542	0.6711	0.1483
O8	0.3593	0.389	1.5693
Mg9	0.3506	0.3453	1.6414
C10	0.6163	0.6077	0.4376
C11	0.5890	0.5870	0.5889
C12	0.5687	0.5518	0.5495
C13	0.5772	0.5377	0.3678
C14	0.6015	0.5577	0.2096
C15	0.4166	0.4155	0.8479
C16	0.3885	0.3933	0.9881
C17	0.4051	0.4386	1.2642
C18	0.4312	0.4604	1.1229
C19	0.4385	0.4493	0.9190
C20	0.4709	0.4741	0.8078
C21	0.5002	0.4726	0.8493
C22	0.5323	0.4991	0.7803
C23	0.5361	0.5282	0.6700
C24	0.5068	0.5299	0.6302
C25	0.4747	0.5033	0.6996
C26	0.4464	0.5063	0.6562
C27	0.4493	0.5342	0.5447
C28	0.4804	0.5598	0.4744
C29	0.5088	0.5088	0.5165
C30	0.5165	0.4961	0.8249
C31	0.5577	0.4681	0.9369
C32	0.5265	0.4426	1.0065
C33	0.4981	0.4448	0.9632
C34	0.6286	0.6102	0.0372
C35	0.6180	0.5924	0.2302
C36	0.3671	0.3823	1.3633
C37	0.3853	0.4053	1.1998

Powder X-ray diffraction

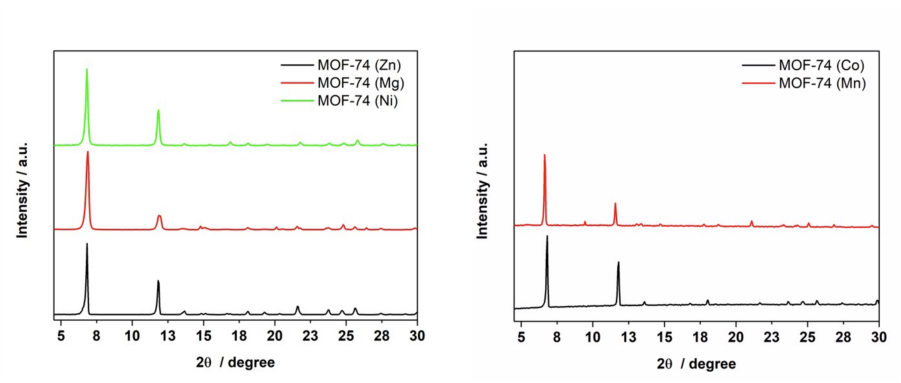

Figure 6.10 – PXRD patterns of the MOF-74(M) bulk materials.

Scanning-electron microscopy

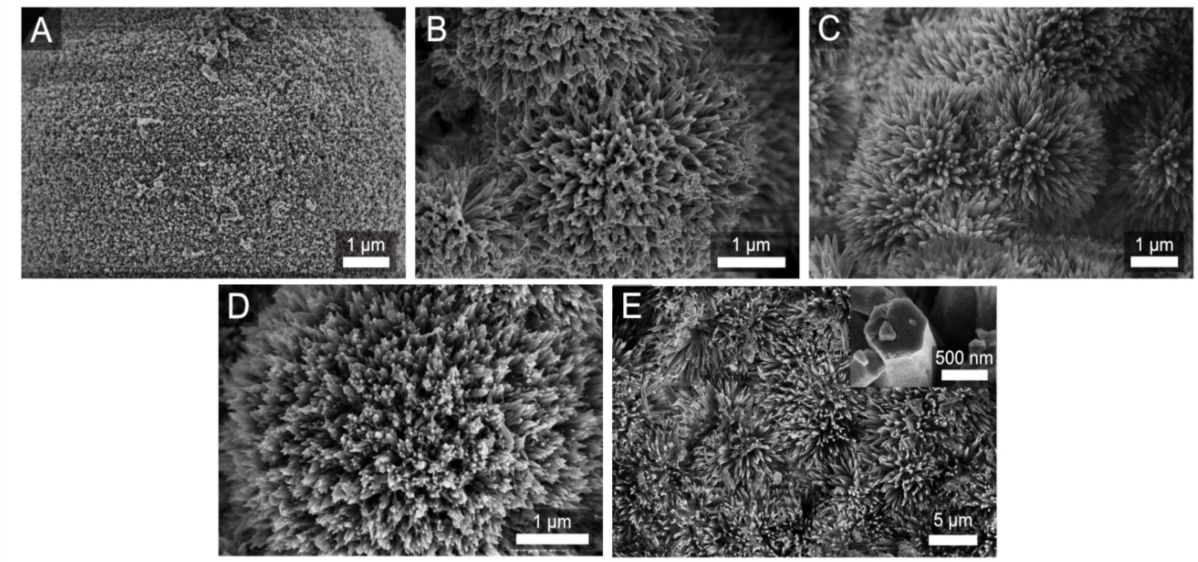

Figure 6.11 – SEM images of the ANMOF-74 bulk materials (A) ANMOF-74(Zn), (B) ANMOF- 74(Mg), (C) ANMOF-74(Ni), (D) ANMOF-74(Co), (E) ANMOF-74(Mn) and a close-up of a hexagonally shaped monolith depicted as inset.

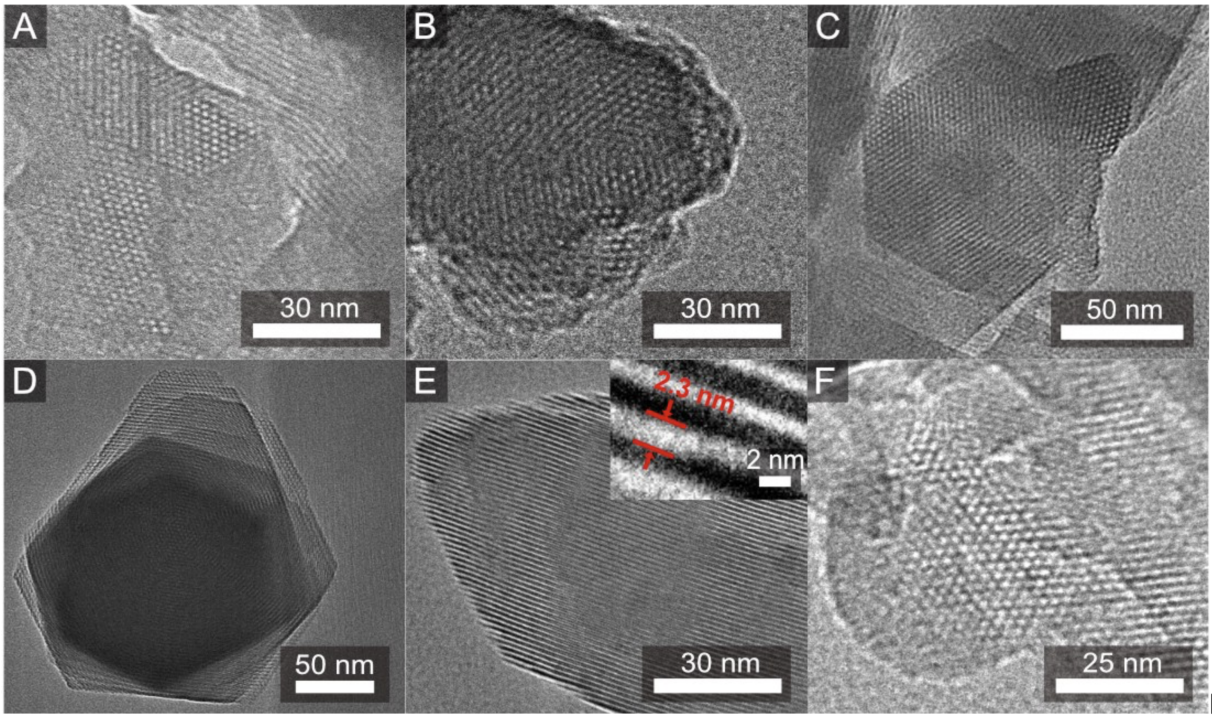

Figure 6.12 – High resolution TEM images of the ANMOF-74(M) series in [001] orientation showing (A) the Zn-, (B) Mg-, (C) Ni-, (D) Co-, (F) Mn-ANMOF-74 materials, respectively. (E) High resolution TEM image of ANMOF-74(Co) in side view showing a close-up of the lattice planes as inset.

UV-VIS spectroscopy and photoluminescence of the ABHB linker

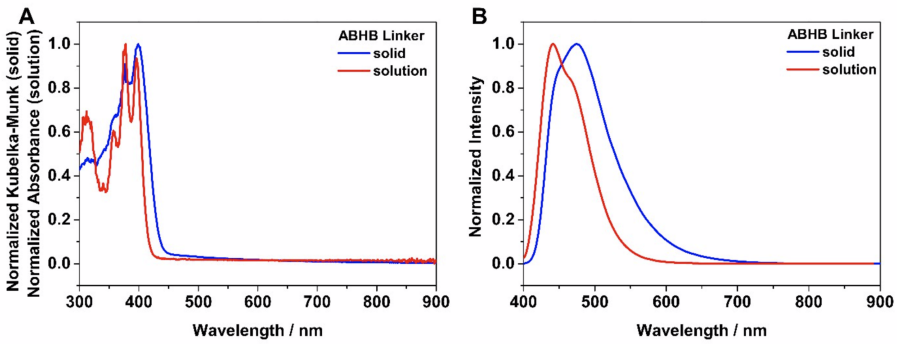

Figure 6.13 – (A) Comparison of the absorption and diffuse reflectance spectra of the ABHB linker in $CHCl_3$ solution (red) and as solid dispersed in $BaSO_4$ (blue). (B) PL spectra of the ABHB linker measured with pulsed 378 nm excitation in $CHCl_3$ solution (red) and as solid (blue).

Tauc plots of the ANMOF-74 series

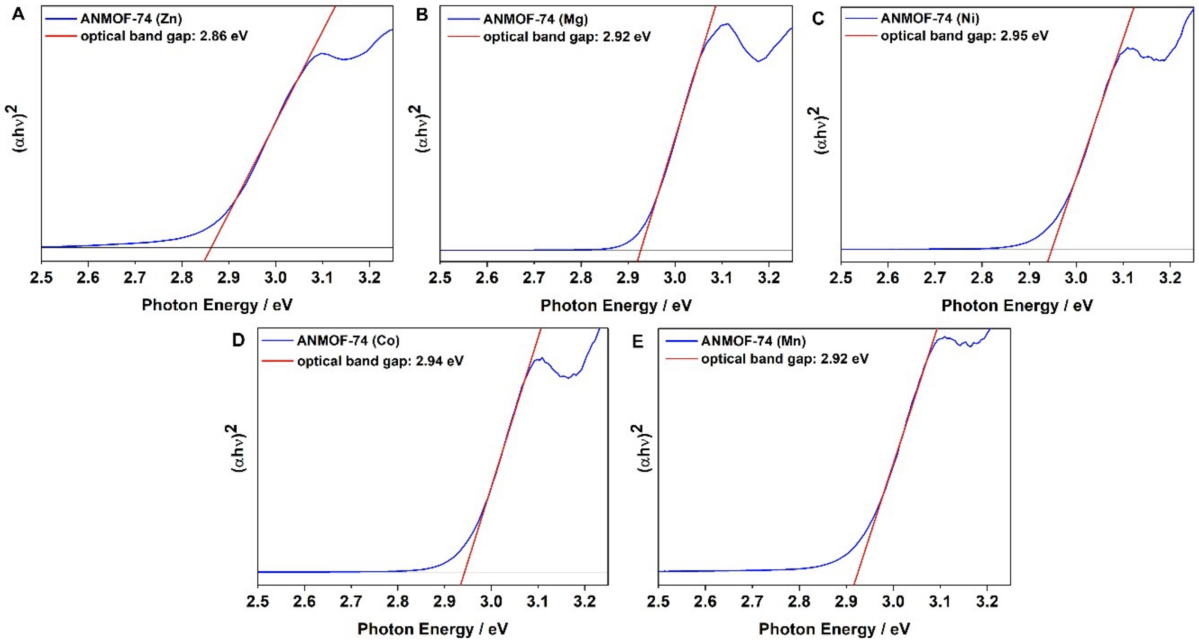

Figure 6.14 – Tauc plots of ANMOF-74(Zn) (A), ANMOF-7(Mg) (B), ANMOF-74 (Ni) (C), ANMOF-74(Co) (D) and ANMOF-74(Mn) (E), suggesting the presence of direct band gaps.

Time-correlated single photon counting (TCSPC) traces

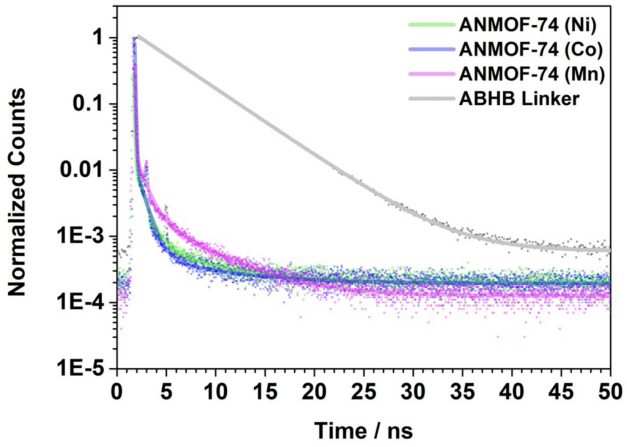

Figure 6.15 – The time-correlated single photon counting (TCSPC) traces corresponding to the PL spectra of ANMOF-74(Ni), ANMOF-74(Co) and ANMOF-74(Mn) as solids and of the ABHB linker in solution which were recorded at the respective emission maximum of each material. The solid lines represent the exponential fits.

Table 22 – The PL lifetimes (τ) of the ANMOF-74(M) series and of the ABHB linker, obtained from triexponential fits (see Figure S5 and 6) the TCSPC traces of the MOFs and from a monoexpontial fit of the TCSPC trace of the ABHB linker, as well as the error and the fractional intensities in percentages, which are the fractions of emitted photons corresponding to the respective lifetimes. We note that the stated error is the fitting error and that it does not necessarily reflect the actual resolution of the setup of around 100 ps.

Sample		τ	**error / ns**	**fract. intensity / %**
ANMOF-74(Zn)	τ_1	0.162	±0.012	22.9
	τ_2	0.79	±0.03	59.5
	τ_3	3.4	±0.2	17.6
ANMOF-74(Mg)	τ_1	0.169	±0.006	28.7
	τ_2	1.03	±0.02	50.0
	τ_3	4.9	±0.12	21.3
ANMOF-74(Ni)	τ_1	0.065	±0.004	55.3
	τ_2	0.80	±0.06	31.9
	τ_3	5.6	±1.0	12.8
ANMOF-74(Co)	τ_1	0.064	±0.003	80.5
	τ_2	0.89	±0.06	15.5
	τ_3	5.1	±0.4	4.0
ANMOF-74(Mn)	τ_1	0.065	±0.003	48.3
	τ_2	0.89	±0.06	28.8
	τ_3	5.1	±0.4	22.9
Anthracene (Monomer)	τ	4.32	±0.011	100

Photoluminescence quantum yield (PLQY) and CIE color space

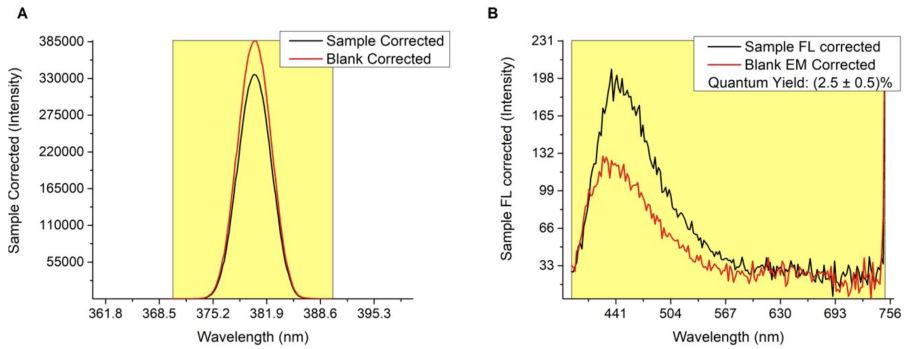

Figure 6.16 – Photoluminescence quantum yield (PLQY) measurement of ANMOF-74(Mg). Rayleigh peak (A) and emission (B) data with integration boundaries.

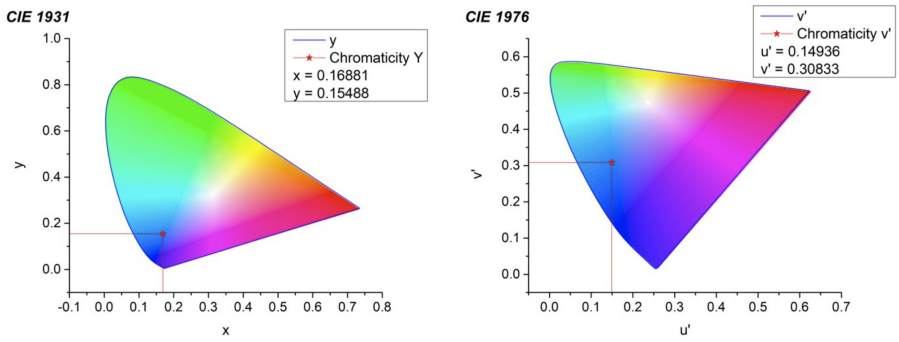

Figure 6.17 – CIE 1931 and CIE 1976 color spaces with the ANMOF-74(Mg) emission and the respective coordinates.

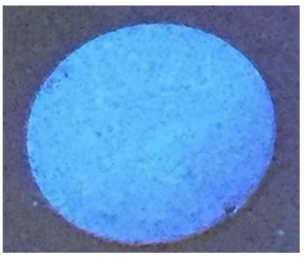

Figure 6.18 – Photo image of a ANMOF-74(Mg) pellet during irradiation with a 365 nm wavelength.

Thermogravimetric analysis (TGA) of the ANMOF-74 series

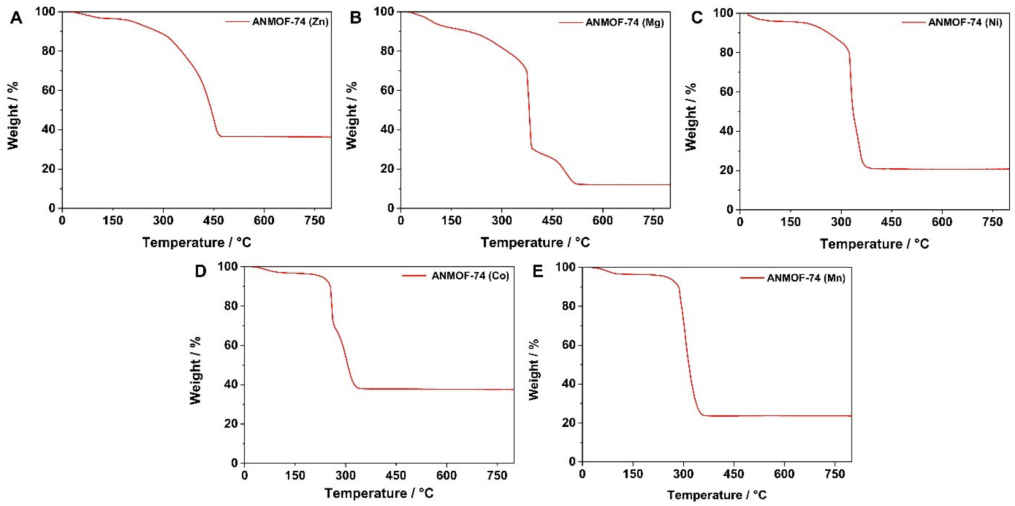

Figure 6.19 – Thermogravimetric Analysis (TGA) of (A) ANMOF-74(Zn), (B) ANMOF-74(Mg), (C), ANMOF-74(Ni), (D) ANMOF-74(Co) and (E) ANMOF-74(Mn) measured as bulk materials (20 mg).

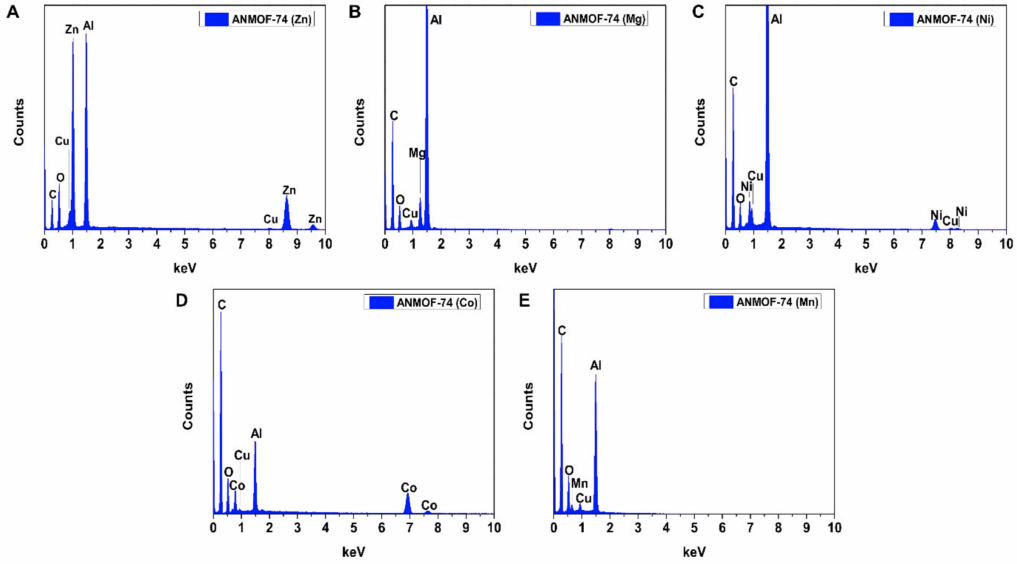

Figure 6.20 – Energy dispersive X-ray (EDX) spectra of (A) ANMOF-74(Zn), (B) ANMOF-74(Mg), (C), ANMOF-74(Ni), (D) ANMOF-74(Co) and (E) ANMOF-74(Mn), measured as bulk materials on an SEM sample holder.

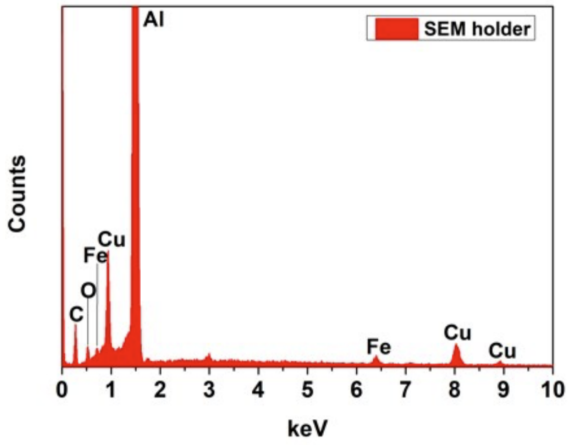

Figure 6.21 – Energy dispersive X-ray (EDX) spectrum of the SEM sample holder.

X-ray photoelectron spectroscopy (XPS) of the ANMOF-74 series

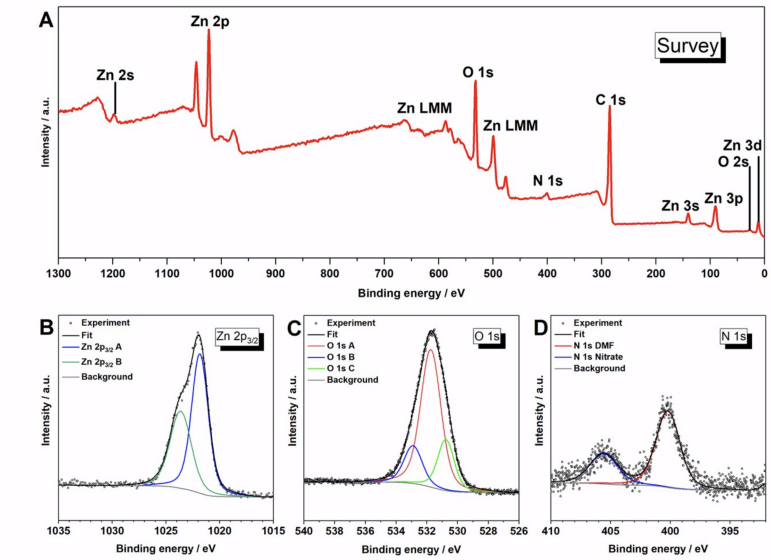

Figure 6.22 – XPS spectra of ANMOF-74(Zn) powder: (A) survey scan, (B) Zn 2p spectrum, (C) O 1s spectrum and (D) N 1s spectrum.

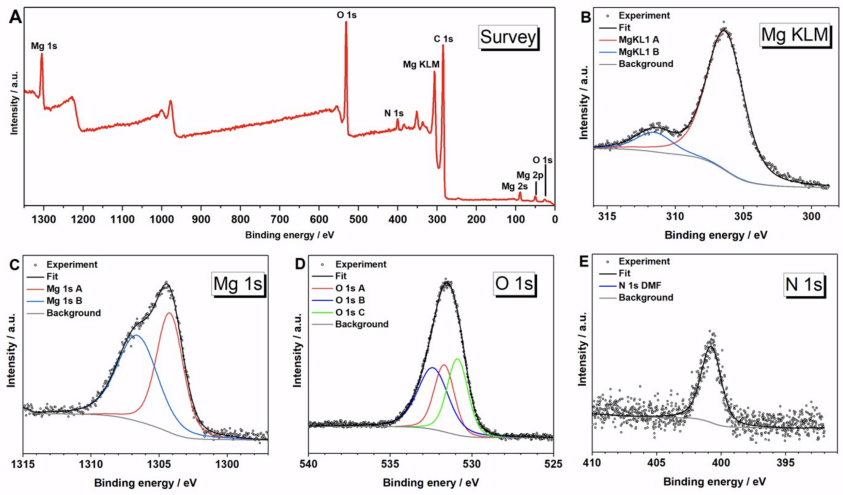

Figure 6.23 – XPS spectra of ANMOF-74(Mg) powder: (A) survey scan, (B) Mg 2p spectrum, (C) O 1s spectrum and (D) N 1s spectrum.

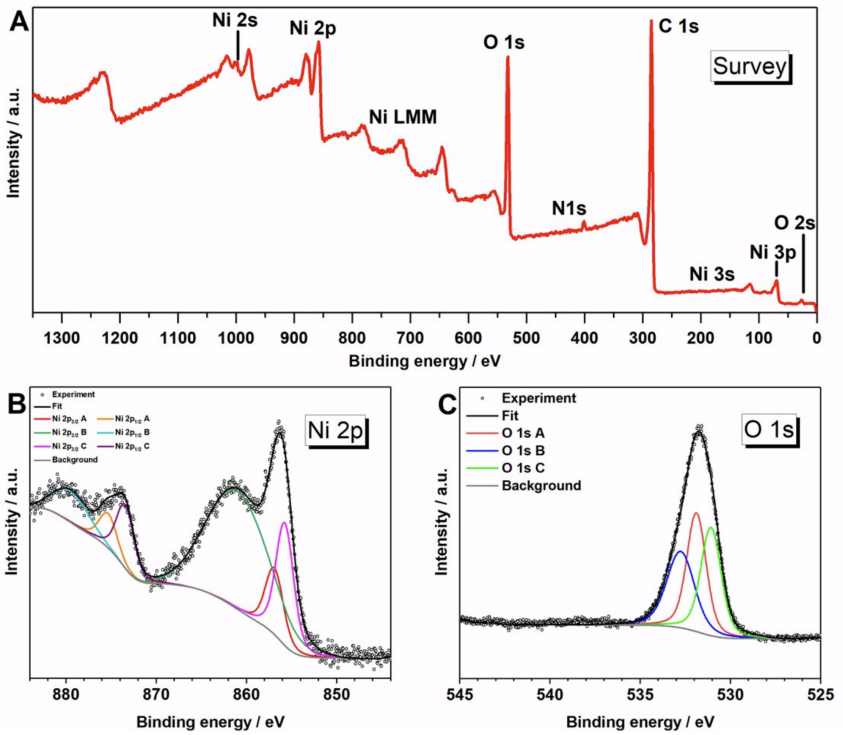

Figure 6.24 – XPS spectra of ANMOF-74(Ni) powder: (A) survey scan, (B) Ni 2p spectrum, (C) O 1s spectrum.

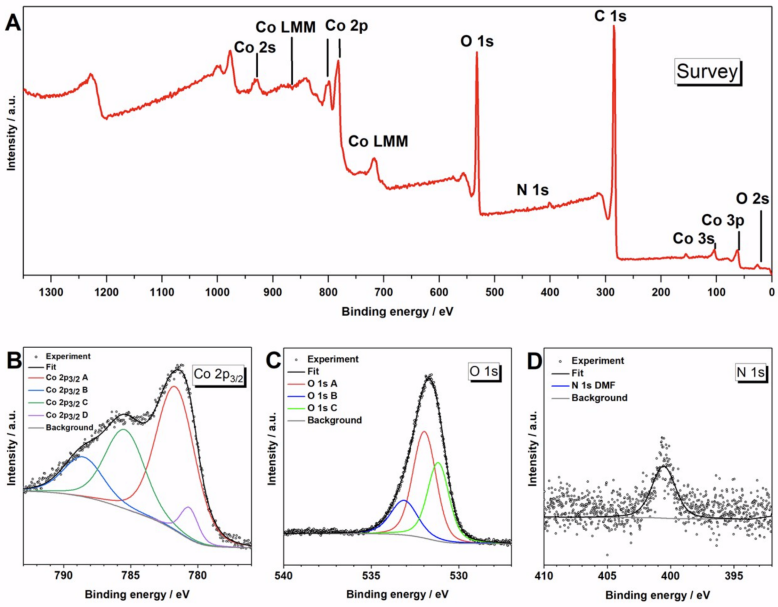

Figure 6.25 – XPS spectra of ANMOF-74(Co) powder: (A) survey scan, (B) Co 2p spectrum, (C) O 1s spectrum and (D) N 1s spectrum.

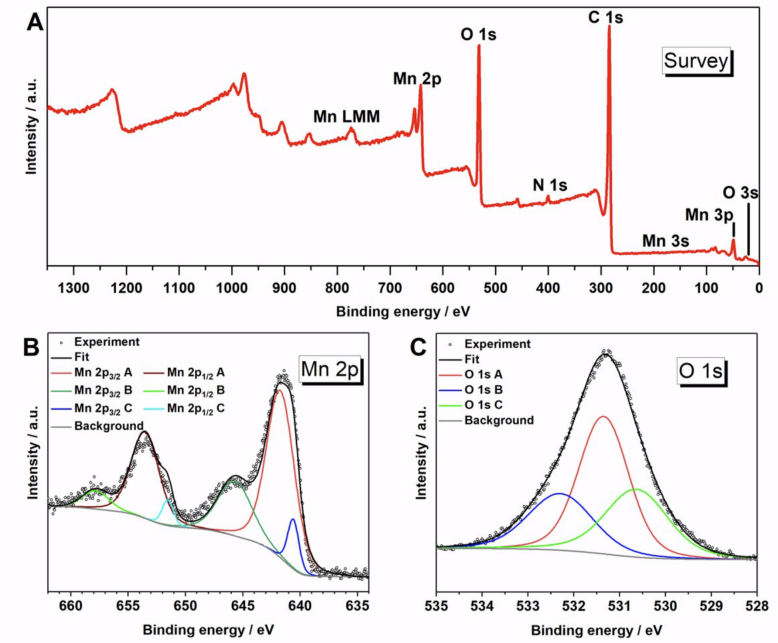

Figure 6.26 – XPS spectra of ANMOF-74(Mn) powder: (A) survey scan, (B) Mn 2p spectrum, (C) O 1s spectrum and (D) N 1s spectrum.

7. An electrically conducting three-dimensional iron-catecholate porous framework

This chapter is based on the following publication:

Andre Mähringer[a,†], Markus Döblinger[a,†], Matthias Hennemann[e,†], Christoph Gruber[a], Dominik Fehn[d], Pouya Hosseini[b], Julian Rotter[a], Irina Santourian[c], Alfred Schirmacher[c], Gunther Wittstock[b], Karsten Meyer[d],Timothy Clark[e], Thomas Bein[a,*], and Dana D. Medina.[b,*] *Submitted.*

[a]Department of Chemistry, Ludwig-Maximilians-Universität (LMU) & Center for NanoScience (CeNS), Butenandtstr. 11, 81377 Munich, Germany.

[b] School of Mathematics and Science, Department of Chemistry, Carl von Ossietzky University of Oldenburg, 26111 Oldenburg, Germany.

[c]Physikalisch-Technische Bundesanstalt Braunschweig und Berlin, Bundesallee 100, 38116 Braunschweig, Germany.

[d]Friedrich-Alexander University Erlangen-Nürnberg (FAU), Department of Chemistry & Pharmacy, Egerlandstr. 1 D-91058 Erlangen, Germany.

[e]Friedrich-Alexander University Erlangen-Nürnberg (FAU), Computer-Chemistry-Center, Department of Chemistry & Pharmacy, Naegelsbachstr. 25, 91052 Erlangen, Germany.

[†]The authors contributed equally to this work.

[*]Corresponding Author.

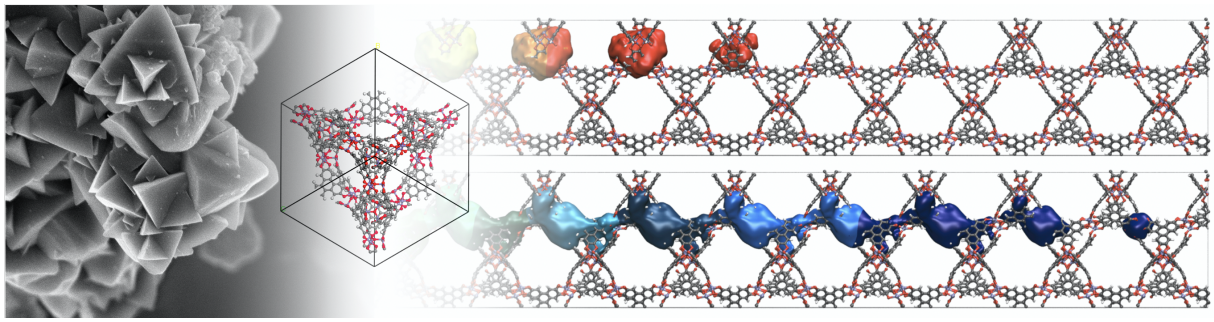

Andre Mähringer designed and coordinated the project. He carried out the experimental synthesis and the structural characterization of the Fe-CAT material.

Abstract

Incorporating electrical conductivity in lightweight, ordered and highly porous materials leads to a new class of electroactive materials. Here, we report the synthesis of a cubic metal-organic framework (MOF) comprising of hexahydroxytriphenylene units and Fe^{III} ions, the Fe-CAT MOF. The MOF is synthesized under solvothermal reaction conditions, yielding a highly crystalline, fine and dark-colored powder. The Fe-CAT MOF crystallites feature tetrahedral morphology and are 300-500 nm in size. Structure analysis and solution using the simulated annealing approach of Fe-CAT MOF followed by density-functional theory refinement of the structure reveal a cubic structure of supertetrahedra arranged in a diamond (dia) topology. Nitrogen sorption analysis indicates a highly porous material with a surface area exceeding 1400 m^2 g^{-1}. Furthermore, the combination of iron ions and semiquinone organic building blocks results in a broadband absorption from 475 nm up to 1900 nm, covering most of the visible range and reaching the near IR region. Reflection grade measurements reveal an excellent absorption capability of 98.5% of the incoming light over the visible spectral region up to 800 nm. Electrical conductivity measurements in the form of pressed pellets reveal a high intrinsic electrical conductivity up to 10^{-3} S cm^{-1}. Quantum mechanical calculation suggest Fe-CAT to be an efficient electron conductor that exhibits continuous charge-carrier pathways through the structure. This report expands the paradigm of intrinsically electroactive three-dimensional metal-organic frameworks, and thus serves as a solid basis for the development of novel highly porous, ordered frameworks with enhanced electrical conductivity.

7.1. Introduction

In recent years, electrical conductivity has been added to the property portfolio of metal-organic framework (MOF) materials.[1–3] This exciting new feature in combination with the central properties of MOFs, high crystallinity and porosity, is expected to pave the way for new horizons in fields such as charge storage, sensing and photovoltaic materials.[4–8] Generally, the vast majority of the MOFs that have been synthesized and characterized exhibits superior properties, either in crystallinity and porosity or in charge migration. Discovering framework materials that feature high porosity and crystallinity paired with electrical conductivity remains a prodigious challenge. To date, electrically conducting MOFs are mainly 2D layered structures, where charge migration occurs via both through-space and through-bond mechanisms.[9–11] Most prominent of these materials is the metal catecholate, M-CAT-1 series consisting of hexahydroxytriphenylene (HHTP) moieties and metal counterparts such as Co^{II}, Ni^{II} or Cu^{II}.[12,13] This family of 2D layered materials crystallizes in a hexagonal symmetry as rod-like crystallites on the nanoscale,

and they additionally feature microporosity with Brunauer-Emmett-Teller (BET) surface areas reaching $350\,m^2\ g^{-1}$. Furthermore, four-point probe electrical conductivity measurements on Cu-CAT-1 single crystals revealed values of up to $0.1\,S\ cm^{-1}$, among the highest reported for a non-doped MOF. The family of layered catecholate-based MOFs was recently extended by employing the rare-earth metals La, Nd, Ho, and Yb in the synthesis. In this series, the lanthanide ions interconnect to the planar ligands into a 3D framework through "out-of-plane" metal-oxo chains. By using rare-earth metals with different ionic radii, a fine-tuning of the stacking distances was achieved. This allowed control over charge-transport perpendicular to the sheets, with the reported electrical conductivity reaching 10^{-5} S cm^{-1}.[14] Exchanging the hydroxyl functionalities of the triphenylene core with amino or thiol groups results in electron-rich building blocks such as 2,3,6,7,10,11-triphenylenehexathiol (THT) or the 2,3,6,7,10,11-hexaminotriphenylene (HATP). Diverse layered frameworks can be obtained by combining these building blocks with 3d transition metals to give record-breaking electrical conductivity reaching $2500\,S\ cm^{-1}$ or absorption shifted into the near IR region.[15–18]. A prominent example is the π-d conjugated $Fe_3(THT)_2(NH_4)_3$, which shows room-temperature charge-carrier mobility up to $220\,cm^2\ V^{-1}\ s^{-1}$ and electrical conductivity values of $0.1\,S\ cm^{-1}$.[5,19] In contrast to their superior electronic properties, these materials feature relatively poor crystallinity and porosity, which is attributed to a high reactive precursor reactivity. However, while electroactive 2D MOFs are well established, electroactive 3D MOFs are largely unknown, thereby imposing a great challenge for their discovery and use.

Particularly interesting is encoding high electrical conductivity in highly porous 3D structures in which charge carriers are expected to be transported mainly through bonds. Examples of conducting 3D frameworks remain very rare in the literature and are mostly centered on mixed-valency iron MOFs.[20–22] One strategy for implementing mixed valency in 3D frameworks was introduced in 2018 by systematically changing the redox state of iron ions in the structure. Here, $K_xFe_2(BDP)_3$ ($0<x<2$; BDP^{2-} = 1,4-benzenedipyrazolate) was obtained by fractional reduction of $Fe_2(BDP)_3$ with potassium naphthalenide, resulting in a two-point probe conductivity increase from $3.5 \times 10^{-7}\,S\ cm^{-7}$ to $0.015\,S\ cm^{-1}$ measured for single crystals.[23] In another approach, iron ions in $Fe_2(BDP)_3$ (BDT = 5,5'-(1,4-phenylene)bis(*1H*-tetrazole)) were oxidized upon exposure to ambient atmosphere to give a mixed valency framework with tunable single-crystal conductivity ranging from 10^{-5} to $1\,S\ cm^{-1}$. A different pathway for introducing mixed valency in 3D frameworks is the integration of redox-active organic building blocks. In this context, Long and coworkers introduced a ferric semiquinoid MOF.[22] This cubic material is composed of FeIII and mixed-valence 2,5-dioxidobenzoquinones that exhibit a conductivity of $0.16\,S\ cm^{-1}$. However, no porosity could be determined. In 2015, Yaghi and coworkers pioneered the 3D M-CAT family by synthesizing Fe-CAT-5, the first 3D catecholate-based frameworks that show ultrahigh proton conductivity ($5.0 \times 10^{-2}\,S\ cm^{-1}$).[24] The structure of Fe-CAT-5 is built from iron and HHTP

bridging units that form a 2-fold interpenetrating network with *srs* topology in which sulfate and dimethylammonium ions are part of the framework. Although these frameworks conduct protons well at higher relative humidity, their electrical conductivity remains unknown. Recently, Dinca and co-workers reported the synthesis of cubic faujasite-like rare-earth-metal HHTP MOFs with intrinsic electrical conductivity values of up to 10^{-5} to 1 S cm^{-1}.[25] Nevertheless, to date, the combination of the transition metal iron with the well-known HHTP building unit to give a non-interpenetrating 3D catecholate-based framework with a defined structure, high porosity and high intrinsic conductivity remains elusive.

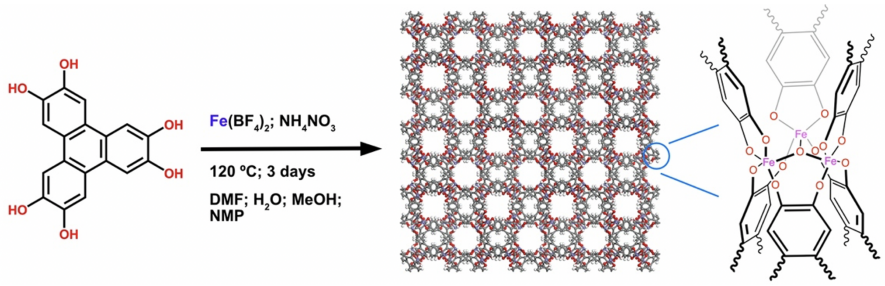

Figure 7.1 – Synthesis scheme of 2,3,6,7,10,11-hexahydroxytriphenylene and an Fe^{II} precursor yielding Fe-CAT. The reaction was conducted under solvothermal synthesis conditions. Fe-CAT shows a cubic porous structure with iron oxo clusters bridging the triphenylene building blocks.

We now present the synthesis of a novel metal-organic framework coined Fe-CAT comprising the trigonal planar building block, 2,3,6,7,10,11-hexahydroxytriphenylene, and Fe^{III} ions (see Figure 7.1). Fe-CAT features a pitch-black color and a ferric catecholate structure within a highly symmetric 3D cubic geometry with the space group F*32*, as interpreted by combining powder X-ray diffraction (PXRD) data, transmission electron microscopy (TEM) analysis, energy-dispersive X-ray spectroscopy (EDX) and structural density-functional theory (DFT) calculations. Furthermore, the microporous Fe-CAT is highly porous with a BET surface area exceeding 1400 m^2 g^{-1}. Total hemispherical reflectance measurements of an Fe-CAT pellet show a broad absorption covering almost the entire UV-VIS and near-IR regions, yielding a total absorption of 98.5% up to 800 nm. Van der Pauw measurements reveal record-breaking intrinsic electrical conductivity values of up to 10^{-3} S cm^{-1} for a 3D MOF. Zero-field ^{57}Fe-Mössbauer, electron paramagnetic resonance (EPR) spectroscopy and superconducting quantum interference devices (SQUID) magnetization analysis in combination with X-ray photoelectron spectroscopy (XPS) measurements were employed to study the iron valency in the framework. Quantum mechanical calculations show that Fe-CAT is an efficient electron conductor but that it cannot transport holes because it exhibits no continuous paths for hole-transport. These findings were resolved by means of direct semiempirical molecular-orbital molecular dynamics (MD). This interesting

combination of properties underlines that 3D frameworks can provide efficient through-bond charge-carrier migration pathways and at the same time remain highly porous and crystalline.

7.2. Results and discussion

Synthesis procedure. Fe-CAT was synthesized under solvothermal reaction conditions. Briefly, $FeBF_4 \cdot 6\,H_2O$ and 2,3,6,7,10,11-hexahydroxytriphenylene precursors were added to a solvent mixture of DMF (dimethylformamide), MeOH (methanol), NMP (*N*-methyl-2-pyrrolidone), water and tetrabutylammonium nitrate (NBu_4NO_3) crystallization additive under argon atmosphere (Figure 7.2). The reaction mixture was sealed under inert conditions and transferred to a preheated oven at 120°C for 48 h. After the given reaction period, the reaction tube was retrieved and upon cooling to room temperature a dark black microcrystalline material was isolated and subsequently activated under dynamic vacuum prior to analysis (for more details see Appendix).

Structure Solution. Powder X-ray diffraction (PXRD) patterns feature sharp reflections up to high 2θ values (20°, see Figure 7.2A) demonstrating the presence of a highly crystalline product. Scanning electron microscopy (SEM) analysis reveals tetrahedral and faceted intergrown crystallites, exhibiting edge-to-edge distances of 400 to 500 nm (see Figure 7.2E, S7.8). Typically, the angles between facets of the tetrahedra observed were around 72°. TEM analysis shows crystalline domains whose faces and lattice planes (d=19 Å) also enclose angles of around 71° (see Figure 7.2F, Table 7.8). These findings suggest a cubic crystal structure whose (111) planes typically intersect at angles of 70.5°. Compositional analysis by TEM and SEM showed the presence of Fe, O and C, with residual amounts of nitrogen. In the absence of a single crystal, further structural characterization was carried out by means of PXRD. In accordance with the above observations, the MOF powder diffraction pattern can be fully indexed in the cubic crystal system with a lattice constant of a = 32.92 (±0.01) Å using the X-cell program and the reflex module from Materials Studio 7.0.[26] The most prominent reflection of the diffraction pattern at 2.1° 2θ is the (111) reflection, whose d-value of 19.01 Å was also observed by TEM. The structure was solved in the space group $F4_132$ by simulated annealing using the program package EXPO2014.[27,28] Subsequently, this structure model was subjected to force field geometry optimization and Rietveld refinement.[29,30] As different structural variants in the $F4_132$ space group, particularly at the metal ligand node, lead to similarly good R_{wp}-values of around 2.5%, the structure was optimized with DFT within the fixed lattice constraints, leading to a final structure model with space group F*23* (Figure 7.2). The average composition determined by EDX spectroscopy (see Figure 7.9, Table 24), $C_{63.1}O_{29.0}Fe_{7.9}$ is close to the nominal refined composition of this structure model $C_{63.2}O_{31.4}Fe_{5.3}$ (without considering hydrogen). For more information, see the chapter Structure solution in the Appendix).

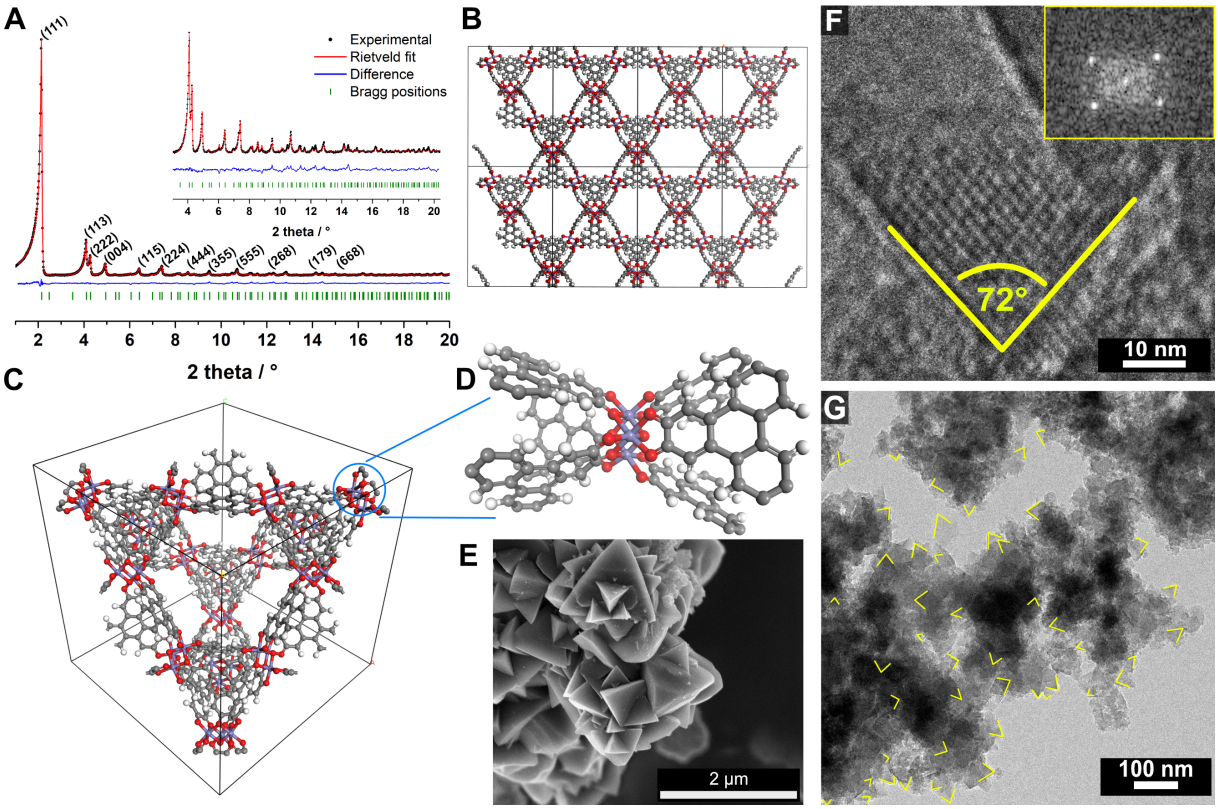

Figure 7.2 – **A** Mo-Kα source diffraction pattern of Fe-CAT. **B** View along the c-axis showing the tetrahedral arrangement of the HHTP ligands in the unit cell. **C** View along the [111] direction visualizing the open pore system of the supertetrahedron comprised of bridging iron and HHTP molecules. **D** Enlarged illustration of the central secondary building unit composed of three Fe ions in a trigonal arrangement coordinated by a central oxygen and stabilized by 3 chelating HHTP units. **E** SEM micrograph showing tetrahedral intergrown crystallites in the size of 300-500 nm. **F** TEM analysis depicts an assemble of tetrahedral crystallites. Inset: FFT from the crystal lattice of an exemplary crystallite agrees well with the lattice constant from the PXRD pattern. **G** Crystalline domains in the sample showing a tetrahedron angle of 72°.

Structure Description. In the structure model, each iron atom bridges two HHTP moieties. Three of these iron bis-catecholate complexes are arranged in a trimeric geometry stabilized by a central oxygen atom (see Figure 7.2D), as observed in a number of other MOFs.[31] The oxo-trimers form the extended vertices of an open supertetrahedron whose faces are the connecting HHTP moieties; each of them is linked to three iron oxo-trimers. The supertetrahedra are corner-connected to four other supertetrahedra, thus forming a porous 3D architecture. Considering a supertetrahedron to be the basic building unit, the structure can be described by a diamond (4-c dia) topology.[32–34] The smallest R_w-values were obtained for a structure model with water present in the pores.

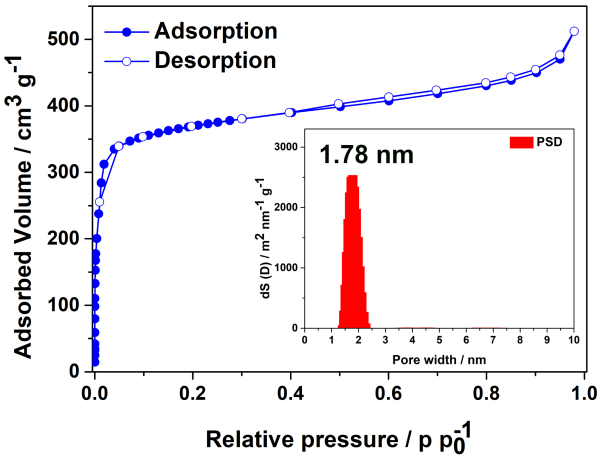

Figure 7.3 – Nitrogen ad- and desorption isotherm. The inset shows the pore size distribution centered at 1.78 nm obtained by quenched density functional density theory (QSDFT) calculations also revealing one type of pores and a narrow pore size distribution.

Material Characterization. Nitrogen ad- and desorption measurements revealed a type Ia isotherm according to the IUPAC nomenclature (Figure 7.3).[35] In the isotherms, the sharp uptake at relatively low-partial pressure ($p/p_0 < 0.1$ and of up to 350 cm^3 g^{-1}) points to a microporous structure. The desorption curve overlaps perfectly with the adsorption curve, indicating a highly reversible gas sorption process. The BET model was applied to the isotherms at low partial pressures ($p/p0 < 0.1$) to give a BET surface area of 1490 m^2 g^{-1} and a pore volume of 0.7 cm^3 g^{-1}. The measured BET surface area and pore volume agree well with the predicted Connolly surface area of 1675 m^2 g^{-1} and pore volume of 1 cm^3 g^{-1} calculated for the cubic model structure. The surface area of this cubic MOF is about four times higher than the average surface area for a corresponding 2D MOF, such as M-CAT-1.[13] In addition, the high surface area indicates that the pores of the MOFs are largely open, excluding the presence of reaction residues. Pore-size distribution was calculated by quenched density functional density theory (QSDFT) calculations, which revealed one type of pores with with a narrow pore size distribution and a mean value 1.78 nm. This measured value is in good agreement with the predicted 2.0 nm pore size from the model structure. The thermal stability of Fe-CAT was investigated by thermogravimetric analysis (TGA), showing structural integrity up to 185°C. At this temperature, a mild weight-loss process emerges, associated with the slow degradation of the framework. At ca. 200°C, a rapid combustion is observed that is attributed to the reaction of iron ions in the MOF forming thermodynamically stable products such as iron oxides (Figure 7.12).

In addition to the EDX analysis, the composition and the presence of guest molecules in the MOF structure was further studied by X-ray photoelectron spectroscopy (XPS) experiments. To

exclude the presence of impurities originating from the reaction precursors such as $FeBF_4 \cdot 6\,H_2O$, the boron spectrum was measured. Here, boron was not detected in the resulting spectrum (Figure 7.13). However, a weak nitrogen signal was identified and related to residual DMF and tetrabutylammonium in the pores.

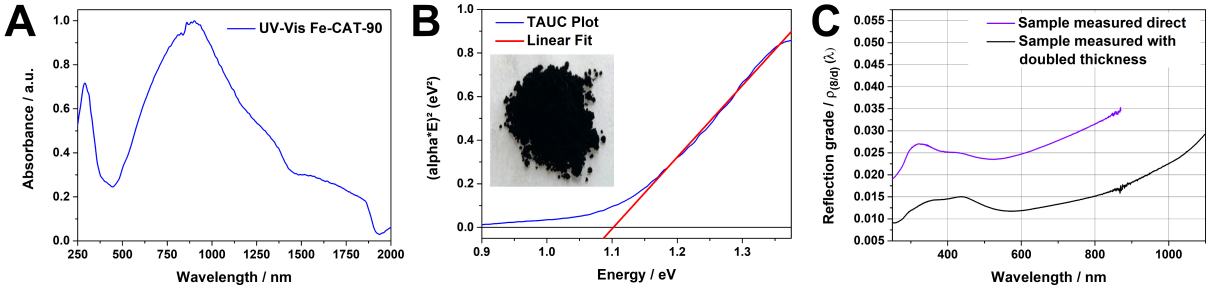

Figure 7.4 – **A** UV-Vis-spectrum of Fe-CAT showing a broad-band absorption ranging from 475 up to 1900 nm giving the material a deep black appearance (inset in B). **B** The material exhibits a direct band gap of 1.09 eV as indicated by the TAUC plot. **C** Reflectance measurements of pelletized samples with different thickness reveal a low-reflection grades of up to 0.015 over the whole visible spectrum up to 800 nm.

Photophysical Properties. The UV-VIS absorption spectrum of Fe-CAT was measured in a diffuse reflectance geometry and constructed using the Kubelka-Munk equation (Figure 7.4). Fe-CAT exhibits a broad absorption that covers large parts of the UV, visible and the near IR regions. The absorption spectrum shows local maxima at 380 nm and 950 nm, and the spectrum onset is located at 1400 nm in the near IR region. The TAUC equation was employed to estimate the MOF band gap. Assuming a direct band gap and using the clear onset at 1400 nm, a direct band-gap of 1.1 eV was determined. Powder photoluminescence measurements were conducted using a 375 nm laser source for excitation, however, no photoluminescence could be detected for the Fe-CAT.

Consistent with the broad-range absorption spectrum, Fe-CAT appears as a pitch-black powder. Because of this, we conducted total hemispherical reflectance measurements to shed light on the quantitative reflection capabilities of the MOF material (Figure 7.4). Here, the upper purple curve corresponds to a mechanically pressed sample of 3 mm thickness and the lower black curve corresponds to a sample with doubled thickness and a manually preparation of the sample surface. Outstandingly, the Fe-MOF samples exhibit reflectance of less than 3% in the visible spectrum regardless of the sample thickness. Strikingly, the highly porous and lightweight 3D MOF, hosting air in ordered cavities, features an absorption value of 98.5% over the whole UV-VIS-near IR region. Hemispherical reflectance measurements have not been reported for MOFs so far, and to the best of our knowledge not performed for porous crystalline compounds in general.

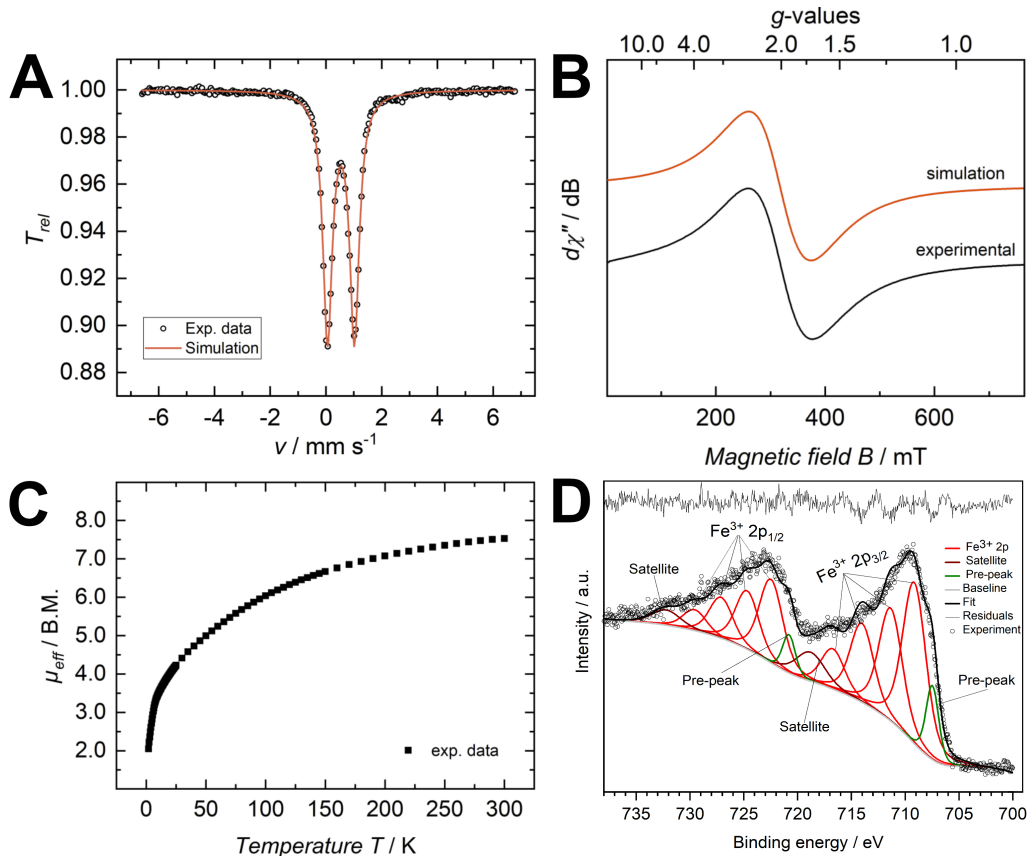

Figure 7.5 – **A** Zero-field ^{57}Fe Mössbauer spectrum of Fe-CAT recorded at 77 K in the solid-state. The Mössbauer spectrum shows one quadrupole doublet with an isomer shift, δ, of 0.54 mm s^{-1} and a quadrupole splitting parameter, ΔEQ, of 0.97 mm s^{-1}. These parameters are in accordance with a high-spin Fe^{III} center. **B** CW X-band EPR spectrum recorded as a microcrystalline sample at 293 K (experimental: black trace; simulation: red trace). **C** Temperature-dependent SQUID magnetization data of a powdery sample of Fe-CAT, recorded from 2-300 K with an applied magnetic field of 1 T. **D** XPS data of the Fe 2p region. The experimental data points are plotted as open circles, the envelope and residuals as solid black line, the multiplet components as red lines and the background as solid grey line.

Iron Valency. One way of enhancing electrical conductivity in 3D MOFs is to use the concept of mixed Fe valency. In this case, "doping" the Fe-based material - either by partial oxidation or reduction - creates defect sites in the framework, thus, enhancing charge-carrier migration.[20,21] In order to study the Fe valency in Fe-CAT, ^{57}Fe Mössbauer analysis at 77 K was employed (Figure 7.5A). The zero-field spectrum shows one symmetric quadrupole doublet with an isomer shift, δ, of 0.54 mm s^{-1} and a quadrupole splitting, ΔEQ, of 0.97 mm s^{-1}. This is in accordance with a single high-spin Fe^{III} coordination site present in Fe-CAT,[36] and confirms the absence of residual FeII precursor material in the sample investigated. In addition, CW X-band EPR spectra of the Fe-CAT powder at 7, 95, and 293 K were recorded. At room temperature, the

spectrum shows a single, broad (W_{iso} = 120 mT) and isotropic feature, centered at g_{iso} = 2.02 (Figure 7.5B), in agreement with the trinuclear ferric repeat unit in Fe-CAT, in which each high-spin, ferric iron ion (d5, $S_{Fe} = 5/2$) is antiferro-magnetically coupled to a spin-frustrated total $S_{tot} = 1/2$ electronic ground state (two degenerate doublet states), with additional intermolecular magnetic interaction due to the covalent network. This also explains the unusually broad EPR signal that further widens with decreasing temperature (W_{iso} = 155 mT at 95 K and W_{iso} = 315 mT at 7 K). This is in agreement with a SQUID magnetization measurement on a solid microcrystalline sample of Fe-CAT, which shows a temperature-dependent magnetic moment, µeff, with a low-temperature value of 2.05 µB at 2 K, characteristic with the doublet ground state. Further, the spin-frustration observed in Fe-CAT leads to fast spin-relaxation, which manifests itself in relatively sharp Mössbauer lines for high-spin ferric species. Also, XPS data recorded for the same sample (Figure 7.5D) agree well with the results of the magnetochemical analysis. Here, the Fe 2p signal is split into two broad Fe $2p_{3/2}$ and Fe $2p_{1/2}$ peaks. Each peak was fitted by four components, which is in agreement with the reported interpretation of signals from high spin Fe^{III}.[37–39] A single low-intensity peak (pre-peak) on the low-binding-energy (BE) side of the envelope was added to account for the formation of Fe ions with a lower oxidation state by the production of defects in neighboring sites. Although an XPS scan at the end of the measurement (Figure 7.13D) confirmed the absence of extensive radiation damage, the appearance of Fe^{II} sites from reduction by secondary electrons is often observed in coordination network compounds and may also play a role here, existing at sub-% range. However, structural defects in the form of Fe^{II} were not identified, strongly supporting the formation of an all-ferric (Fe^{III}) framework.

Electrical conductivity. Electrical conductivity measurements of Fe-CAT were performed using two-point-probe measurement on crystalline pellets of the material. The MOF pellet samples were prepared using 100 mg of the activated material and applying pressure using a KBr press standard instrument (for further information see SI). SEM micrographs of the pelletized sample confirm that the tetrahedral faceted crystallite morphology of the bulk material is preserved after compression (see Figure 7.10). The thickness of the pellets was measured by a slide gauge to be 500 µm. A linear sweep I-V scan was performed by applying voltage in the range of −5 to 5 V to give a linear ohmic resistance curve and electrical currents in the microampere range (Figure 7.6). The curve thus obtained was fitted by a linear regression and the slope of the linear function yielded an electrical conductivity of 2.4×10^{-4} S cm^{-1}. Further four-point probe van der Pauw measurements were conducted using the same pelletized samples to give an electrical conductivity value of 3.1×10^{-3} S cm^{-1}. Regardless of the specific techniques used, the conductivity values are ca. 1000 times higher than those of previously reported state-of-the-art 3D MOF materials, thereby setting a record intrinsic electrical conductivity in 3D metal-catecholate based materials.

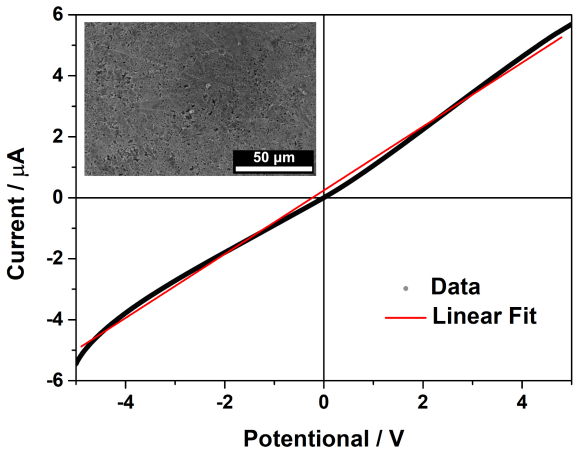

Figure 7.6 – **A** Calculated hole- and **B** electron-transport paths. Isocontour plots for 8 time steps (24 fs each) of the electron (green to blue) and hole density (green to red; contour level = 1.2×10^{-5} e-Bohr^{-3}). The initial Gaussian function is shown as transparent sphere. Isocontour plots of **C** the PM6 local electron affinity (contour level = 0 kcal mol^{-1}) and D local ionization energy (contour level = 330 kcal mol^{-1} = 14.3 eV).

Charge-carrier pathway simulations. Since Fe-CAT is clearly an electroactive material, we elucidated the possible charge carrier migration pathways in the framework, using direct semiempirical molecular-orbital molecular-dynamics (MD) simulations and subsequent charge-propagation simulations. For the MD simulation, five picoseconds of PM640 direct semiempirical molecular-orbital MD on the periodic structure flooded with water (see SI for further details) were calculated, and a snapshot from the end of the simulation used for imaginary-time-evolution simulations[41,42] of electron- and hole-transport. Details of all the simulations are given in the SI. The charge-transport simulations are based on the local average ionization energy[43] and the local electron affinity[44,45] for holes and electrons, respectively, and give the calculated conductance paths (see Figure 7.7). The electron-transport path moves through the lattice *via* the iron centers and the connecting ligands.The path is continuous, indicating polaron-transport along conducting chains of atoms. This result can be rationalized by considering both the iron centers (Fe^{II}/Fe^{III}) and the catechol moieties (catechol/semiquinone)ref to be redox active. The ligands can in this case provide reducible paths for transporting electrons between iron centers. This mechanism will be described in more detail in a later study. In contrast, the hole-transport path is discontinuous with local charge centers largely located on the water clusters used to flood the MOF. This indicates hopping conductance between water basins with little involvement of the MOF framework. Although imaginary time propagation cannot give quantitative mobilities,[41,42] we note that the electron moves essentially twice as far as the hole in the two equivalent simulations shown above. These results are expected from the local ionization

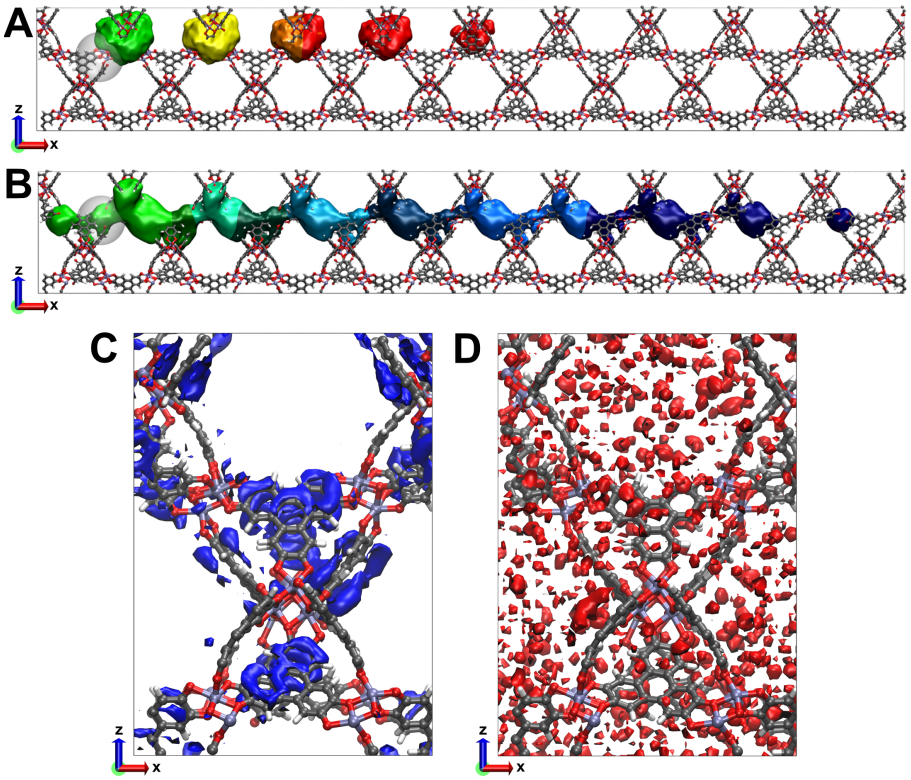

Figure 7.7 – I-V curves of a pelletized Fe-CAT sample showing an ohmic resistance and an electrical conductivity of 10^{-4} S cm^{-1}. The homogeneous compressed crystallites are shown as an inset.

energy and local electron affinity maps (Figure 7.7C, D). The local electron affinity isodensity surface plotted at a value of 0 kcal mol^{-1} shows an almost continuous envelope around the MOF framework, indicating that electrons can move relatively freely (Figure 7.7C). In contrast, the local ionization energy isosurface (depicted at 330 kcal mol^{-1}) shows isolated islands with no continuous easily ionizable path through the network (Figure 7.7D). This leads to the hopping conductance between water clusters shown in Figure 7.7A. Thus, the simulations suggest that Fe-CAT is an efficient electron conductor but that it cannot transport holes because it exhibits no continuous paths for hole transport through the MOF framework and because its ionization potential is high. The local electron affinity, on the other hand, shows continuous bound transport paths along the framework of the MOF.

7.3. Conclusion

In this work, we present the synthesis of a cubic ferric catecholate framework material coined Fe-CAT. The Fe-CAT MOF is obtained in a solvothermal reaction as a dark black powder that

consists of intergrown tetrahedral crystallites in the 300-500 nm size range. The structure was solved from powder X-ray diffraction data using a Mo-Kα source by indexing and a subsequent simulated annealing step. The unit cell obtained was subjected to a DFT optimization and Rietveld refinement to give a final structure model with the cubic space group F*23*. The structure of Fe-CAT is composed of iron-connected supertetrahedra to give a diamond-like topology. The tetrahedra are composed of four triphenylene units that form the facets and are interconnected by a defined trinuclear iron-oxo cluster. The Fe-CAT is microporous with a BET surface area exceeding 1400 $m^2\ g^{-1}$. Moreover, Fe-CAT combines this high surface area with electrical conductivity of about $10^{-3}\ S\,cm^{-1}$, which is exceptionally high intrinsic conductivity for a 3D-connected framework. The deep black appearance of the material was studied by reflectance measurements, giving a remarkably low degree of reflection up to 1.5% in the visible spectral regime for a porous framework. The nature of the ferric repeat unit was elucidated by means of XPS, EPR and ^{57}Fe Mössbauer measurements, indicating the presence of a purely ferric, high-spin Fe^{III} framework. However, at this point, we cannot exclude the presence of semiquinone impurities giving rise to iron (II) sites at a sub-% range. To gain further insights into the electrical conductivity of Fe-CAT, we performed quantum mechanical calculations, which suggest the Fe-CAT to be an efficient electron conductor that exhibits continuous paths through the conducting framework atoms. This work sheds light on the interplay on the electronic properties, porosity, electrical conductance and broad-band absorption and serves for a future design of electrically conducting metal-organic frameworks.

References

[1] Sun, L., Campbell, M. G. & Dinca, M. Electrically Conductive Porous Metal-Organic Frameworks. *Angew. Chem. Int. Ed.* **55,** 3566-3579 (2016).

[2] Xie, L. S., Skorupskii, G. & Dinca, M. Electrically Conductive Metal-Organic Frameworks. Chem. Rev. **120,** 8536-8580 (2020).

[3] Medina, D. D., Mähringer, A. & Bein, T. Electroactive Metalorganic Frameworks. *Isr. J. Chem.* **58,** 1089 (2018).

[4] Campbell, M. G., Liu, S. F., Swager, T. M. & Dinca, M. Chemiresistive Sensor Arrays from Conductive 2D Metal-Organic Frameworks. J. Am. Chem. Soc. **137,** 13780-13783 (2015).

[5] Arora, H., Dong, R., Venanzi, T., Zscharschuch, J., Schneider, H., Helm, M., Feng, X., Canovas, E. & Erbe, A. Demonstration of a Broadband Photodetector Based on a Two-Dimensional Metal-Organic Framework. Adv. Mater. **32,** 1907063 (2020).

[6] Feng, D., Lei, T., Lukatskaya, M. R., Park, J., Huang, Z., Lee, M., Shaw, L., Chen, S., Yakovenko, A. A., Kulkarni, A., Xiao, J., Fredrickson, K., Tok, J. B., Zou, X., Cui, Y. & Bao, Z. Robust and conductive two-dimensional metal-organic frameworks with exceptionally high volumetric and areal capacitance. Nat. Energy **3,** 30-36 (2018).

[7] Mähringer, A., Jakowetz, A. C., Rotter, J. M., Bohn, B. J., Stolarczyk, J. K., Feldmann, J., Bein, T. & Medina, D. D. Oriented Thin Films of Electroactive Triphenylene Catecholate-Based Two-Dimensional Metal-Organic Frameworks. ACS Nano **13,** 6711-6719 (2019).

[8] Scheurle, P. I., Mähringer, A., Jakowetz, A. C., Hosseini, P., Richter, A. F., Wittstock, G., Medina, D. D. & Bein, T. A highly crystalline anthracene-based MOF-74 series featuring electrical conductivity and luminescence. Nanoscale **11,** 20949-20955 (2019).

[9] Xie, L. S., Alexandrov, E. V., Skorupskii, G., Proserpio, D. M. & Dinca, M. Diverse π-π stacking motifs modulate electrical conductivity in tetrathiafulvalene-based metal-organic frameworks. Chem. Sci. **10,** 8558?8565 (2019).

[10] Jia, H., Yao, Y., Zhao, J., Gao, Y., Luo, Z. & Du, P. A novel two-dimensional nickel phthalocyanine-based metal-organic framework for highly efficient water oxidation catalysis. J. Mater. Chem. A **6,** 1188-1195 (2018).

[11] Huang, X., Sheng, P., Tu, Z., Zhang, F., Wang, J., Geng, H., Zou, Y., Di, C.-a., Yi, Y., Sun, Y., Xu, W. & Zhu, D. A two-dimensional π-d conjugated coordination polymer with extremely high electrical conductivity and ambipolar transport behaviour. Nat. Commun. **6,** 7408 (2015).

[12] Day, R. W., Bediako, D. K., Rezaee, M., Parent, L. R., Skorupskii, G., Arguilla, M. Q., Hendon, C. H., Stassen, I., Gianneschi, N. C., Kim, P. & Dinca, M. Single Crystals of Electrically Conductive Two-Dimensional Metal-Organic Frameworks: Structural and Electrical Transport Properties. ACS Cent. Sci. **5,** 1959-1964 (2019).

[13] Hmadeh, M., Lu, Z., Liu, Z., Gandara, F., Furukawa, H., Wan, S., Augustyn, V., Chang, R., Liao, L., Zhou, F., Perre, E., Ozolins, V., Suenaga, K., Duan, X., Dunn, B., Yamamto, Y., Terasaki, O. & Yaghi, O. M. New Porous Crystals of Extended Metal-Catecholates. Chem. Mater. **24,** 3511-3513 (2012).

[14] Skorupskii, G., Trump, B. A., Kasel, T. W., Brown, C. M., Hendon, C. H. & Dinca, M. Efficient and tunable one-dimensional charge transport in layered lanthanide metal-organic frameworks. Nat. Chem. 12, 131-136 (2020).

[15] Dong, R., Zheng, Z., Tranca, D. C., Zhang, J., Chandrasekhar, N., Liu, S., Zhuang, X., Seifert, G. & Feng, X. Immobilizing Molecular Metal Dithiolene-Diamine Complexes on 2D Metal-Organic Frameworks for Electrocatalytic H_2 Production. Chem. Eur. J. **23,** 2255-2260 (2017).

[16] Dou, J.-H., Sun, L., Ge, Y., Li, W., Hendon, C. H., Li, J., Gul, S., Yano, J., Stach, E. A. & Dinca, M. Signature of Metallic Behavior in the Metal-Organic Frameworks M_3(hexaiminobenzene)$_2$ (M = Ni, Cu). J. Am. Chem. Soc. **139,** 13608?13611 (2017).

[17] Sheberla, D., Sun, L., Blood-Forsythe, M. A., Er, S., Wade, C. R., Brozek, C. K., Aspuru-Guzik, A. & Dinca, M. High Electrical Conductivity in Ni-(2,3,6,7,10,11-hexaiminotriphenylene)$_2$, a Semiconducting Metal-Organic Graphene Analogue. J. Am. Chem. Soc. *136,* 8859-8862 (2014).

[18] Jin, Z., Yan, J., Huang, X., Xu, W., Yang, S., Zhu, D. & Wang, J. Solution-processed transparent coordination polymer electrode for photovoltaic solar cells. Nano Energy **40,** 376-381 (2017).

[19] Dong, R., Han, P., Arora, H., Ballabio, M., Karakus, M., Zhang, Z., Shekhar, C., Adler, P., Petkov, P. S., Erbe, A., Mannsfeld, S. C. B., Felser, C., Heine, T., Bonn, M., Feng, X. & Canovas, E. High-mobility band-like charge transport in a semiconducting two-dimensional metal-organic framework. Nat. Mater. **17,** 1027-1032 (2018).

[20] Xie, L. S., Sun, L., Wan, R., Park, S. S., DeGayner, J. A., Hendon, C. H. & Dinca, M. Tunable Mixed-Valence Doping toward Record Electrical Conductivity in a Three-Dimensional Metal-Organic Framework. J. Am. Chem. Soc. **140,** 7411-7414 (2018).

[21] Park, J. G., Aubrey, M. L., Oktawiec, J., Chakarawet, K., Darago, L. E., Grandjean, F., Long, G. J. & Long, J. R. Charge Delocalization and Bulk Electronic Conductivity in the Mixed-Valence Metal-Organic Framework Fe(1,2,3-triazolate)$_2$(BF_4)$_x$. J. Am. Chem. Soc. **140,** 8526-8534 (2018).

[22] Darago, L. E., Aubrey, M. L., Yu, C. J., Gonzalez, M. I. & Long, J. R. Electronic Conductivity, Ferrimagnetic Ordering, and Reductive Insertion Mediated by Organic Mixed-Valence in a Ferric Semiquinoid Metal-Organic Framework. J. Am. Chem. Soc. **137,** 15703-15711 (2015).

[23] Aubrey, M. L., Wiers, B. M., Andrews, S. C., Sakurai, T., Reyes-Lillo, S. E., Hamed, S. M., Yu, C.-J., Darago, L. E., Mason, J. A., Baeg, J.-O., Grandjean, F., Long, G. J., Seki, S., Neaton, J. B., Yang, P. & Long, J. R. Electron delocalization and charge mobility as a function of reduction in a metal-organic framework. Nature Mater **17,** 625-632 (2018).

[24] Nguyen, N. T. T., Furukawa, H., Gandara, F., Trickett, C. A., Jeong, H. M., Cordova, K. E. & Yaghi, O. M. Three-Dimensional Metal-Catecholate Frameworks and Their Ultrahigh Proton Conductivity. J. Am. Chem. Soc. **137,** 15394-15397 (2015).

[25] Skorupskii, G. & Dinca, M. Electrical Conductivity in a Porous, Cubic Rare-Earth Catecholate. J. Am. Chem. Soc. **142,** 6920-6924 (2020).

[26] Neumann, M. X-Cell: a novel indexing algorithm for routine tasks and difficult cases. Journal of Applied Crystallography **36,** 356-365 (2003).

[27] Altomare, A., Corriero, N., Cuocci, C., Falcicchio, A., Moliterni, A. & Rizzi, R. Direct-space solution in the EXPO package: the combination of the HBB-BC algorithm with GRASP. J. Appl. Crystallogr. **51,** 505-513 (2018).

[28] Altomare, A., Corriero, N., Cuocci, C., Moliterni, A. & Rizzi, R. The hybrid big bang-big crunch method for solving crystal structure from powder diffraction data. Journal of Applied Crystallography **46,** 779-787 (2013).

[29] Rappe, A. K., Casewit, C. J., Colwell, K. S., Goddard, W. A. & Skiff, W. M. UFF, a full periodic table force field for molecular mechanics and molecular dynamics simulations. J. Am. Chem. Soc. **114,** 10024-10035 (1992).

[30] Young, R. A. The Rietveld Method (Oxford University Press, 1995).

[31] Lebedev, O. I., Millange, F., Serre, C., van Tendeloo, G. & Ferey, G. First Direct Imaging of Giant Pores of the Metal-Organic Framework MIL-101. Chem. Mater. **17,** 6525-6527 (2005).

[32] BRAGG, W. The structure of the diamond. Nature **91,** 557 (1913).

[33] Kim, D., Liu, X. & Lah, M. S. Topology analysis of metal-organic frameworks based on metal-organic polyhedra as secondary or tertiary building units. Inorganic Chemistry Frontiers **2,** 336-360 (2015).

[34] Li, M., Li, D., O'Keeffe, M. & Yaghi, O. M. Topological Analysis of Metal-Organic Frameworks with Polytopic Linkers and/or Multiple Building Units and the Minimal Transitivity Principle. Chem. Rev. **114,** 1343-1370 (2014).

[35] Matthias Thommes, Katsumi Kaneko, Alexander V. Neimark, James P. Olivier, Francisco Rodriguez-Reinoso, Jean Rouquerol & Kenneth S.W. Sing. Physisorption of gases, with special reference to the evaluation of surface area and pore size distribution (IUPAC Technical Report). Pure and Applied Chemistry **87,** 1051-1069 (2015).

[36] Gorun, S. M., Papaefthymiou, G. C., Frankel, R. B. & Lippard, S. J. Synthesis, structure, and magnetic and Moessbauer properties of mononuclear and asymmetric, oxo-bridged trinuclear iron(III) complexes of a new polyimidazole ligand. J. Am. Chem. Soc. **109,** 4244-4255 (1987).

[37] Gupta, R. P. & Sen, S. K. Calculation of multiplet structure of core p-vacancy levels. Phys. Rev. B **10,** 70-77 (1974).

[38] Gupta, R. P. & Sen, S. K. Calculation of multiplet structure of core p-vacancy levels. II. Phys. Rev. B **12,** 15-19 (1975).

[39] Grosvenor, A. P., Kobe, B. A., Biesinger, M. C. & McIntyre, N. S. Investigation of multiplet splitting of Fe 2p XPS spectra and bonding in iron compounds. Surf. Interface Anal. **36,** 1564-1574 (2004).

[40] Stewart, J. J. P. Optimization of parameters for semiempirical methods V: Modification of NDDO approximations and application to 70 elements. Journal of Molecular Modeling 13, 1173-1213 (2007).

[41] Kriebel, M., Hennemann, M., Beierlein, F. R., Medina, D. D., Bein, T. & Clark, T. Propagation of Holes and Electrons in Metal-Organic Frameworks. Journal of Chemical Information and Modeling **59,** 5057-5064 (2019).

[42] Kriebel, M., Sharapa, D. & Clark, T. Charge Transport in Organic Materials: Norm-Conserving Imaginary Time Propagation with Local Ionization Energy as the External Potential. Journal of Chemical Theory and Computation **13,** 6308-6316 (2017).

[43] Sjoberg, P., Murray, J. S., Brinck, T. & Politzer, P. Average local ionization energies on the molecular surfaces of aromatic systems as guides to chemical reactivity. Canadian Journal of Chemistry 68, 1440-1443 (1990).

[44] Clark, T. The local electron affinity for non-minimal basis sets. Journal of Molecular Modeling **16,** 1231-1238 (2010).

[45] Ehresmann, B., Groot, M. J. de, Alex, A. & Clark, T. New Molecular Descriptors Based on Local Properties at the Molecular Surface and a Boiling-Point Model Derived from Them. Journal of Chemical Information and Computer Sciences **44,** 658-668 (2004).

7.4. Appendix

7.4.1. Characterization

X-ray diffraction

Powder X-ray diffraction suitable for Rietveld refinement was carried out using Mo-Kα radiation in Debye-Scherrer geometry on a StadiP diffractometer (STOE & Cie, Darmstadt, Germany) equipped with a MYTHEN 1K detector (Dectris, Baden, Switzerland; angular range $\Delta 2\theta = 12.5°$), and a Ge(111) monochromator singling out the Mo-Kα radiation (0.709300 Å). Samples were loaded into glass capillaries with 0.5 mm diameter and 0.01 mm wall thickness (Hilgenberg GmbH, Malsfield, Germany). Data was recorded in the angle-range between 2θ = 1-50° with a step width of 0.3°/step.

X-ray diffraction (XRD) analyses of the pressed pellet and the reference powder were performed on a Bruker D8 diffractometer in Bragg-Brentano geometry with Ni-filtered Cu Kα (λ = 1.54060 Å) radiation operating at 40 kV and 30 mA with a position-sensitive detector (LynxEye).

Scanning electron microscopy (SEM)

SEM images were recorded on a FEI Helios NanoLab G3 UC electron microscope with an acceleration voltage of 2 kV from a field emission gun. For the cross-section analysis substrates were partially cut and broken manually to reveal fresh cross-sections. *Prior* to SEM analysis the samples were coated with a thin carbon layer by carbon fiber flash evaporation in high vacuum.

Transmission electron microscopy (TEM)

TEM images were collected on a FEI Titan Themis 60-300 microscope at an acceleration voltage of 300 kV. Powder samples were prepared by crushing the particles with a razor blade and subsequently depositing the powder onto a copper grid supporting a thin electron transparent carbon film.

UV-VIS spectroscopy

UV-Vis spectra were recorded using a PERKIN ELMER UV VIS/NIR Lambda 1050 spectrophotometer equipped with a 150 mm InGaAs integrating sphere. Diffuse reflectance spectra were collected with a Praying Mantis (Harrick) accessory and were referenced to barium sulfate powder as white standard.

Nitrogen sorption

Ad- and desorption measurements were performed at 77.3 K on an Autosorb 1 (Quantachrome instruments, Florida, USA) with nitrogen of 99.9999% purity. The samples were activated under high vacuum at 120°C for at least 12 h. Evaluation of ad- and desorption isotherms was carried

out with the program AsiQwin v.3.01 (Quantachrome instruments, Florida, USA). For BET calculations, pressure ranges of the nitrogen isotherms were chosen with the help of the BET assistant in the AsiQwin software. In accordance with the ISO recommendations, multipoint BET tags equal to or below the maximum in V $\times$ $(1 - p/p_0)$ were chosen.

Thermogravimetric analysis

Thermogravimetric analysis of the samples was performed using a NETZSCH STA 449C with a heating rate of 2.35°C/min and a heating range up to 600°C under a stream of synthetic air.

Electrical conductivity measurements

Electrical conductivity was measured on a Metrohm Autolab PGStat302N.

Total Hemispherical reflectance in geometry 8°/di

The total hemispherical reflectance was determined with an Agilent Cary 5000 double-beam spectrophotometer equipped with an external diffuse reflectance accessory eDRA. This system collects the total reflectance of diffuse reflecting specimen with an integration sphere of diameter d = 150 mm. The influx angle of the collimated radiation with respect to sample normal is 8°, the described measurements were performed in the gloss component included scheme. As the sample diameter was only 20 mm the standard sample port of the sphere was reduced by a self-made $BaSO_4$-coated port reducer to 15 mm diameter and the eDRA optics for small spot measurement was used resulting in an oval spot of about 10 mm height and 4 mm width.

As a low spectral reflection of the sample was expected it was measured in a two-step process relative to a calibrated Spectralon white standard. In a first step a dark grey reflection standard with about 8% reflectance was measured against the white standard. Then the sample reflectance was determined against the grey standard. In both steps, the reference port was equipped with a nominal 25% reflectance standard. The zero-line of measurement was determined with open port by letting the influx radiation diffuse into an approx. 80 cm deep black cabinet with virtual zero back-reflection, shielded against the shaded laboratory environment.

A further measurement was performed after doubling the cell's depth to exclude or reduce a possible back reflection from the stamp cell's base; this is especially important for the near RD spectral range. This sample was produced with new material and by manual pressing only. The observed difference in reflectance compared to the result for the mechanically pressed sample, however, can be assigned to the differently prepared surfaces. The manually prepared sample visibly exhibited a lower gloss component.

X-ray photoelectron spectroscopy

XPS was performed using an ESCALAB 250 Xi instrument (Thermo Fisher, East Grinsted, UK) with monochromatized Al Kα ($h\nu$ = 1486.6 eV) radiation focused to a spot of 500 µm diameter at the surface of samples. Spectra were measured with pass energies of 200 eV for survey scans and 10 eV for high-resolution spectra. Charging was compensated by use of an internal electron flood gun. Peak fitting was performed by the software Avantage, version 5.9904 (Thermo Fisher) using a Shirley background ("Smart Shirley") and a convolution of Gaussian and Lorentzian functions for each signal component. All spectra were referenced to remaining adventitious carbon at 284.8 eV.

^{57}Fe-Mössbauer

Zero-field ^{57}Fe-Mössbauer spectra were recorded on a WissEl Mössbauer spectrometer (MRG-500) at a temperature of 77 K in constant acceleration mode. ^{57}Co/Rh was used as γ-radiation source. WinNormos for Igor Pro software was used for the quantitative evaluation of the spectral parameters (least squares fitting to Lorentzian peaks). The minimum experimental line widths were 0.21 mm s^{-1} (full width at half maximum, FWHM). The temperature of the sample was controlled by a MBBC-HE0106 Mössbauer He/N_2 cryostat within an accuracy of ±0.3 K. Least-square fitting of the Lorentzian signals was carried out with the Mfit software, developed by Dr. Eckhard Bill (MPI Mülheim/Ruhr). The isomer shifts were reported relative to γ-iron reference at 300 K.[1]

Magnetism data

Magnetism data of micro-crystalline and powdered samples (10.0-25.0 mg) loaded within polycarbonate gel capsules were collected on a Quantum Design MPMS-3 SQUID magnetometer. DC susceptibility was recorded in the temperature range of 2-300 K with an applied DC field of 1 T, if not stated otherwise. Values of the magnetic susceptibility were corrected for core diamagnetism of the sample using tabulated Pascal's constants.[2] For simulation and analysis of the data, the program JulX2, written by Dr. Eckhard Bill (MPI Mülheim/Ruhr) was used.[3]

EPR spectra were recorded on a JEOL continuous wave spectrometer JES-FA200, equipped with an X-band Gunn diode oscillator bridge, a cylindric mode cavity, and a helium cryostat. The samples were measured in the solid state under nitrogen atmosphere in quartz glass EPR tubes at 293, 95, and 7 K. The spectra shown were measured using the following parameters: microwave frequency = 8.959 GHz, modulation width 1.0 or 0.5 mT, microwave power 1.0 mW, modulation frequency 100 kHz, and a time constant of 0.1 s. Analysis and simulation of the data was done using the software "eview" and "esim", written by Dr. Eckhard Bill (MPI for Chemical Energy Conversion, Mülheim an der Ruhr),[4,5] on the basis of a spin-Hamiltonian description of the electronic ground state:

$$\hat{H} = D\left(\hat{S}_z^2 - \frac{1}{3}S(S+1) + \frac{E}{D}\left(\hat{S}_x^2 - \hat{S}_y^2\right)\right) + \mu_B \underline{g}\,\overrightarrow{S} \tag{7.1}$$

Here, S represents the total spin quantum number of the coupled system, D and E/D are the axial and rhombic zero-field parameters, respectively, and $\underline{g}$ is the g-matrix. Calculations are based on the $S = 5/2$ routines developed by Gaffney and Silverstone.[6]

7.4.2. Experimental

General

All materials were purchased from Sigma Aldrich, Acros or TCI Europe in the common purities purum, puriss or reagent grade. The materials were used as received without additional purification and handled in air unless otherwise noted. The water utilized in the synthesis was obtained from a Merck-Milipore Mili-Q purification system.

Synthesis of Fe-CAT-90

A solid mixture of HHTP (hexahydroxtriphenylene) (20 mg), $FeBF_4 \cdot 6\,H_2O$ (42.4 mg) and NBu_4NO_3 (20 mg) was dissolved in 3.5 mL DMF under inert conditions in an Ar-filled glovebox. 250 µL each of NMP (*N*-methyl-2-pyrrolidon), deionized water and methanol were added. The glass vial was capped, sonicated for 15 min and heated to 120°C for 48 h. The reaction mixture was then washed with dimethyl-formamide, methanol and water to obtain a black powder.

Preparation of pellets

Pellets with 1 cm diameter (obtained from several described batches) for electrical conductivity measurements were fabricated with 100 mg of the respective MOF bulk material with a standard Paul-Weber KBr press with 45 kg cm^2 pressure.

7.4.3. Additional information

Scanning-electron microscopy of Fe-CAT bulk material

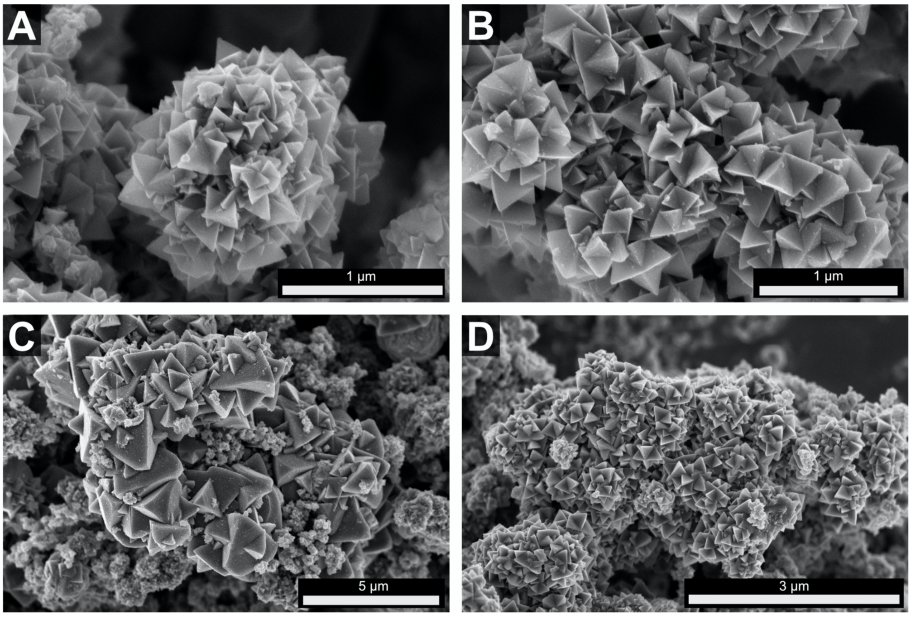

Figure 7.8 – SEM micrographs of Fe-CAT. The images show intergrown tetrahedral shaped crystallites in the size of 300-500 nm. No other morphology could be detected in the sample.

Energy-dispersive X-ray analysis of Fe-CAT pressed pellet

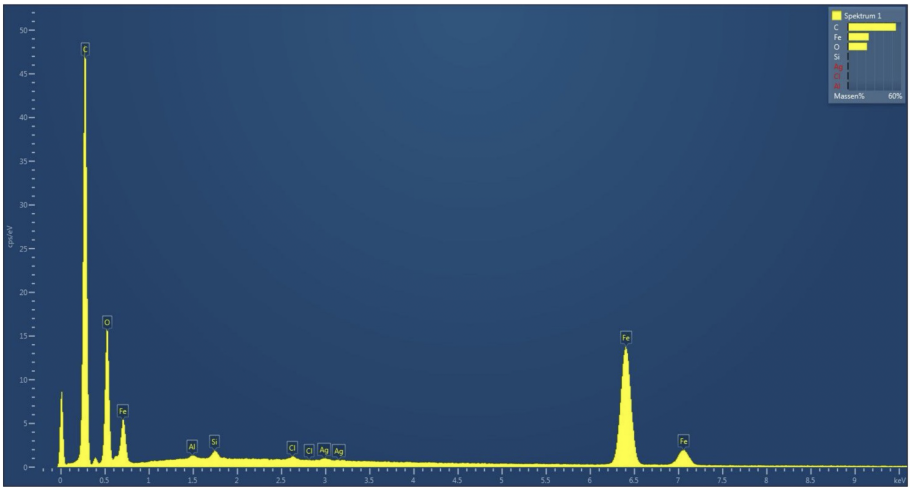

Figure 7.9 – EDX analysis of Fe-CAT confirming only the presence of the elements C, O, and Fe.

Statistical data of the crystallite angle

Table 23 – Measured angles of the crystallites. Data from Figure 7.2F. Mean angle of 72°.

No.	Parameter	Angle/°
1		67.761
2		75.976
3		67.872
4		73.355
5		76.271
6		68.715
7		73.926
8		72.851
9		73.920
10	Mean	72.294
11	SD	3.336
12	Min	67.761
13	Max	76.271

Statistical data of the crystallite angle

Table 24 – Results of the EDX experiments and comparison to theoretical values.

	Spot 1	Spot 2	Spot 3	Spot 4	Ave. / exp.	Ratio / exo.	Ratio / theo.
Element	Atom %	Atom %	Atom %	Atom %	Atom %	/	/
C	62.65	62.24	61.56	65.08	62.88	/	/
O	30.29	30.25	28.26	26.87	28.91	/	/
Si	0.15	0.45	0.49	0.07	0.29	/	/
Fe	6.91	7.05	9.69	7.98	7.91	/	/
Sum	100	100	100	Atom %	Atom %	/	/

The silicon signal is a residual from sample preparation or a detector artifact. The average composition without Si is $C_{63.1}O_{29.0}Fe_{7.9}$.

Powder X-ray diffraction (Cu-Kα) of Fe-CAT

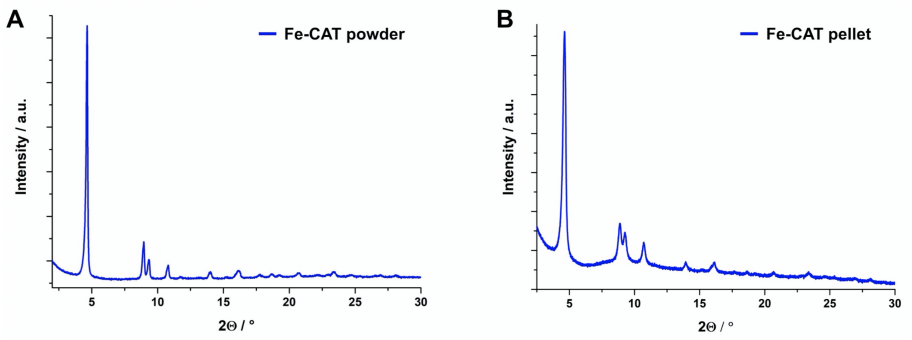

Figure 7.10 – **A** PXRD of Cu-CAT powder recorded with Cu-Kα radiation on a Bruker D8 Discover and **B** for a pellet sample.

Additional view on the crystal structure with and without crystal water

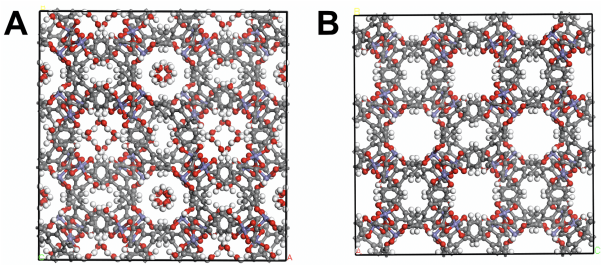

Figure 7.11 – View along the [010] direction of the unit cell. The structure is shown with (left) and without (right) crystal water.

Thermogravimetric analysis of Fe-CAT

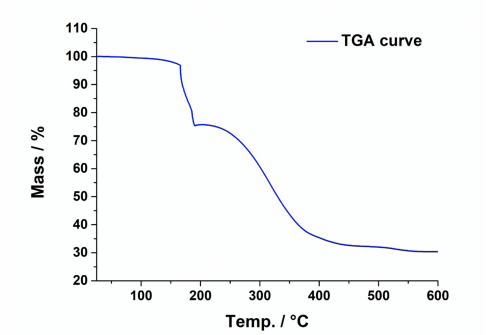

Figure 7.12 – Thermogravimetric analysis (TGA) of Fe-CAT under a stream of synthetic air. First mass loss located at 175°C, most probably crystal water. Second mass is accompanied by a combustion reaction of the transition metal to thermodynamically more favored metal oxides at 185°C.

X-ray photoelectron spectroscopy of compressed Fe-CAT

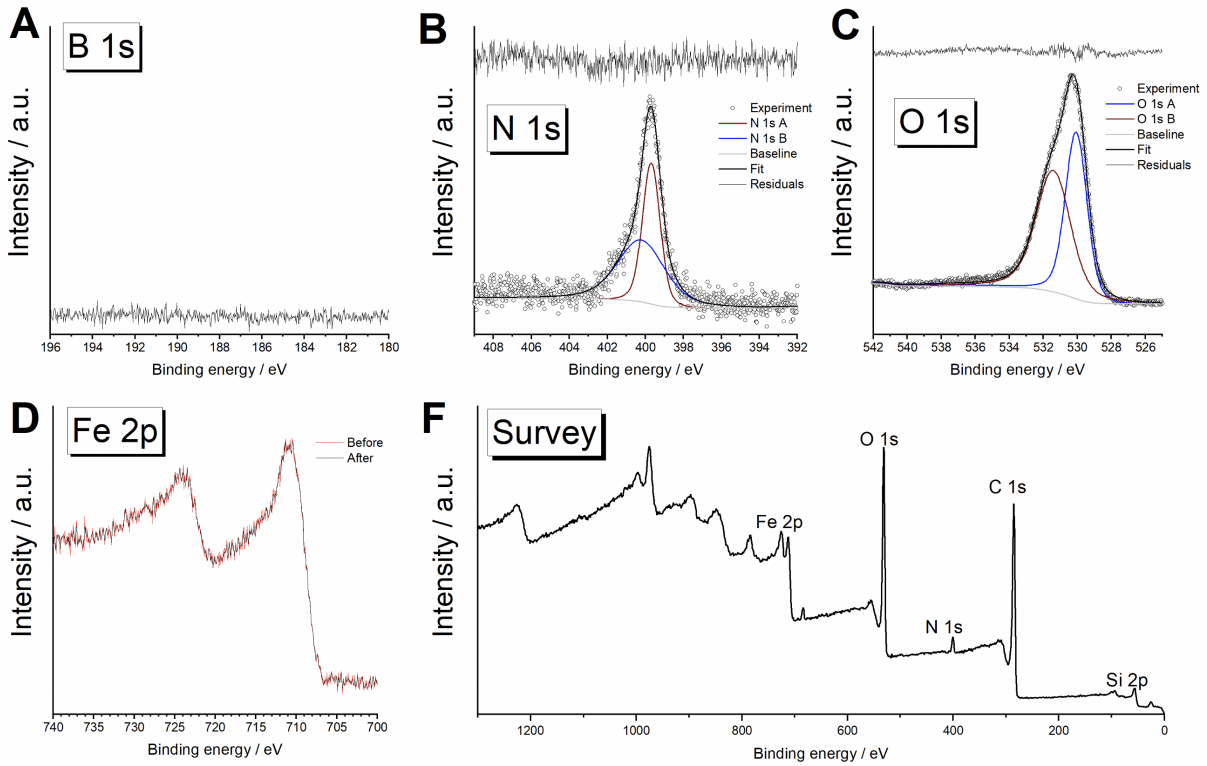

Figure 7.13 – XPS analysis of Fe-CAT for binding energy of B 1s, N 1s, Fe 2p, O 1s and the survey scan. **A** No boron impurities could be detected in the sample. **B** two types of nitrogen, which are not nitrate impurity, were detected. We attribute the signals to residual DMF and tetrabutylammonium in the sample. **C** Furthermore, two kinds of oxygen are recorded at 530.04 eV (hydroxyl group) and 531.28 eV, which could originate from water in the pores and in the powder sample. **D** As we know in some compounds, we have secondary electron damaging especially for transition metals. Therefore, one extra spectra at the end of analysis confirmed the absence of major reduction effects of secondary electrons on Fe^{III}. **F** Survey scan of the sample.

Figures 7.5C and 7.13D show that high-spin Fe^{III} occurs in Fe-CAT causing multi splitting for Fe $2p_{3/2}$ and Fe $2p_{1/2}$ peaks. This spectrum was fitted by considering the multiplet splitting from theoretical calculation. For the fit, the peak area ratios (Figure 7.14, Table 25) were fixed to the intensity ratios of the theoretical calculation.[7–9] The energy separation between the multiplet components depends on the chemical nature of the substance under investigation and was allowed to change collectively. The ratio of Gaussian and Lorentzian contribution as well as the full width at half maximum of all multiplet components was forced to be identical.

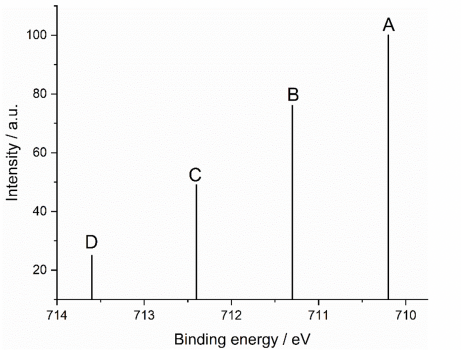

Figure 7.14 – The lines show the approximate position and intensity of the spectral components of Fe^{III} high spin in Oh structure according to the calculations in Ref. [7–9]

Table 25 – The intensity ratio between the components of the multiplet pattern for the Fe^{III} high spin in O_h structure.

Component	relative Intensity
A	1.00
B	0.76
C	0.46
D	0.25

7.4.4. Zero-Field ^{57}Fe-Mössbauer, EPR-spectroscopy & VT SQUID magnetization data

General information

Table 26 – General considerations

Repeat unit	
Chemical Formula	$C_{36}H_{12}Fe_3O_{13}$
Molecular Weight M_W	819.83 g/mol
Expected Oxidation States	Fe^{III}
Diamagnetic Correction χ_{dia}	-358.00×10^{-6} eμ/mol

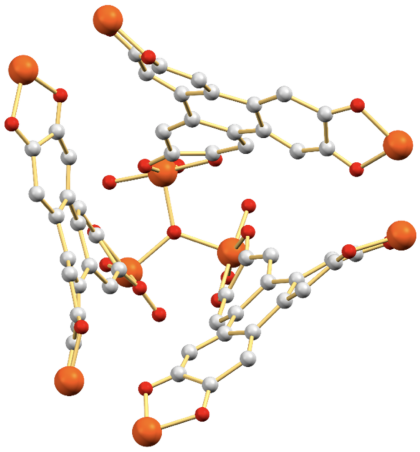

Figure 7.15 – Repeat unit of Fe-CAT for used as input data for zero-field ^{57}Fe-Mössbauer, X-band EPR spectroscopy and VT SQUID magnetization data.

X-band EPR spectroscopy

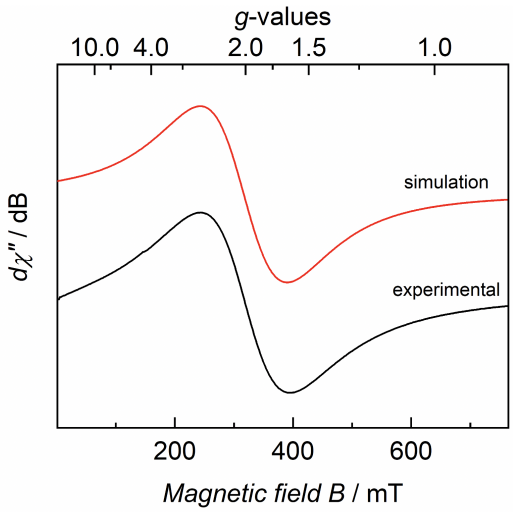

Figure 7.16 – CW X?band EPR spectrum of Fe-CAT recorded as a solid at 95 K (black trace) and its simulation (red trace). Experimental conditions: microwave frequency = 8.959 GHz, modulation width = 1.0 mT, microwave power = 1.0 mW, modulation frequency = 100 kHz, time constant = 0.1 s. Simulation parameters: effective spin $S = 1/2$, effective g-values $g_{iso} = 2.02$, linewidths $W_{iso} = 155$ mT.

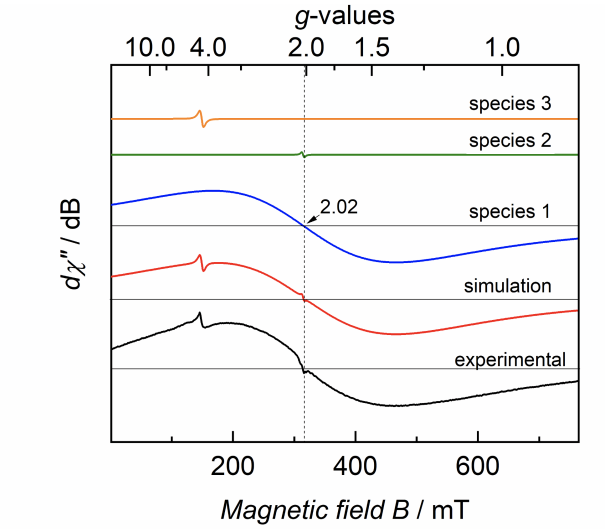

Figure 7.17 – CW X?band EPR spectrum of Fe-CAT recorded as a solid at 7 K (black trace), its simulation (red trace), main species (blue trace) plus very minor impurities (green and orange trace) in the subpercent range. Experimental conditions: microwave frequency = 8.959 GHz, modulation width = 0.5 mT, microwave power = 1.0 mW, modulation frequency = 100 kHz, time constant = 0.1 s. Simulation parameters for species 1: effective spin $S = 1/2$, effective g-values $g_{iso} = 2.02$, linewidths $W_{iso} = 315$ mT. Simulation parameters for species 2: effective spin $S = 1/2$, effective g-values $g_{iso} = 2.04$, linewidths $W_{iso} = 4.00$ mT. Simulation parameters for species 3: effective spin $S = 3/2$, effective g-values $g_{iso} = 4.30$, linewidths $W_{iso} = 14.0$ mT.

VT SQUID magnetization data

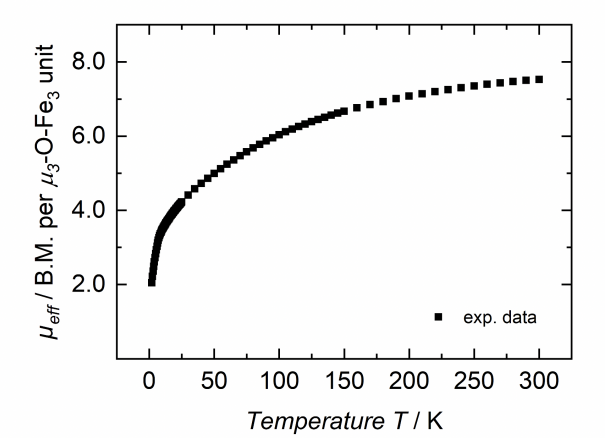

Figure 7.18 – Temperature-dependent SQUID magnetization data of a microcrystalline, solid sample of Fe-CAT, recorded with an applied magnetic field of 1 T (m = 18.9 mg, $\chi_{dia} = -358.00 \times 10^{-6}$ eμ/mol.

Table 27 – Temperature-dependent SQUID magnetization data of a microcrystalline, solid sample of Fe-CAT, recorded with an applied magnetic field of 1 T (m = 18.9 mg, $\chi_{dia} = -358.00 \times 10^{-6}$ eμ/mol.

Temperature / K	μ_{eff} / B.M.
2.00	2.05
300	7.53

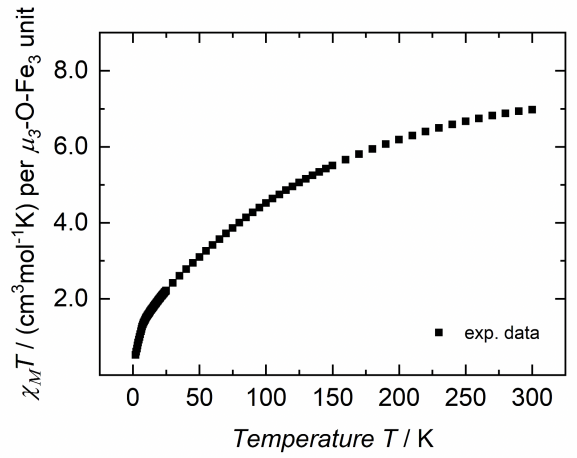

Figure 7.19 – Temperature-dependent SQUID magnetization data of a microcrystalline, solid sample of Fe-CAT, recorded with an applied magnetic field of 1 T (m = 18.9 mg, χ_MT = -358.00×10^{-6} eμ/mol.

Table 28 – Temperature-dependent SQUID magnetization data of a microcrystalline, solid sample of Fe-CAT, recorded with an applied magnetic field of 1 T (m = 18.9 mg, χ_MT = -358.00×10^{-6} eμ/mol.

Temperature / K	μ_{eff} / B.M.
2.00	0.52
300	6.98

7.4.5. Structure solution

Powder X-ray diffraction (PXRD) data were collected using a STOE STADI-P diffractometer in Debye-Scherrer geometry employing a Mo-Kα source, due to the typical fluorescence of Cu-Kα radiation for Fe-containing materials, see Figure 7.16. All reflections of the diffraction pattern could be indexed in the cubic system with lattice constants of 32.92 Å using the program X-cell .[10] The most likely space groups according to reflection statistics were F*d-3m*, F*d-3* and F4_132. For intensity extraction, a Pawley refinement using a Pearson VII function with Finger-Cox-Jephcoat correction was used. The low-angle tail of the first, dominating reflection at 2.1° is distorted by the influence of primary beam and beam stop. Therefore, the background was subtracted

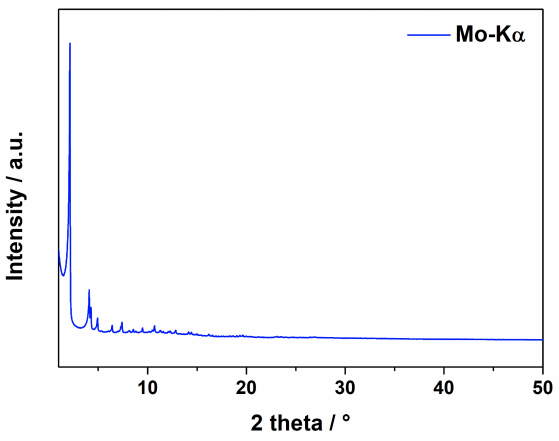

Figure 7.20 – PXRD of Cu-CAT powder recorded with Mo-Kα radiation from 1 to 50° 2θ.

manually. The parametrization was first determined by fitting over 3.0°-20.3°, excluding the first reflection. Using this parametrization, the tail of the first reflection was reconstructed. Finally, the Pawley refinement was performed for a range of 1.1°-20.3°, leading to Rwp = 1.72% and Rp = 3.68%, respectively. The structure was solved with the EXPO 2014 software package in the space group F4_132 using a direct-space approach (simulated annealing combined with a hybrid big bang - big crunch algorithm), employing a FeO_2C_6 fragment, representing the asymmetric unit.[11,12] All trials led to similar structures, with a diamond structure (dia) topology of supertetrahedra connected via trimeric iron clusters. The HHTP moieties forming the faces of the tetrahedra were also visible in all trials, showing various degrees of distortion. An oxygen atom in the center of the trimeric cluster was added manually before refinement, leading to an oxo-trimer arrangement, similar to many other MOFs, for example MIL-101.[13] This initial model was subjected to force field geometry optimization (Forcite). Rietveld refinement was performed in a range between 1.1°-20.3°, as reflection intensities beyond 20.3° are very low. Hereby, the triphenylene units were treated as a rigid body. The smallest Rwp-values were obtained for additional electron density such as water present in the pores. Because of the *dia* topology is made up of supertetrahedra, opposing tetrahedral surfaces connected *via* Fe deviate from an 180° angle. Structurally, this may imply a twisted bis-catechol coordination around Fe or a distortion of the HHTP groups, which make up the faces of the tetrahedra. For the two variants and combinations of the two, similar R-values were obtained. We therefore performed further density functional theory (DFT) calculations on different structure variants using DMol3.[14,15] The structure without crystal water was optimized without symmetry constraints using the generalized-gradient approximation (GGA) with the Perdew-Wang-91 (PW91) functional,[16] in which the semi-empirical Tkatchenko-Scheffler (TS) scheme[17] for the dispersion correction was included. The calculations were performed with a double numerical basis including d type

polarization functions on all non-hydrogen atoms (DND 3.5) and semi-core pseudopotentials (DSPP) for the core electrons. The spin-unrestricted formalism with a thermal smearing of 0.03 Ha was used. The convergence criteria for the geometry were 2.0×10^{-5} Ha, 0.004 Ha/Å, and 0.005 Å for the energy, force, and displacement, respectively, in which the self-consistent field convergence was set less than 1.0×10^{-5} Ha. The optimization resulted in a structure model in which Fe has a twisted bis-catechol coordination while the HHTP moieties remain largely planar. In this model, the oxygen atom in the middle of the triangular Fe-cluster is shifted perpendicular to the plane of the triangle from the central position. A further oxygen atom from a catechol group of a neighboring HHTP unit completes the slightly distorted octahedral coordination of Fe^{III}. These changes break the F4_132 symmetry, resulting in the space group F*32*. The Rietveld refinement of this structure, keeping the atomic coordinates of the DFT calculation, delivers $R_{wp} = 2.40\%$ and R = 6.74%, respectively (see *F-200515-n2-pawley-Tempfree-3-Rietveld-2-40* files). Some large temperature factors indicate a structural disorder and flexibility, which is expected since reflection intensities decay rapidly with increasing angle. The average composition determined by EDX, $C_{63.1}O_{29.0}Fe_{7.9}$ is close to the nominal refined composition of the structure $C_{63.2}O_{31.4}Fe_{5.3}$.

Table 29 – Final refinement parameters of the Fe-CAT.

Name	Fe-CAT
Refined Composition:	$C_{63.2}O_{31.4}Fe_{5.3}$ / ($C_{576}O_{286.24}H_{384}Fe_{48}$)
Mass formula (g/mol)	14565.7
Crystal system	Cubic
Space group	F *32* (196)
a(Å)	32.89770 ± 0.00103
V(Å^3)	35603.82
Crystal density (g/cm^3)	0.679294
R_p	6.74%
R_{wp}	2.40%

7.4.6. Charge-carrier pathway simulations

PM6 direct semiempirical molecular-orbital Born-Oppenheimer molecular dynamics (MD) with periodic boundary conditions was used to study the dynamic behavior of the structure using the EMPIRE19 program.[18–20] The spin-unrestricted formalism was used to calculate the broken-symmetry singlet state. The initial structure was obtained by optimizing the crystal structure

without crystal water and without symmetry constraints on the same level. This resulted in a structure that was very similar to the DFT optimized structure described above. The primitive cell (A, B, C) used for structure optimization was transformed into a cubic cell (X, Y, Z) using the following transformation: $X = A; Y = B - C; Z = C + B - A$. The resulting cell is twice the size of the original primitive cell. The cavities were filled with water to allow potential reactions between water molecules and the MOF, and to create a background level for the local properties. The resulting structure was then equilibrated using an NVT ensemble with a Berendsen thermostat at 300 K for 5 ps using 0.5 fs time steps. The energy and temperature diagrams of the MD simulation are shown in Figure 7.21.

The final structure from the MD was used to generate three-dimensional local electron affinity [21,22] and local-ionization energy [23] maps with the EH5cube program, [24] stored in Gaussian cube-file format [25] as orthogonal cells. Propagation of the hole or electron density in imaginary time used an in-house program. [26] Simulations of charge-transport were performed by applying a linear term to the external potential, describing a homogeneous electric field in the x-direction, as described in reference [26]. The simulations use the NVE ensemble, so that no constant temperature can be defined. A spherical Gaussian distribution was used as starting density of the electron or hole. The conduction paths were visualized with VMD. [27]

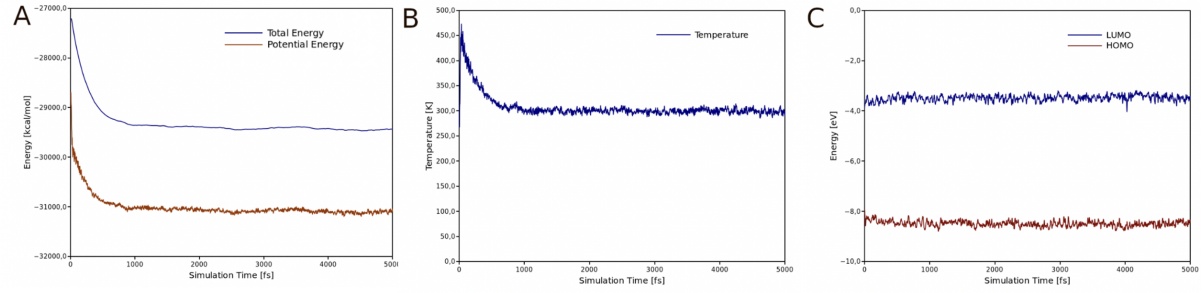

Figure 7.21 – MD simulation results: **A)** Total energy (blue) and potential energy (red); **8** Temperature; **C)** HOMO energy (red), LUMO energy (blue).

References

[1] E. Bill, Mössbauer Program mcal, **2019**
[2] G. A. Bain, J. F. Berry, J. Chem. Educ. **2008,** 85, 532.
[3] E. Bill, SQUID Program julX2, **2019.**
[4] E. Bill, EPR Program eview, **2019.**
[5] E. Bill, EPR Program esim, **2019.**
[6] Gaffney, B. J., Silverstone J. J., Simulation of the EMR Spectra of High-Spin Iron in Proteins (Plenum Press, New York, **1993**).
[7] R. P. Gupta, S. K. Sen, Phys. Rev. B **1974,** 10, 70.
[8] R. P. Gupta, S. K. Sen, Phys. Rev. B **1975,** 12, 15.
[9] A. P. Grosvenor, B. A. Kobe, M. C. Biesinger, N. S. McIntyre, Surf. Interface Anal. **2004,** 36, 1564.
[10] M. Neumann, Journal of Applied Crystallography **2003,** 36, 356.
[11] A. Altomare, N. Corriero, C. Cuocci, A. Moliterni, R. Rizzi, Journal of Applied Crystallography **2013,** 46, 779

[12] A. Altomare, N. Corriero, C. Cuocci, A. Falcicchio, A. Moliterni, R. Rizzi, J. Appl. Crystallogr. **2018,** 51, 505.
[13] O. I. Lebedev, F. Millange, C. Serre, G. van Tendeloo, G. Ferey, Chem. Mater. **2005,** 17, 6525.
[14] B. Delley, J. Chem. Phys. **1990,** 92, 508-517.
[15] B. Delley, J. Chem. Phys. **2000**, 113, 7756-7764.
[16] J.P. Perdew, Y. Wang, Phys. Rev. B **1992,** 45, 13244-13249.
[17] A. Tkatchenko, M. Scheffler, Phys. Rev. Lett. **2009,** 102, 073005.
[18] M. Hennemann, T. Clark, J. Mol. Model. **2014,** 20, 2331.
[19] J. T. Margraf, M. Hennemann,.B. Meyer, T. Clark, J. Mol. Model. **2015,** 21, 144.
[20] J. T. Margraf, M. Hennemann, T. Clark, J. Mol. Model. **2020,** 26, 43.
[21] B. Ehresmann, M. J. de Groot, A. Alex, T. Clark, J. Chem. Inf. Comp. Sci. **2004,** 44, 658-668.
[22] T. Clark, J. Mol. Model. **2010,** 16, 1231-1238.
[23] P. Sjoberg, J. S. Murray, T. Brinck, P. Politzer, Can. J. Chem. **1990,** 68,1440-1443.
[24] M. Hennemann, EH5cube; Cepos InSilico GmbH, Obermichelbach, **2019.**
[25] https://gaussian.com/cubegen/ accessed 16th May **2019.**
[26] M. Kriebel, D. Sharapa, T. Clark, J. Chem. Theory Comput. **2017,** 13, 6308-6316.
[27] W. Humphrey, A. Dalke, K. Schulten, J. Molec. Graphics, **1996,** 14,. 33-38. http://www.ks.uiuc.edu/Research/vmd/

8. Summary and outlook

During the course of this thesis we explored electroactive porous metal-organic frameworks - their on-surface synthesis and applications. The presented work can be divided into two major sections. In the first part, we introduced VAC as a fast and facile method for the on-surface synthesis of 2D layered MOFs, namely the M-CAT-1 series, on various substrate types. In the second section, we discussed the synthesis of two novel electroactive MOF series and their potential use in energy-storage or conversion.

We started our journey with the VAC method displaying a suitable tool for producing high-quality 2D MOF thin films. Using VAC we established the growth of the whole layered M-CAT-1 series onto various substrates including gold, glass, quartz and ITO. Hereby, the needle-like crystallites of M-CAT-1 were aligned normal to the substrate plane, achieving the on-surface synthesis of highly crystalline, oriented, homogeneous and compact films. Owing to the thickness at the nanometer range, electrical measurements were conducted as well as transient absorption spectroscopy for this class of materials. These techniques rendered the M-CAT-series as a photoactive material.

Fine-tuning of the VAC experimental parameters and detailed understanding gave us control over the surface morphology of M-CAT-1 thin films. We successfully linked the surface morphology to the modulators used in the synthesis protocol. Nanostructured as well as smooth surfaces were retrieved and the wetting properties were studied by contact-angle measurements. In this context, highly nanostructured films showed superhydrophilic and underwater superoleophobic properties. Based on the obtained properties, we built a proof-of-principle anti-fog coating working in a large temperature window.

Finally, we transferred the optimized VAC process from flat surfaces to 3D shaped objects. Here, we synthesized patches of oriented and crystalline M-CAT-1 nano-architectures on gold-coated stainless-steel meshes. The superhydrophilic and underwater superoleophobic properties of these meshes were demonstrated by the separation of various notorious oily pollutants such as crude oil, hexane, or silicone oil from water. The high purity of the filtrated water was monitored by means of COD measurements. Interestingly, the superhydrophilic properties enabled higher flux compared to non-modified meshes, rendering this MOF nano-architecture a promising candidate for separating oil-water at a large scale.

The above methods were merged into an international patent application claiming the VAC process as a universal technique for the synthesis of MOFs and related materials on various surfaces in a highly crystalline and oriented manner with tunable morphology. We state that

the VAC method is not only useful in aspects of basic research but might also be employed for industrial applications.

In the next project, we integrated a photoactive anthracene core into the well-known MOF-74 topology. Here, we successfully linked the importance of linker design to the obtained electrical conductivity. Based on the anthracene core we dramatically increased the electrical conductivity by six orders of magnitude compared to the pristine MOF-74.

Lastly, the synthesis of a novel cubic iron catecholate framework structure has been presented. The ferric compound showed several interesting properties, ranging from light absorbance over the whole visible and NIR spectral range up to high electrical conductivity. Furthermore, the framework revealed microporosity with a large BET surface area, rendering this novel compound a new type of light-weight and highly conducting material. Quantum mechanical calculations elucidate efficient electron paths along the framework backbone.

In summary, this thesis highlights the importance of high quality thin films since it opens a horizon of opportunities in materials science. Thin films can be more efficiently characterized by photophyscial and electrochemical means, charge carrier paths can be studied as a function of crystal orientation and devices can be designed. In the future, the knowledge gathered and discussed in this thesis could be transferred to more demanding 2D MOF based systems, *e.g.,* amino or thiol functionalized catechol compounds. MOFs arising from these building blocks are regarded as highly promising for many energy related application, however, the film synthesis of these materials remains a challenge. In this context, this work plays an important role in the understanding and experimental design for processing MOF into high-quality thin films.

Superhydrophilic and underwater superoleophobic surfaces generated from this work might serve as a blueprint for the design of novel nano-architectures showing extreme wetting properties. The reuse of wastewater and related water resources remain a world-wide problem to address, which is expected to become even more important in the near future since water consumption is continuously growing due to different global developments, *e.g.,* increasing wold population, climate change or rising water use in agriculture. In the context of oil-water separation, the knowledge from this thesis can be used finding solutions for emerging issues such as water scarcity by recovering water from contaminated sources. Aspects such as higher water flux can also be used in other research fields such as functional coatings in aerodynamics, underwater-coatings for metals, *e.g.,* in pipelines.

The integration of the sterically more demanding anthracene core in the MOF-74 structure demonstrates the potential of this versatile topology. In the realm of organic framework synthesis, the novel MOF-74 series serves as versatile and robust platform for the future integration of additional photoactive linker motives.

Finally, we demonstrated the synthesis of a novel ferric catecholate-based diamond topology. Based on this archetype structure, a variety of different collaborations and projects emerge on the horizon. First, the valency of the iron-oxo-cluster needs to be elucidated in detail to shed light on the origin of electrical conductivity as well as the color of this material. Detailed quantum mechanical studies are planned to verify the fine details of the charge carrier pathways along the framework backbone. The objective of this project is the synthesis of an isoreticular series of ferric MOFs built up from iron ions and catechol analogs.

In the end, I wish to note that in my view the beauty of the chemistry dealing with porous framework materials lies in the seemingly endless ocean of opportunities for today's chemists. I do hope that this thesis will provide some fruitful inspiration for the next scientific generation focusing on the film growth process and the design of electroactive MOFs.

A. Miscellaneous

The following two sections give a short overview about further projects, which have also been carried out, but unfortunately could not be completed and integrated as full chapters *prior* to the submission of this thesis. The overview contains a list of the contributing authors, the preliminary title and a short abstract giving the outline of the respective project.

Furthermore, the list of publications is given including all manuscripts being submitted and accepted during my academic career. The list is followed by a summary of the oral and poster presentations given as well as all the workshops and seminars attended. The chapter is concluded by the curriculum vitae.

A.1. Electrical conductivity in a helical and highly crystalline ethyne-anthracene based MOF-74

Manuscript in preparation. The following section contains a short description of unpublished work related to the ethyne-anthracene based MOF-74 project. The work was carried out in collaboration with Patricia I. Scheurle and Alexander Biewald.

Patricia I. Scheurle[†,a,b], Andre Mähringer[†,a,b], Alexander Biewald[a,b], Achim Hartschuh, [a,b] Dana D. Medina[*,a,b], and Thomas Bein[*,a,b] *Manuscript in prep.*

[a]Department of Chemistry, Ludwig-Maximilians-Universität (LMU), Butenandtstr. 11 (E), 81377 Munich, Germany.

[b]Nanosystems Initiative Munich (NIM) and Center for NanoScience (CeNS), Schellingstr. 4, 80799 Munich, Germany.

[†] The authors contributed equally to this work.

[*]Corresponding Author.

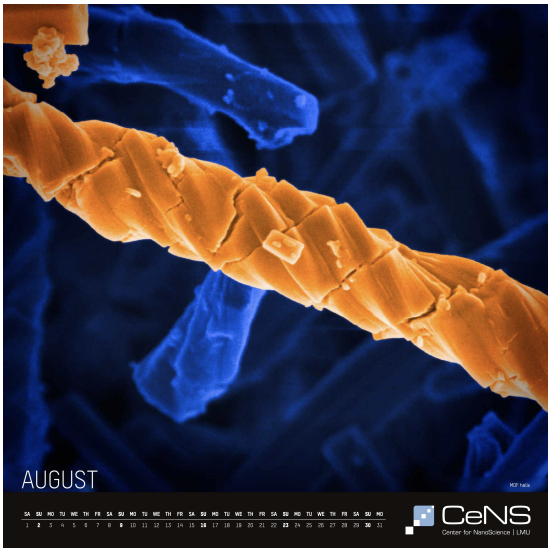

Andre Mähringer took part in the design and synthesis of the organic linker. He performed the structural simulations, carried out the linker synthesis, Pawley refinements and electrical conductivity studies.

Abstract

Over past two decades metal-organic frameworks have attracted enormous attention due to their high porosity, crystallinity, chemical variety and defined topologies. This portfolio of interesting properties opens a wide field of possible applications such as gas storage, molecular sieving or sensing. One prominent example is given by the well-established MOF-74 family. This class of materials is constructed from a linear di-hydroxy-carboxyl-functionalized phenyl core and 3d transition metals forming hexagonal channels. Hereby, the linker is interconnected in the *c*-direction by infinite helical metal-oxo chains forming hexagonal pore apertures in various sizes depending on the utilized linker system. In recent years, more electron-rich and photoactive building blocks have been incorporated in the MOF-74 topology to expand into applications such as energy storage and -conversion, transistors or solar cells. So far only a limited series of different motifs were reported in the literature among which are the NDI and ANMOF-74 representatives. Both systems feature a rather rigid linker geometry with limited or nearly no flexibility of the central photoactive core.

In this work, we expand the series of MOF-74 by integrating a novel and more flexible and electron-rich linking motif into the framework backbone. By adding two acetylene motifs to an adjacent central anthracene core terminated by phenyl groups decorated with ortho-hydroxy para-carboxylic functionalities we designed the building block 4,4'-(anthracene-9,10-diylbis(ethyne-2,1-diyl))bis(2-hydroxybenzoic acid), abbreviated AEHA. Using the AEHA building block and the divalent metal-ion Mn^{2+}, a highly crystalline ethyne-anthracene based MOF-74 structure (EAMOF-74) was obtained under solvothermal synthesis conditions. The structure of EAMOF-74 was elucidated by employing structural simulations and Pawley-refinement of the measured powder X-ray diffraction pattern. Structural refinements and simulations confirm the presence of a hexagonal lattice and a mesoporous structure. Interestingly, scanning electron microscopy revealed an unusual bulk morphology of helical rod-like crystallites in the size range of several microns with hexagonal cross-sections. The ratio between left- and right-twisted crystallites was determined to be 1:1, showing the presence of a racemate mixture. UV-VIS and single-crystal photoluminescence characterization shed light on the photophysical properties introduced by the AEHA core. Furthermore, van-der-Pauw measurements were conducted to access the electrical conductivity of the material.

A.2. Single-crystals of rare-earth metal catecholate based frameworks featuring defined emission profiles and electrical conductivity

Manuscript in preparation. The following section contains a short description of unpublished work related to the rare-earth metal catecholate based framework project. The work was carried out in collaboration with Marina Schönherr and Alexander Biewald.

Marina Schönherr[†,a,b], Andre Mähringer[†,a,b], Alexander Biewald[†,a,b], Patricia I. Scheurle[a,b], Achim Hartschuh[a,b], Thomas Bein[a,b], and Dana D. Medina[*,a,b] *Manuscript in prep.*

[a]Department of Chemistry, Ludwig-Maximilians-Universität (LMU), Butenandtstr. 11 (E), 81377 Munich, Germany.

[b]Nanosystems Initiative Munich (NIM) and Center for NanoScience (CeNS), Schellingstr. 4, 80799 Munich, Germany.

[†] The authors contributed equally to this work.

[*]Corresponding Author.

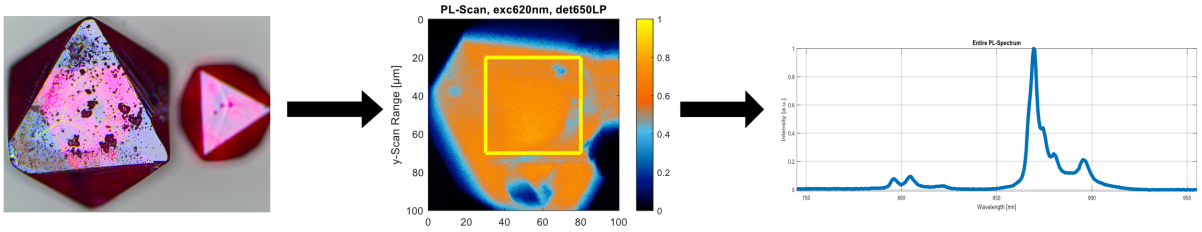

Andre Mähringer took part in the design of this project as well as the organization. Furthermore, he assisted in the linker synthesis, electrical conductivity analysis and the photophysical studies.

Abstract

Metal-organic frameworks comprising rare-earth metals based on catecholates have recently been reported. The combination of the catechol linkage motif and lanthanide(III) ions resulted in porous and crystalline frameworks featuring electrical conductivity. However, their photophyscial properties were not studied and remained elusive. Motivated by these discoveries, we prepared a series of lanthanide frameworks based on the 1,2,4,5-tetrahydroxy (THB) building block.

Eight single-crystals of respective lanthanide(III) ions (Nd, Sm, Eu, Ho, Er, Yb, Lu, Y) with different crystal structures, both literature-known (Nd, Sm, Eu, Ho, Er) and novel (Yb, Lu, Y) could be isolated. The obtained materials were analyzed by light microscopy and suitable crystals were selected and subjected to single-crystal X-ray analysis. Owing to the excellent data sets measured, the structures of all materials were successfully solved, revealing a stacked structure. One THB ligand bridges two lanthanide ions resulting in a hexagonal and ribbon-like 2D layered structure. A view along the *c*-axis shows that the sheets are build up from undulating six-membered rings giving hexagonal pore apertures. Further structural characterization by means of of PXRD, EDX, SEM, IR and TGA was performed. Furthermore, electrical conductivity analysis were carried out on ground and pressed pellets, confirming that charge carriers can percolate in this class of materials with electrical conductivity values reaching $10^{-7}\,\mathrm{S\,cm^{-1}}$.

For photophysical characterization, UV-VIS-NIR and PL spectroscopy on powders was performed. Interestingly, the selected materials showed sharp photonic emission bands as well as corresponding absorption features in their spectra. Moreover, single-crystal PL data were measured in collaboration with the Prof. Hartschuh research group at LMU. Here, selected lanthanide-based MOFs show defined characteristic emission profiles in the near-infrared region with lifetimes reaching 80 ns.

A.3. Taking stock of stacking

The following section is based on the manuscript:

Andre Mähringer[a,b], and Dana D. Medina[*,a,b], *Nat. Chem.* **2020,** 12, 980-987.

The manuscript was published as part of the *Nature Chemistry* news & views thematic issue - covalent organic frameworks.

[a]Department of Chemistry, Ludwig-Maximilians-Universität (LMU), Butenandtstr. 11 (E), 81377 Munich, Germany.

[b]Nanosystems Initiative Munich (NIM) and Center for NanoScience (CeNS), Schellingstr. 4, 80799 Munich, Germany.

*Corresponding Author.

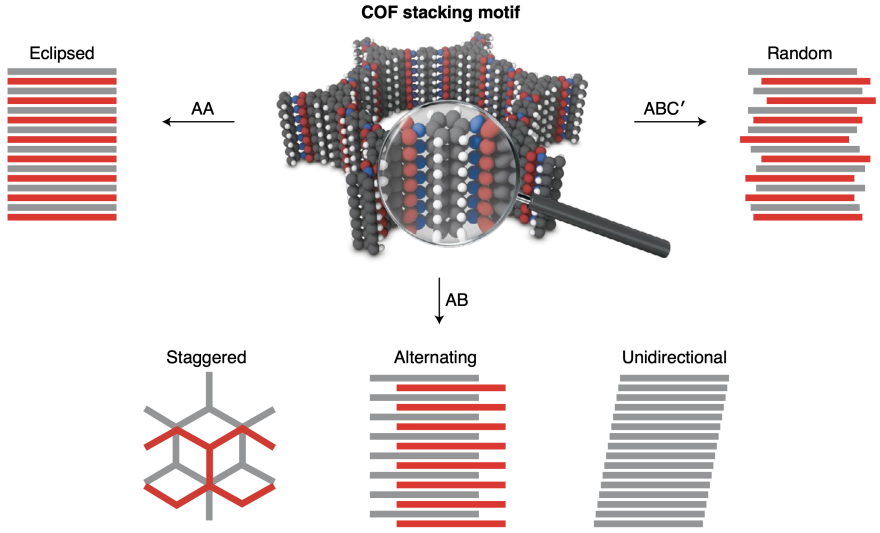

https://doi.org/10.1038/s41557-020-00568-z

Abstract

The manner in which adjacent sheets stack in layered covalent organic frameworks largely influences their material properties, including chemical stability, crystallinity and porosity. The layer stacking of COF has now been probed locally, showing disorder that is not detected through long-range characterization.

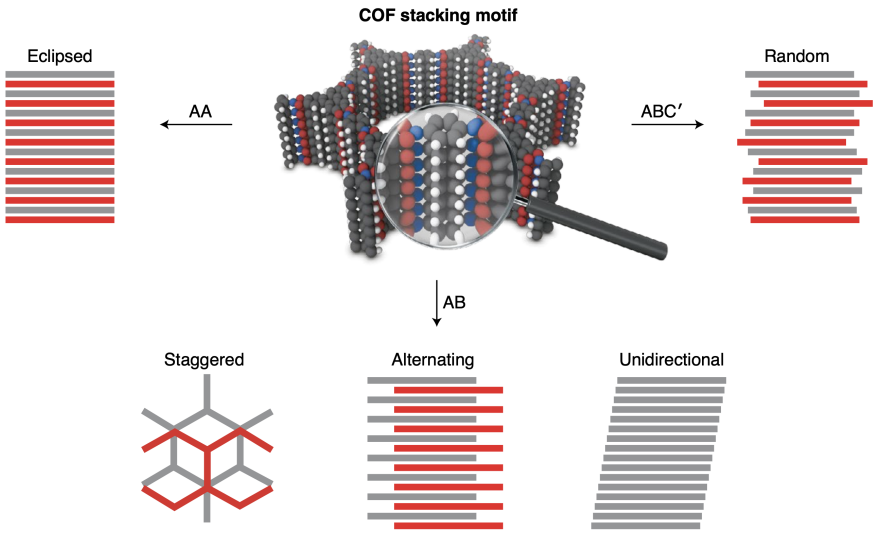

Figure A.1 – Visualization of different COF stacking motifs. Ordered types of layer stacking include the eclipsed mode, which means no layer offset (AA-stacking), and the systematic layer offset (AB-stacking). For the latter, staggered (in which the pore openings of one layer are obstructed by the nodes of adjacent layers; top-view shown), alternating, or unidirectional stacking types (side-view shown) are specified. A representative boronate-linked COF (reported in ref. [1]) is shown on this illustration; colour code for the COF: C, grey; b, blue; O, red; H, white. Adapted from ref. [6] under a Creative Commons license CC bY 3.0.

Since their discovery, covalent organic frameworks (COFs) have generated immense scientific excitement because of their thermal stability, vast chemical versatility and highly crystalline and porous structures capable of hosting guest molecules [1,2]. In the realm of porous materials, layered COFs – also referred to as two-dimensional COFs – are a particular case whose porosity and long-range order arise from the spontaneous assembly of extended molecular layers. In a nutshell, aromatic building blocks with defined geometry and symmetry undergo in-plane condensation polymerization, forming sheets that stack together through weak $\pi-\pi$ interactions to yield porous, crystalline, layered COFs. This rudimentary description gives a good overview of the formation process but conceals a wealth of details. Commonly, COF building blocks comprise aromatic cores frequently functionalized with peripheral heteroatom moieties that connect through polar,

reversible covalent bonds, such as imine bonds, to form layers[3]. Upon stacking, a certain degree of offset between adjacent layers is highly probable owing to electrostatic repulsion[4]. Just how sheets stack also largely impacts the COF properties more generally, such as chemical stability, crystallinity and pore accessibility (Fig.A.1). Better understanding, and in turn controlling, this structural aspect therefore holds great potential to help tailor COFs with the desired properties for specific applications. Despite its importance, the manner in which adjacent sheets stack is not straightforward to establish. Typically, a structure model is interpreted based on experimental powder X-ray diffraction (PXRD) data combined with a structure simulation derived from the building block geometry and unit cell refinement. Although the molecular structure of individual organic layers can be inferred with high certainty, the experimental data set is often not sufficient to determine the stacking mode precisely. Now, writing in *Chemical Science*, Bettina Lotsch, Maxwell Terban and co-workers have successfully assessed the layer-stacking mode of a known 2D tripheny-triazine imine-linked material[5] (TTI-COF) through a combination of total X-ray scattering data, stacking fault simulations and structure refinement[6]. The TTI-COF is formed by acid-catalysed condensation of two building blocks, both consisting of a nitrogen-rich triphenyl-triazine core, one functionalized with aldehyde peripheral groups and the other with amine ones (Fig. A.2).

For the present study, two variants of this COF were prepared at two different temperatures; the resulting COFs − referred to as HT and LT − are both crystalline and porous. At the higher temperature (120°C) a thermodynamically controlled process is enabled during which structural defects are easily repaired by the dynamic reversible bonds, yielding a stable product[7]. At the lower temperature (room temperature) the error-correction process is less efficient, resulting in kinetically trapped structural faults. Spectroscopic methods such as Fourier-transform infrared (FT-IR) and solid-state nuclear magnetic resonance (ssNMR), in combination with electron microscopy, were used to identify structural discrepancies between the two COFs. The FT-IR analysis showed characteristic amine and aldehyde bands in both COFs, though these were found to be significantly stronger in the LT form. This is attributed to trapped molecular fragments or unconsumed aldehydes and amines on the COF surface. In addition, the characteristic bands for triazine are shifted to lower frequencies in the LT form, which was assigned to a variation in stacking interaction.^{13}C and ^{15}N ssNMR broadened signals also indicated a wider distribution of the local chemical environment, which points to a greater disorder of the LT form. Transmission and scanning electron microscopy revealed significantly smaller domain sizes in the LT sample compared to the HT form. A substantial difference between the two COFs was their capacity to adsorb nitrogen gas − which represents a measure of their surface area. Here, the LT form showed a significantly lower surface area (338 m^2 g^{-1} compared to 1,308 m^2 g^{-1} for the HT form). Based on these results, the researchers concluded that in the case of the LT form, the internal

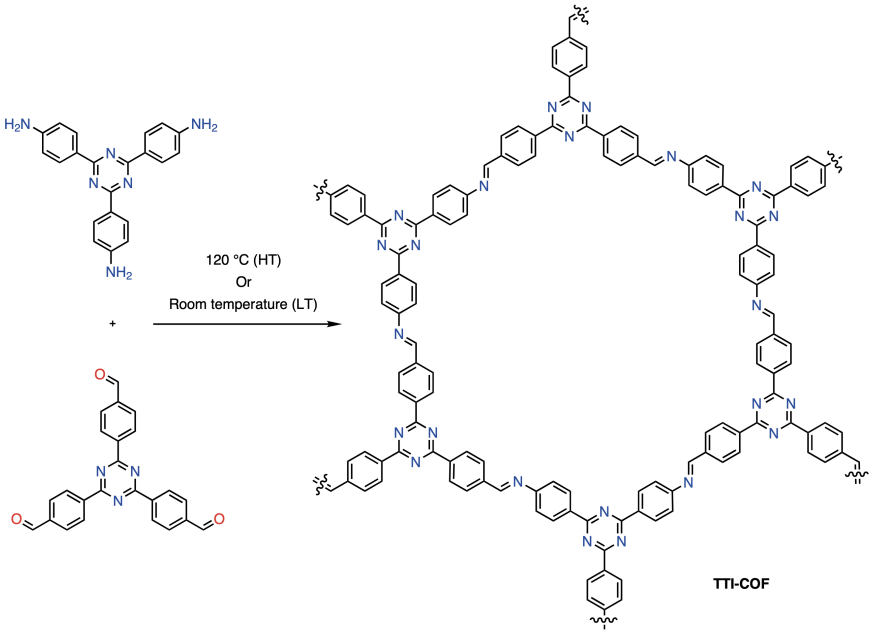

Figure A.2 – Reaction scheme for the imine-linked COF synthesis. The co-condensation of two triphenyl-triazine building blocks, one functionalized at its periphery with aldehyde groups and the other with amine ones, leads to the formation of the layered TTI-COF.

surface area is mostly inaccessible due to pore blockage. In addition, the nitrogen gas desorption curve of the LT form was accompanied with a hysteresis at relatively low partial pressures, which is attributed to limited diffusion of the guest out of the pore channels. Interestingly, the PXRD pattern of both COF forms indicate crystalline samples. Here, the HT form features splitting at several reflections, which is associated with symmetry reduction, whereas the diffraction pattern of the LT form showed single reflections with apparent broadening. As described by the researchers, briefly, ordered types of layer stacking include the eclipsed mode, which means no layer offset (AA-stacking), and the systematic layer offset (AB-stacking) (Fig.A.1). For the latter, staggered (a vertex of one pore is above the elevated pore opening), alternating or unidirectional stacking types are distinguished. In addition to these ordered modes, random stacking (ABC') is also possible. Based on the experimental PXRD data obtained and the modeling of the structures, atom position and structure refinement for both COF forms first indicated that a unidirectional AB-stacking model describes the HT form well, whereas a high-symmetry AA-stacking eclipsed model describes the LT form. Further characterization, however, in particular the structure refinement based on the LT structure model, also indicated that the framework is under considerable structural strain. In combination with a relatively low structural definition

obtained by gas sorption and electron microscopy, it pointed to the previous assessment − the high-symmetry AA-stacking model − being unlikely for the LT form. The researchers turned to total X-ray synchrotron-irradiation scattering analysis, which provides structural information also at short range (on the atom-to-atom distance scale) to further elucidate both COF structures. The interpretation of the data indicated a combination of an increased disorder in the layer offset − including distortion of pore shape, the presence of molecules trapped in the pores (such as unreacted or partially reacted building blocks, fragments, solvent), limited crystallite size for the LT form compared to the HT one, and relatively short coherence length in the stacking direction for both forms. In combination with structure refinement methods, the total scattering analysis pointed to a unidirectional AB-stacking model to describe both the LT and the HT COFs. Yet, although the overall data collected for HT is consistent with this, the findings for the LT form still conflict with the seemingly high-symmetry stacking mode obtained by the PXRD analysis. To clarify the stacking mode of the LT form, high-throughput stacking fault simulations, providing a large number of possible structure models, were used in combination with structure refinement. Through this approach, the researchers obtained the best structural fit with a random stacking model (ABC') − that is, random layer offsets − which can be translated to apparent single, non-split, broad reflections in the PXRD pattern of the LT form as the average structure. This is attributed to insufficient structure error correction and the formation of kinetically trapped stacking motifs when the COF is formed at room temperature, compared to the highly dynamic process occurring at high temperatures.

This interesting scientific journey between different characterization methodologies and possible COF structures shows that, in the context of defining the stacking mode, PXRD can, in some cases, be misleading. To date, only in rare cases does the PXRD analysis of COFs unravel a specific layer arrangement and the formation of defined molecular aggregates. These findings call for further investigation of the stacking mode of numerous layered COFs thought to adopt the AA-eclipsed conformation, when it is likely an average structure instead. In the absence of structural information derived from single crystals, a combination of high-quality experimental data and theoretical calculations can assist in identifying, with relatively high certainty, the stacking mode in COFs. In turn, this may also help to better understand structure−property relationships in these materials, and develop strategies controlling the manner in which layers stack − which is a significant aspect of COFs, and highly dependent on the sheets' chemical composition[8]. In future studies, it will be particularly interesting to connect the type of COF stacking mode and properties of COF-based devices, such as solar cells or transistor devices. Furthermore, identifying fragile COFs with weak interlayer interactions could pave the way for dynamic COF structures suitable for sensing applications. Beyond COFs, the present approach is also expected to be useful to probe the local structure of a variety of materials, such as hybrid

or inorganic compounds with short and long-range order particularly, where stacking interactions are a prominent part of the structure.

References

[1] Cote, P. A. et al. *Science* **310,** 1166-1170 (2005).
[2] El-Kaderi, H. M. et al. *Science* **316,** 268-272 (2007).
[3] Loseh, M. et al. *Adv. Funct. Mater.* **28,** 1705553 (2018).
[4] Lukose, B. et al. *Chem. Eur. J.* **17,** 2388-2390 (2011).
[5] Haase, F. et al. *Mater. Chem. Front.* **1,** 1354-1361 (2017).
[6] Pütz, M. A. et al. *Chem. Sci.* https://doi.org/10.1039/d0sc03048a (2020).
[7] Hu, L. et al. *ACS Appl. Nano Mater.* **3,** 6239-6269 (2020).
[8] Martinez-Abadia, M. & Mateo-Alonso, A. *Adv. Mater.* **32,** 2002366 (2020).

A.4. List of publications

I Energy efficient, ultrahigh-flux separation of oily pollutants from water with superhydrophilic nanoscale metal-organic framework architectures

Andre Mähringer, Matthias Hennemann, Timothy Clark, Thomas Bein, and Dana D. Medina. *Angew. Chem. Int. Ed.* **2021,** 60, 2-10.

II Highly conducting wurster-type twisted covalent-organic frameworks

Julian M. Rotter, Roman Gunthermann, Michael Auth, Andre Mähringer, Andreas Sperlich, Vladimir Dyakonov, Dana D. Medina and Thomas Bein. *Chem. Sci.* **2020,** 11, 12843.

III Taking stock of stacking

Andre Mähringer and Dana D. Medina. *Nat. Chem.* **2020,** 12, 985-987.

IV Oriented thin films of electroactive triphenylene catecholate-based two-dimensional metal-organic frameworks

Andre Mähringer, Andreas C. Jakowetz, Julian M. Rotter, Bernhard J. Bohn, Jacek K. Stolarczyk, Jochen Feldmann, Thomas Bein, and Dana D. Medina. *ACS Nano* **2019,** 13, 6711-6719.

V Nanostructured and oriented metal-organic framework films enabling extreme surface wetting properties

Andre Mähringer, Julian M. Rotter, and Dana D. Medina. *Beilstein J. Nanotechnol.* **2019,** 10, 1994-2003.

VI A highly crystalline anthracene-based MOF-74 series featuring electrical conductivity and luminescence

Patricia I. Scheurle, Andre Mähringer, Andreas C. Jakowetz, Pouya Hosseini, Alexander F. Richter, Gunther Wittstock, Dana D. Medina, Thomas Bein. *Nanoscale.* **2019,** 43, 20949-20955.

VII On-surface synthesis of highly oriented thin metal-organic framework films through vapor-assisted conversion

Erika Virmani, Julian M. Rotter, Andre Mähringer, Tobias von Zons, Adelheid Godt, Thomas Bein, Stefan Wuttke, Dana D. Medina. *J. Am. Chem. Soc.* **2018,** 14, 4812-4819.

VIII Electroactive Metalorganic Frameworks

Dana D. Medina, Andre Mähringer, Thomas Bein. *Isr. J. Chem.* **2018,** 58, 1089.

IX Efficient Yellow-Orange Phosphor $Lu_4Ba_4[Si_9ON_{16}]O:Eu^{2+}$ and Orange-Red Emitting $Y_4Ba_4[Si_9ON_{16}]O:Eu^{2+}$: Two Oxonitridosilicate Oxides with Outstanding Structural Variety

Christian Maak, Robin Niklaus, Franziska Friedrich, Andre Mähringer, Peter J. Schmidt, and Wolfgang Schnick. *Chem. Mater.* **2017,** 29, 8377-8384.

A.5. Patents

I Method for producing a metal organic framework film, metal organic framework film and use of a metal organic framework film

Andre Mähringer, Julian M. Rotter and Dana D. Medina. *WO2020157051*, Priority data 19154149.1 **29.01.19** EP.

A.6. Conferences

Oral presentations

I Dec. 2018 – *MOF 2018,* 6th International Conference in Auckland, New Zealand.

II Apr. - May 2018 – *DocMOF* Symposium 2018 in Burghausen, Germany.

Poster presentations

I Oct. 2019 – *EUROMOF 2019*, 3rd International Conference in Paris, France.

II Sep. - Oct. 2019– *SolTech Symposium* in Erlangen, Germany.

III Sep. 2019 – *e-conversion conference*, 1st International Conference in Venice, Italy.

IV Mar. 2019 – *31. Deutsche Zeolith-Tagung* in Dresden, Germany.

V Oct. 2018– *SolTech Symposium* in Würzburg, Germany.

VI Sep. 2018 – *CeNS Anniversary Conference 2018* in Venice, Italy.

A.7. Workshops and seminars

I Jan. - Feb. 2020 – Business basics. *Career Service, Ludwig-Maximilians-Universität München.*

II Aug. 2019 – Workshop in Scientific communication and poster presentation. *Doctoral Symposium, Technische Universität München.*

III Jul. 2019 – NIM summer retreat (Career and poster session). *Kloster Seeon im Seeon-Seebruck.*

IV Aug. 2018 – NIM summer retreat (rhetoric workshop and poster session). *Bergsee am Spitzingsee.*

V Jun. 2018 – Workshop in electrochemical characterization of coordination polymers. *Carl von Ossietzky Universität Oldenburg.*

VI Sep. 2017 – Workshop in electrochemical properties of coordination polymers. *COORNETs Workshop.*

VII Jan. 2019 – Basics in first aid. *Rettungsdienstschulen Bayern GmbH.*